Reshaping Elastomers with Light: First Principles Model of Diffusion–Induced Deformation

Thesis by

Ryan M. Turner

In Partial Fulfillment of the Requirements

for the Degree of

Doctor of Philosophy

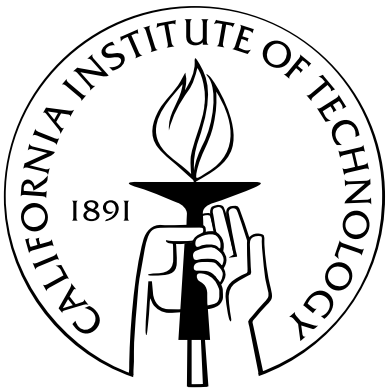

California Institute of Technology

Pasadena, California

2012

(Defended February 17, 2012)

To my grandpa, William Kenneth Turner, who modelled and taught the values of hard work necessary to finish this body of work.

Acknowledgements

I would like to begin by thanking the person most directly involved in this project: my advisor, Julie Kornfield. She has been invaluable as both a source of scientific insight and knowledge as well as a personal life coach. One of the most valuable things I learned while working for her is that my career is only one aspect of my life. I am particularly thankful for the freedom to explore job opportunities, including teaching at local community colleges, while under her tutelage.

I would also like to thank my professional colleagues, particularly Anna Pandolfi for introducing me to finite elements and for fascinating conversations about science, Alan Wineman for introducing us to the ideas of mixture theory, Robin Selinger and Charles Gartland for their help in developing a point–by–point finite element implementation coupling diffusion and deformation, and Rosanna Zia for providing me with assistance in solid mechanics. I would also like to thank my other committee members, John Brady and Zhen–Gang Wang, for providing insight into theoretical questions when Julie and I were at a complete loss.

The next two people have been extremely influential in helping me finish my degree: Anne Hormann and Marcy Fowler. Thank you for ensuring that I had meeting times with Julie regardless of deadlines and for all the hard work you put into the administrative details that I'm sure we don't always see. I also really appreciated all the advice and assistance that each of you provided in areas outside of the lab, particularly to Marcy for her support over the last couple months with all the thesis craziness. Without you two, no science would ever get done. Along that vein, I would also like to thank Kathy Bubash, Laura Lutz King, and Karen Baumgartner. In particular, Kathy's helpfulness is one of the main reasons I decided to come to Caltech.

I would like to thank the Kornfield group, past and present, for creating a friendly lab atmosphere, many laughs, and stimulating conversations (not always about science): Ralph (Ameri) David, Zuleikha Kurji, Paul Pirogovsky, Amy Fu, Yan Xia, Matthew Mattson, Rohan Hule, Ladan (Loddie) Foose, Artemis Ailianou, Ming-Hsin (Jeremy) Wei, Joyce Huynh, Ruoyu Zhang, Yasutoyo Kawashima, Dennis Ko, Wendy Gu, Boyu Li, Robert Tanner, Eric Pape, Charles Nickerson, Michael Mackel, Raphael Verduzco, Neal Scruggs, Derek Thurman, Lucia Fernandez–Ballester, Brad Olsen, Diana Smirnova, Shuichi Kimata, Bahar Bingol, Meisam (Iman) Hajimorad, Vivek Narsimshan, Carly Bond. I would like to particularly thank Ameri for bringing Ticket to Ride into the office and

our Friday lunch games, and Zuli for her unending empathy, encouragement, and optimism over the past seven years.

Of course with only half of my life spent in the lab, I have a great many other people to thank. I'd like to thank my family: my mom and step–dad for supporting me through high school and undergrad, both financially and with unconditional love and emotional support; my brother Andy for helping me revise this thesis and for his friendship that has grown the last seven years; my grandma and grandpa, whom I got to know better while living with them for four months; my dad and step–mom, who have always supported me; my aunts Lois and Joy, whom I've always looked up to as teachers; my cousin Alan for great gaming during the holidays; and the rest of my family, that would take up a thesis in itself to list.

I'd also like to thank my friends during this period of my life: Dr. Anthony Pullen for great scientific and spiritual discussions and his wife Bethany Pullen for their friendship, Julie Moreland and her new husband Daniel, Matthew Bayless, Annie Paek, Novita Liman, Keya Schaeffer, Yoon Seo, Rob Nelson, HRock friends past and present (David Phongsa, Gabriel Ahn and all the other Covenant Brothers, the Adams, the Higashis, the Ahns, the Pokrifkas, the list goes on...). You have all supported me, encouraged me, challenged me, and taught me more than I could ever express or repay. During the past seven years, I have grown as a man because of all of you. Thank you for your friendship.

Finally, I would like to thank my boyfriend, my best friend, and one of the best men I know: Gabriel Valdovinos. I would never have finished my thesis without his encouragment and help. He has had to put up with so much during the past couple months and I am exceedingly thankful for his support during this time. I appreciate it and love you immensely.

Abstract

Elastomeric photopolymers are a new class of materials originally developed at Caltech for use as intraocular lenses. These materials consist of a host network swollen with short–chain, photoreactive "macromers." Using a light source for selective photopolymerization, gradients in free macromer molecules are created, driving diffusion–induced shape change. Although models exist for external flow of solvent into a swelling gel or for gel deswelling caused by externally imposed forces, no known model exists to account for reaction–induced diffusion–deformation for a force–free material in which solvent can neither enter nor leave. To predict this unique reaction–diffusion-induced shape change, we propose a simple "two-component" model which treats macromer as converting directly into network strands. This model is first shown to be in good agreement with experimental data on the equilibrium swelling of elastomeric photopolymers [1]. We then use mixture theory to develop constitutive laws for the system stress and the flux of macromer by ensuring that the second law of thermodynamics holds. Finally, we implement the theory to a variety of problems—including a finite–element model of the light–adjustable lens—in each case systematically detailing the relative importance of the material parameters on the magnitude and rate of shape change. We determined that the shape change depends upon the rate of consumption of macromer (specified by the initial extent of reaction profile and the initial volume fraction of macromer) and is independent of the network modulus or the macromer molar mass. In addition, we found that the macromer molar mass serves only to determine the rate at which the deformation proceeds, whereas the network modulus serves to determine the magnitude of the internal forces experienced in the photopolymer.

Contents

List of Figures

List of Tables

List of Symbols

$\mathbf{v}_m, v_i^m$	Spatial velocity field of macromer	43
$\mathbf{v}_N, v_i^N$	Spatial velocity field of network	43
$\mathbf{v}, v_i$	Barycentric velocity field	43
V	Spatial volume	13
V_0	Initial volume	37
V_α	(Ch. 4) Volume of cell α	70
V_m	Spatial volume of macromer	15
V_{eq}	Volume at equilibrium	37
V_N	Spatial volume of network (initial, plus that inherited by reaction)	15
dV	Differential volume, spatial configuration	12
dV^d	Differential volume, dry network	12
dV_0	Differential volume, initially-swollen network	19
dV_α	Differential volume of species α	32
$dV_{\alpha 0}$	Differential volume of species α in reference	32
dV_f	Differential volume of fixed species	32
dV_R	Differential volume right after reaction	32
W	External work, extensive	14
Ω^d	The dry network body; reference configuration (§2.2)	11
Ω_0	Initially swollen network body; reference configuration (§2.3 onward)	11
$\Omega(t)$	Spatial configuration body	19
$\partial\Omega_1$	Boundary of $\Omega(t)$ on which deformation is specified	36
$\partial\Omega_2$	Boundary of $\Omega(t)$ on which stresses are specified	36
Ω_m	Reference configuration for macromer, mixture theory model	42
Ω_N	Reference configuration for network, mixture theory model	42
x	Cartesian coordinate, spatial configuration	88
$\boldsymbol{x}, x_i$	Spatial position	19
X	Cartesian coordinate, reference configuration	76
$\boldsymbol{X}^d, X_I^d$	Reference position (§2.2)	11
$\boldsymbol{X}$	Reference position, X_I (§2.3 onwards); spatial position, X_i (§2.2)	11
$\boldsymbol{X}_m, X_I^m$	Reference position for macromer, mixture theory model	42
$\boldsymbol{X}_N, X_I^N$	Reference position for network, mixture theory model	42
ξ	Extent of reaction	22
ξ_i	(§6.5.2) Extent of reaction profile for the ith reaction	128
ξ_I	(Ch. 5 and 6) Surface extent of reaction nearest the light source	77
y	Cartesian coordinate, spatial configuration	88
Y	Cartesian coordinate, reference configuration	76

Chapter 1

Elastomeric Photopolymers

1.1 Development of Elastomeric Photopolymers: The Light–Adjustable Lens

A cataract is a clouding of the intraocular lens in the eye due to changes in protein structure [2]. Cataracts are very common: over 1.5 million cataract surgeries are performed yearly in the United States alone and over 60% of people over the age of 60 have cataracts [2]. In tandem with the population progressively living to older age, cataract surgery has developed from the primative method of couching—a procedure in which the cloudy lens was dislocated into the vitreous cavaity of the eye by being struck with a blunt object—to modern surgical methods [3]. Current surgical methods make use of a two-step procedure. First, the cloudy lens is removed via phacoemulsification, a procedure in which the cloudy lens is shattered with ultrasound and the pieces removed through a small incision. Using the same incision, a foldable intraocular lens is surgically implanted to replace the old lens.

By carefully selecting the implanted lens prior to surgery, modern surgeons strive to achieve postoperative emmetropia—perfect vision—for each patient. However, complications such as those due to wound healing, displacement, and rotation of the lens in the lens cavity, and posterior capsule opacification cause fewer than 50% of patients who had emmetropia before surgery to retain it after surgery [4]. In addition, many patients have other preexisting ocular defects—myopia, hyperopia, and astigmatism—which further deter surgeons from correcting vision perfectly. Although patients can be fit for corrective spectacles after the operation, several alternative methods have been developed [4]. One notable solution is to use a multifocal lens containing concentric zones of differing lens power allowing a patient to focus both at near and far distance [5]. Another solution uses a three–piece intraocular lens with an inflatible diaphragm; the lens is adjusted by injection or removal of a fluid [6]. The second method is postoperatively invasive while the first requires knowledge of the wound healing process before implantation. An ideal intraocular lens would be non–invasively

adjustable after operation.

Because of the position of the lens in the eye post–operation, a reasonable non–invasive adjustment would involve light. For example, an entire branch of research has centered around light-activated polymers [7]. One class of materials developed are liquid crystal elastomers (LCE) which can undergo deformation due to isomerization in the presence of light. Theory has been developed to predict that LCE beams will curve when exposed to Beer's law decaying light profiles through the depth [8–12]; bending an initially flat beam creates an optical element. Because such shape changes are non–invasive and reversible, these materials show particular promise for applications in microfluidics [13]: examples include light–driven micropumps [14], micro cantilevers [15], and optically driven nanoscale actuators [16]. However, because the shape changes in LCEs are reversible and imprecise and the materials themselves tend to be relatively opaque, these materials would not produce a reasonable intraocular implant. A more translucent material is necessary and the shape changes need to be stable and reproducable with a fine degree of precision.

A second type of material that meets these qualifications is a photopolymer [17]. A photopolymer consists of a glassy polymer backbone filled with small monomor particles. Irradiation with light causes monomer particles trapped inside the polymer backbone to photopolymerize, causing local volume changes as well as local changes in refractive index and modulus. Because the photopolymerization is permanent and a large degree of control can be exerted on the light–source, submicron features which are permanent and precise can be written into a photopolymer and stored; for this reason, a main application of photopolymers is in holographic storage devices [18, 19]. However, these materials have several limitations. First, the polymers used are glassy, inhibiting their use in intraocular lenses that must be folded and inserted through a small incision during surgery. More importantly, the glassy nature of the polymer makes diffusion occur exceedingly slowly and write times are only reasonable for changes on the order of microns. Although this is appropriate for holographic storage, the write time would be prohibitively long for adjustments to an object of the length scale of millimeters, such as an intraocular lens. Lastly, the materials used for these photopolymers are toxic: monomer can leach out of the polymer backbone and into the eye.

Observing the constraints inherent in photopolymers, Schwartz, Grubbs, and Kornfield designed an elastomeric photopolymer using an elastomeric matrix backbone as opposed to the rigid, glassy one [20]. This material allows changes in shape to proceed due to reaction–diffusion rather than local volume changes. The elastomeric photopolymer consists of an elastic host network (Fig. 1.1a) which is swollen with short–chain molecules—called macromer—and photoinitiator (Fig. 1.1b). The short–chain molecules are designed to be chemically identical to the host network chains except for photo–reactive end–caps which allow for cross–linking of the free chains by irradiation with light. When a region of the photopolymer is exposed to the frequency of light that activates the photoinitiator, the macromer molecules in that region polymerize into an interpentrating network (IPN) within the

original host network (Fig. 1.1c). The depletion of free macromer by the polymerization reaction creates chemical potential gradients in the polymer gel: the chemical potential is higher in zones that were not irradiated since they have more macromer. These gradients drive diffusion of the free chains from the non–irradiated regions into the irradiated regions. Since the elastomeric photopolymer is an incompressible gel, the transfer of mass between regions results in local volume changes as the macromer chains diffuse. The regions that were irradiated swell as there is a net influx of mass, whereas the regions that were not irradiated shrink as they lose mass to the irradiated regions. This causes a net global shape change (Fig. 1.1d). To maintain the desired shape of the photopolymer for long–term use, the material can be uniformly irradiated to cross–link any left-over free molecules once the desired shape has been obtained (Fig. 1.1e). This "locks in" the shape of the material and prevents possible leaching of the free chains or photoinitiator into the surrounding medium. A lens crafted of elastomeric photopolymer can then be non–invasively adjusted after operation by selective irradiation [20].

Clinically, the light–adjustable lens is implanted in the patient and wound healing is allowed to occur. Once the lens has stabilized, a clinician can use a Fitzeau interferometer to determine the precise correction needed by that patient to achieve emmetropia [21]. Clinically, the irradiative "adjustment" proceeds for a minute or two and the material is designed so that the resulting diffusion–deformation process is complete within 12–18 hours [4]. The clinician then examines the patient and determines whether subsequent corrections are necessary; because only small amounts of macromer need to be consumed to achieve necessary corrections [4], plenty of free macromer remains available for subsequent correction. Once all corrections have been made, the final shape of the lens is "locked in" by reacting the remaining macromer using a stronger irradiation than that used during the treatment. This guarantees that any created change in lens shape will be stable and eliminates the possibility of reactive molecules transferring from the lens to the body in future years.

The light–adjustable lens has achieved clinical success in postoperatively adjusting hyperopia [22], myopia [23], and astigmatism [24,25]. However, the developed irradiation profiles to achieve a desired correction—known in the industry as nomograms—are complicated and determined experimentally through trial and error [21]. Some nonograms have been elusive to attain in the clinic: for example, a patient needing both a spherical (myopic or hyperopic) correction and an astigmatic correction must receive each day-long treatment separately because no known nomogram has been found to make both corrections at the same time. Another specific example of the limitations of experimentation-based determination of nomograms is found during the lock–in process. Because of the intensity of the irradiation field used during lock–in, a significant amount of scattering agent must be put in the matrix to protect the patient's retina [26]. However, the addition of even a small amount of UV blocker causes a change in lens shape for a simple, uniform irradiation profile. Rather than attempt

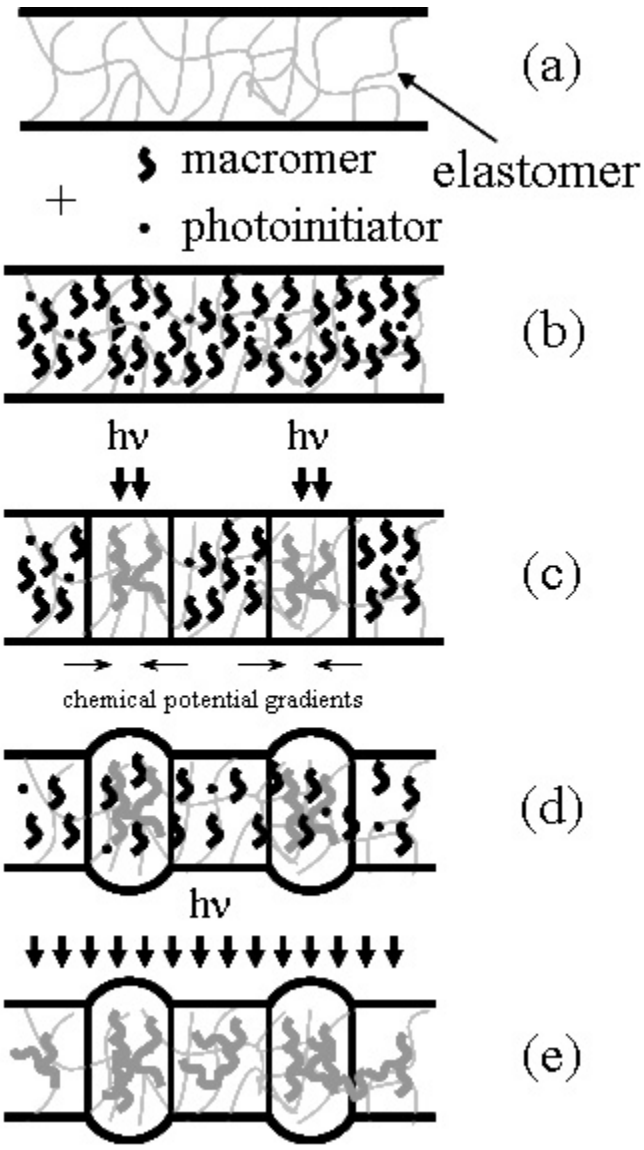

Figure 1.1: An elastomeric photopolymer is a gel made of a supporting elastic matrix (a) into which a solvent of short–chain molecules with reactive end–caps and photoinitiator is swollen (b). When the photopolymer is selectively irradiated with light, the free chains in the irradiated regions photopolymerize to form an interpenetrating network (c). This creates gradients in the chemical potential of the free chains and results in diffusion of the chains from non–irradiated regions to irradiated regions (d). Due to the incompressibility of the gel, the net effect of transfer of the free chains is that the irradiated regions swell, whereas the non–irradiated regions shrink. Once the desired shape for the photopolymer is obtained, it can be "locked–in" by uniformly irradiating the material to remove any remaining free chains (e).

to examine the underlying physics which would provide a tool–kit for nomogram design, the clinic continues to operate through experimental trial and error.

In earlier work, Pandolfi and Ortiz made a first attempt to explain the underlying physics of the light–adjustable lens [27]. Although the model developed therein successfully predicted final lens power changes, the simulations developed were unable to predict the kinetics of shape change. To clinicians, the rate at which the adjustment occurs is of as much importance as the magnitude of the adjustment itself. In addition, the model made no connection to material design parameters, despite the availability of experimental data [1] and the nomograms presented are parameter fit from nomograms already established through experimental trial and error. In this sense, the model developed is more reactive than predictive. Given the limitations of this preliminary theoretical work, we set out to propose a model based upon first principles which could be used to predict both the rate and the magnitude of shape changes experienced in elastomeric photopolymer lenses.

One of the primary goals of this work is to connect theory with experiment. The data presented in Pape's Ph.D. thesis [1] provides a starting ground for modeling from first principles. This work considers all the material design parameters necessary in creating an elastomeric photopolymer: initial network creation, extent of equilibrium swelling with macromer as well as rates of diffusion, and reaction rates for the photopolymerization process. Because the materials used therein consist of a PDMS network with PDMS bis–methacrylate end–capped macromers (§B.1), we also draw upon experiments and theory performed by Cohen and co–workers [28–31]. In this manner, we seek to develop a theoretical tool–kit founded on experimentally adjustable material parameters which predicts the effects of those parameters on the magnitude and rate of shape change.

There are many features of elastomeric photopolymers which makes modeling them unique. Elastomeric photopolymers are self–contained: material neither enters nor leaves because the macromer chains are designed to have a stronger affinity for the network than the surroundings. As such, all reaction and diffusion, occurs internally. Furthermore, there are no external forces acting on the system; in the light–adjustable lens, for example, the only force experienced on the lens is on a small area attached to the thin haptics that keep the lens from rotating and shifting. For this reason, all shape change experienced is due solely to the motion of macromer molecules: it is the spatial conversion of material which provides the driving force for all shape change. In this way, there is an intimate coupling of reaction, diffusion and deformation which requires a multidisciplinary approach to the problem.

1.2 Existing Theories on Solvent–Driven Deformation of Polymer Gels

We begin by discussing existing theoretical work on diffusion–deformation behavior in polymer gels. The pioneering work on the swelling of polymer gels is attributed to Flory and Rehner [32–35]. Using statistical mechanics, the network chains are modeled as random walks. Under the action of a solvent, the network chains stretch and they experience a net decrease in entropic configurations. The solvent, on the other hand, experiences a net entropic gain by mixing with the network. Equilibrium is established when these two entropic forces are in balance: the amount of macromer that can swell into a given gel is determined by thermodynamics. The choice of material parameters, then, sets limits on the amount of initial material available for reaction–diffusion in elastomeric photopolymers. We extend the work of Flory and Rehner in Ch. 2 to elastomeric photopolymers.

The first proposed model of the kinetics of diffusion in polymeric gels is due to Tanaka, Hocker, and Benedek [36], later modified by Tanaka and Fillmore [37]. The original model was successful at predicting the kinetics of swelling spherical gels but failed for general anisotropic swelling [38]. Only recently has a body of work been developed which can successfully capture general anisotropic swelling behavior: the stress–diffusion coupling model (SDCM) [39–41]. This theory couples polymer diffusion to deformation by using an equivalent of Darcy's law, treating the gel as a porous solid. Although the authors have successfully applied this model to several anisotropic problems [40–44], their work is based on external pressure gradients driving flow into the gel. As such, they are able to treat the volume fraction inside the gel as constant in time, implying that the gel is always in chemical equilibrium with the solvent bath. In our applications, the material is self contained: there are no external pressures driving flow into the gel. Furthermore, it is the spatially varying nature of the volume fraction field coupled to local concentration of volume that causes shape change. For this reason, the use of the SDCM equivalent of Darcy's law would be inappropriate for elastomeric photopolymers.

Because of the inability to use the kinetic constitutive relation of the SDCM, we turn to another body of work: mixture theory [45–48]. At its basis, mixture theory is essentially just an extension of the continuum model from one continuum to multiple, overlapping continua [49]. Each point in space is assumed to be occupied by all constituents of the material; that is, each constituent is assumed to satisfy the continuum approximation. In this way, each component has associated with it unique material properties such as density, velocity, and internal energy. One of the distinct advantages of mixture theory is its inheritance from general continuum mechanics of a systematic method for developing constitutive relations which implicitly satisfy the second law of thermodynamics [50]. An example of the importance of a developed constitutive law intrinsically obeying the second law is seen in work modeling growth in tissue [51]. These authors question the theoretically similar work

performed in [52] solely because the developed constitutive relations do not take the second law into account. Because mixture theory allows the direct incorporation of thermodynamic knowledge into the constitutive equations, we can systematically develop constitutive laws predicting the stress and kinetics in elastomeric photopolymers from first principles.

Since its inception in the 1960s, mixture theory has provided a rigorous framework for treating previously intractable problems in a variety of fields. Early successes in mixture theory included modeling the flow of a Newtonian fluid through an elastic solid [53], propagation of waves through a solid–liquid mixture [54], and deformation of a mixture of two non–linear elastic solids [54]. More recently, applications have blossomed to include modeling of phase transitions and particulate mixtures (see [55] for sources and more examples). Mixture theory has also been used to model growth processes in biology for use in fields such as cartilage engineering [51, 56, 57], muscle and tendon engineering [52], and in modeling the aorta [58].

Rajagopal, Wineman and coworkers have used mixture theory to model the transient swelling of a polymer network due to solvent [59]. Using a free energy for swelling given from general polymer physics [60], the authors derive constitutive relations for the partial stress tensors of both the solvent and the polymer that implicitly satisfy the second law of thermodynamics. After neglecting inertial effects and body forces, the authors solve a steady, one–dimensional problem in which a fluid is moving through a polymeric solid in a variety of geometries [59, 61–63]. Although the only experimental data with which the authors could compare results was in the case of pressure-driven flow through a flat plate [64], the non–linear diffusive behavior observed in experiment was successfully predicted [59].

Although we will follow the ideas of Rajagopal and Wineman, in deriving a relationship for the flux of macromer in terms of a driving force in Ch. 3, we note that there is an inherent complication in solving the mixture theory equations directly: the inability to indepedently apply boundary conditions for each component [65–67]. There are several ways around this: for example, a few authors have avoided this complexity by translating the differential equations of mixture theory into a variational problem [68, 69]. Using non–equilibrium thermodynamic principles [70, 71], these authors developed a variational model of the time–dependent behavior of a swelling gel in which the boundary conditions were forced to hold implicitly; this model was shown to be equivalent to the mixture-theory model developed by Rajagopal and Wineman. The model developed requires two specified functionals: 1) the free energy which is minimized in time and 2) a dissipative energy functional used to determine the constitutive law for the flux of solvent. Although exisiting theory can be used for the free energy functional of a polymeric gel (Flory and Rehner), Baek and Srinivasa had to chose a relation for the dissipative energy functional such that it returned the constitutive laws of mixture theory. In general—such as in the case of including reaction—specification of the dissipative energy functional is non–trivial.

Around the same time, simultaneous approaches not requiring a dissipative functional were developed by a number of authors [72–76]. Like mixture theory, these authors make use of the second law of thermodynamics to postulate a constitutive law for the flux of solvent into a swelling gel. The differences between each of these models is minor and all authors solve one or two types of problems: force and deformation of a gel caused by an externally imposed flux of macromer, or the flux of macromer caused by an externally imposed mechanical force. None of these developed theories provide a framework for a force-free, self–contained elastomeric photopolymer in which deformation is caused by reaction due to a light source.

This thesis expands the works of the above authors by including the effects of reaction specific to elastomeric photopolymers. In the photopolymer, many components are present and have particularly complex time dependence during and shortly after irradiation: photoinitiator, radical fragments of the photoinitiator, propagating radicals, unreacted macromer, original host network, and interpenetrating network (IPN) formed by polymerization of macromer. In addition, passive dye molecules may be included to attenuate light with depth in the sample. As a preliminary model, we make several simplifying approximations. Based on clinical experiments in which the photopolymer is only exposed for a short amount of time (< 5 min) relative to the time it takes for diffusion (≈ 1 day), we first treat reaction as instantaneous. In addition, we furthermore treat the initial extent of reaction as a one–to–one mapping with the irradiation field, rather than specifying the complexities of ray tracing and other optical effects. Finally, experimental characterization of photoelastomers has revealed that the effective crosslink density of the network is only weakly modified by formation of the IPN: the elastic modulus increases by less than a factor of two [1]. We will show that, to good approximation, this allows the created IPN to be modeled as additional network strands supplementing the original network; that is, a specified extent of reaction profile will be assumed to convert macromer directly into network. Although it is not *a priori* obvious that this "two-component model" is a good approximation, we will show that the model can successfully capture the qualitative behavior of elastomeric photopolymers.

1.3 Summary of Chapters

The remainder of this thesis proceeds as follows:

- Chapter 2 begins with a review of the thermodynamic analysis done by Flory and Rehner to introduce nomenclature and methodology used throughout this thesis. After reviewing classical equilibrium gel swelling via the Flory–Rehner equation, we present the details of the "two-component model" in which macromer is modelled to convert directly and instantaneously into network strands. The physical consequences of this model are discussed and compared to experimental work done by [1]. The parameter space in which the two-component model is a

good approximation is discussed and a small adjustment to this model (the "three-component" model) is proposed for regions in which the two-component model fails. Finally, a methodology is proposed in which the equilibrium shape of an elastomeric photopolymer can be found from the initial extent of reaction profile by minimization of the free energy functional developed.

- Chapter 3 presents the framework for solution of general transient problems in terms of mixture theory. The governing differential equations are shown to be the same as those obtained from the variational approach derived in Ch. 2. In addition, the second law of thermodynamics is used to postulate a constitutive relationship between the flux of macromer and a driving force. The resulting kinetic law is examined and compared to the work of other authors.

- Chapter 4 takes the theory developed in Ch. 2 and 3 and applies it to a simple case of two small elements in thermodynamic contact. To illustrate the importance of the various material parameters, two systems are studied: one in which chain stretching is completely ignored (the "slip" case) and the other in which chain stretching is included (the "conforming" case). These studies examine simplifications that can be made to the model based upon the appropriate clinical parameter space.

- Chapter 5 applies the theory of Ch. 2 to a beam constrained to a solid surface. This expands the two-cell model to a system with one–dimensional gradients due to the extent of reaction profile. The stresses and strains generated are predicted and connected to material parameters and reaction profile parameters. In addition, the developed stresses and strains are used to determine the deformation the beam would attain were it released and allowed to attain a constant curvature.

- Chapter 6 finishes the thesis with an examination of light–induced deformations of a fully three–dimensional, transient, light–adjustable lens. A novel finite element model is used to apply the model equations of Ch. 2 and 3 to predict shape changes in time. Using axisymmetric profiles, the lens-power changes are shown to be due to diffusion, and the magntiude of the power changes are examined in terms of material and light parameters. We also provide a preliminary examination of the effects of changing the light profile on the observed power change.

Chapter 2

Equilibrium Analysis from Thermodynamics

2.1 Introduction

We begin our study on predicting the reaction–induced deformation of elastomeric photopolymers by first considering their thermodynamics. It is the balance between stretching of network chains and mixing free energies which gives our materials, their unique properties. We must therefore develop a free-energy based upon this balance; minimization of this free energy will drive the deformation of the material in time. The free energy developed must be consistent with first principles and have a connection to experimentally determined material parameters. It must be able to correctly predict the swelling and mechanical properties of these materials as well as provide a connection between reaction–diffusion–deformation. The conclusion to this chapter presents an energy minimization method which determines the final equilibrium shape for a system; we will show in Ch. 3 how the same free energy can also be used to solve transient problems with mixture theory.

In pursuit of developing a free energy functional, we begin by first considering the stretching of the dry network (§2.2.1). Reviewing the classical derivation of the expression for the energy of stretching network chains in an affinely deformed network will allow us to introduce the notation and physical principles that are used throughout this thesis. We then consider the free energy of swelling such a network with small–chain macromers (§2.2.2). Following Flory [35], we assume additivity of stretching and mixing energies and discuss how it is the competition between mixing and stretching which gives our material its unique properties (§2.2.3). In §2.3, we include the effects of reaction through two different models: 1) the "two-component" model, which treats photopolymerized macromer as additional host network strands, and 2) the "three-component" model, which allows the macromer to become a separate species of dispersed nodules. In both cases, we ignore the heat of reaction, assuming that the major energy contribution is due to the swelling and stretching of network chains. Comparison to experimental data illustrates that the two-component model is

sufficient to predict both the increase in material modulus experienced upon photocuring and the equilibrium swelling behavior of photocured samples. The three-component model is shown to be a plausible correction to the two-component model in the case where the nodular nature of the macromer upon reaction becomes more important. We finish this chapter by illustrating the energy minimization principle that will be used throughout the rest of this work. This energy minimization is shown to lead to the same relations as those obtained through classical continuum mechanics (discussed in Ch. 3).

2.2 Thermodynamics of Network Swollen with Macromer before Reaction

Consider a host of precursor chains having an average molar mass M_p and some known polydispersity index. We first consider the pure host network formed from these precursor chains, through some cross–linking process. The character of the network is measured in terms of M_c, the average molecular weight of a network strand between cross–link junctions. In general, this value will be different from M_p because of the possibility of loops, dangling chains and other structural defects depending upon reaction conditions and the functionality of the cross–linker [28]. In addition, there is also discussion in the field as to whether entanglements act as crosslinks or restrict the motion of crosslinks [30]. For the purposes of our discussion here, we will take the character of the network to be defined by the shear modulus after the sample has been cured and any solvent has been extracted (denoted G_{dry}). In practice, the value of M_c is deduced from the modulus and represents an estimate on the length between network strands, hiding the details of network defects (dangling chains, loops, entanglements, etc.). Theoretical results will be compared to the results of Pape who carefully chose reaction conditions to minimize the number of defects inherent in the network [1].

We now examine deformations of this host network; this will be useful in modeling how chains are stretched upon swelling with solvent. Since the crosslinked network has not yet been swollen, we call this material the "dry network." To denote variables related to this stage, we use d as a superscript. For example, we label the region of space that the crosslinked network occupies as Ω^d (Fig. 2.1). We take this initial, dry network as the reference configuration for this section (§2.2). The position of each material point in Ω^d is marked by a vector $\boldsymbol{X}^d$ relative to some coordinate system. When the dry network is put in a bath of solvent, it swells. Let the swollen configuration of the object be Ω_0; this is the spatial configuration for this section (§2.2, note that it becomes the reference configuration in §2.3). Each spatial point is given a different label $\boldsymbol{X}$. We use Einstein and Berkeley notation throughout: the subscript that indicates the vector component is upper case for the reference configuration (X_I^d being equivalent to $\boldsymbol{X}^d$) and lowercase for the spatial component (X_i being equivalent to $\boldsymbol{X}$). There is a one–to–one mapping, χ_i, between each point in the reference

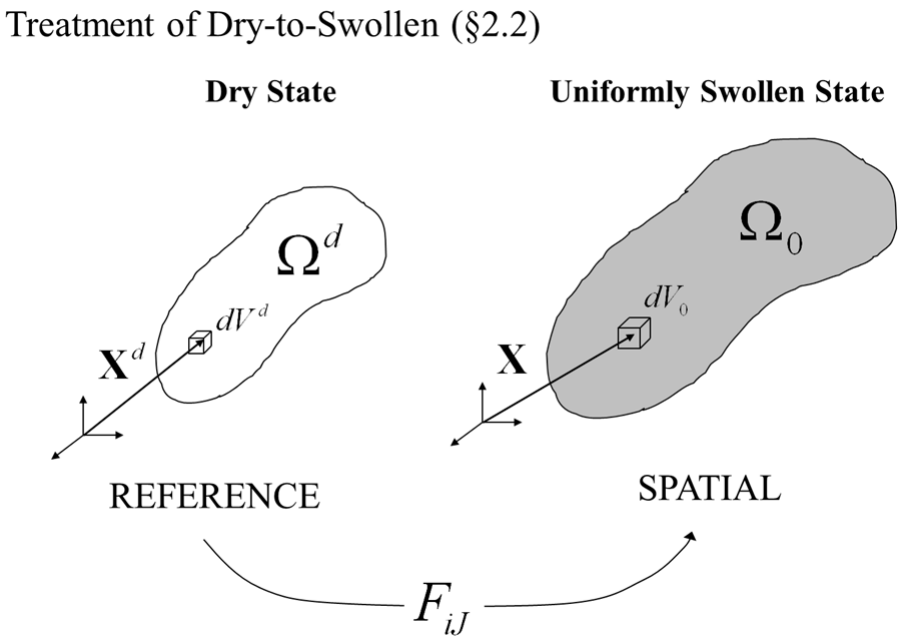

Figure 2.1: The kinematics of deformation in §2.2: A dry host network (occupying Ω^d) absorbs small-molecule macromer chains to occupy the region Ω_0. Note that the superscript "d" is used throughout this thesis to indicate the "dry state" and is not an exponent.

configuration and each spatial point

$$X_i = \chi_i(\boldsymbol{X}^d). \tag{2.2.1}$$

The gradient of this mapping

$$F_{iJ}(\boldsymbol{X}^d) = \frac{\partial \chi_i(\boldsymbol{X}^d)}{\partial X_J^d}, \tag{2.2.2}$$

is the deformation gradient. For example, the determinant of F_{iJ} measures local volume changes

$$\det F_{iJ} = \frac{dV}{dV^d}. \tag{2.2.3}$$

Here dV^d is the infinitesmal volume of the material point located at X_I^d in the reference configuration and dV is the volume of that point after it is swollen and located at X_i.

2.2.1 Thermodynamics of Stretching the Dry Network

Having defined our system kinematics, let us review the thermodynamics associated with stretching the dry network. Assuming that our network deforms affinely (i.e., any macroscopically imposed deformation is uniformly distributed at a microscopic level across the chains) and that the network chains obey Gaussian statistics, the entropy loss from an initially unstressed state due to stretching

the material along three directions in an orthonomal basis is [35]:

$$\Delta S = -\frac{k\nu_e}{2}\left[\alpha_x^2 + \alpha_y^2 + \alpha_z^2 - 3 - \ln\left(\alpha_x\alpha_y\alpha_z\right)\right]. \tag{2.2.4}$$

Here, k is the Boltzmann constant, ν_e is the number of effective elastic chains and α_i is the principle stretch in the ith orthonormal direction. To be more general, we rewrite this expression in terms of a lab reference frame using the deformation gradient F_{iJ}:

$$\Delta S = -\frac{k\nu_e}{2}\Big(\operatorname{tr} F_{iJ}F_{jJ} - 3 - \ln\det F_{iJ}\Big). \tag{2.2.5}$$

Note that only the invariants of F_{iJ} can contribute to the free energy since the system energy has to be independent of any solid body rotation of the sample. The first term, $\operatorname{tr} F_{iJ}F_{jJ} - 3$, represents the decrease in configurational entropy of the Gaussian chains as caused by the externally imposed deformation. It will be positive in swelling deformations, since swelling will stretch the network chains and decrease the entropy of the system. The second term, $\ln\det F_{iJ}$, does not appear in most works on polymeric elastomer deformation because, to good approximation, it is incompressible ($\det F_{iJ} = 1$). In the case of a swelling deformation, however, the final volume through which the chains are distributed increases. This increased volume yields more available configurations to the network cross–links and therefore acts to *increase* the entropy of the system, in sharp contrast to linear chain stretching effects [77].

2.2.2 Initially Swollen Network

When a dry network is placed in contact with a reservoir of small chain macromer molecules, entropic contributions drive the diffusion of the chains into the network, causing it to swell. There are now three contributions to the system energy: 1) the energy of stretching the host network chains as macromer is imbibed; 2) the entropy gained through the mixing of host network and macromer chains, and 3) the enthalpy cost due to solvent–solute interactions. We now introduce the subscripts m to refer to the free macromer species and N to refer to the network. Here, we are concerned with deformations induced by the osmotic pressure of the bulk solvent. The corresponding stress (illustrated below, $\mathcal{O}(10^6$ Pa)) is much less than the stress required to fully extend network strands. Therefore, the bond lengths and angles are not perturbed and, consequently, the internal energy is unchanged ($\Delta U = 0$). The change in system free energy is then purely entropic ($\Delta F = -T\Delta S$). Per unit of spatial volume, V, the change in elastic stretching free energy due to swelling is

$$\frac{\Delta F}{V} = -T\frac{\Delta S}{V} = \frac{1}{2}G_{\text{dry}}\phi_N\Big(\operatorname{tr} F_{iJ}F_{jJ} - 3 - \ln\det F_{iJ}\Big). \tag{2.2.6}$$

Note that the prefactor in (2.2.6) has been rewritten in terms of G_{dry}, the original, dry network shear modulus:

$$G_{\text{dry}} = \frac{kT\nu_e}{V^d} = \frac{m_{N0}RT}{M_c V^d} = \frac{\rho_{N0}RT}{M_c}, \tag{2.2.7}$$

where m_{N0} is the mass of the network, ρ_{N0} is the pure network density, and R is the universal gas constant; the factor of $\phi_N = V^d/V$, the volume fraction of network, takes into account that only network chains are stretched in a swollen gel. Because the system is swelling, the local volume changes

$$\det F_{iJ} = \frac{dV}{dV^d} = \frac{1}{\phi_N} \tag{2.2.8}$$

are non–zero: $\phi_N \leq 1$ so $\det F_{iJ} \geq 1$ as the material swells.

Aside from an energetic penalty due to solvent–solute interactions, we assume ideal mixing of our two components. If the pure component densities of macromer and network are the same, there will be no change in volume upon mixing; experimental measurements confirm this to good approximation [1]. Following [35], the mixing entropy gain for bringing two pure-component polymer species together is

$$\Delta S_{mix} = -k\left(n_m \ln \phi_m + n_N \ln \phi_N\right), \tag{2.2.9}$$

where n_α is the number of molecules of species α and ϕ_α is the volume fraction of species α. As noted by Flory, $n_N = 1 \ll n_m$ for a system in which component N is a single molecule (i.e, a cross–linked network). Therefore, the network contribution to mixing entropy is negligible. This gives an effective entropy of mixing of

$$\Delta S_{mix} = -kn_m \ln \phi_m. \tag{2.2.10}$$

Although it is generally less than the entropy of mixing, there can also be an enthalpy change upon mixing chemically dissimlar components. The simplest approximation for this is a linear variation with the number of N–m contacts:

$$\Delta H_{mix} = kT\chi n_m \phi_N, \tag{2.2.11}$$

where χ is a binary interaction parameter measuring the energy penalty per repeat unit of macromer. When χ is positive, the network–macromer contact is unfavorable and mixing is penalized. The free-energy change of mixing macromer into a dry network is a combination of (2.2.10) and (2.2.11):[1]

$$\Delta F_{mix} = kTn_m(\ln \phi_m + \chi\phi_N). \tag{2.2.12}$$

[1] This is only true in the absence of external work. In general, $\Delta G = \Delta H - T\Delta S = \Delta F + W$ where W is the work done on the system.

In stating these relations, we have made the same assumptions as Flory, including ignoring volume change on mixing and packing effects due to differences in macromer and network volume. Departures from these assumptions can be corrected by making the χ parameter dependent upon other parameters (such as temperature) but we do not do so here.

Noting that n_m is related to the pure component density of macromer ρ_{m0} by

$$n_m = \frac{\rho_{m0} V_m}{M_m} \mathcal{N}_A \tag{2.2.13}$$

(V_m being the volume of macromer, M_m the macromer molar mass, and $\mathcal{N}_A$ Avogadro's number), and with the definition of macromer volume fraction $\phi_m = V_m/V$, (2.2.12) can be written as

$$\frac{\Delta F_{mix}}{V} = \frac{\rho_{m0} RT}{M_m} \phi_m \Big(\ln \phi_m + \chi \phi_N \Big). \tag{2.2.14}$$

We define the prefactor for the mixing term as $G_{\rm OS}$, the osmotic modulus:

$$G_{\rm OS} = \frac{\rho_{m0} RT}{M_m}. \tag{2.2.15}$$

Since we assume no volume change upon mixing, $V = V_m + V_N$ and $\phi_m + \phi_N = 1$ (see [78]) so that the free energy of mixing depends only upon ϕ_m.

Combining the contributions of mixing (2.2.14) and stretching (2.2.6), the total free energy per unit volume is

$$\frac{\Delta F}{V} = G_{\rm dry} \frac{1}{2} \phi_N \Big(\operatorname{tr} F_{iJ} F_{jJ} - 3 - \ln \det F_{iJ} \Big) + G_{\rm OS} \phi_m \Big(\ln \phi_m + \chi \phi_N \Big). \tag{2.2.16}$$

From this expression, we see that there are two characteristic energy scales: one energy density is the osmotic modulus $G_{\rm OS}$ generated by the mixing of macromer and the other the shear modulus $G_{\rm dry}$ due to the stresses borne by the network. As has been seen, both are entropic in origin. For the case in which the pure component density of macromer and network are the same ($\rho_{m0} = \rho_{N0}$), the two are not independent: their ratio depends upon the single parameter:

$$\epsilon \equiv \frac{G_{\rm dry}}{G_{\rm OS}} = \frac{M_m}{M_c}. \tag{2.2.17}$$

This parameter is small due to the significant difference in size between macromer and network chains. For the sample materials we will consider here (PDMS networks and PDMS macromer, Appendix B), $0.01 \leq \epsilon \leq 0.33$. The smallness of ϵ implies that the osmotic modulus is significantly larger than the shear modulus. Therefore, the osmotic modulus is taken as the characteristic energy

scale with which we define the *dimensionless* free energy per unit volume, A:

$$A(F_{iJ}, \phi_m, \phi_N) \equiv \frac{\Delta F}{G_{\rm OS} V} = \phi_m \ln \phi_m + \chi \phi_m \phi_N + \frac{1}{2}\epsilon \phi_N \Big(\mathrm{tr}\, F_{iJ} F_{jJ} - 3 - \ln \det F_{iJ} \Big). \qquad (2.2.18)$$

The first term represents ideal mixing, whereas the other two terms can be considered corrections due to (1) enthalpy of mixing effects (which scale with χ) and (2) chain stretching (which scale with ϵ). The smaller the size of macromer chains relative to network chains, the less chain stretching affects the system energy.

2.2.3 Swelling Equilibrium

When a dry network sample is placed in a bath of macromer, it swells until it reaches a point at which the decrease in free energy due to the entropy of mixing macromer into the network becomes equal to the free energy cost of elastic stretching of network strands. This state of swelling equilibrium is closely related to osmotic equilibrium, as aptly stated by Flory:

> "A close analogy exists between swelling equilibrium and osmotic equilibrium. The elastic reaction of the network structure may be interpreted as a pressure acting on the solution, or swollen gel. In the equilibrium state this pressure is sufficient to increase the chemical potential of the solvent in the solution so that it equals that of the excess solvent surrounding the swollen gel. Thus the network structure performs the multiple role of solute, osmotic membrane, and pressure generating device." [35]

In this section, we review swelling equilibrium to convey the physical significance of our expression for the free energy [35]. For a system swollen with macromer, the difference between the chemical potential of macromer inside the gel μ_m and the chemical potential of the pure macromer μ_{m0} is[2]

$$\mu_m - \mu_{m0} = \left(\frac{\partial \Delta F}{\partial n_m} \right)_{T, n_N}. \qquad (2.2.19)$$

At equilibrium, $\mu_m = \mu_{m0}$ for a network swollen in an infinite bath of macromer. For isotropic swelling,[3] $\mathbf{F} = \phi_N^{-1/3}\mathbf{I}$, where $\mathbf{I}$ is the identity matrix, so that $\det \mathbf{F} = 1/\phi_N$ (2.2.8). Under this isotropic deformation, (2.2.18) reduces to $A(\phi_m, \phi_N)$. Replacing the number of macromer molecules with their volume fraction using (2.2.13), the chemical potential difference can be written in terms of A, ϕ_m and ϕ_N:

$$\frac{\mu_m - \mu_{m0}}{kT} = A + \phi_N \left(\frac{\partial A}{\partial \phi_m} - \frac{\partial A}{\partial \phi_N} \right). \qquad (2.2.20)$$

[2]Recall that, in the absence of external work, $G = F$. For this derivative, pressure is also kept constant, but to avoid confusion with further expressions we do not include it explicitly here.

[3]There is a body of work that indicates that the time–dependent swelling of gels depends on the boundary conditions, and need not be isotropic [38,73]; these authors agree, however, that the final equilibrium state is isotropically swollen for a system with force-free boundaries.

Evaluating the derivatives, we arrive at

$$\frac{\mu_m - \mu_{m0}}{kT} = (\phi_m + \phi_N)\ln\phi_m + \phi_N + \chi\phi_N^2 + \epsilon\left(\phi_N^{1/3} - \frac{1}{2}\phi_N\right). \tag{2.2.21}$$

This can be written solely as a function of ϕ_m (since $\phi_N = 1 - \phi_m$):

$$\mu \equiv \frac{\mu_m - \mu_{m0}}{kT} = \ln\phi_m + 1 - \phi_m + \chi(1-\phi_m)^2 + \epsilon\left[(1-\phi_m)^{1/3} - \frac{1}{2}(1-\phi_m)\right]. \tag{2.2.22}$$

We define μ as the dimensionless chemical potential difference between macromer within the gel and free macromer; we will refer to μ throughout the rest of this thesis simply as the chemical potential. The first three terms represent the chemical potential due to mixing, whereas the last bracketed term represents an addition to the chemical potential from the elastic stretching. It is this additional contribution which prevents infinite swelling.

The equilibrium volume fraction of macromer $\phi_{m,eq}(\epsilon,\chi)$ is given by the transcendental equation obtained by setting $\mu = 0$ ($\mu_m = \mu_{m0}$), called the Flory–Rehner equation:

$$-\left[\ln\phi_{m,eq} + 1 - \phi_{m,eq} + \chi(1-\phi_{m,eq})^2\right] = \epsilon\left[(1-\phi_{m,eq})^{1/3} - \frac{1}{2}(1-\phi_{m,eq})\right]. \tag{2.2.23}$$

The maximum amount of swelling allowed for a particular ϵ and χ pairing is $\phi_{\max} \equiv \phi_{m,eq}(\epsilon,\chi)$ (Figure 2.2). At a given χ and network strand length, the smaller the macromer (smaller ϵ), the greater the equilibrium swelling (larger $\phi_{\max}$). For a given macromer size, the more unfavorable the interactions (increasing χ), the less the network swells (smaller $\phi_{\max}$).

A standard experimental procedure allows the use of the Flory–Rehner equation to determine χ for a given macromer/network pair [1]. The shear modulus G_{dry} of a network is measured by rheometry. The same network is then swollen to equilibrium in a bath of macromer with osmotic modulus G_{OS} (2.2.15). Once the equilibrium swelling ratio Q_{eq} is experimentally determined, the equilibrium volume fraction can be found from $Q_{eq} = 1/(1-\phi_{m,eq})$. Calculating ϵ from the modulus (2.2.17), (2.2.23) is used to determine the χ value for that host matrix/macromer pair. Experimental values obtained by Pape are included in Appendix B.2.

It is convenient to define the left–hand side of (2.2.23) as the osmotic pressure Π generated in the network due to the imbibition of macromer ϕ_m:[4,5]

$$-\Pi(\phi_m) = \ln\phi_m + 1 - \phi_m + \chi(1-\phi_m)^2. \tag{2.2.24}$$

[4]Note, with our osmotic energy scale, that the osmotic pressure is $\mathcal{O}(1)$, as we would expect.

[5]This is the same expression given in Rubenstein and Colby [79] except written in terms of the volume fraction of macromer rather than network.

At equilibrium, this osmotic pressure is balanced by an elastic reaction which scales as $\mathcal{O}(\epsilon)$: the right–hand side of (2.2.23). For most applications, the network is not saturated completely (not swollen to full capacity) with macromer until it reaches equilibrium. In such cases, the osmotic pressure is larger than the stretching forces (the system would imbibe more macromer than it has if it could) and dominates the free-energy contribution in (2.2.18). Even though the stretching contribution is small like ϵ in these cases, it is still essential in determining the system shape, as we shall see.

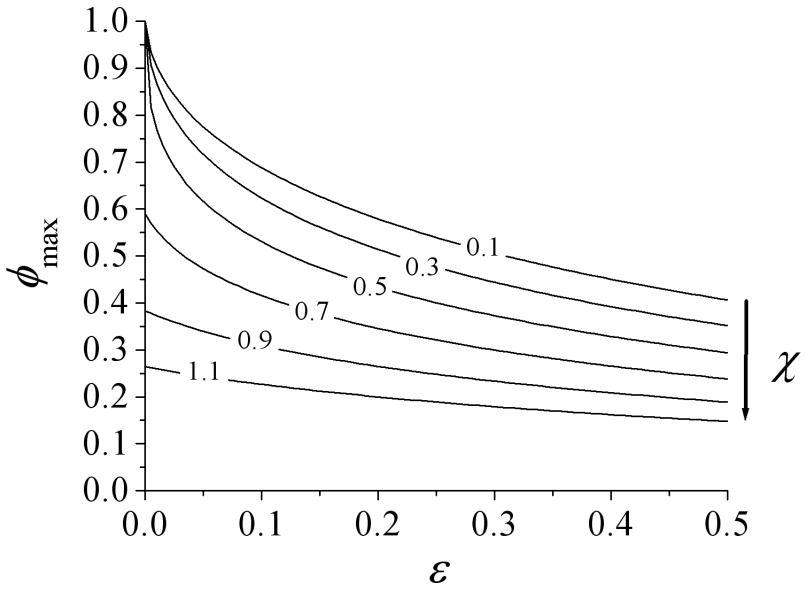

Figure 2.2: The maximum allowable volume fraction of macromer, $\phi_{\max}$, decreases 1) as the molecular weight of macromer increases relative to the molecular weight between cross–links ($\epsilon \equiv M_m/M_c$), and 2) with unfavorable macromer–matrix interations ($\chi > 0$).

2.3 Elastomeric Photopolymer after Reaction

The preceeding sections recapitulate the established thermodynamics of networks and gels in the context of photoelastomers. In this section, we treat the new problem presented by allowing reaction of macromer molecules to create chemical potential gradients in the elastomer so that diffusion–induced deformation occurs.

Consider a system of host network initially swollen in a macromer bath until it reaches a desired volume fraction of macromer $\phi_0 \leq \phi_{\max}$. This initially-swollen network is then subjected to a photopolymerization process which causes some of the macromer to photopolymerize. For the purpose of analyzing the change in shape of an implant initially swollen to ϕ_0, it is more convenient to redefine the reference coordinates to be those of the swollen system prior to irradiation (Fig. 2.3).

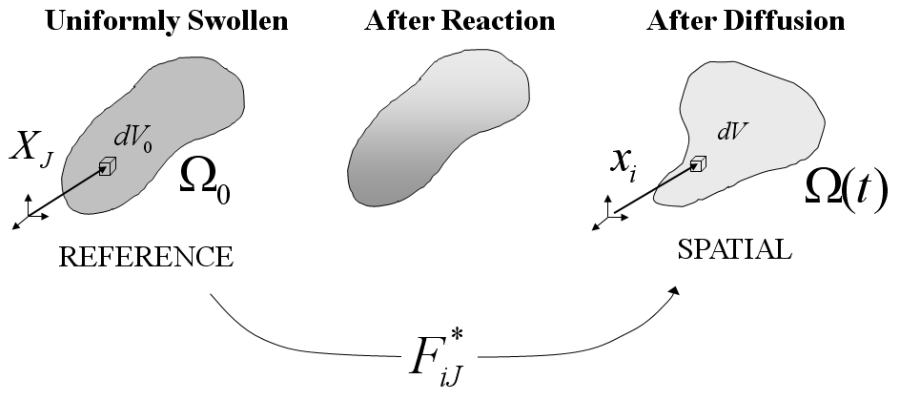

Figure 2.3: The kinematics of deformation in §2.3 (in constrast to Fig. 2.1): a swollen host network (occupying Ω_0) is taken as the reference configuration; each material volume dV_0 is labeled X_J. This initially swollen elastomer is then exposed selectively to light, causing a spatially resolved depletion of macromer. At any point in time during the reaction–diffusion–deformation process, each material point moves to a point x_i in the spatial configuration $\Omega(t)$ and occupies a volume dV.

Let the domain of the initially-swollen system be Ω_0, with each material point in the system be labeled with $\boldsymbol{X}$ (X_I) relative to this new reference coordinate system. Each point also has a volume associated with it: dV_0. We selectively irradiate this initially-swollen system with light and model the reaction–diffusion–deformation of the body in time. At any point in time t , we define the spatial configuration $\Omega(t)$ to be the collection of all material points mapped from the reference configuration to the current time; the initial condition for $\Omega(t)$ is $\Omega(0) = \Omega_0$. In the spatial configuration, each material point occupies a position x_i and a volume dV.

From the above analysis of an initially swollen network (§2.2.2), we know that

$$\frac{dV_0}{dV^d} = \frac{1}{1-\phi_0} \equiv Q_0. \tag{2.3.1}$$

We have defined Q_0 as the initial swelling ratio of the system. The subsequent deformation from the initial swollen reference is denoted $\mathbf{F}^*$; relative to the dry network (before macromer was introduced), the total deformation gradient is then a combination of $\mathbf{F}^*$ and the initial isotropic expansion $\mathbf{F}_0 = Q_0^{1/3}\mathbf{I}$:

$$\mathbf{F} = \mathbf{F}^* \cdot \mathbf{F}_0 = Q_0^{1/3}\mathbf{F}^*. \tag{2.3.2}$$

In terms of $\mathbf{F}^*$, the dimensionless free energy (2.2.18) is

$$A(F^*_{iJ}, \phi_m, \phi_N) = \phi_m \ln \phi_m + \chi\phi_m\phi_N + \frac{1}{2}\epsilon\phi_N\Big(Q_0^{2/3}\mathrm{tr}\, F^*_{iJ}F^*_{jJ} - 3 - \ln Q_0 - \ln\det F^*_{iJ}\Big). \tag{2.3.3}$$

Since $\det \mathbf{F}^* > 1$ indicates that locally the material has expanded relative to the initial swelling and $\det \mathbf{F}^* < 1$ that the material has contracted, $\det \mathbf{F}^*$ will be an important parameter to measure deformations in the system.

We now consider the polymerization process. In his thesis, Pape found that the modulus change due to photopolymerization of methacrylate end–capped PDMS macromer in PDMS network depended on volume fraction [1]. At low volume fraction ($\phi_0 < 0.1$), the effect of reaction on the modulus is better modeled by formation of nodules. This, he argued, was due to radicals first crosslinking all of the macromers in its vicinity and then capturing macromers that diffuse to it. At high volume fraction ($\phi_0 > 0.2$), the effect of photopolymerization of macromer on modulus was stronger, suggesting formation of a bicontinous, interpenetrating network. He was, however, unable to prove this last hypothesis due to the paucity of models successfully predicting the modulus increase of interpenetrating PDMS networks.

Within the same year, Yoo and co–workers characterized the mechanical and swelling properties of PDMS interpenetrating networks [31]. Although their cross–linking of the short–chain macromer proceeded through heating rather than light, they used macromers of similar length (0.8–5.7 kg/mol) and networks with similar modulus (0.7–0.21 MPa) as those used in Pape's thesis. In order to characterize the materials, they measured the shear modulus of their created IPNs and compared them to theoretical work by Okumura [80]. Okumura considered two extreme models for an IPN: an equal-strain model and an equal-stress model. While the equal-strain model was found to significantly overpredict the modulus of the IPNs in Yoo et al., the equal-stress model gave relatively good accord (i.e., slightly underpredicted modulus). This, coupled with the discovery that the interpenetrating networks have a similar power–law behavior ($G \sim Q^{-1.88}$) as unimodal networks ($G \sim Q^{-1.91}$), lead the authors to conclude that there is effective load transfer between the two networks. Thus, they concluded that the photopolymerized PDMS short–chains behaved as a bicontinuous IPN in host PDMS.

Because of the conclusions of Yoo and co–workers, we would expect that the resulting photopolymerized macromer chains are uniformly entangled with the host network and supplement it as if they were a uniform, secondary network. Because the macromer chains have a smaller molecular weight than the network chains, the resulting interpenetrating network should have a smaller molecular weight between crosslinks, but is otherwise chemically similar to the host network. Since the secondary network is more tightly linked than the host network, it should resist further swelling more strongly than the original network. Rather than include the details of this IPN using the equal-stress model, we make a simplification in which macromer chains are assumed to react directly into network chains. We will refer to this model as the "two-component model:" the two components being free, unreacted macromer and network (the original network augemented with extra chains). Although it is not *a priori* obvious that this is a good assumption, requiring macromer to become

network forces the macromer–turned–network chains to retain all the original network properties before reaction, including a state of stretch present due to initial swelling with macromer. As we shall see, this theoretical artifice actually captures the mechanical behavior of the material at small volume fractions and will be shown to yield qualitatively similar results to the equal-stress model used by Yoo et al.

Although we will show that this "two-component" model is sufficient in every way to qualitatively capture experimental data (§2.3.2), we initially recognize that the different cross–linking chemistry of our small molecules from those of Yoo et al—specifically the molecular repulsion due to the methacrylate end–groups—could result in dispersed nodules, especially for lower molar masses of macromer. For this reason, we also consider an alternate model in which the macromer chains photopolymerize into discrete nodules. Following Pape's determination that phase separation does not occur for these systems [1], we assume these nodules act as a continuous filler. We will call this second model the "three-component model" since we will consider separately free macromer, original host network, and polymerized macromer nodules. Although there are many models that can be used to represent the modulus increase due to fillers [81], we choose the Kerner equation [82].

Analgous to the equal strain and equal-stress limits proposed by Okumura, we will furthermore show that the "two-component" and "three-component" models provide bounds for the cured material modulus: the two-component model underpredicts the modulus increase due to photopolymerization, whereas the three-component model overpredicts it. As such, we assume that the actual situation is intermediate between two limiting cases: conversion of macromer into network strands and conversion of macromer into filler. We furthermore show that this model captures both the experimentally determined modulus of the PDMS materials studied by Pape and the equilibrium-swelling behavior of these materials after reaction.

2.3.1 Two-Component Model

When an initially swollen sample is subjected to a profile of light intensity $I(\boldsymbol{X}, t)$, we assume that initial macromer is locally converted into host network in a spatially resolved pattern. We futher assume that there is no volume change upon reaction. Since one material is converting to another, the only way this can hold is if both materials have the same density, and formation of new bonds (which increase density) has negligible effect. In general, photopolymerization using monomers produces an increase in density. Here, macromer are used and the volume contraction due to covalent bond formation is negligible: PDMS macromer and network systems, for example, have experimentally been determined to shrink less than 1% at complete cure [1]; volume changes due to reaction can be safely neglected. Since photopolymerized macromer chains in this model are indistinguishable from network chains, the polymerized macromer chains attain all the characteristics inherent in the network chains. As previously noted, these reacted chains are prestretched.

Because there are only two components at any point in time, we note that ϕ_N can be eliminated by $\phi_N = 1 - \phi_m$. For brevity, from here on we drop the subscript m and let ϕ be the volume fraction of macromer. The ratio of an element's volume in the spatial configuration at time t to the initially dry network (§2.2) is

$$Q(\boldsymbol{X}, t) \equiv \frac{dV}{dV^d}. \tag{2.3.4}$$

This volumetric ratio $Q(\boldsymbol{X}, t)$ now differs from the familiar swelling ratio dV/dV_N. The two are equal to each other in the initial spatial configuration ($Q(\boldsymbol{X}, 0) = Q_0$) because no reaction has occurred ($dV_N = dV^d$). Subsequent conversion of macromer into network results in creation of new host network so that $dV_N > dV^d$. Consequently, Q can be viewed as the product of the swelling ratio (dV/dV_N) and the ratio of the current amount of network to that inherited from the initial network (dV_N/dV^d):

$$Q = \frac{dV}{dV^d} = \frac{dV}{dV_N} \cdot \frac{dV_N}{dV^d}. \tag{2.3.5}$$

By the definition of the volume fraction of macromer, $dV/dV_N = 1/(1-\phi)$. The ratio of the current amount of network to that inherited from the initial network, $\theta(\boldsymbol{X}, t)$, can be found by integrating the instantaneous rate of creation of network r_m in dV up to time t:

$$\theta(\boldsymbol{X}, t) = \frac{dV_N}{dV^d} = 1 + \int_0^t \frac{r_m(\boldsymbol{X}, t)}{\rho_{m0}} Q(\boldsymbol{X}, t) dt. \tag{2.3.6}$$

The rate of reaction depends on the light flux reaching dV, the photoinitiator concentration, and the local concentration of macromer. We call the parameter θ the *conversion parameter* since its value completely characterizes the local, transient conversion of macromer into network. With the definition of ϕ and θ, (2.3.5) becomes:

$$Q(\boldsymbol{X}, t) = \frac{\theta(\boldsymbol{X}, t)}{1 - \phi(\boldsymbol{X}, t)}. \tag{2.3.7}$$

Note that (2.3.7) shows the interrelationship among the deformation ($Q = \det \mathbf{F}$), the chemical reaction (θ), and the diffusion of the macromer (which governs the transient volume fraction $\phi(\boldsymbol{X}, t)$).

In light–adjustable lens applications, the irradiation time is short (order of min) compared to the time for re–equilibration (order of days). Reaction occurs significantly only during irradiation, decaying to zero within $\approx$ 5 min once the light source is turned off [1]. Since the time scale for diffusion is much greater than that for reaction, we can simplify our problem by decoupling the reaction from the diffusion–deformation process. This can be done by assuming instantaneous reaction at $t = 0$:

$$\frac{r_m(\boldsymbol{X}, t)}{\rho_{m0}} = \phi_0 \xi(\boldsymbol{X}) \delta(t), \tag{2.3.8}$$

with $\xi(\boldsymbol{X})$ the extent of reaction of macromer and $\delta(t)$ being the delta function. We can model ξ

based upon plausible irradiation profiles in order to connect (2.3.8) to experiment. In the limit of instantaneous reaction (2.3.8), the conversion parameter (2.3.6) is fully specified by the extent of reaction $\xi(\boldsymbol{X})$ and the initial swelling ratio:

$$\theta(\boldsymbol{X}) = 1 + \frac{\phi_0}{1-\phi_0}\xi(\boldsymbol{X}). \tag{2.3.9}$$

The conversion parameter is a measure of how much total macromer has reacted. Physically, $\theta(\boldsymbol{X})$ is the ratio of the local volume fraction of network immediately after the reaction to that inherited from the original network $(1-\phi_0)$. This increases linearly with the product of the extent of reaction, $\xi(\boldsymbol{x})$, and the volume fraction of macromer present when the reaction occurred, ϕ_0. With $0 \leq \phi_0 \leq 0.3$ (the usual operating range for these swollen gels), $1 \leq \theta \leq 1.4$.

Since we wish to rewrite all of these expressions relative to the initially swollen configuration (as opposed to the dry network), the expression for Q (2.3.7) is simply normalized by Q_0:

$$Q^* = \det \mathbf{F}^* \equiv \frac{Q}{Q_0} = \frac{\theta^*}{1-\phi}, \tag{2.3.10}$$

where the asterisk denotes "with respect to the initially swollen state" and

$$\theta^* = \frac{\theta}{Q_0} = 1 - (1-\xi)\phi_0. \tag{2.3.11}$$

When the current volume fraction of macromer in a material element is greater than that present after reaction ($\phi(\boldsymbol{X},t) > (1-\xi)\phi_0$), $\det \mathbf{F}^* > 1$: macromer has diffused into the element and caused it to swell. Likewise, an element will contract ($\det \mathbf{F}^* < 1$) if the current volume fraction is less than that present after reaction ($\phi(\boldsymbol{X},t) < (1-\xi)\phi_0$).

Since we only have two components, the system free energy is taken directly from (2.3.3):

$$A(F^*_{iJ},\phi) = \phi\ln\phi + \chi\phi(1-\phi) + \frac{1}{2}\epsilon\,(1-\phi)\left(Q_0^{2/3}\mathrm{tr}\,F^*_{iJ}F^*_{jJ} - 3 - \ln Q_0 - \ln\det F^*_{iJ}\right). \tag{2.3.12}$$

that is, we assume that the reaction does not change the system free energy other than through depletion and creation of components. Since the set of variables F^*_{iJ} and ϕ are not independent (see (2.3.10), the free energy (2.3.12) can be rewritten as solely a function of F^*_{iJ}. This is the energy we minimize in §2.4 in order to solve global problems.

2.3.2 Region of Validity of the Two-Component Approximation

We now examine the validity of the two-component approximation by comparing the results predicted by the model to experimental data on cured PDMS macromer in PDMS host network [1]. We begin by showing that the increase of shear modulus upon curing is captured by the model. Using the

predicted shear modulus, we then illustrate that the equilibrium swelling predicted by the two-component model is also in agreement with experiment.

To determine the theoretically predicted value of G_{cured}, the effective modulus of the network now augmented with macromer–turned–network chains, assume a sample is irradiated such that it experiences a uniform extent of reaction ξ. Although the experiments in [1] are performed at complete cure ($\xi = 1$), for now we consider ξ arbitrary to determine a general expression. Because macromer is converted uniformly, no chemical potential gradients are created and the material will not deform due to the diffusion of free macromer. With no volume change upon reaction, the volume of the material also remains unchanged (i.e., $Q_0 = dV_0/dV^d$ unchanged). Recall that the volume ratio of network after reaction to the dry network is the conversion parameter $\theta = dV_N/dV^d$ (2.3.9). Extracting any left-over macromer from the system results in a net deswelling of the material by the volume ratio

$$\theta^* = \frac{dV_N}{dV_0} = \frac{\theta}{Q_0}. \tag{2.3.13}$$

For the example of complete cure, $dV_N = dV_0$ and the system does not deswell at all ($\theta^* = 1$); arbitrary extents of reaction will then have $\theta^* \leq 1$. Assume this deswelling occurs isotropically so that the deformation due to extraction is $F_{iJ}^{\text{extract}} = \theta^{*1/3}\delta_{iJ}$ (δ_{ij} the identity tensor). We then subject this cured and dried network to a shear deformation

$$\mathbf{F}_\delta = \begin{pmatrix} 1 & 0 & 0 \\ \delta & 1 & 0 \\ 0 & 0 & 1 \end{pmatrix}, \tag{2.3.14}$$

where δ is a small shear strain. The total deformation due to extraction and shearing is $\mathbf{F}^* = \theta^{*1/3}\mathbf{F}_\delta$. The free energy of the cured and dried ($\phi = 0$) network under this shear becomes (2.3.12)

$$A(\delta) = \frac{1}{2}\epsilon\left(\theta^{2/3}\left(\delta^2 + 3\right) - 3 - \ln\theta\right). \tag{2.3.15}$$

The derivative of the free energy with respect to the shear strain is the shear stress. In dimensionless form,

$$\tau = \left(\frac{\partial A}{\partial \delta}\right) = \epsilon\theta^{2/3}\delta. \tag{2.3.16}$$

The prefactor of δ is the dimensionless shear modulus

$$\epsilon\theta^{2/3}$$

predicted for a cured and dried elastomeric photopolymer. In dimensional terms, this equates to:

$$G_{\text{cured}} = G_{\text{dry}}\theta^{2/3}. \tag{2.3.17}$$

At complete cure ($\xi = 1$), $\theta = Q_0$ (2.3.11) and theory predicts that the relative modulus of the network increases by a factor $Q_0^{2/3}$ due to the augmentation of macromer chains becoming network chains. Note that this simplistic model predicts that the modulus increase depends only upon conversion parameter, independent of the length of macromer chains: the identity of the macromer chains is lost due to the assumption that reaction converts macromer chains into network chains. Although this gross assumption cannot be justified *a priori*, comparison with experimental data will demonstrate the efficacy of this approach.

Experimental data also shows an increase in modulus upon cure: Figure 2.4 shows experimentally determined $G_{\text{cured}}/G_{\text{dry}}$ at complete reaction ($\xi = 1$) [1]. Alongside this data we present the corresponding modulus increase predicted by the two-component model (2.3.17). As can be seen, the two-component model (lower solid curve) provides a lower bound on the modulus, essentially equivalent to the equal-stress model of Yoo and co–workers (lower dotted curve). For $\phi_0 \leq 0.2$, the two-component model is in good agreement with the data and predicts that the modulus increases less than 50% for all macromer molar masses. For this reason, (2.3.17) provides a good approximation to the cured modulus for $\phi_0 \leq 0.2$. For longer macromer chains ($M_m = 3000$ – 5000 g/mol), the two-component approximation holds to larger ϕ_0: this is expected because the longer macromer chains are more like network chains. For shorter chains at larger volume fractions, however, the two-component model significantly underpredicts the experimentally determined moduli. In these cases, we assume that the cured macromer molecules behave more like isolated nodules than interpenetrating networks; this will be corroborated through the predictions of the three-component model (§2.3.3) which treats macromer as reacting into isolated nodules.

Using these predictions for the increase in relative modulus upon cure, we proceed to compare the equilibrium swelling for a cured system predicted by the two-component model to experiment. The two-component predictions for equilibrium swelling after cure are determined through a method analogous to §2.2.3. First, we must determine the chemical potential of penetrant for the cured and reswollen gel using the free energy developed for the two-component model. Consider a network swollen in a bath of macromer to Q_0 and uniformly cured to an arbitrary extent of reaction ξ. Excess macromer is then extracted, deswelling the system to the volume V_N, representing a deformation of $F_{iJ}^{\text{extract}} = \theta^{*1/3}\delta_{iJ}$ (see the beginning of this section). This cured and dried network is then reswollen in a bath of the same macromer. As the gel swells with macromer to volume fraction ϕ, the network chains undergo isotropic expansion by the ratio $dV/dV_N = 1/(1-\phi)$. The net deformation from the initially swollen state is then $\mathbf{F}^* = \left(\theta^*/(1-\phi)\right)^{1/3}\delta_{iJ} = Q^{*1/3}\delta_{iJ}$ (2.3.10). Placing this

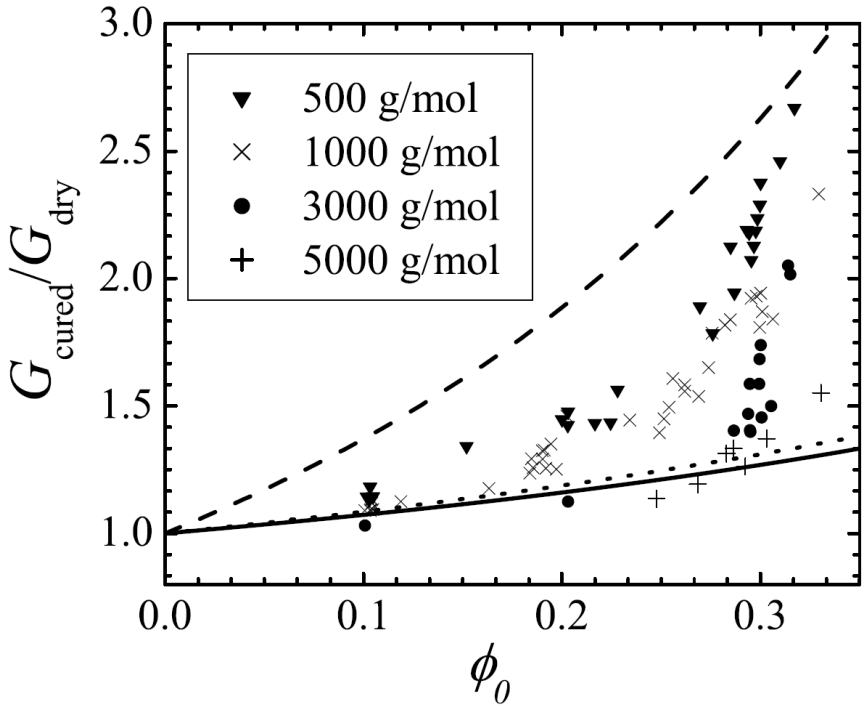

Figure 2.4: The relative modulus increase in PDMS elastomers due to complete reaction ($\xi = 1$) of bismethacrylate endcapped PDMS short–chain macromer as a function of the initial swelling volume fraction ϕ_0. Symbols show experimental data for four different macromer chain lengths presented in the Ph.D. thesis of Eric Pape [1]. Curves show model predictions. The solid curve below the data is the prediction of the "two-component model" (§2.3.1) which provides a lower bound for the increase in material modulus upon polymerization. The two-component model is in keeping with the equal-stress model used by Yoo and co–workers [31] (the dotted line: 23 k molecular weight host network cured with 2.3 k short chains; other short chain lengths produce nearly the same curve). The two-component model provides a good approximation in the case of relatively high macromer molecular weight where the fully photopolymerized material most closely resembles an interpenetrating network. The "three-component model" (§2.3.3) treats the reacted macromer as hard–bodied nodules that act as filler through the Kerner equation (2.3.30) [82]. This can be seen as an upper bound on the material modulus (dashed line). The three-component model better captures the short chain, nodular effects of reaction at large volume fractions.

deformation into (2.3.12), the chemical potential (2.2.19) predicted by the two-component model is:

$$\mu = \ln\phi + 1 - \phi + \chi\,(1-\phi)^2 + \epsilon\left[\theta^{2/3}(1-\phi)^{1/3} - \frac{1}{2}(1-\phi)\right]. \tag{2.3.18}$$

The system reaches equilibrium when $\mu = 0$. Call the equilibrium swelling volume fraction for the cured and reswollen system $\phi = \phi'_{eq}$ (different from the value for the original network ϕ_{eq}). It is related to the equilibrium swelling ratio after cure, Q'_{eq}, by:

$$Q'_{eq} = \frac{dV}{dV_N} = \frac{1}{1-\phi'_{eq}}. \tag{2.3.19}$$

The two-component model prediction of ϕ'_{eq} proceeds by solving $\mu = 0$ (2.3.18):

$$-\left[\ln\phi'_{eq} + 1 - \phi'_{eq} + \chi\left(1-\phi'_{eq}\right)^2\right] = \epsilon\theta^{2/3}(1-\phi'_{eq})^{1/3} - \frac{1}{2}\epsilon(1-\phi'_{eq}), \tag{2.3.20}$$

as a function of ϵ, θ, and χ. This equation can be thought of as the Flory–Rehner equation for the two-component model: it predicts the equilibrium swelling of cured systems under the two-component approximation in the same way that the Flory–Rehner equation predicts the equilibrium swelling of the original system (§2.2.3). Note that the two-component Flory–Rehner equation 2.3.20) reduces to the Flory–Rehner equation (2.2.23) when there is no reaction ($\xi = 0$, $\theta = 1$).

Because the χ values used to predict equilibrium swelling are not known *a priori*, they must be found through experiment. One method of doing this revolves around measuring equilibrium swelling for a system and then fitting χ with the Flory–Rehner equation [83]. Using equilibrium swelling data obtained for methacrylate end–capped PDMS macromer swollen into PDMS network [1], we determined the χ values for network–macromer pairings using the Flory–Rehner equation (2.2.23). These can be considered to be the "original" χ values before the system has been cured. The open circles in Fig. 2.5 illustrate these original χ values. The values of χ are found to depend strongly on the choice of macromer molar mass: $M_m = 500$ g/mol having $0.7 < \chi < 0.85$, $M_m = 1000$ g/mol having $0.4 < \chi < 0.55$ g/mol, and $M_m = 3000$ g/mol having $0.1 < \chi < 0.3$. These correspond to poor, near-theta, and good solvents, respectively: as the number of silicone repeat units in the macromer backbone increases, the solvent becomes more like the network and experiences less repulsion. Compared to the effect of changing macromer chain length, the χ parameter is relatively insensitive to the network chain length, represented by G_{dry}. Pape gives the reason for the observed slight increase in χ as the network gets tighter (G_{dry} increasing, M_c decreasing) as molecular sieving of the polydisperse macromer sample. A regression fit for the χ values as a function of G_{dry} is performed in §B.2 and the results are shown as the straight lines in Fig. 2.5.

For the two-component model to be self–consistent, χ should not change upon cure: macromer chains become network chains and inherit all network characteristics, including their interaction with

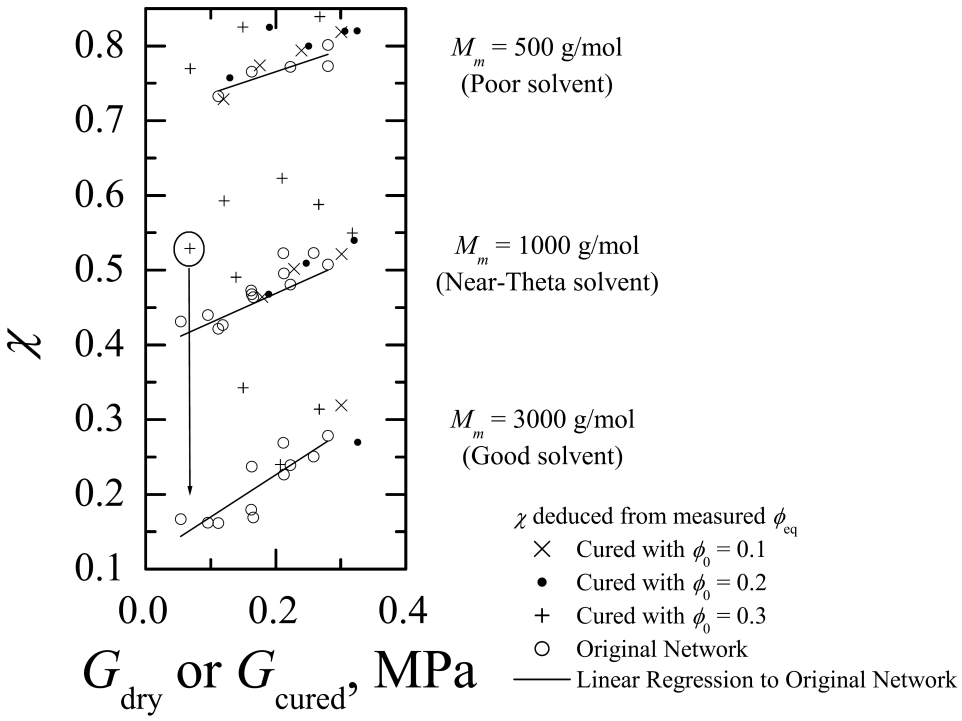

Figure 2.5: Fit χ values using equilibrium swelling data for methacrylate end–capped PDMS in PDMS network as a function of G_{dry}, M_m, and ϕ_0 [1]. The original network χ values are obtained by using the Flory–Rehner equation (2.2.23) and the least-squares regression parameters on the original data as a function of G_{dry} are given in §B.2 (Table B.1). The cured χ values (obtained at complete cured, $\xi = 1$) are calculated using the Flory–Rehner equation modified for the two-component model (2.3.20).

macromer molecules. To test for self–consistency, we calculate the χ values for a cured system using equilibrium swelling obtained for fully cured gels ($\xi = 1$) which were reswollen with the same molar mass of macromer. To determine the χ value predicted by the two-component model, the original network modulus G_{dry} and the initial volume fraction of macromer ϕ_0 were used to calculate the cured modulus from theory (2.3.17). These were then used, along with equilibrium swelling ratios in (2.3.20), to fit χ. The obtained χ values for the cured systems are shown in Figure 2.5. At small volume fraction ($\phi_0 \leq 0.2$), the χ value at a given molar mass does not change significantly upon curing macromer into the matrix; the model is self–consistent. In practical terms, this means that, for $\phi \leq 0.2$, χ can be approximated as having a particular value dictated by the macromer size and end-group structure, but independent of cure of macromer into the network. It should also be noted that the more significant deviations at larger volume fraction are due to underprediction of the cured modulus (Fig. 2.4).

We illustrate the effectiveness of using these original χ values by comparing the theoretical equilibrium swelling results obtained from (2.3.20) with raw experimental data. To do so, we first

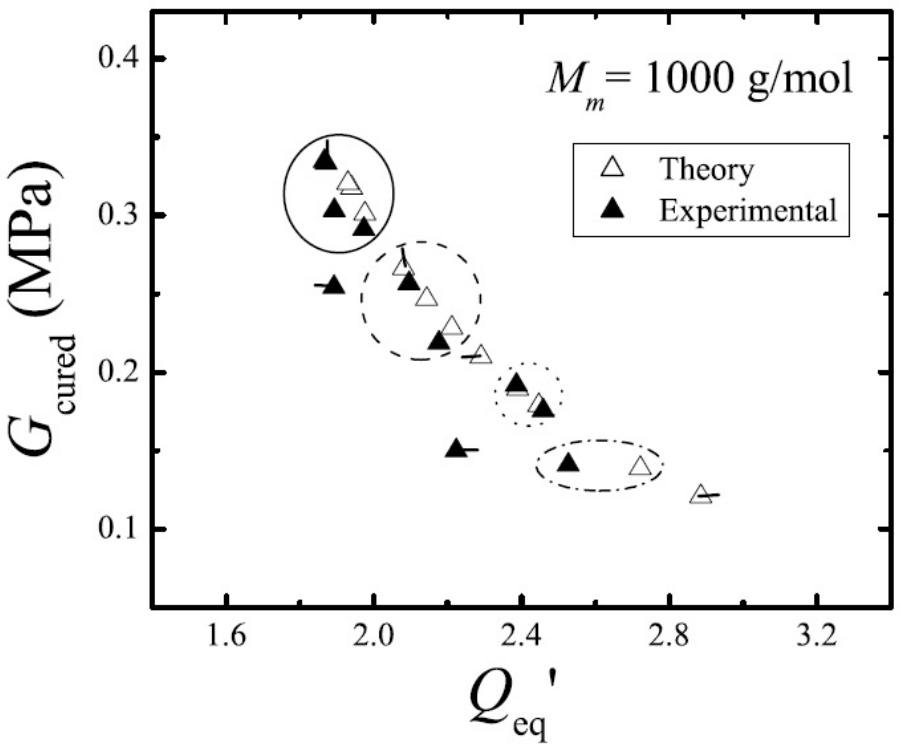

Figure 2.6: The modulus of model PDMS networks fully cured with M_m = 1000 g/mol bis-methacrylate endcapped macromer is plotted as a function of the equilibrium swelling ratio after cure. The solid symbols represent the experimental data from [1] and the open symbols represent the two-component model prediction for each data point. The circles group sets of similar G_{dry}: (line) $0.28 \geq G_{\text{dry}} > 0.25$ MPa (except the up pip point which has 0.213 MPa), (dash) $G_{\text{dry}} \approx 0.21$ MPa, (dot) $G_{\text{dry}} \approx 0.16$ MPa, and (dash–dot) $G_{\text{dry}} \approx 0.11$ MPa. Except for the three points with pips—all at $\phi_0 = 0.3$—the theoretical results lie near the experimental results.

use a pair of real material parameters (G_{dry}, M_m) to calculate the theoretical model parameters χ and ϵ for use in (2.3.20). This is done in Appendix B, Table B.2. Using these determined parameters, Fig. 2.6 shows experimentally obtained results for the modulus of fully cured materials as a function of their equilibrium swelling ratio after cure (filled triangles). The open triangles are the corresponding theoretical points obtained from the two-component model. Only three points—the ones with the pips—are significantly removed from their theoretical predictions. These are the only points where $\phi_0 \approx 0.3$ and the deviation is due to the modulus being significantly underpredicted (Fig. 2.4).

Inspired by the ability to predict the experimental swelling data pointwise, we turn to the power-law scaling behavior of the cured modulus with equilibrium swelling. The literature models $G \sim Q_{eq}^{\alpha}$, the value of α determined by the type of solvent [79]. Specifically, $\alpha = -8/3$ (i.e., -2.67) for a theta solvent ($\chi = 0.5$) and $\alpha = -7/4$ (i.e., 1.75) for an athermal solvent ($\chi = 0$). Although there is no scaling theory for poor solvents, the general trend expects α to continually decrease as the solvent

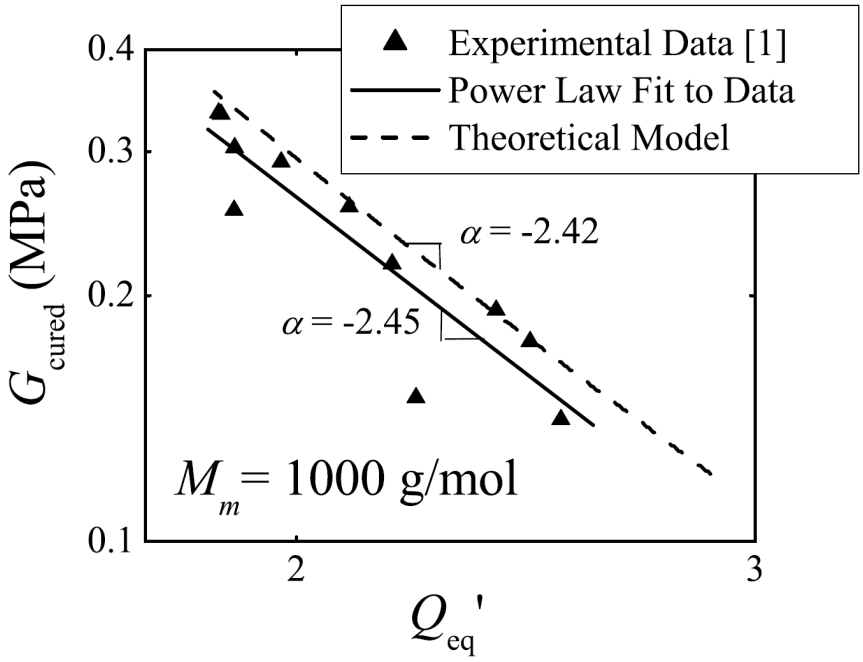

Figure 2.7: Log–log plot of the two-component predicted equilibrium swelling (2.3.20) for M_m = 1000 g/mol. Data points are obtained by varying G_{dry} and calculating G_{cured} for a specific value of ϕ_0 through (2.3.17). The theoretical line shows only the case of $\phi_0 = 0.2$: the results for $\phi_0 = 0.1$ and $\phi_0 = 0.3$ are not shown, as they overlay the $\phi_0 = 0.2$ line with nearly the same slope. The χ values used to calculate these curves are evaluated from a linear regression to real data (Table B.1). Also shown is the experimental data, and a power law fit to that data using least–squares regression. The slope of the theory is essentially the same as that of the experimental data although the theory predicts a slightly higher degree of equilibrium swelling than seen experimentally.

quality gets progressively more poor. From Fig. 2.5, we see that the increasing molar masses of macromer span the range of poor, to near-theta, to good solvent in host network, respectively: the repulsive effect of the methacrylate endgroups is mediated by including more repeat units with the same chemistry as the network backbone. Figure 2.7 demonstrates the scaling behavior predicted by the two-component model for the theta solvent case (M_m = 1000 g/mol). Although the two-component model slightly overpredicts the experimentally determined values (triangles), the scaling behavior ($\alpha = -2.42$) is nearly the same as that obtained by performing regression on the data ($\alpha = -2.45$); it is also near the literature value of $\alpha = -2.67$. The power law exponents behavior for the other macromer molar masses are shown in Table 2.1. The scaling exponent depends upon the molar mass of macromer—and therefore the macromer solvent quality—but is nearly independent of ϕ_0. The scaling exponents for all cases are nearly the same as those determined directly from experimental data and also show agreement with literature [79].

Using experimental data for materials appropriate in light–adjustable implants, we have illustrated that the assumption inherent in the two-component model can successfully capture experi-

M_m, **g/mol**	**Solvent Quality**	**Scaling Theory** [79]	α^*			
			$\phi_0 = 0.1$	$\phi_0 = 0.2$	$\phi_0 = 0.3$	Data**
500	Poor	$\alpha < -2.67$	-6.05	-5.97	-5.88	-5.57
1000	Near Theta	$\alpha = -2.67$	-2.38	-2.41	-2.46	-2.45
3000	Good	$-2.67 < \alpha < -1.75$	-2.29	-2.32	-2.38	-2.33

* $G_{\text{cured}} \sim Q_{eq}^{\alpha}$
** Obtained through regression of experimental data obtained from [1].

Table 2.1: Scaling exponents obtained from the modified Flory-Rehner equation (2.3.20) as a function of ϕ_0 and M_m obtained by variation of G_{dry}. The power–law fit to each theory produced $r^2 > 0.99$; the experiment data had r^2 of 0.94 for $M_m = 500$ and 3000 g/mol and 0.82 for 1000 g/mol. The scaling exponent depends only upon the macromer molar mass and not the volume fraction of macromer. They are also in agreement with the values obtained experimentally [1] and cited in the literature [79].

mental observations. For small amounts of initial swelling ($\phi_0 \leq 0.2$), we were successfully able to predict the relative modulus increase upon cure. We also showed that the model is self–consistent: using the χ value before cure, we found the theoretical predictions for equilibrium swelling of cured systems to be in keeping both with experimental data and with literature scaling behavior for $\phi \leq 0.2$. At larger values of the volume fraction, the modulus was significantly underpredicted, particularly for smaller molar masses of macromer (Fig. 2.4), leading to more significant discrepancies in the equilibrium swelling behavior. This discrepancy can be corrected by creating an alternate "three-component model" which allows for the creation of a third, nodule species from macromer upon reaction. This third species acts as an inert particulate filler and will be shown to enhance the relative material modulus beyond that observed in the two-component model.

Before we finish with the two-component model and move on to the three-component model, however, we briefly determine the two-component expression for the shear modulus after curing and reswelling to any general volume fraction ϕ; this will be useful in the following chapters where we make extensive use of the two-component model. First, the system is reacted and deswollen, attaining a modulus G_{cured} (2.3.17). We then reswell this cured material isotropically to a volume fraction ϕ; this corresponds to $F^*_{iJ} = (\theta^* Q^*_{\text{reswell}})^{1/3}\delta_{iJ}$, $Q^*_{\text{reswell}} = 1/(1-\phi)$, the swelling ratio relative to the cured and dried network . Upon submitting this to the shear deformation (2.3.14), we use the same method as before to obtain the shear modulus:

$$G_{\text{shear}}(\phi;\theta) = G_{\text{cured}}(\theta)(1-\phi)^{1/3} = G_{\text{dry}}\theta^{2/3}(1-\phi)^{1/3}. \tag{2.3.21}$$

The scaling behavior $(1-\phi)^{1/3}$ with solvent volume fraction ϕ has been shown to be typical of swollen gels [79]. Because making appropriate choices for θ and ϕ reduce G_{shear} to either G_{cured} or G_{dry}, G_{shear} is the most general expression for the shear modulus. Due to the dimensionless nature of solution throughout the rest of this work, it is more convenient to define the dimensionless

shear modulus

$$G \equiv \frac{G_{\text{shear}}}{G_{\text{os}}} = \epsilon\theta^{2/3}(1-\phi)^{1/3}. \tag{2.3.22}$$

Here, we use G without subscript to denote the dimensionless shear modulus after curing and reswelling to a volume fraction ϕ.

2.3.3 Three-Component Model

We now turn to the three-component model which can be used at larger volume fractions to more accurately predict the modulus of a material, specifically at smaller molar masses of macromer. In particular, smaller molar masses of macromer are unable to form long–range, interpenetrating networks; instead, the macromer molecules diffuse to a radical initiation point (which cannot diffuse) and form nodules. In this section, macromer is assumed to react into dispersed nodules; this third species will be referred to via subscript n. We assume that these created nodules are large enough that they cannot diffuse, but rather enhance the material modulus as filler. Fig. 2.4 illustrates that the modulus predicted with this model provides an upper bound to the experimentally determined data Fig. 2.4.

Using the same simplification of instantaneous reaction that produces a conversion profile $\xi(\boldsymbol{X})$ at $t = 0$, the volume of macromer remaining in a small volume immediately after reaction will be $dV_m = dV_{m0}(1-\xi)$, with dV_{m0} being the volume of macromer in that volume before reaction. Since all reacted macromer is converted to nodules and no nodules exist before reaction, the volume of nodules after reaction will be $dV_n = dV_{m0}\xi\rho_{m0}/\rho_{n0}$, ρ_{n0} , the pure component density of the nodules. The volume of network after reaction is the same as that before reaction $dV_N = dV_{N0}$. The ratio of total volume right after reaction dV_R to total volume right before reaction is

$$Q_R = \frac{dV_R}{dV_0} = \frac{dV_m + dV_N + dV_n}{dV_{m0} + dV_{N0}} = 1 + \phi_0\xi\left(\frac{\rho_{m0}}{\rho_{n0}} - 1\right). \tag{2.3.23}$$

The usual increase in density when monomers are polymerized [17] is negligible when *macromer* are polymerized (i.e., the nodule density is approximately the same as the macromer density, $\rho_{m0} \approx \rho_{n0}$): $Q_R = 1$ and there is no change in volume upon reaction. The volume of fixed-species (both network and nodules) is

$$dV_f = dV_N + dV_n = dV_0(1-\phi_0) + dV_0\phi_0\xi. \tag{2.3.24}$$

The volume of fixed species remains constant at each point after reaction since these species cannot diffuse; it is also completely specified by the extent of reaction profile and material parameters. The fixed species volume fraction, ϕ_f, however, will change due to diffusion of macromer: $\phi_m + \phi_N + \phi_n =$

1 so that $\phi_f = \phi_N + \phi_n = 1 - \phi_m$. The conversion parameter θ is designated as

$$\theta = \frac{dV_f}{dV_N} = \frac{dV_f}{dV_0}\frac{dV_0}{dV_N} = \frac{1-(1-\xi)\phi_0}{1-\phi_0}, \tag{2.3.25}$$

which has a similar meaning to the conversion parameter in (2.3.9) of the previous section: it is the ratio of the fixed-species volume after reaction—now with contributions from the host network and reacted macromer considered separately—to the initial network volume. It also completely characterizes the extent of reaction. Note that the expression for (2.3.25) is the same as θ in the previous section (2.3.9); this is because we have assumed $\rho_{n0} = \rho_{m0}$. Since $\phi_f = dV_f/dV$, the volume fractions of network and nodules are

$$\phi_N = \frac{dV_N}{dV} = \frac{dV_N}{dV_f}\phi_f = \frac{1}{\theta}(1-\phi_m) \tag{2.3.26}$$

and

$$\phi_n = \frac{dV_n}{dV} = \frac{dV_n}{dV_f}\phi_f = \frac{\theta-1}{\theta}(1-\phi_m), \tag{2.3.27}$$

respectively.

The volume ratio $Q = \det F_{iJ}$ for the three-component system is

$$Q = \frac{dV}{dV^d} = \frac{dV}{dV_N} = \frac{1}{\phi_N} = \frac{\theta}{1-\phi_m}. \tag{2.3.28}$$

Recall that superscript d denotes the "dry" network (prior to swelling with macromer). Note that this is also the same expression as that for the two-component case (2.3.7), with θ now having the more general meaning discussed above. In this way, the definition of θ^* (2.3.11) and Q^* (2.3.10) given above are also the same: the distinction between θ^* for the two different models is one of interpretation and not mathematics.

We now examine the form of the free energy for this three-component model. Consider the three contributions to the free energy: entropy of mixing (2.2.10), enthalpy of mixing (2.2.11), and chain stretching (2.2.16). We treat our nodules as having approximately infinite molecular weight and zero diffusivity: there is negligible free energy gain upon mixing nodules and so the entropy of mixing remains unchanged. The enthalpy of mixing, however, now has three pairwise interactions: macromer–network, nodules–network, and macromer–nodules. The first is important and is the same as (2.2.11). The experimental data discussed above (Fig. 2.5) illustrated that the χ value of a given system did not change significantly upon reaction and was independent of the macromer used. This motivates the assumption that the created nodules repel the macromer to the same extent that the original network strands do. In light of this similar repulsive behavior, we further conclude that any interaction between the nodules and the network would be negligible in comparison. With these

assumptions, the enthalpy of mixing is given solely by:

$$\Delta H_{mix} = kT\chi n_m(\phi_N + \phi_n). \tag{2.3.29}$$

The energy due to chain stretching has to be modified to bolster the material modulus appropriate to a particulate filler. Although there are many such models available [81], we chose one of the more versatile relations: the Kerner equation [82]. The Kerner equation has been shown to replicate experimental data at small volume fractions of filler; at larger filler-volume fractions, however, the Kerner equation tends to significantly underpredict the material modulus [81]. Because our currently designed systems for intraocular lenses operate at initial macromer volume fractions of less than 0.3—yielding nodule volume fractions lower than that—we take the model as a good approximation. As we will see, the Kerner equation is also especially illustrative because it allows a transition between the "two-component" and "three-component" models.

We choose to use the simplified form of the Kerner equation—which assumes that the filler species is infinitely stiff—since the nodules are assumed to be significantly stiffer than the host matrix; this is particularly true for small M_m, where the approximation of nodules is more appropriate. The dry composite modulus G_c of filler in a matrix with original modulus G_{dry} is then given by

$$G_c = G_{\text{dry}}\left(1 + \frac{\phi_n}{\phi_N}\lambda\right). \tag{2.3.30}$$

The parameter λ is a function of the matrix Poisson ratio, ν_N,

$$\lambda = \frac{15(1-\nu_N)}{(8-10\nu_N)}; \tag{2.3.31}$$

$\lambda = 2.5$ when the network is incompressible ($\nu_N = 0.5$). Using (2.3.30), we modify the free energy of stretching from (2.2.6) to

$$\frac{\Delta F_{el}}{V} = \frac{1}{2}G_{\text{dry}}\left(1 + \frac{\phi_n}{\phi_N}\lambda\right)\phi_f\Big(\operatorname{tr} F_{iJ}F_{jJ} - 3 - \ln\det F_{iJ}\Big), \tag{2.3.32}$$

ϕ_f appearing since the network and nodules together are the species that contribute to the free energy of stretching. Placing the relationships for network and nodule volume fractions (2.3.26) and (2.3.27) into (2.3.32), combining the three energetic contributions above and non–dimensionalizing by the osmotic modulus as before, the free energy for the three–component model is

$$A(F_{iJ},\phi_m,\phi_N,\phi_n) = \phi_m\ln\phi_m + \chi\phi_m\phi_f + \frac{1}{2}\epsilon\left(1 + \frac{\phi_n}{\phi_N}\lambda\right)\phi_f\Big(\operatorname{tr} F_{iJ}F_{jJ} - 3 - \ln\det F_{iJ}\Big). \tag{2.3.33}$$

The expression for the network and nodule volume fractions (2.3.26)–(2.3.27) can be used to simplify

(2.3.33) by using ϕ (dropping the subscript m) to denote the volume fraction of macromer —the only independent volume fraction. Also changing the reference to the initially swollen network, (2.3.33) becomes

$$A(F^*_{iJ},\phi) = \phi\ln\phi + \chi\phi(1-\phi) + \frac{1}{2}\epsilon'(1-\phi)\Big(Q_0^{2/3}\mathrm{tr}\,F^*_{iJ}F^*_{jJ} - 3 - \ln Q_0 - \ln\det F^*_{iJ}\Big). \tag{2.3.34}$$

Here, we have modified ϵ by including the extra term bolstering the network modulus by nodules:

$$\epsilon' = \epsilon\Big(1 + (\theta-1)\lambda\Big) \tag{2.3.35}$$

with $\lambda = 2.5$. The only change in the free energy between the two and three-component models is in this ϵ' term. If λ is set to zero, $\epsilon' \to \epsilon$ and we recover the two-component model.

Following the thought experiment presented in §2.3.2 to determine the cured modulus for the two-component model, we uniformly irradiate a sample to extent of reaction ξ, deswell the material isotropically by the volume ratio θ^*, and then subject it to a shear deformation (2.3.14). Under the same arguments as the previous section, the shear modulus for the three-component composite relative to the host network is

$$\frac{G_{\text{cured}}}{G_{\text{dry}}} = \Big(1 + (\theta-1)\lambda\Big)\theta^{2/3}. \tag{2.3.36}$$

This equation is plotted at full reaction against ϕ_0 ($\lambda = 2.5$) in Figure 2.4, alongside the two-component model. Notice that the modulus increase for the three-component model is greater than that predicted by the two-component model by the prefactor $1 + (\theta - 1)\lambda$. In fact, the three-component model provides an upper bound on the material modulus: the experimental data falls neatly between the two-component and three-component model. In general, the three-component model lies closer to the actual material modulus for smaller molar masses of macromer. This is because smaller chains are less capable of forming a persistent, secondary network than the longer chains and so tend to form locally dense nodules.

Choosing an appropriate value of λ between 0 and 2.5 and using ϵ' instead of ϵ allows corrections to the two-component model. For the remainder of this thesis, we choose to solely make use of the two-component model. It should be noted, however, that this model tends to underpredict the modulus at larger values of ϕ_0 when the macromer molar mass is large, and the results can be corrected by the three-component model.

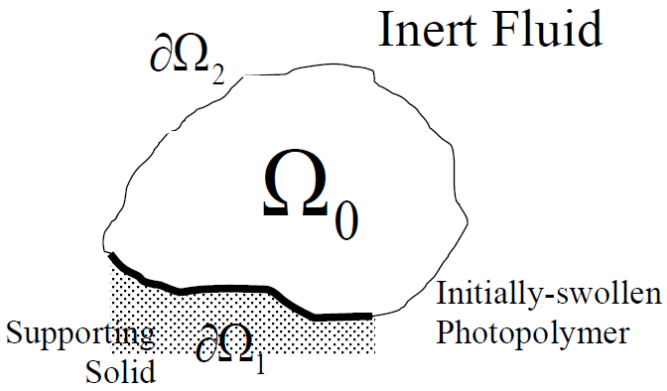

Figure 2.8: A solid elastomeric photopolymer occupies a region of space Ω_0 at time $t = 0$; the initial swelling ratio is Q_0. The gel is attached to a supporting solid along a portion of its boundary, $\partial\Omega_1$. Along the remainder of its boundary, $\partial\Omega_2$, the photopolymer is in contact with an inert fluid and can deform freely.

2.4 Variational Form and Differential Equivalence

We have illustrated the success of the two-component model in predicting the equilibrium swelling behavior of PDMS elastomers photoreacted with PDMS short chains. We now wish to apply the free energy developed above to solve a variety of problems. Consider a general problem in which a lump of elastomeric photopolymer is uniformly swollen by Q_0 (2.3.1) to occupy the reference region Ω_0 (Fig. 2.8). Let us assume that this solid is attached to a fixed substrate along a portion of its boundary, $\partial\Omega_1$. The remainder of its boundary, $\partial\Omega_2$, is exposed to an inert fluid that provides negligible attraction to macromer; the material is allowed to deform freely but no material inside the photopolymer is allowed to leave. Irradiating this material will cause gradients in macromer concentration, driving diffusion of the free macromer species. The body Ω_0 is deformed by this diffusion into the configuration $\Omega(t)$. We wish to determine the configuration $\Omega(t)$.

We now apply the developed free energy to determine the equilibrium (long–time) deformation of an elastomeric photopolymer given an initial conversion parameter θ. Since the system is closed to macromer transport, the gel will reach equilibrium at long times: this equilibrium corresponds to a minimization of the free energy of the gel. Using the dimensionless free energy per unit volume A we derived above (2.3.12), the system free-energy change at equilibrium is

$$F \equiv \frac{\Delta F}{G_{\rm OS} V_{eq}} = \frac{1}{V_{eq}} \int_{\Omega_{eq}} A(F^*_{iJ}, \phi) dV, \tag{2.4.1}$$

with V_{eq} being the volume of $\Omega_{eq} \equiv \Omega(t \to \infty)$, and the osmotic modulus (2.2.15) being taken as constant over the photopolymer sample.[6] In writing this expression, we have omitted the usual work

[6]The macromer molar mass and density, as well as the system temperature, tend to remain constant in space for applications of photoelastomers (2.2.15).

term [68] because we take the boundary $\partial\Omega_2$ to be force free.[7]

Since material neither leaves nor enters the system through the boundary, conservation of mass places a global constraint on the energy minimization, namely conservation of total volume

$$V_{eq} = V_0. \tag{2.4.2}$$

Here, V_0 is the total volume the system occupies before deformation

$$V_0 = \int_{\Omega_0} dV_0. \tag{2.4.3}$$

With

$$V_{eq} = \int_{\Omega_{eq}} dV = \int_{\Omega_0} Q^* dV_0, \tag{2.4.4}$$

Q^* defined in (2.3.10), the constrained energy $\widetilde{F}$ is given by:

$$\widetilde{F} \equiv F - p(V_{eq} - V_0) = \frac{1}{V_0}\int_{\Omega_0} \left[AQ^* - p(Q^* - 1)\right] dV_0. \tag{2.4.5}$$

The Lagrange multiplier p cannot depend upon position inside the gel since the constraint is global. We also note that the role of p is to act as a sort of pressure which constrains the gel from attaining configurations that do not conserve volume.

Since (2.3.10) gives a relationship for Q^* and ϕ in terms of the deformation gradient and the reaction parameter, $\widetilde{F}$ can be considered to be a function solely a function of $\mathbf{F}^*$ and the parameter θ^*. For a specified reaction parameter field, minimization of $\widetilde{F}$ yields

$$\delta\widetilde{F} = 0 = \frac{1}{V_0}\int_{\Omega_0} \left\{ \left[\frac{\partial A(\mathbf{F}^*, \phi)}{\partial F^*_{iJ}} + \frac{\partial A(\mathbf{F}^*, \phi)}{\partial \phi}\frac{\partial \phi}{\partial Q^*}\frac{\partial Q^*}{\partial F^*_{iJ}} \right] Q^* + A\frac{\partial Q^*}{\partial F^*_{iJ}} - p\frac{\partial Q^*}{\partial F^*_{iJ}} \right\} \delta F^*_{iJ} dV_0. \tag{2.4.6}$$

Using the expressions for Q^* (2.3.10), the energy density A (2.3.12), and the osmotic pressure $\Pi(\phi)$ (2.2.24), and recalling the relation $\frac{\partial \det \mathbf{F}^*}{\partial \mathbf{F}^*} = \det \mathbf{F}^* \mathbf{F}^{*-T}$, (2.4.6) becomes

$$\int_{\Omega_0} P_{iJ}\delta F^*_{iJ} dV_0 = 0 \tag{2.4.7}$$

with first Piola–Kirchhoff stress tensor

$$P_{iJ} = Q^*\frac{\partial A}{\partial F^*_{iJ}} - \left[\Pi(\phi) + p\right] Q^* {F^*_{iJ}}^{-1}. \tag{2.4.8}$$

[7] In principle, there will be a force exerted by the inert fluid on the surface due to an external constant pressure. This can be easily eliminated, however, by measuring all stress relative to this standard pressure. Note that no forces can be applied along $\partial\Omega_1$ because we have already specified that the gel is attached to these surfaces. To allow for more general cases in which forces are applied at the boundaries, the external work term that should be added is given by $W_= - \int_{\partial\Omega} \sigma_{ij} n_j (x_i - X_I) dS$, where σ_{ij} is the Cauchy stress tensor for the system and n_j is the unit normal to dS.

With χ_i^* the mapping from Ω_0 to Ω—analogous to (2.2.1)—we can use integration by parts to write (2.4.7) as

$$-\int_{\Omega_0} P_{iJ,J}\delta\chi_i^* dV_0 = 0, \tag{2.4.9}$$

the boundary terms disappearing since $\partial\Omega_2$ is stress free and $\partial\chi_i^* = 0$ on $\partial\Omega_1$. For this relation to hold for arbitrary variations in χ_i^*,

$$P_{iJ,J} = 0 \tag{2.4.10}$$

must hold pointwise inside the material. We can write this in terms of the Cauchy stress using the Piola transform

$$Q^*\sigma_{ij} = P_{iJ}F_{jJ}^* \tag{2.4.11}$$

so that

$$\sigma_{ij} = -p\delta_{ij} - \Pi(\phi)\delta_{ij} + \frac{\partial A}{\partial F_{iJ}^*}F_{jJ}^*. \tag{2.4.12}$$

The Piola transform can also be used on (2.4.10) to yield the spatial equation of conservation of momentum

$$\sigma_{ij,j} = 0. \tag{2.4.13}$$

We will see in the next chapter that the relations (2.4.12) and (2.4.13) written from energy minimization correspond to the conservation principles and constitutive laws derived using a traditional continuum mechanics approach for a system in which inertial and gravitational forces are negligible.

2.5 Supplemental Material

2.5.1 Equilibrium Swelling Data for M_m = 500 and 3000 g/mol

In Figure 2.9, we show the theoretical prediction (2.3.20) for equilibrium swelling alongside the experimentally determined data [1] for macromer molar masses of (a) 500 and (b) 3000 g/mol, respectively. For M_m = 500 g/mol (Fig. 2.9a), the pipped data points are the furthest removed from their theoretical counterparts for the same reasoning as the M_m = 1000 g/mol: they are at $\phi_0 = 0.3$ and the modulus is significantly undepredicted. The worst prediction occurs at the particularly low value of $G_{\text{dry}} = 0.054$ MPa (the right pip point), similar to that seen for the right pip point in Fig. 2.6. For M_m = 3000 g/mol (Fig. 2.9b), there is not as much discrepancy for the points at $\phi_0 = 0.3$ because the modulus is not as significantly underpredicted at this molar mass. However, the discrepancy between the right pip point is again due to the particularly small value of $G_{\text{dry}} = 0.054$ MPa. Both of these results—along with those obtained for M_m = 1000 g/mol—indicate that two-component swelling theory gives a better prediction of the actual behavior for $\phi_0 < 0.3$ and $G_{\text{dry}} > 0.1$ MPa.

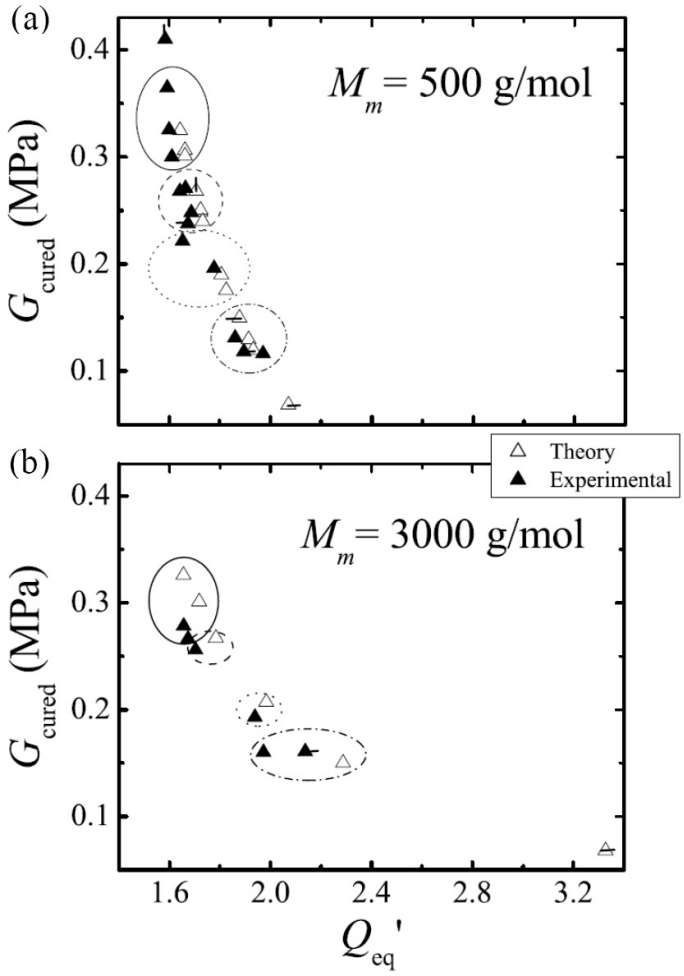

Figure 2.9: The analog of Figure 2.6 (§2.3.2) for (a) $M_m = 500$ g/mol and (b) $M_m = 3000$ g/mol. For most of the data, the theoretical predictions (open triangles) lie near the experimental data (solid triangles). The circles group sets of similar $G_{\rm dry}$: (line) $0.28 \geq G_{\rm dry} > 0.25$ MPa, (dash) $G_{\rm dry} \approx 0.21$ MPa (except the closed left pip point in (a) which has $G_{\rm dry} = 0.118$ MPa), (dot) $G_{\rm dry} \approx 0.16$ MPa, and (dash–dot) $G_{\rm dry} \approx 0.11$ MPa (except the right pip points in both figures which have $G_{\rm dry} = 0.54$ MPa). (a) The points with pips are significantly removed from their corresponding theoretical prediction. These discrepancies are for the same reason as the data for $M_m = 1000$: they are at the high value of $\phi_0 = 0.3$ and the modulus is underpredicted. The worst fit point (right pip) occurs for the softest network $G_{\rm dry} = 0.054$ MPa. (b) The points with $\phi_0 = 0.3$ are a better fit at $M_m = 3000$ g/mol than for the other two molar masses due to the fact that the modulus is not significantly underpredicted at this molar mass (Fig. 2.4). As with the other two molar masses, we note that the model poorly fits the smallest value of $G_{\rm dry} = 0.054$ MPa (right pip point).

Chapter 3

Differential Formulation from Mixture Theory

3.1 Introduction

The previous chapter centered on modeling the equilibrium deformation of elastomeric photopolymers by developing a free-energy functional consistent with experimentally observed data. This was done by using a statistical mechanical model originally developed by Flory [35] which considered contributions to the motion of individual atoms and molecules. Consideration of the thermodynamic behavior of individual molecules allowed us to imbed important material design parameters directly into the model. The key focus of that chapter was the development of a simple "two-component" free-energy functional in which macromer chains react directly into network chains. This simplification to the system was shown to capture the qualitative and quantitative equilibrium swelling behavior of elastomeric photopolymers throughout most of the clinically relevant parameter space.

An equilibrium treatment, however, is insufficient to predict the *dynamics* of an elastomeric photopolymer: the time-dependent process of *how* the system approaches equilibrium. For many applications, the dynamics are just as important. For example, physicians using a light–adjustable lens need to know how long it takes the lens to attain its equilibrium shape so that they know when it is appropriate to "lock in" that shape. As can be expected, minimization of an energy functional does not allow one to capture transient behavior: the energy achieves the smallest possible value without consideration of kinetics. In general, it is necessary to write governing differential equations which can track the reaction–diffusion–deformation behavior in time. On this, we focus this chapter.

Although we focus on a differential formulation for modeling transient behavior, it should be noted that there is a developing body of work which considers a variational form for transient processes. In a way similar to energy minimization, Ziegler proposed maximization of a dissipation functional will yield the same governing equations as transient conservation laws [71]. Baek and co–workers have applied this idea to the development of swelling in a gel [68, 69]. This new body of

work poses promise in connecting transient conservation laws with thermodynamic principles. As previously mentioned (Ch. 1), however, it is non–trivial to write the necessary dissipation functionals required to include reaction. Although we have considered using this theory, we will not discuss it here.

Instead, we choose to write a differential formulation for modeling the light–induced shape change of an elastomeric photopolymer. Motivated by A. Wineman and co–workers, who modelled the steady–state swelling behavior of a variety of geometrically different gels [59, 62, 63], we use a mixture theory model. This model uses conservation principles to write system differential equations accounting for the movement of mass, momentum, and energy for each species within the system, in keeping with Newton's laws and the laws of thermodynamics. The development of the equations of mixture theory can be found in many different sources (e.g. [47–49]). Unfortunately, discrepancies between the different formulations have resulted in some confusion in the field [46]. This uncertainty stems from the way *overall* system parameters are defined based on individual *constituent* parameters. Barring slight changes in notation, we tend to follow the formulation given in Atkin and Craine [46]; this is because it has been most widely cited in the literature and shows how the results obtained connect to those of other authors. We briefly present a derivation of the governing equations of mixture theory from first principles in Appendix A.

In order to close the system of equations, constitutive equations need to be developed. In traditional continuum mechanics applications, an appeal is always made to the second law of thermodynamics in order to determine permissible constitutive relations. Mixture theory inherits from traditional continuum mechanics the merits of the second law through the Clausius–Duhem inequality [49,50]. With this thermodynamic knowledge being incorporated into the constitutive equations, we can close the underspecified system of equations developed from conservation principles and solve a variety of problems. In determining the governing equations, it is our goal to be explicit regarding any assumptions made in order to ensure model robustness. We also employ scaling analysis to make rational choices for approximations. Lastly, we strive to connect the meaning behind the mathematics to experimentally measurable quantities in order to enable experimentalists to validate the model and use it for future research. Based on the success of the "two-component" model in capturing equilibrium swelling behavior seen in the last chapter, we present the governing differential equations here for this model only, leaving an extension for the "three-component" model to future work.

3.2 Kinematics

Because mixture theory tracks the important scalar and vector fields for each individual component, the model now requires a separate reference configuration for each component (Fig. 3.1). We take

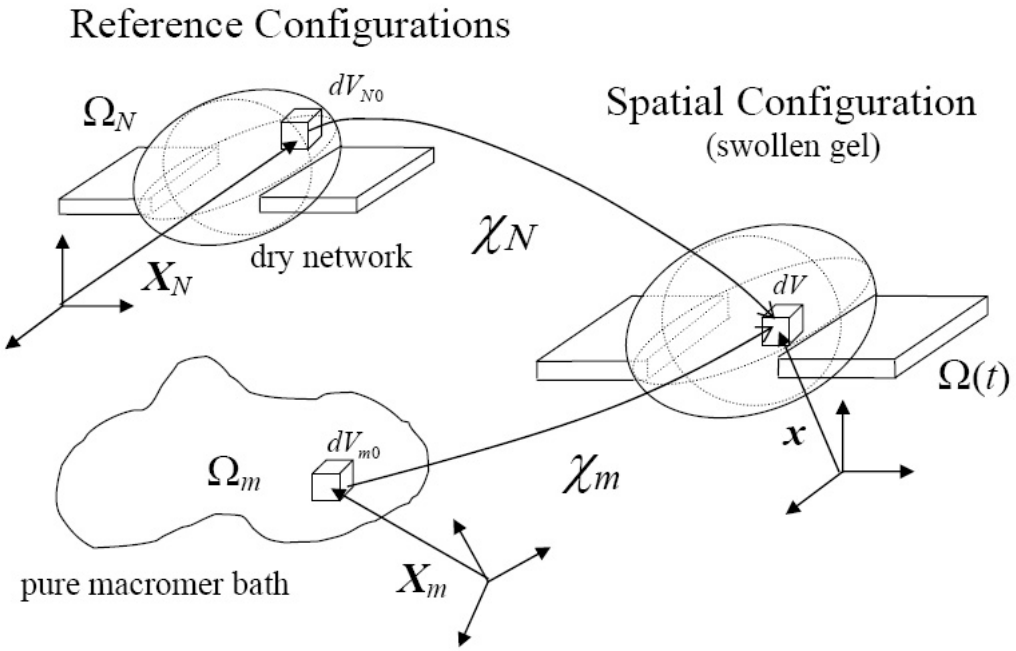

Figure 3.1: The reference states of the network and macromer are defined as the pure component species. A volume element located at point $\boldsymbol{X}_N$ in the network reference configuration Ω_N is mapped to a volume element located at $\boldsymbol{x}$ in the spatial configuration $\Omega(t)$. This spatial volume element also contains a volume element of macromer located at $\boldsymbol{X}_m$ mapped from the macromer reference Ω_m.

reference states for the macromer, m, and the network, N, to be the pure component states of both prior to mixing. Call the reference state of macromer Ω_m labeled with points $\boldsymbol{X}_m$ and that for the network Ω_N labelled with points $\boldsymbol{X}_N$. Although there are separate reference configurations for each species, there is only one spatial configuration which all species share. That is, at every point in time, a differential volume of pure macromer that was at $\boldsymbol{X}_m$ in the macromer reference is then at $\boldsymbol{x}$ in the spatial configuration $\Omega(t)$; likewise, a differential volume of pure network at $\boldsymbol{X}_N$ is located at that same point (Figure 3.1). This gives rise to the mappings:

$$x_i = \chi_i^m(\boldsymbol{X}_m, t) \tag{3.2.1}$$

and

$$x_i = \chi_i^N(\boldsymbol{X}_N, t) \tag{3.2.2}$$

(the same indexing scheme is used as in Ch. 2: upper–case letters remind us of the reference configuration, lower–case letters the spatial configuration). It should be mentioned at this point that because the macromer is a liquid, its reference state is not well defined: the macromer liquid does not have a definite shape, and any random deformation will produce a new but equivalent reference state. It should also be noted that such deformations do not change the energy of the macromer.

For this reason, the mapping χ_i^m is not particularly useful. In fact, the system deformation can be described solely in terms of the network deformation gradient:

$$F_{iJ}^N(\boldsymbol{X}_N, t) = \frac{\partial \chi_i^N}{\partial X_J^N}(\boldsymbol{X}_N, t). \tag{3.2.3}$$

Since the macromer deformation gradient is of no particular use, we call the network deformation gradient *the* deformation gradient F_{iJ}; this is in line with the definition of the deformation gradient used in Chapter 2 (§2.2).

Although the actual mapping χ_i^m is not particularily useful because it measures deformations of the liquid, the velocity of the liquid is of importance. The time derivatives of each mapping (3.2.1) and (3.2.2) are the species velocity fields. Although both spatial and reference velocity fields can be defined (§A.2), this work focuses on the spatial quantities: $v_i^m(\boldsymbol{x}, t)$ and $v_i^N(\boldsymbol{x}, t)$ defined over $\Omega(t)$. It should be noted that the variables v_i^N and F_{iJ} are not independent, because they are related through (3.2.2): knowledge of the time–dependent deformation of network determines the velocity of the network.

We define the pure component density fields ρ_{m0} and ρ_{N0} uniform over each reference configuration. The corresponding spatial density fields $\rho_m(\boldsymbol{x}, t)$ and $\rho_N(\boldsymbol{x}, t)$ are allowed to vary with position. We choose to work in terms of the spatial volume fractions of each species (A.2.5):

$$\phi_m(\boldsymbol{x}, t) = \frac{\rho_m(\boldsymbol{x}, t)}{\rho_{m0}} \tag{3.2.4}$$

and

$$\phi_N(\boldsymbol{x}, t) = \frac{\rho_N(\boldsymbol{x}, t)}{\rho_{N0}}. \tag{3.2.5}$$

For two species, the definition of volume fraction requires $\phi_m + \phi_N = 1$. For this reason, we again define $\phi \equiv \phi_m$ and let $\phi_N = 1 - \phi$, as in Ch. 2.

Using (3.2.4) and (3.2.5), the spatial density field (A.2.4) can be written in terms of macromer volume fraction:

$$\rho(\boldsymbol{x}, t) = \rho_m(\boldsymbol{x}, t) + \rho_N(\boldsymbol{x}, t) = (\rho_{m0} - \rho_{N0})\phi(\boldsymbol{x}, t) + \rho_{N0}. \tag{3.2.6}$$

When the two pure component species have different densities, the spatial density field will vary spatially with macromer volume fraction. In order to enforce incompressibility, we require $\rho = \rho_{N0} = \rho_{m0}$ be uniform and constant. As previously mentioned in §2.3.1, this has been observed to good approximation. The barycentric velocity $\mathbf{v}(\boldsymbol{x}, t)$ (A.2.7) is then the volume fraction weighted average of the species component velocities:

$$\mathbf{v}(\boldsymbol{x}, t) = \phi(\boldsymbol{x}, t)\mathbf{v}_m(\boldsymbol{x}, t) + (1 - \phi(\boldsymbol{x}, t))\mathbf{v}_N(\boldsymbol{x}, t). \tag{3.2.7}$$

Rather than use the component velocities, we instead define the flux of macromer J_i^m:

$$J_i^m \equiv \rho_m \left(v_i^m - v_i\right) = \rho\phi(1-\phi)\left(v_i^m - v_i^N\right) \tag{3.2.8}$$

and the flux of network J_i^N

$$J_i^N \equiv \rho_N \left(v_i^N - v_i\right) = -\rho\phi(1-\phi)\left(v_i^m - v_i^N\right). \tag{3.2.9}$$

The second equality for both equations comes by placing in the expression for v_i (3.2.7) in terms of component velocities; the reason we write the second equality in (3.2.8) will become clear when we determine constitutive laws below. Note that $J_i^m = -J_i^N$ for a two-component system.

3.3 Conservation Principles

3.3.1 Conservation of Mass

The mass conservation equations for each species are (A.3.8)

$$\frac{\partial \rho_m}{\partial t} + \frac{\partial}{\partial x_i}(\rho_m v_i^m) = r_m \tag{3.3.1}$$

and

$$\frac{\partial \rho_N}{\partial t} + \frac{\partial}{\partial x_i}(\rho_N v_i^N) = r_N, \tag{3.3.2}$$

with r_α the rate of creation of species α through reaction. For macromer converting into network chains, $r_N = -r_m$. Writing (3.3.1) in terms of the total derivative D/Dt (A.5.10) and the diffusive flux of macromer $J_i^m(\boldsymbol{x}, t) = \rho_m(v_i^m - v_i)$, we arrive at the equation of conservation of mass in terms of macromer concentration:

$$\frac{D\rho_m}{Dt} + \frac{\partial J_i^m}{\partial x_i} = r_m, \tag{3.3.3}$$

This relation will be used to solve transient problems in Ch. 6. Although (3.3.3) can be solved for an evolving volume fraction profile ϕ during reaction by including a reaction rate as a function of volume fraction, we instead choose to focus on cases in which reaction occurs much more rapidly than diffusion (discussed in §2.3). We then specify an extent-of-reaction profile which serves to set an initial condition for the volume fraction profile.

To compare to the equilibrium solution (Ch. 2), we write mass conservation over the reference configuration (A.3.7) in terms of network concentration:

$$\det F_{iJ}(\boldsymbol{X}_N, t) = \frac{\theta_N(\boldsymbol{X}_N, t)}{\phi_N(\boldsymbol{\chi}_N(\boldsymbol{X}_N, t), t)}. \tag{3.3.4}$$

With $\phi_N = 1 - \phi$, $\det F_{iJ} \equiv Q$ relative to the pure network reference (which is dry network) and $\theta \equiv \theta_N$, this equation is the same as that in Ch. 2 (2.3.7). With this equation, the details of the volume fraction development through time are not specified via a differential equation, making this equation particularly useful for the equilibrium solutions. In particular, specifying the conversion parameter θ at the initial time allows a simple relationship (3.3.4) between the volume fraction and the deformation. This removes a degree of freedom in the energy minimization principle discussed in §2.4.

The second independent conservation of mass equation used for both equilibrium and transient analysis is the incompressibility constraint. This is obtained by summing (3.3.1) and (3.3.2) together and introducing the definitions of total spatial density (3.2.6) and barycentric velocity (3.2.7):

$$\frac{\partial \rho}{\partial t} + \frac{\partial}{\partial x_i}(\rho v_i) = 0. \tag{3.3.5}$$

Simplified to the incompressible case ($\rho =$ constant),

$$\frac{\partial v_i}{\partial x_i} = 0. \tag{3.3.6}$$

The equation of incompressibility is a constraint on the velocity field. With the definition of $\mathbf{v}$ above (3.2.7), this equation is the same as that used in the stress–diffusion coupling model of Doi [40].

3.3.2 Conservation of Linear Momentum

Under the assumption that reaction has completed before diffusion begins, the equations of conservation of linear momentum for the two species are (A.3.22):

$$\rho_m \frac{\partial v_i^m}{\partial t} + \rho_m v_i^m v_{i,j}^m = \sigma_{ij,j}^m + \rho_m g_i - b_i \tag{3.3.7}$$

and

$$\rho_N \frac{\partial v_i^N}{\partial t} + \rho_N v_i^N v_{i,j}^N = \sigma_{ij,j}^N + \rho_N g_i + b_i. \tag{3.3.8}$$

Here, σ_{ij}^α is the partial stress on species α (such that the total stress $\sigma_{ij} = \sigma_{ij}^m + \sigma_{ij}^N$), g_i is the acceleration due to gravity and b_i is the internal body force per unit volume exerted by the macromer on the network. In writing these equations, we have required $b_i^N = -b_i^m = b_i$ to satisfy Newton's third law and have assumed that the only external body force is due to gravity.

Using appropriate material parameters for PDMS elastomeric photopolymers, we perform a scaling analysis on these conservation equations (§B.5.1). As would be expected for a system in which species slowly diffuse, the inertial terms on the left–hand sides of the equation are $\mathcal{O}(10^{-19})$ relative to the stresses and internal forces in the system. The gravitational forces are also small

($\mathcal{O}(10^{-5})$), leaving the following simplified relations:

$$\sigma^m_{ij,j} - b_i = 0 \tag{3.3.9}$$

and

$$\sigma^N_{ij,j} + b_i = 0, \tag{3.3.10}$$

i.e., the internal forces acting on each species are balanced by the divergence of each partial stress. These relations sum to a force free system

$$\sigma_{ij,j} = 0 \tag{3.3.11}$$

as would be expected for a system with no external forces. The reader may then question: how does the object deform without any application of external forces? It does so through b_i. As the macromer diffuses through the network, it exerts an internal force on the network, causing chains to deform in a non–uniform pattern. This results in a net warping of the material although no net force is observed on the system. We now turn to developing expressions for the partial stresses and diffusive body force in terms of volume fraction, system deformation, and material parameters.

3.4 Constitutive Equations for the Light–Adjustable Lens

We now have a system of differential equations to solve: two scalar mass conservation equations, (3.3.3) and (3.3.4), and two vector equations for conservation of linear momentum, (3.3.9)–(3.3.10). The variable fields that we would like to solve for are

$$\rho_m, v^m_i, v^N_i, F_{iJ}, \sigma^m_{ij}, \sigma^N_{ij}, b_i$$

as functions of position x_i and time. Notice that among the list of variables, ρ_N is not included because $\rho_m + \rho_N = \rho$, a specified constant. It should also be noted that v^N_i and F_{ij} are not indepedent: they are both derivatives of the same mapping χ^N_i (3.2.2) so that $\dot{F}_{iJ} = v^N_{i,j}F_{jJ}$ (the overdot represents a time derivative). Even with these simplifications, there are still more variables than equations, and so we pursue the usual route of specifying constitutive relations. For reasons that will shortly become apparent, all our constitutive relations will be written in terms of derivatives of the Helmholtz free energy per unit volume A: the appropriate thermodynamic functional for incompressible, isothermal systems.

In continuum mechanics—and therefore the subset of mixture theory—the Clausius–Duhem inequality is used to postulate constitutive relations that are in keeping with the second law of thermodynamics. For the incompressible, isothermal two-component system of macromer instantaneously

reacting to network ($r_m = 0$), the Clausius–Duhem inequality (A.4.6) becomes:

$$\frac{DA}{Dt} - \sigma_{ij}^m v_{i,j}^m - \sigma_{ij}^N v_{i,j}^N - b_i \left(v_i^m - v_i^N\right) + \Theta + \psi v_{i,i} \leq 0, \tag{3.4.1}$$

Θ given in (A.4.8). The term $\psi v_{i,i}$ represents the incompressibility constraint on the velocity field (3.3.6): ψ is a Lagrange multiplier as yet to be determined. The relative velocity $v_i^m - v_i^N$ is the important dynamic variable that can be related to the flux of macromer J_i^m through (3.2.8). Although we will introduce J_i^m shortly, making use of the relative velocity $v_i^m - v_i^N$ allows the following development to proceed more symmetrically.

Following a method taking advantage of the two–component nature of the system, and introduced by Green and Naghdi [45], Θ can be incorporated into the definitions of σ_{ij}^m, σ_{ij}^N, and b_i without affecting the governing equations (3.3.9) and (3.3.10). With this simplification and writing v_i in terms of the species velocities (3.2.7), (3.4.1) becomes

$$\frac{DA}{Dt} - (\sigma_{ij}^m - \psi\phi\delta_{ij}) v_{i,j}^m - \left(\sigma_{ij}^N - \psi(1-\phi)\delta_{ij}\right) v_{i,j}^N - (b_i - \psi\phi_{,i}) \left(v_i^m - v_i^N\right) \leq 0. \tag{3.4.2}$$

The free energy of the system only depends upon the thermodynamic system variables: namely, ϕ (or ρ_m) and F_{iJ}.[1] Placing a free energy of the functional form

$$A = A(\phi, F_{iJ}) \tag{3.4.3}$$

into (3.4.2), we can expand out the material derivative in terms of ϕ and F_{iJ} multiplied by the corresponding partial derivatives of A. However, it is more illustrative to expand out the total derivative DA/Dt using the definition of the barycentric velocity (3.2.7):

$$\frac{DA}{Dt} = \frac{\partial A}{\partial t} + v_i A_{,i} = \frac{\partial A}{\partial t} + v_i^N A_{,i} + \phi A_{,i} \left(v_i^m - v_i^N\right) = \frac{D^{(N)} A}{Dt} + \phi A_{,i} \left(v_i^m - v_i^N\right) \tag{3.4.4}$$

where

$$\frac{D^{(N)} A}{Dt} \equiv \frac{\partial A}{\partial t} + v_i^N A_{,i} \tag{3.4.5}$$

can be seen as the rate of change of the free energy following along a particular network strand. Placing this relationship and the variable dependence of the free energy (3.4.3) allows us to write (3.4.4) as:

$$\frac{DA}{Dt} = \frac{\partial A}{\partial \phi} \frac{D^{(N)}\phi}{Dt} + \frac{\partial A}{\partial F_{iJ}} \frac{D^{(N)} F_{iJ}}{Dt} + \phi A_{,i} \left(v_i^m - v_i^N\right). \tag{3.4.6}$$

[1] For a non–isothermal case, temperature would need to be included in this list as well.

The system kinematics (3.2.1) yields:

$$\frac{D^{(N)}F_{iJ}}{Dt} \equiv \dot{F}_{iJ} = v^N_{i,j}F_{jJ}. \tag{3.4.7}$$

We can define the partial total derivative with respect to macromer as

$$\frac{D^{(m)}\phi}{Dt} = \frac{\partial\phi}{\partial t} + v^m_i\phi_{,i}; \tag{3.4.8}$$

the two partial total derivatives are related by $D^{(N)}\phi/Dt = D^{(m)}\phi/Dt - \phi_{,i}(v^m_i - v^N_i)$. Using conservation of mass of macromer (3.3.3) and the kinematics (3.4.7) expands (3.4.6):

$$\frac{DA}{Dt} = \frac{\partial A}{\partial\phi}\left[-\phi v^m_{i,i} - \phi_{,i}(v^m_i - v^N_i)\right] + \frac{\partial A}{\partial F_{iJ}}F_{jJ}v^N_{i,j} + \phi A_{,i}\left(v^m_i - v^N_i\right). \tag{3.4.9}$$

This is placed back into the Clausius–Duhem inequality (3.4.2):

$$\begin{aligned} -\left(\sigma^m_{ij} - \psi\phi\delta_{ij} + \phi\frac{\partial A}{\partial\phi}\delta_{ij}\right)v^m_{i,j} - \left(\sigma^N_{ij} - \psi(1-\phi)\delta_{ij} - \frac{\partial A}{\partial F_{iJ}}F_{jJ}\right)v^N_{i,j} \\ - \left(b_i - \psi\phi_{,i} - \phi A_{,i} + \frac{\partial A}{\partial\phi}\phi_{,i}\right)\left(v^m_i - v^N_i\right) \quad \leq \quad 0. \end{aligned} \tag{3.4.10}$$

3.4.1 Static and Dynamic Contributions

Following the derivation in Rajagopal and Wineman [59, 84], we expect each of the stress tensors and the internal body force to consist of two parts: a "dynamic" part and a "static" part. The static part of each partial stress tensor is an equilibrium stress due only to the current deformation and can be represented in terms of the the Helmholtz free-energy functional. The dynamic portion of a stress tensor exists due to the deformation rate and is identically zero at equilibrium. We denote the static variables with "$\hat{}$" and the dynamic variables with "$\widetilde{}$":

$$\sigma^\alpha_{ij} = \hat{\sigma}^\alpha_{ij} + \widetilde{\sigma}^\alpha_{ij}, \tag{3.4.11}$$

and

$$b_i = \hat{b}_i + \widetilde{b}_i. \tag{3.4.12}$$

Once these relations are placed into (3.4.10), the constitutive laws for the equilibrium variables can be found by noting that the equilibrium stresses and force should not contribute to entropy generation for any arbitrary deformation rates. The resulting expressions for the equilibrium stresses are the same as those obtained in the work of Rajagopal and Wineman [59]:

$$\hat{\sigma}^m_{ij} = \psi\phi\delta_{ij} - \phi\frac{\partial A}{\partial\phi}\delta_{ij} \tag{3.4.13}$$

and

$$\hat{\sigma}_{ij}^{N} = \psi(1-\phi)\delta_{ij} + \frac{\partial A}{\partial F_{iJ}} F_{jJ}. \tag{3.4.14}$$

The expression for the equilibrium internal body force can also be written in the same form as that done by Rajagopal and Wineman by expanding out the free-energy gradient. It is more illustrative, however, to leave it in a slightly different form congruent with what we have done above:

$$\hat{b}_i = \psi\phi_{,i} + \phi A_{,i} - \frac{\partial A}{\partial \phi}\phi_{,i}. \tag{3.4.15}$$

Inserting (3.4.13)–(3.4.15) into (3.4.10), the entropy inequality now only has contributions due to the dynamic portions:

$$\widetilde{\sigma}_{ij}^{m} v_{i,j}^{m} + \widetilde{\sigma}_{ij}^{N} v_{i,j}^{N} + \widetilde{b}_i \left(v_i^m - v_i^N \right) \geq 0. \tag{3.4.16}$$

Each of these terms represents a work done which acts only to increase system entropy. For purely reversible processes, the dynamic terms would all be equivalently zero; for an irreversible process, the entropy must increase. Following Hong et al. [72], we assume that the network can instantaneously relax to its equilibrium configuration at every moment of diffusion; this is essentially ignoring any viscoelastic effect in the network chains. As such, there should be no dynamic contribution to the network stress: $\widetilde{\sigma}_{ij}^{N} = 0$. The macromer chains, on the other hand, may contribute work as they diffuse by network chains. We consider two contributions: one due to the internal viscosity of the macromer chains themselves (accounted for in $\widetilde{\sigma}_{ij}^{m}$) and the other due to the friction of macromer chains on network strands as they diffuse (accounted for in $\widetilde{b}_i$). Both of these processes must be chosen such that system entropy increases (3.4.16).

To begin specifying constitutive relationships for these two variables, material frame indifference dictates that $\hat{\sigma}_{ij}^{N}(\phi, F_{iJ})$ (3.4.14) can only be a function of the symmetric tensor $F_{iJ}F_{jJ}$; this forces the free-energy functional A to depend only upon the invariants of F_{iJ}. In addition, $\hat{\sigma}_{ij}^{N}$ itself must be symmetric because it is a function of a symmetric tensor. Since there are no dynamic contributions to the network stress, σ_{ij}^{N} is then itself symmetric. Conservation of angular momentum for a two–component system [46]

$$\boldsymbol{\sigma}_m - \boldsymbol{\sigma}_m^T = \boldsymbol{\sigma}_N^T - \boldsymbol{\sigma}_N = 0 \tag{3.4.17}$$

then dictates that σ_{ij}^{m} also be a symmetric tensor.

In order to satisfy material objectivity, the constitutive equations for the dynamic variables $\widetilde{\sigma}_{ij}^{m}$ and $\widetilde{b}_i$ can only depend upon objective quantities. By taking our system as isotropic and using linear Onsager relationships, we can write expressions for the dynamic macromer stress as

$$\widetilde{\sigma}_{ij}^{m} = \gamma D_{kk}^{m}\delta_{ij} + 2\mu D_{ij}^{m}. \tag{3.4.18}$$

Here, $D^m_{ij} = v^m_{i,j}$ is the symmetric rate of deformation tensor and γ and μ are constitutive parameters describing the dissipative nature of the macromer fluid. To satisfy the Clausius–Duhem inequality (3.4.16) for any general deformation, $\gamma, \mu > 0$. In essence, we have modeled the dissipative character of the macromer as a Newtonian fluid. From several shear experiments on pure macromer (§B.5.2), this holds true at small shear rates appropriate to those experienced in application.

We specify a constitutive law for the dynamic internal stress that is linearly proportional to the relative velocity as macromer moves by network:

$$\widetilde{b}_i = \frac{1}{\mathcal{D}}\phi(1-\phi)(v^m_i - v^N_i). \tag{3.4.19}$$

The proportionality constant is the inverse of the diffusivity of a macromer molecule in network, $\mathcal{D}$, by the Stokes–Einstein relation. We include the prefactor $\phi(1-\phi)$ for reasons that will become apparent below. Choosing (3.4.19) implies

$$\widetilde{b}_i(v^m_i - v^N_i) = \frac{1}{\mathcal{D}}\phi(1-\phi)(v^m_i - v^N_i)(v^m_i - v^N_i). \tag{3.4.20}$$

This insures positive entropy production as long as $\mathcal{D} > 0$ (3.4.16). Besides the fact that we assume our stresses are symmetric, the chosen dynamic constitutive equations (3.4.18) and (3.4.19) are the same as those of [59], aside from the factor $\phi(1-\phi)$ in (3.4.19).

A scaling analysis indicates that we may ignore the dynamic macromer stress terms relative to the equilibrium terms (§B.5.2). This is essentially because of the small viscosity of macromer ($\mathcal{O}(10^{-2})$) and small deformation rate: the viscous terms scale as $\mathcal{O}(10^{-12})$ times smaller than the elastic stretching terms. This produces final constitutive relations for the partial stresses:

$$\sigma^m_{ij} = \psi\phi\delta_{ij} - \phi\frac{\partial A}{\partial \phi}\delta_{ij} \tag{3.4.21}$$

$$\sigma^N_{ij} = \psi(1-\phi)\delta_{ij} + \frac{\partial A}{\partial F_{iJ}}F_{jJ}. \tag{3.4.22}$$

A scaling analysis of the internal body force indicates that the equilibrium and dynamic portion scale similarily; we therefore find a constitutive law for the internal body force of

$$b_i = \psi\phi_{,i} + \phi A_{,i} - \frac{\partial A}{\partial \phi}\phi_{,i} + \frac{1}{\rho\mathcal{D}}J^m_i. \tag{3.4.23}$$

Here, we have replaced the relative velocity in the dynamic internal body force (3.4.19) with the flux of macromer (3.2.8). Placing the constitutive laws (3.4.21) and (3.4.23) into conservation of

momentum of macromer (3.3.9) imparts meaning to the Lagrange multiplier ψ:

$$\phi\left[\psi - A - \frac{\partial A}{\partial \phi}\right]_{,i} = \frac{1}{\rho\mathcal{D}} J_i^m. \tag{3.4.24}$$

As with the other variables, we break ψ into a dynamic and a static part:

$$\psi = \hat{\psi} + \widetilde{\psi}. \tag{3.4.25}$$

Placing this relation into (3.4.27) and allowing

$$\hat{\psi} = A + \frac{\partial A}{\partial \phi} \tag{3.4.26}$$

yields an effective constitutive relationship for the flux of macromer

$$J_i^m = \rho\mathcal{D}\phi\widetilde{\psi}_{,i}. \tag{3.4.27}$$

The static part of ψ does not contribute to the flux by definition; the dynamic part provides a potential for the flux exactly like the chemical potential in Fick's law. Here, however, $\widetilde{\psi}$ is not a specified functional but rather a Lagrange multiplier that has to be determined through solution of the system of equations and the incompressibility constraint. At equilibrium, the material should not deform: $J_i^m = 0$ and $\widetilde{\psi}$ must be independent of position by (3.4.27). This is in keeping with the derivation performed in Ch. 2 (§2.4): at equilibrium, there is a position-independent Lagrange multiplier $-p$ (not to be confused with pressure) which insures the final and initial system volumes are equivalent. To distinguish between the equilibrium and transient cases through the rest of this work, we use $-p$ to represent the Lagrange multipler corresponding to keeping the total volume fixed at equilibrium (Ch. 2 (2.4.2)) and $\widetilde{\psi}$ to denote the transient, position-dependent Lagrange multiplier associated with the differential expression of incompressibility: a divergence-free velocity field (Ch. 3 (3.3.6)).

3.4.2 Analysis of Constitutive Relations

Placing the expressions for ψ (3.4.25)–(3.4.26) into the equation for the partial stresses (3.4.21)–(3.4.22) and summing them together yields a relationship for the total stress:

$$\sigma_{ij} = \widetilde{\psi}\delta_{ij} - \Pi\delta_{ij} + \frac{\partial A}{\partial F_{iJ}} F_{jJ}. \tag{3.4.28}$$

Here, we have defined the osmotic pressure

$$\Pi(\phi) \equiv -\left[A + (1-\phi)\frac{\partial A}{\partial \phi}\right] = -\left[\ln\phi + 1 - \phi + \chi(1-\phi)^2\right], \tag{3.4.29}$$

the second equality arising by using the free-energy developed in Ch. 2 (2.3.12), and yielding the same expression for the osmotic pressure derived there (2.2.24). Note the stress obtained by this differential method (3.4.28) is equivalent to the result for energy minimization presented in Ch. 2 (2.4.12) at equilibrium: the Lagrange multiplier $\widetilde{\psi}$ reduces to $-p$.

From our stress balance (3.3.11) and using the chosen constitutive law (3.4.27) to eliminate the unknown $\widetilde{\psi}$ provides physical insight:

$$\frac{1}{\mathcal{D}\phi} J_i^m = \Pi_{,i} - \left(\frac{\partial A}{\partial F_{iJ}} F_{jJ}\right)_{,j}. \tag{3.4.30}$$

As discussed in Ch. 2, we can consider our system to have two opposing forces per unit volume: an osmotic force driving macromer to mix with network strands and an elastic force as those network strands stretch opposing further mixing of macromer. Both are experienced internally at every point and respectively represent the two terms on the right–hand side of (3.4.30). At equilibrium, thermodynamics tells us that these two terms exactly balance each other (§2.2.2). In this case, $J_i^m = 0$ and there is no diffusion of macromer. If the osmotic driving force is greater than the elastic force, macromer will diffuse in ($J_i^m > 0$): there is more drive for macromer to enter the network than the stretching resistance. Analogously, if the elastic force is greater than the osmotic force, macromer will diffuse out ($J_i^m < 0$): the chains are stretched beyond equilibrium and so will spontaneously expel macromer. The difference between these two driving forces at any point in time gives complete information about the diffusion of macromer at that point in time. In this way, we can capture the transient behavior of our system even after scaling dynamic stress terms out.

We now expand out the elastic term in (3.4.28) in order to further eludicate the significance of the expressions developed. Written in terms of $F^*_{iJ} = Q_0^{-1/3} F_{iJ}$, the deformation gradient relative to the initially swollen system, the stretching contribution to the stress is given as:

$$\frac{\partial A}{\partial F_{iJ}} F_{jJ} = \epsilon(1-\phi)^{1/3}\theta^{2/3}\frac{1}{Q^{*2/3}} F^*_{iJ}F^*_{jJ} - \frac{1}{2}\epsilon(1-\phi)\delta_{ij}. \tag{3.4.31}$$

The prefactor to the first term is the dimensionless shear modulus of the material, obtained from Ch. 2 (2.3.22):

$$G(\phi;\theta) \equiv \frac{G_{\text{shear}}(\phi;\theta)}{G_{\text{os}}} = \epsilon\theta^{2/3}(1-\phi)^{1/3}. \tag{3.4.32}$$

We may view (3.4.31) in a different light by breaking the deformation gradient into two parts: a purely isotropic part due to changes in volume, and a conforming part, F^c_{iJ} , so that $F^*_{iJ} = Q^{*1/3} F^c_{iJ}$.

We furthermore define

$$e^c_{ij} = F^c_{iJ}F^c_{jJ} - \delta_{ij} \tag{3.4.33}$$

as the conforming (non–volumetric) strain tensor (not to be confused with traditional notation for the Eulerian strain tensor). The stretching contribution (3.4.31) can be written compactly as:

$$\frac{\partial A}{\partial F_{iJ}}F_{jJ} = G(\phi;\theta)e^c_{ij} + \epsilon\theta^{2/3}(1-\phi)^{1/3}\delta_{ij} - \frac{1}{2}\epsilon(1-\phi)\delta_{ij}, \tag{3.4.34}$$

that is, the stretching contribution has been broken into an isotropic part and a conforming part. Placing this relation in the stress (3.4.28):

$$\sigma_{ij} = \widetilde{\psi}\delta_{ij} + \left(-\Pi + \epsilon\theta^{2/3}(1-\phi)^{1/3} - \frac{1}{2}\epsilon(1-\phi)\right)\delta_{ij} + \sigma^c_{ij}, \tag{3.4.35}$$

with $\sigma^c_{ij} = G(\phi;\theta)e^c_{ij}$ representing the linear relationship between the anisotropic stress and the conforming strain. We can use the expression for the chemical potential of an isotropically swollen sample after cure (2.3.18) to simplify the above expression to:

$$\sigma_{ij} = \widetilde{\psi}\delta_{ij} + \mu\delta_{ij} + \sigma^c_{ij}. \tag{3.4.36}$$

Another way this expression can be understood is by using the constitutive law developed for the flux (3.4.27) along with the stress balance (3.3.11) to eliminate $\widetilde{\psi}$:

$$J^m_i = -\rho\mathcal{D}\phi\mu_{,i} - \rho\mathcal{D}\phi\sigma^c_{ij,j}. \tag{3.4.37}$$

When a deformation is isotropic, $e^c_{ij} = 0$ (3.4.33) and $\sigma^c_{ij} = 0$. For this case, the flux of macromer becomes directly proportional to the negative chemical potential gradient: Fick's law. For a general deformation, however, our constitutive model indicates that there is an effect of anisotropic stress σ^c_{ij} on the flux of macromer. This is to be expected since the chain stretching effects energetically repel macromer.

Other relationships aside from Fick's law have also been used in modeling diffusions in gels. For example, Doi and co–workers use Darcy's law in their stress–diffusion coupling model [40]. Interestingly, if the parameter $\widetilde{\psi}$ is the hydrostatic pressure, such as in a case in which imposed pressure dominates the flow, we recover Darcy's law. In our system, however, there is no imposed external pressure: the flow is all driven through internal chemical potential gradients. For this reason, we use the developed constitutive law (3.4.37) for the remainder of this thesis. Values of $\mathcal{D}$ are obtained by modifying data in [1] using (3.4.37). The details of this calculation are done in Appendix §B.4: the values of diffusivity as a function of molar mass of macromer are given in Table B.3.

3.5 Conclusion

The stress-balance equation (3.4.30) and the mass-balance equation (3.3.3), together with the constitutive laws (3.4.28) and (3.4.37), can now be solved to determine the transient diffusion–deformation behavior of an elastomeric photopolymer. We will illustrate the use of these equations to solve sample problems in Ch. 4 and 6. Specifically in Ch. 4, we further examine the connection between the equations developed here and those developed by the equilibrium approach of Ch. 2. In addition, we illustrate that a simplification is possible to the flux constitutive law (3.4.37) for clinically relevant material parameters.

Chapter 4

Two-Cell Models

4.1 Introduction

The previous two chapters have developed a theory from first principles to predict the reaction–diffusion–deformation behavior of elastomeric photopolymers. Although we have also shown that this theory correctly predicts macroscopic swelling behavior (Ch. 2), we wish to determine the relative importance of the material parameters introduced in those sections. In this chapter, we set out to illustrate the salient features—both equilibrium and transient—of our model. We do this by considering a "toy problem". With eventual three–dimensional, finite–element implementation in mind, we consider the transfer between two small-volume elements over which material properties can be assumed constant. The equilibrium analysis of this case (§4.2) allows us to determine a relevant parameter space, as well as a basic understanding of how material parameters affect the solution. The transient analysis of the "two-cell model" (§4.3) provides insight into the constitutive law developed for the flux in Ch. 3 (3.4.37). We will show that the full form developed in Ch. 3 can be well approximated by a gradient in chemical potential, therefore neglecting anisotropic stress contributions. This will simplify the governing equations necessary to solve a fully three–dimensional problem (Ch. 6).

In these studies, we consider two small-volume elements, say two adjacent elements taken at random from a three–dimensional mesh. Each of these "cells" is subjected to a different amount of irradiation and therefore experiences a different extent of reaction. Material then diffuses into the cell that has the larger extent of reaction—and therefore less macromer after reaction—until the two cells are at equilibrium. For the purposes of determining important material parameters, we consider the most extreme case: one cell experiences extent of reaction ξ while the other cell is completely unreacted. We will use the "two-component model" developed in Ch. 2 to model the reaction as instantaneous, with macromer molecules transforming directly into network. We consider first the equilibrium case and then move on to the transient case.

4.2 Equilibrium

In Ch. 2, we developed a free-energy functional (2.3.12) which consisted of an ideal mixing term and two corrections due to non–idealities: 1) χ, representing repulsive forces between macromer and network, and 2) ϵ, the elastic stretching of network chains. In order to determine the relative importance of these material parameters on the final solution, we compare the result of energy minimization for the two cells to the ideal mixing solution, which can be specified *a priori*. We discussed in Ch. 2 that the osmotic forces will be larger than the elastic stretching forces for materials swollen to a volume fraction $\phi_0 \leq \phi_{\max}$ (§2.2.3). We are now in a position to quantify this statement. For this reason, we present two equilibrium models: one in which elastic stretching effects are ignored by allowing the cells to move past each other (the "slip" case) and one which includes the elastic coupling between cells (the "conforming" case).

4.2.1 The Slip Case

Consider first the "slip" case (Fig. 4.1). Let the cells be chemically identical and initally swollen to the same swelling ratio Q_0 with macromer. We assume that the cells are in contact with each other so that macromer can diffuse across the interface between them freely (Fig. 4.1a), but there is no mechanical coupling between them (the interface is stress free). This simplifies our starting analysis and allows the cells to freely expand or contract isotropically and independently of each other (slip case). We subject Cell 1 to a light source which uniformly converts a fraction ξ of the macromer inside the cell into network. The volume fraction of macromer in this cell immediately after reaction is:

$$\phi_1(t=0) = \phi_0(1-\xi). \tag{4.2.1}$$

The volume fraction in Cell 2 remains unchanged ($\phi_2(t=0) = \phi_0$). Since the chemical potential (2.3.18) is greater in Cell 2, there is a net flux of macromer from Cell 2 into Cell 1. This causes Cell 2 to shrink and Cell 1 to expand (Fig. 4.1b).

There are two fully equivalent ways to describe the equilibrium state of the system. Thermodynamically, the chemical potential of macromer is the same in Cells 1 and 2 at equilibrium (this constraint is obtained by energy minimization (§2.4) under the system constraints). Mechanically, there is no gradient in the stress at equilibrium (Ch. 3). The equivalence of these two perspectives is relatively easy to see in this simple example because the deformation and stress are isotropic ($F^*_{iJ} = {Q^*}^{1/3}\delta_{iJ}$) in the slip case. From (3.4.36) in Ch. 3, we see that the stress can be written as $\sigma_{ij} = (\widetilde{\psi} + \mu)\delta_{ij}$ because $\sigma^c_{ij} = 0$ for an isotropic deformation. Additionally, $\widetilde{\psi}$ must be constant at equilibrium so that there is no flux of material, $J^m_i = 0$ (see Ch. 3, (3.4.37)). The requirement that $\sigma_{ij,j} = 0$ (3.3.11) then leads to

$$\mu_1 = \mu_2, \tag{4.2.2}$$

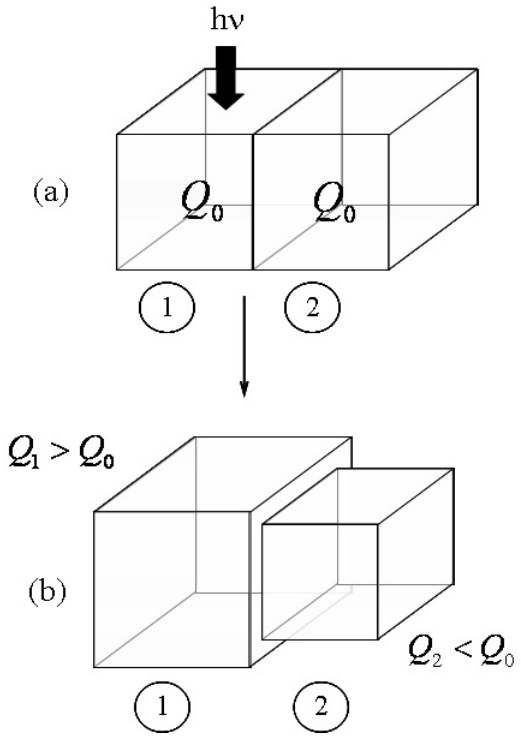

Figure 4.1: Consider the case of an elastomeric photopolymer slab cut into two cells (a). These cells are in contact so that they are allowed to exchange macromer but not required to conform to each other (that is, they can slip past each other on the adjoining edge). The first cell is irradiated with light so that the material inside reacts uniformly with extent of reaction ξ whereas the second cell is left unreacted. Since the chemical potential in Cell 1 is smaller than that of Cell 2 due to the reaction, material diffuses from Cell 2 into Cell 1, causing Cell 1 to swell and Cell 2 to shrink (b).

μ_α being the chemical potential in cell α. This is, of course, the thermodynamic statement of the problem. Using the expression for the chemical potential derived from the two-component model (2.3.18), we can solve (4.2.2) for the equilibrium distribution, $Q_1(t \to \infty)$ and $Q_2(t \to \infty)$, subject to the constraint of conversation of total system volume.

Consider the ideal mixing solution as a first approximation: the equilibrium volume fraction of macromer is taken to be the same in both cells. This is expected to be a good approximation for small ϵ and small χ because the free energy for those cases (2.3.12) approaches the ideal mixing free energy. The final value of volume fraction in both cells will then be an average of the amounts in each cell right after reaction: $\bar{\phi} = \frac{1}{2}(\phi_1(t=0) + \phi_2(t=0)) = \phi_0(1 - \frac{1}{2}\xi)$. Using this relation in (2.3.10), we can write the fractional change in volume $q \equiv (Q - Q_0)/Q_0 = Q^* - 1$ as a function of extent of reaction ξ:

$$q_{\text{id}}(\xi) = \frac{Q - Q_0}{Q_0} = \pm \frac{\frac{1}{2}\frac{\phi_0}{1-\phi_0}\xi}{1 + \frac{1}{2}\frac{\phi_0}{1-\phi_0}\xi}. \tag{4.2.3}$$

The plus sign in the above equation corresponds to Cell 1, which will experience an increase in swelling, whereas the minus sign corresponds to Cell 2, which will deswell by the same amount in order to obey the system conservation of mass.

The actual, energy–minimizing solution will provide a fractional change in volume $q(\xi)$, which is less than q_{id}. This is because of non–idealities included in the free-energy expression (2.3.12): the stretching of network chains (scaled as ϵ) and the enthalpy of mixing (scaled as χ). We define the percent difference between the actual and ideal fractional change in volume by

$$\delta(\xi) = \frac{q_{\text{id}}(\xi) - q(\xi)}{q_{\text{id,max}}}, \tag{4.2.4}$$

with $q_{\text{id,max}} = \phi_0/(2 - \phi_0)$ being the maximum fractional volume change for the ideal case (the maximum fractional volume change always occurs at $\xi = 1$ (see (4.2.3)). We expect that δ will increase as the non–ideal contributions to the free energy become more important (that is as χ and ϵ increase). Fig. 4.2 shows the deviation from ideal behavior, $\delta(\xi)$, as a function of experimentally measurable parameters in Table B.2. The bold lines can be used to compare between figures and represent the data set $M_m = 1000$ g/mol, $G_{\text{dry}} = 0.18$ MPa, and $\phi_0 = 0.2$. As G_{dry} increases (ϵ increases), the stretching contribution to the free energy becomes larger and the deviation from ideal mixing behavior becomes larger (Fig. 4.2a). Increasing the macromer molar mass is shown to also increase the deviation (Fig. 4.2b). Note that M_m influences both χ and ϵ non–idealities in the stretching free energy: increasing the repeat units in the macromer decreases the repulsion with the network (decreases χ) but also decreases the osmotic modulus (increases ϵ). The non–idealities resulting from increasing ϵ are seen to be more important than those of χ through increasing deviations with increasing M_m. This implies that we cannot decrease non–idealities from mixing by simply

increasing macromer chain length. Finally, increasing ϕ_0 means that there is more material available for redistribution, allowing for larger deformations and therefore larger deviations (Fig. 4.2c). In fact, the initial amount of swelling will be shown below to solely determine the degree of shape change possible in elastomeric photopolymers.

Because deviations increase for increasing G_{dry}, M_m, and ϕ_0, we can identify a particular set of experimental parameters as yielding the maximum possible deviation. For the parameter sets shown in Table B.2, this parameter set is $G_{\text{dry}} = 0.28$ MPa, $M_m = 3000$ g/mol, and $\phi_0 = 0.3$. We refer to this parameter set as the "high extreme". Likewise, the minimum deviations will be at the lowest possible choices of these parameters: $G_{\text{dry}} = 0.10$ MPa, $M_m = 500$ g/mol, and $\phi_0 = 0.1$, the "low extreme". In Fig. 4.3, we show these two extreme parameter sets alongside the "average" parameter set $G_{\text{dry}} = 0.18$ MPa, $M_m = 1000$ g/mol, and $\phi_0 = 0.2$, the same bold curve shown in each pane of Fig. 4.2. We note that all deviations fall below about 6% for the slip case (Fig. 4.3a), indicating that an ideal mixing approximation is good for all relevant parameter choices. As a point of illustration, however, we include the results for the conforming case alongside the slip case (Fig. 4.3b, details of calculations shown below). The errors are nearly a factor of three times larger than in the slip case, indicating that the coupling between cells is important in determining the final equilibrium shape. The slip case, however, has provided an illustration of the capability of reaction to induce shape change, as well as illustrated the effects of non–idealities on the final shape change.

4.2.2 The Conforming Case

We now consider the case in which the two small volume cells are forced to deform together because they share a conforming boundary (conforming case). In keeping with our use of tetrahedra for meshing in Ch. 5, we choose the two cells to be two regular tetrahedra (side length a) attached along the XY plane (Figure 4.4). As above, we assume the cells are chemically identical and initally swollen to the same swelling ratio Q_0; we take the initially swollen system as the reference configuration (Fig. 4.4a). Because of symmetry, it is more convenient to work in terms of polar coordinates: R, Φ, and Z in the reference configuration, and r, φ, and z in the spatial configuration.

For this problem, the deformation is axisymmetric (Fig. 4.4b): diffusion can occur only along the Z–axis so that Cell 1 lengthens by a factor $\lambda_1(t)$ along the Z–axis and Cell 2 shrinks a factor $\lambda_2(t)$ along the Z–axis. Because the two tetrahedra are attached, however, they must also stretch (or contract) together in the plane. We call the stretch factor associated with the coupling between cells $\beta(t)$: this is the key factor differentiating the "conforming" case from the "slip" case. The spatial location of points in Cell α as a function of the reference positions can written in cylindrical coordinates as (see Figure 4.4b):

$$r(t) = \beta(t)R$$

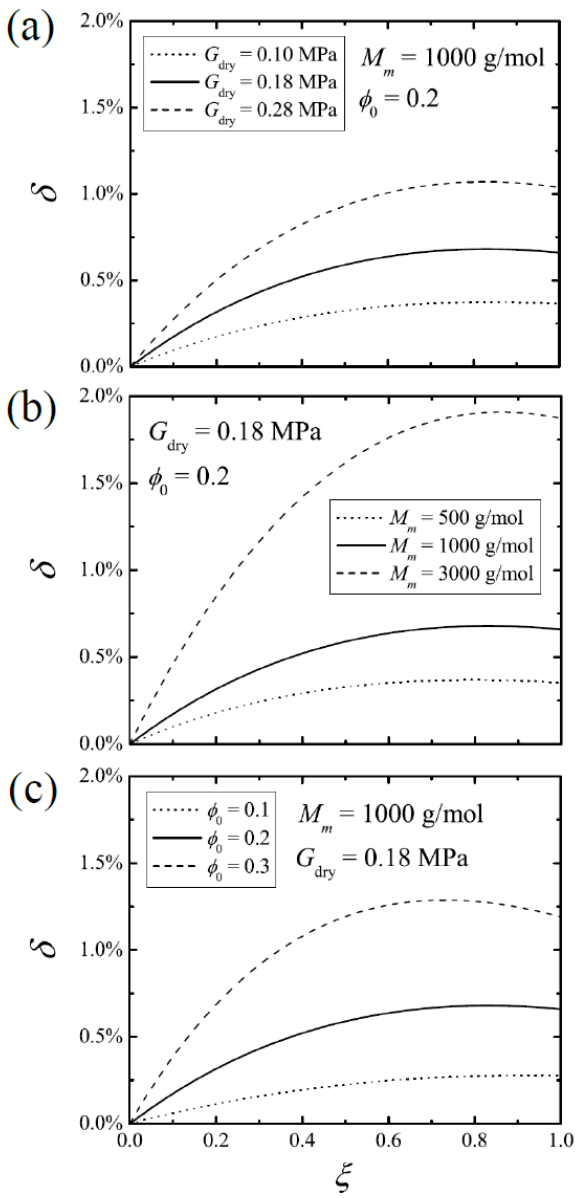

Figure 4.2: Deviations from ideal mixing results for the two-cell slip case. The deviations are shown as a function of the extent of reaction in the first cell ξ and as functions of material parameters: (a) G_{dry} (at fixed M_m and ϕ_0); (b) M_m (at fixed G_{dry} and ϕ_0), and (c) ϕ_0 (at fixed M_m and G_{dry}). For comparison, the bold curve is the same in all three figures. (a) As the host network becomes more stiff (G_{dry}—non–dimensionally, ϵ—increasing), non–idealities due to chain stretching become more significant. (b) Increasing the macromer chain length has two opposing effects (Table B.2): 1) a decrease in χ as the macromer has more repeat units causes an increase in solubility and 2) an increase in ϵ due to a corresponding decrease in the osmotic modulus (2.2.15). Observing that the non–idealities are larger as M_m increases indictates that the latter contribution dominates: increasing M_m increases the non–idealities. (c) As the amount of material available to redistribute increases (ϕ_0 increasing), there are also larger deviations from ideal mixing. Note that for the material parameter choices shown, no deviation is greater than 2%.

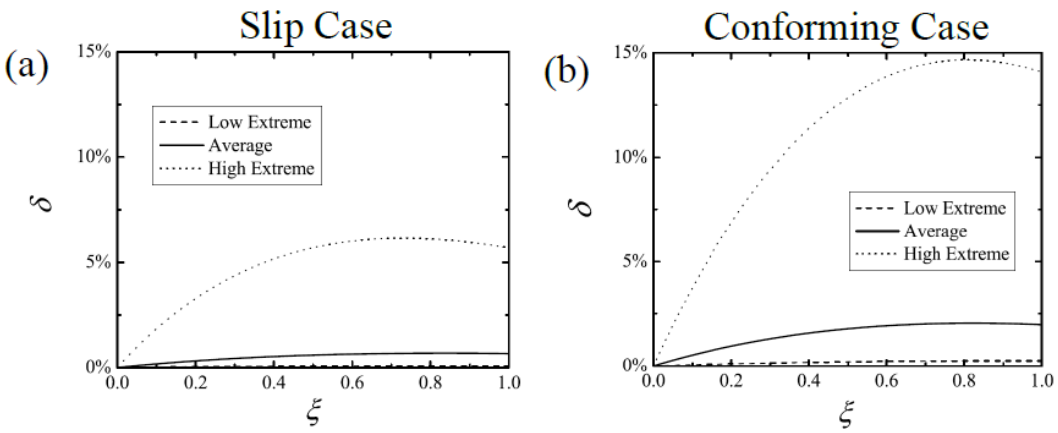

Figure 4.3: Deviations from ideal mixing for the two cells studies as functions of the extent of reaction, ξ, in Cell 1 (Cell 2 unreacted) for both (a) the slip case and (b) the conforming case. The parameter sets are chosen to show the extreme possible deviations: "high extreme" refers to the parameter set $G_{\text{dry}} = 0.28$ MPa, $M_m = 3000$ g/mol, and $\phi_0 = 0.3$ while "low extreme" refers to the parameter set $G_{\text{dry}} = 0.1$ MPa, $M_m = 500$ g/mol, and $\phi_0 = 0.1$. Also shown is the "average" parameter set $G_{\text{dry}} = 0.18$ MPa, $M_m = 1000$ g/mol, and $\phi_0 = 0.2$, the same bold curve as in Fig. 4.2 and Fig. 4.5. Although the errors in the slip case are less than 6%, forcing the cells to deform together increases the error by nearly a factor of three.

$$\begin{aligned} \varphi(t) &= \Phi \\ z(t) &= \lambda_\alpha Z. \end{aligned} \tag{4.2.5}$$

The deformation gradient of Cell α in cylindrical coordinates is then:

$$\mathbf{F}_\alpha^* = \begin{bmatrix} \beta(t) & 0 & 0 \\ 0 & \beta(t) & 0 \\ 0 & 0 & \lambda_\alpha(t) \end{bmatrix}. \tag{4.2.6}$$

The determinant of the deformation gradient is related to the volume swelling ratio Q_α^* and volume fraction ϕ_α by (see (2.3.4)):

$$\det \mathbf{F}_\alpha^* = \beta^2 \lambda_\alpha \equiv Q_\alpha^* = \frac{\theta_\alpha^*}{1-\phi_\alpha}. \tag{4.2.7}$$

We now proceed to determine the equilibrium deformation ($t \to \infty$) through energy minimization. The free-energy density in Cell α can be expressed as (2.3.12):

$$\begin{aligned} A_\alpha(\phi_\alpha, \lambda_\alpha, \beta) = {} & \phi_\alpha \ln \phi_\alpha + \chi \phi_\alpha (1-\phi_\alpha) \\ & + \frac{1}{2}\epsilon(1-\phi_\alpha)\Big[Q_0^{2/3}(2\beta^2 + \lambda_\alpha^2) - 3 - \ln Q_0 - \ln \beta^2 \lambda_\alpha\Big]. \end{aligned} \tag{4.2.8}$$

The energy to minimize is the sum of free energies of the two cells modified by a Lagrange multiplier

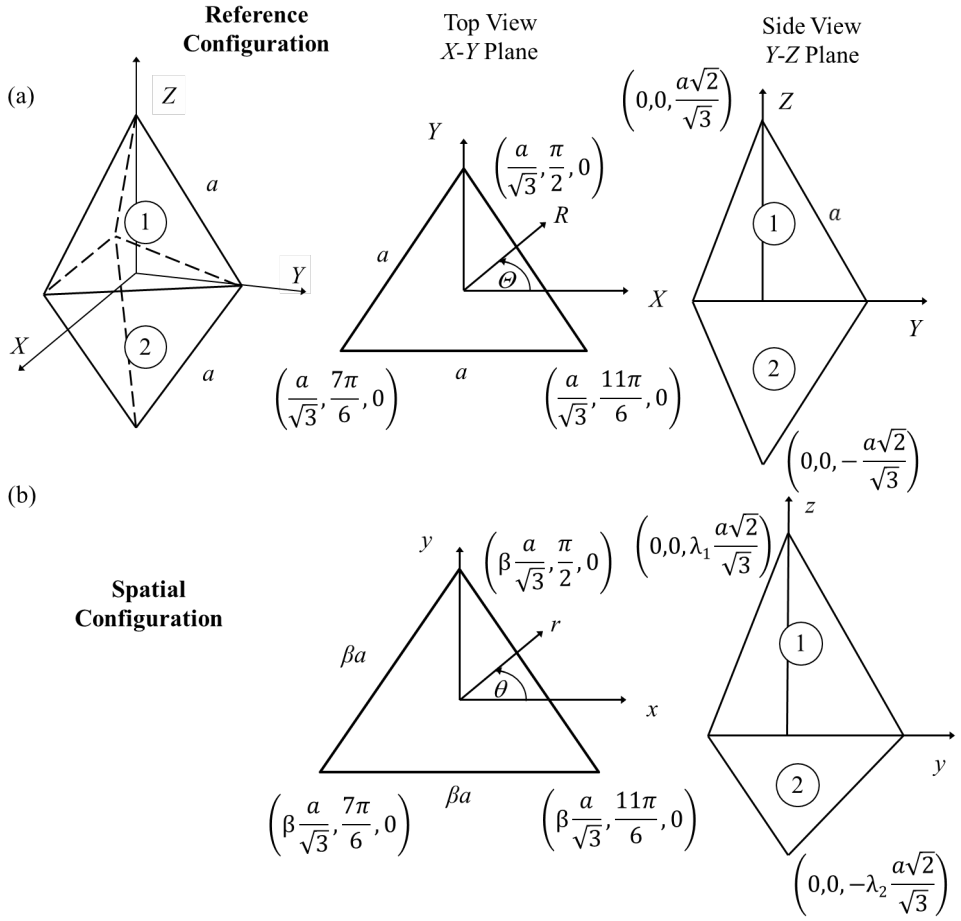

Figure 4.4: Now the two cells, chosen to be regular tetrahedra, are required to conform along their common boundary in the XY plane (a). We take the reference configuration to be the system initially swollen to swelling ratio Q_0. Due to symmetry about the Z axis, polar coordinates are used. As in the slip case, Cell 1 is assumed to react to extent of reaction ξ whereas Cell 2 remains unreacted. We therefore expect Cell 1 to expand and Cell 2 to contract (b). We measure the lengthening of Cell 1 along the Z–axis with the factor $\lambda_1(t)$, and the corresponding shrinkage in Cell 2 with the factor $\lambda_2(t)$. Because the cells are coupled together, the deformation cannot occur isotropically: we assume that the cells expand (or contract) axisymmetrically by a factor $\beta(t)$ on the adjoining plane.

p to enforce conservation of volume (2.4.5):

$$F = A_1(\phi_1, \lambda_1, \beta)Q_1^* + A_2(\phi_2, \lambda_2, \beta)Q_2^* - p(Q_1^* + Q_2^* - 2). \tag{4.2.9}$$

We take the independent variables for the minimization to be Q_1^*, Q_2^*, β: ϕ_α and λ_α can be written as functions of Q_α^* and β through conservation of mass (4.2.7). Minimization of (4.2.9) in terms of its independent variables yields:

$$\begin{aligned}\delta F = &\left[A_1 + Q_1^*\frac{\partial A_1}{\partial \phi_1}\frac{\partial \phi_1}{\partial Q_1^*} + Q_1^*\frac{\partial A_1}{\partial \lambda_1}\frac{\partial \lambda_1}{\partial Q_1^*} - p\right]\delta Q_1^* + \left[A_2 + Q_2^*\frac{\partial A_2}{\partial \phi_2}\frac{\partial \phi_2}{\partial Q_2^*} + Q_2^*\frac{\partial A_2}{\partial \lambda_2}\frac{\partial \lambda_2}{\partial Q_2^*} - p\right]\delta Q_2^* \\ &+ \left[Q_1^*\left(\frac{\partial A_1}{\partial \lambda_1}\frac{\partial \lambda_1}{\partial \beta} + \frac{\partial A_1}{\partial \beta}\right) + Q_2^*\left(\frac{\partial A_2}{\partial \lambda_2}\frac{\partial \lambda_2}{\partial \beta} + \frac{\partial A_2}{\partial \beta}\right)\right]\delta\beta = 0.\end{aligned} \tag{4.2.10}$$

The equations that must be satisfied for arbitrary variations are then

$$\begin{aligned}A_1 + Q_1^*\frac{\partial A_1}{\partial \phi_1}\frac{\partial \phi_1}{\partial Q_1^*} + Q_1^*\frac{\partial A_1}{\partial \lambda_1}\frac{\partial \lambda_1}{\partial Q_1^*} - p &= 0 \\ A_2 + Q_2^*\frac{\partial A_2}{\partial \phi_2}\frac{\partial \phi_2}{\partial Q_2^*} + Q_2^*\frac{\partial A_2}{\partial \lambda_2}\frac{\partial \lambda_2}{\partial Q_2^*} - p &= 0\end{aligned} \tag{4.2.11}$$

$$\begin{aligned}&Q_1^*\left(\frac{\partial A_1}{\partial \lambda_1}\frac{\partial \lambda_1}{\partial \beta} + \frac{\partial A_1}{\partial \beta}\right) \\ &\quad + Q_2^*\left(\frac{\partial A_2}{\partial \lambda_2}\frac{\partial \lambda_2}{\partial \beta} + \frac{\partial A_2}{\partial \beta}\right) = 0.\end{aligned} \tag{4.2.12}$$

Using the free energy expression (4.2.8) and conservation of mass (4.2.7), the derivatives can be evaluated and the governing equations can be written succinctly as:

$$\begin{aligned}\mu_1^{conf} &= \mu_2^{conf} \\ \tau_1 + \tau_2 &= 0\end{aligned} \tag{4.2.13}$$

(the actual expressions for μ_α^{conf} and τ_α obtained through the minimization are given below). The first equation parallels equilibrium with respect to macromer transport, as seen in the slip case above. However, the expression for the effective chemical potential here, μ_α^{conf}, differs from the isotropic result, μ_α (2.3.18), due to the anisotropic deformation within the cells. We use μ_α^{conf} to denote the effective chemical potential in the conforming case:

$$\mu_\alpha^{conf}(\phi_\alpha, \Lambda_\alpha) \equiv \mu_\alpha(\phi_\alpha) + G_\alpha(\phi_\alpha)\left(\Lambda_\alpha^{4/3} - 1\right). \tag{4.2.14}$$

Here, we use the definition of the dimensionless shear modulus G developed in Ch. 3 (3.4.32) and define $\Lambda_\alpha = \lambda_\alpha/\beta$ as the ratio of each element's axial stretch to its radial stretch. The second

governing equation (4.2.13) represents a balance of internal tensile stresses acting at $r = \beta a/\sqrt{3}$. Since there are no external forces, the force one cell exerts has to be equal and opposite the force exerted by the second cell through Newton's 3rd Law. The expression for this tensile stress is:

$$\tau_\alpha = G(\phi_\alpha)\Lambda_\alpha^{1/3}\left(\beta^2 - \lambda_\alpha^2\right). \tag{4.2.15}$$

Note that the tensile stress is in the positive r–direction when there is more radial stretch than axial stretch ($\beta > \lambda_\alpha$) and that the tensile stress is negative when there is more axial stretch than radial stretch ($\beta < \lambda_\alpha$). Based on the assumed deformation (Fig. 4.4), we expect the tensile strain from the first cell, τ_1, to be negative and that from the second cell, τ_2, to be positive.

Before we solve these equations, we show equality of derivation using the differential approach. Under the differential approach of Ch. 3, the conforming portion of the deformation gradient is:

$$\mathbf{F}_\alpha^c \equiv \frac{1}{Q_\alpha^{*\,1/3}}\mathbf{F}_\alpha^* = \begin{bmatrix} \Lambda_\alpha^{-1/3} & 0 & 0 \\ 0 & \Lambda_\alpha^{-1/3} & 0 \\ 0 & 0 & \Lambda_\alpha^{2/3} \end{bmatrix}. \tag{4.2.16}$$

The conforming stress tensor is then (3.4):

$$\boldsymbol{\sigma}_\alpha^c = \begin{bmatrix} G_\alpha\left(\Lambda_\alpha^{-2/3} - 1\right) & 0 & 0 \\ 0 & G_\alpha\left(\Lambda_\alpha^{-2/3} - 1\right) & 0 \\ 0 & 0 & G_\alpha\left(\Lambda_\alpha^{4/3} - 1\right) \end{bmatrix}. \tag{4.2.17}$$

In this case, $\sigma_{ij}^c \neq 0$ because the deformation occurs anisotropically. Using the expression for the stress (3.4.36), we note that:

$$\begin{aligned} \sigma_{rr}^\alpha = \sigma_{\theta\theta}^\alpha &= -p + \mu_\alpha + G_\alpha\left(\Lambda_\alpha^{-2/3} - 1\right) \\ \sigma_{zz}^\alpha &= -p + \mu_\alpha + G_\alpha\left(\Lambda_\alpha^{4/3} - 1\right) \end{aligned} \tag{4.2.18}$$

and that there is no shear stress in cylindrical coordinates. Because there are no external stresses along the axis, $\sigma_{zz}^\alpha = 0$ for both cells. This leads to:

$$\mu_1 + G_1\left(\Lambda_1^{4/3} - 1\right) = p = \mu_2 + G_2\left(\Lambda_2^{4/3} - 1\right), \tag{4.2.19}$$

the second equality arising because p is independent of position (§3.4). Noting the definition of the effective chemical potential (4.2.14), we arrive at the first of our governing equations (4.2.13): equality of chemical potential.

To derive the second governing equation, we consider the radial stresses σ_{rr}^α. Although we know

that there is no external radial force, there are internal radial forces generated as the two cells deform together. For each cell, these forces act radially at $r = \beta a/\sqrt{3}$ and must be equal and opposite in order for there to be no net force. In terms of the stresses σ^{α}_{rr}, each force will be $\sigma^{\alpha}_{rr} A_{\alpha}$ where A_{α} represents the surface area on which the stress acts, proportional to $\beta\lambda_{\alpha}$. The internal force balance then becomes:

$$\sigma^{1}_{rr}\lambda_1\beta + \sigma^{2}_{rr}\lambda_2\beta = 0. \tag{4.2.20}$$

Using the expression for conforming chemical potential (4.2.14) and the radial stress (4.2.18), this becomes:

$$\left[-p + \mu_1^{conf} + G_1\left(\Lambda_1^{-2/3} - \Lambda_1^{4/3}\right)\right]\lambda_1\beta + \left[-p + \mu_2^{conf} + G_2\left(\Lambda_2^{-2/3} - \Lambda_2^{4/3}\right)\right]\lambda_2\beta = 0. \tag{4.2.21}$$

With (4.2.19):

$$G_1\Lambda_1^{1/3}\left(\Lambda_1^{-1} - \Lambda_1\right)\lambda_1\beta + G_2\Lambda_2^{1/3}\left(\Lambda_2^{-1} - \Lambda_2\right)\lambda_2\beta = 0 \tag{4.2.22}$$

reduces to $\tau_1 + \tau_2 = 0$ using the definition of τ_{α} (4.2.15). Having shown the equivalence of the energy minimization and continuum mechanics approach generally as well as for these two toy examples, we will proceed in the rest of this thesis to use both methods interchangably.

We again take the ideal mixing solution (4.2.3) as a first approximation to the solution of (4.2.13). Defining $\delta(\xi)$ in the same way as (4.2.4), we can compare the errors in this approximation between the slip and conforming cases. Fig. 4.5 illustrates the errors generated for the conforming case using the same parameter sets as the slip case (Fig. 4.2). We obtain the same qualitative behavior as the slip case: deviations from ideal mixing increase with increasing (a) G_{dry}, (b) M_m, and (c) ϕ_0. However, the magnitude of the deviations is roughly three times larger for all parameter sets, indicating that there is a significant quantitative difference when the cells exert a force on each other. For example, Fig. 4.3b indicates that the largest magnitude of the deviations for the "high extreme" parameter set is about 15%, whereas it is about 6% for the slip case. Even so, most parameter sets for the conforming case still produce less than 5% deviation (Fig. 4.5). Data for the axial stretch β is not presented, as all choices of parameter sets in Table B.2 result in $\beta \approx 1$ with variations of less than 2%. This indicates that the cells preferentially deform solely along the principle axis with the radial aspect remaining fixed in order to avoid creation of in–plane stresses. In Ch. 5, we will see how the forced generation of in–plane stresses in a constrained beam will cause the beam to bend to relieve the stresses.

Because certain parameter choices for real systems predict significant departures from ideal mixing (4.5), it becomes important to determine when an ideal mixing result, which is more easily obtained, can be used in place of the full detailed model. For example, consider a system that is held fixed at constant ϕ_0, say $\phi_0 = 0.3$. At this particular value of ϕ_0, we explore the parameter

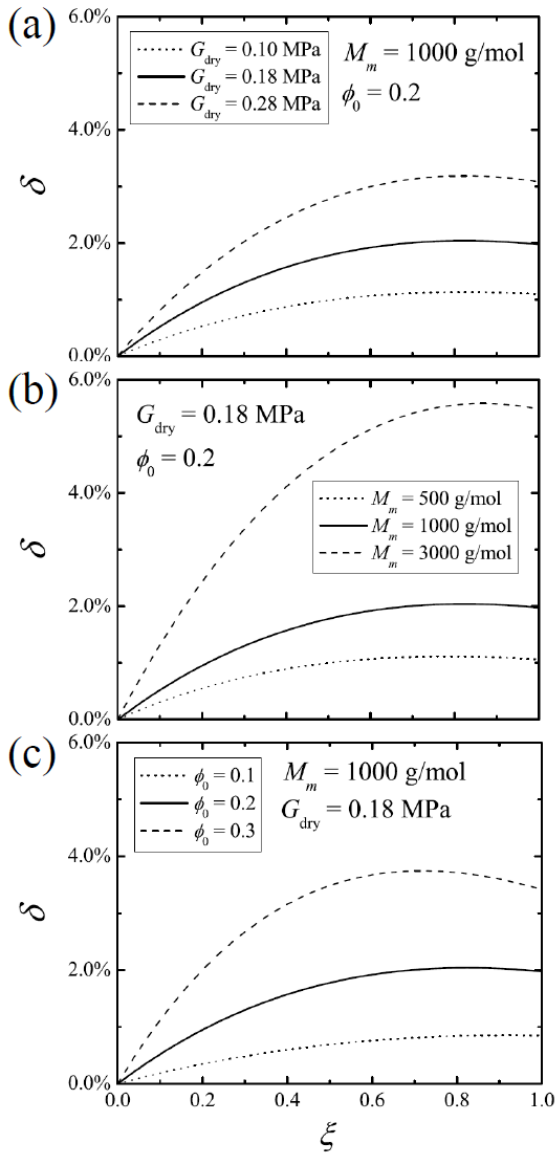

Figure 4.5: Deviations from ideal mixing results for the two-cell conforming case. The deviations are shown as a function of the extent of reaction in the first cell ξ and as functions of material parameters: (a) G_{dry} (at fixed M_m and ϕ_0); (b) M_m (at fixed G_{dry} and ϕ_0); and (c) ϕ_0 (at fixed M_m and G_{dry}). Just as in the slip case, the deviations from ideal mixing increase with increasing G_{dry}, M_m, and ϕ_0. Comparison with Fig. 4.2 illustrates that the errors are roughly three times larger when the cells deform together.

space of ϵ and χ values, examining the deviations from ideal mixing for each pair (Fig. 4.6a). There are three regions in the parameter space: two are separated by a contour line drawn for $\phi_0 = 0.3$ and the last is the shaded region. At smaller values of ϵ and χ, the deviations from ideal mixing are small: Region I represents the region of possible choices of χ and ϵ for $\phi_0 = 0.3$ in which the deviations from ideal mixing will be small (taken as $\delta < 5\%$). Recall from Ch. 2 that there are also limits of parameter pairs (ϵ, χ) that will yield thermodynamically stable initially-swollen systems (Fig. 2.2). These inaccessible parameter pairs are represented by the shaded region (Region III) to the right of the contour line and above the physical limit line in Fig. 4.6a. To the right of the contour line and below the physical limit line (Region II), larger values of ϵ and χ are physically admissable but yield deviations from ideal mixing larger than 5%. Thus, any choice of parameters in Region I (to the left of the contour line) can be modelled by an ideal mixing approximation with minimal error for $\phi_0 = 0.3$.

We now expand the ideas above to include other choices of ϕ_0 (Fig. 4.6b). At any given contour-line value of ϕ_0, we can imagine a plot similar to (Fig. 4.6b): there is a region below and to the left of the contour line in which ideal mixing will yield deviations of less than 5% (smaller values of χ and ϵ). The shading to the right of each contour line and above the physical limit line represents a region in which the parameters are not physically admissiable for that particular value of ϕ_0. To the right and below the shaded region, the choices of χ and ϵ are admissable but yield deviations from ideal mixing larger than 5%. Also included in the figure are three dotted lines, each one at a particular value of M_m with points associated with values of 0.1 MPa $\leq G_{\text{dry}} \leq$ 0.28 MPa. The dashed line represents $M_m = 500$ g/mol, the dotted line $M_m = 1000$ g/mol, and the dash-dot line $M_m = 3000$ g/mol. These lines allow ease of comparison of Fig. 4.6b with PDMS systems.

Because we are examining an extreme case in which two nearby elements experience large gradients in concentration, the actual deviations from ideal mixing for any real system can be guaranteed to be smaller than the deviations predicted by this conforming two-cell model. Therefore, Fig. 4.6b can be used to determine whether an ideal mixing model is appropriate to model a given system based upon the material parameters. As we shall see in the next section and subsequent chapters, ideal mixing allows for simplifications in the governing equations for the transient model in addition to the equilibrium simplification already discussed. Based on Fig. 4.6, then, ideal mixing will be a good approximation for $\phi_0 < 0.3$ for smaller molar mass of macromer ($M_m = 500$ or 1000 g/mol); most light–adjustable lenses operate in this parameter range. When dealing with systems at larger molar mass ($M_m = 3000$ g/mol), the deviations from ideal mixing are significantly larger, especially for $\phi_0 = 0.3$.

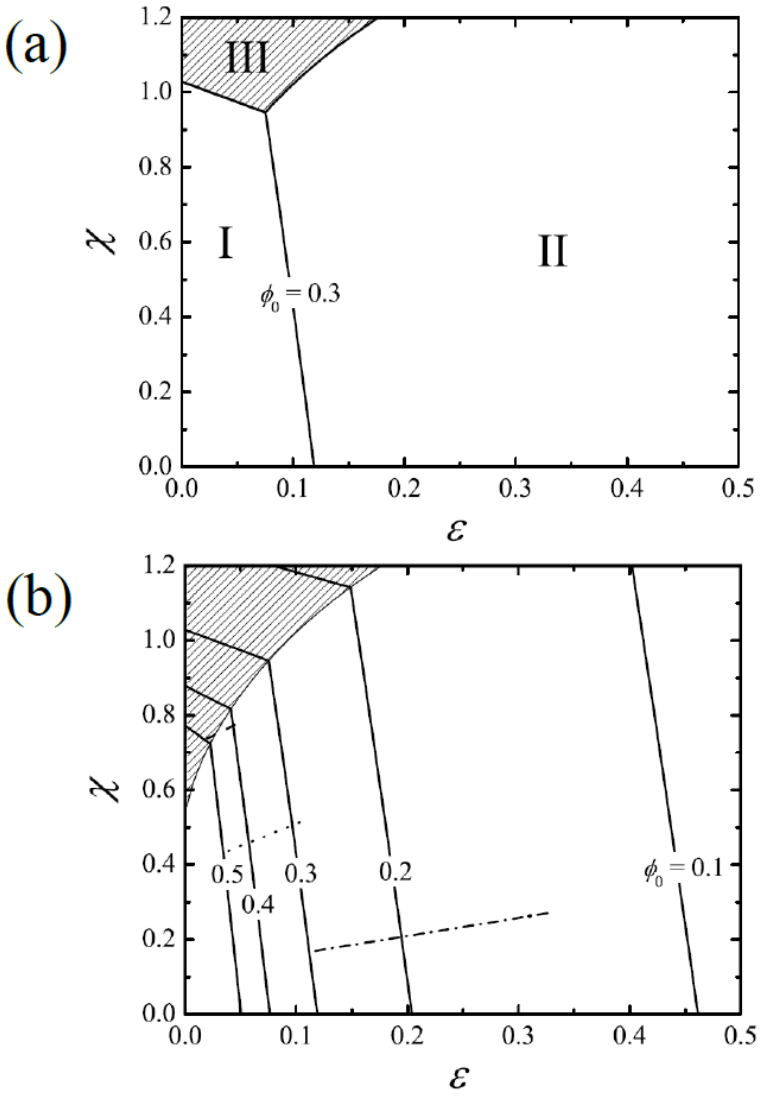

Figure 4.6: Parameter space illustrating where the deviations from an ideal mixing approximation are negligible (taken as $\delta < 5\%$) for the conforming case. (a) At any given choice of ϕ_0 (here specifically illustrated with $\phi_0 = 0.3$), there are three regions. For smaller choices of ϵ and χ (Region I, below the contour line), deviations from ideal mixing are less than 5%: ideal mixing is a good approximation. The shaded region to the right of the contour line and above the physical limit line (Region III) represents inaccessible values of χ and ϵ due to the thermodynamics of the initially swollen system (recall Fig. 2.2 from Ch. 2). To the right of the contour line and below the physical limit line (Region II), the values of ϵ and χ are accessible but the deviations from ideal mixing are greater than 5%. We therefore look below and to the right of a contour line at any value of ϕ_0 (b) in order to determine what parameter sets yield good approximations for ideal mixing. For purposes of comparison to experimental data [1], dashed lines show parameter sets for PDMS systems at constant values of M_m, G_{dry} varying from 0.1 to 0.28 MPa (dashed: $M_m = 500$ g/mol; dotted: $M_m = 1000$ g/mol; dash-dot: $M_m = 3000$ g/mol). It can be seen that small macromer molar masses (500 g/mol and 1000 g/mol) will yield good approximations to ideal mixing for $\phi_0 \leq 0.3$ while deviations are more significant for $M_m = 3000$ g/mol.

4.3 Transient

We now perform a transient analysis on both of the two-cell systems described above. Recall from Ch. 3 the expression for the flux derived by eliminating the Lagrange multiplier:

$$J_i^m = -\rho\mathcal{D}\phi\mu_{,i} - \rho\mathcal{D}\phi\sigma^c_{ij,j}. \tag{4.3.23}$$

The flux has two contributions: the first is due to the isotropic expansion caused by transfer of material (represented by a chemical potential gradient) and the second is caused by the divergence of an anisotropic conforming stress. In the slip case, the system deforms isotropically and so the anisotropic term is zero:

$$J_i^{m,s} = -\rho\mathcal{D}\phi\mu_{,i}, \tag{4.3.24}$$

diffusion is driven solely by gradients in chemical potential. The conforming case, on the other hand, must include the conforming stress (4.3.23). Comparison between the slip and conforming cases then allows an estimate as to the magnitude of the contribution of the conforming stress $\sigma^c_{ij,j}$ to the flux. We also compare both slip and conforming solutions to an ideal mixing approximation for the flux:

$$J_i^{m,\mathrm{id}} = -\rho\mathcal{D}(1-\phi)\phi_{,i}. \tag{4.3.25}$$

The factor of $1-\phi$ distinguishes the difference between a small molecule diffusing into a gel and the traditional relation for counter–diffusion of two small molecules (see the discussion in Appendix B.4).

In this section, we wish to compare between these three flux constitutive laws (4.3.23)–(4.3.25). The ideal result assumes the ideal mixing assumption (4.3.25) in which the flux is taken as a gradient in volume fraction; this neglects both anisotropic and isotropic deformation. The conforming case, on the other hand, includes both isotropic and anisotropic deformations (4.3.23). The slip case represents a condition somewhere in between these two, in which isotropic deformations are included but anisotropic deformations are neglected (4.3.24). We will show in this section that anisotropic deformations contribute negligibly to the flux for even the most extreme clinical parameter sets. We will therefore argue that it is sufficient in the applications of elastomeric photopolymers to use the gradient in chemical potential (4.3.24) rather than the full form of the flux (4.3.23).

We begin by considering the slip case. Because the only chemical potential gradient is in the z direction, we define

$$J_s \equiv \frac{J_z^m H}{\rho\mathcal{D}} = -\phi\frac{\partial\mu}{\partial\bar{z}} \tag{4.3.26}$$

as the dimensionless flux in the z–direction for the slip case (recall $\sigma^c_{ij,j} = 0$). Here, we take H as

the distance separating the two cells ($\Delta z = H$) and we have non–dimensionalized z by H,

$$\bar{z} \equiv \frac{z}{H}, \tag{4.3.27}$$

so that (4.3.26) is discretized simply:

$$J_s = -\bar{\phi}\left(\mu_1 - \mu_2\right).^{1} \tag{4.3.28}$$

Here, $\bar{\phi} = \frac{1}{2}\left(\phi_1 + \phi_2\right)$ is the average volume fraction between cells and μ_α is the chemical potential in cell α.

In dimensional terms, a quantity of macromer $J_z^m A$ is transferred from Cell 2 to Cell 1 in time Δt, A being the characteristic cross–sectional area between Cell 1 and 2. Conservation of mass for Cell 1 then states:

$$\rho V_1(t + \Delta t) = \rho V_1(t) + J_z^m A \Delta t \tag{4.3.29}$$

with V_1 being the volume of Cell 1 (note that no network is transferred between cells). Dividing through by ρ and V_0, the initial volume of the cell, we may non–dimensionalize the equation,

$$Q_1^*(\mathscr{T} + \Delta\mathscr{T}) = Q_1^*(\mathscr{T}) + \frac{AH}{V_0} J_s(\mathscr{T})\Delta\mathscr{T}, \tag{4.3.30}$$

with $\mathscr{T}$ being the dimensionless time (non–dimensionalized by $H^2/\mathcal{D}$). Since the cross–sectional area for the slip case is not well defined, we take $A = V_0/H$ to simplify the equation.[2] With conservation of total volume, the net system of equations is then:

$$\begin{aligned} Q_1^*(\mathscr{T} + \Delta\mathscr{T}) &= Q_1^*(\mathscr{T}) + J_s(\mathscr{T})\Delta\mathscr{T}, \\ Q_2^*(\mathscr{T} + \Delta\mathscr{T}) &= Q_2^*(\mathscr{T}) - J_s(\mathscr{T})\Delta\mathscr{T}. \end{aligned} \tag{4.3.31}$$

The initial conditions for the equations are specified through the original extent of reaction (4.2.1): recall that Q^* and ϕ are related via (2.3.10). The solution proceeds by first evaluating the chemical potential in each cell (2.3.18), then the flux (4.3.28), and finally updating the new volumes in each cell using the governing equations (4.3.31). Note that each cell deforms isotropically at each point in time: there are no stresses from either the environment or the cells on each other. As such, the only coupling between cells is conservation of total system volume.

We next consider the conforming case. In this case, we need to use the full form for the constitutive law for the flux (4.3.23) by including the additional term $\sigma^c_{ij,j}$. From (4.2.17), we can evaluate

[1] Based upon our choice of H, $\Delta\bar{z} = 1$.

[2] An alternative choice for A only affects the time scale to the problem; since we are considering a "toy case" where there are no real length scales and we cannot report real diffusion times, the choice is therefore unimportant.

J_z^m, the only non–zero component of the flux:

$$J_z^m = -\rho\mathcal{D}\phi\frac{\partial}{\partial z}\left(\mu + G(\Lambda^{4/3} - 1)\right) \equiv -\rho\mathcal{D}\phi\frac{\partial\mu^{conf}}{\partial z}; \tag{4.3.32}$$

the last equality makes use of the conforming chemical potential that we defined in §4.2.2 (4.2.14). This equation can be non–dimensionalized and discretized in the same way as the slip case:

$$J_c = -\bar{\phi}\left(\mu_1^{conf} - \mu_2^{conf}\right), \tag{4.3.33}$$

J_c being the flux for the conforming case. Non–dimensional conservation of mass will also be the same (4.3.30): although there is now a well-defined area of contact, we again choose $A = V_0/H$ in order to compare the dimensionless-time solutions of the conforming case to the slip case.[3] For this reason, we can make use of the same governing equations for the slip case (4.3.31) using the conforming definition of the flux (4.3.33). In the conforming case, however, these two equations are not sufficient to solve the problem: we also need to determine $\beta(\mathscr{T})$, the in–place stretch as it develops in time. As at equilibrium, we must solve for β at each point in time using the stress balance: $\tau_1 + \tau_2 = 0$. This is equivalent to assuming that our system can relax instantly after each diffusion step and is the same assumption made by Hong et al. in their model of the swelling of elastomeric strands with solvent [72]. The system of equations governing the transient conforming problem are then:

$$\begin{aligned} Q_1^*(\mathscr{T} + \Delta\mathscr{T}) &= Q_1^*(\mathscr{T}) + J_c(t)\Delta\mathscr{T}, \\ Q_2^*(\mathscr{T} + \Delta\mathscr{T}) &= Q_2^*(\mathscr{T}) - J_c(t)\Delta\mathscr{T}, \qquad (4.3.34) \\ \tau_1(\mathscr{T}) + \tau_2(\mathscr{T}) &= 0. \qquad (4.3.35) \end{aligned}$$

At each dimensionless time step, we solve the stress balance to determine the value of β, then use that value along with the volume fraction to find J_c from (4.3.33). This updates the volume fraction to compute the next time step.

We compare the ideal mixing solution (4.3.25) to both the slip and conforming solution. The equivalent dimensionless and discretized ideal flux

$$J_{\text{id}} = -(1 - \bar{\phi})(\phi_1 - \phi_2) \tag{4.3.36}$$

does not depend upon the deformation of the cells. As such, placing the ideal flux approximation follows the same equations as the slip model (4.3.31): the stress balance has no effect on the ideal solution.

[3] As before, this only changes the time scale of the problem and is irrelevant to the dimensionless solution.

As before, we report $q(\mathscr{T}) = Q^*(\mathscr{T}) - 1$ as the percent change in volume from the initially swollen state with q_{id} being the ideal result (using J_{id}), q_s the slip result, and q_c the conforming result. We compare the conforming ("full") solution q_c to both the ideal mixing solution q_{id} and the slip solution q_s. As before, we define the deviation from ideal mixing with

$$\delta(\mathscr{T}) \equiv \frac{q_{\text{id}}(\mathscr{T}) - q_c(\mathscr{T})}{q_{\text{id,max}}}, \tag{4.3.37}$$

$q_{\text{id,max}}$ again given by $\phi_0/(2-\phi_0)$ to scale the deviation (see (4.2.4)). This is a positive quantity ($q_{\text{id}} > q_c$). We also define:

$$\kappa(\mathscr{T}) \equiv \frac{q_s(\mathscr{T}) - q_c(\mathscr{T})}{q_{\text{id,max}}} \tag{4.3.38}$$

as the deviation of the slip solution relative to the full solution. Again positive ($q_s > q_c$), this deviation is obtained through the use of gradients in the chemical potential (4.3.24) in place of the full flux. Both the ideal solution and the slip solution require the evaluation of scalar fields only and would be preferred for a finite element approach.

Figure 4.7a shows q_{id}, q_s and q_c for the parameter set $M_m = 3000$ g/mol, $G_{\text{dry}} = 0.28$ MPa, $\phi_0 = 0.3$, and $\xi_1 = 0.75$[4] ($\xi_2 = 0$); the "high extreme" parameter set was chosen because the difference between the three solutions should be the largest based upon equilibrium results. All solutions illustrate linear scaling at small time, a transition around $\mathscr{T} = 1$, and an eventual tapering off to an equilibrium value at large $\mathscr{T}$. The long–time solution for each curve is found to be in agreement qualitatively and quantitatively with the equilibrium value obtained above: the ideal case predicts the maximum final swelling, followed by the slip case, followed by the conforming case. Fig. 4.7b replots these curves by rescaling each by their long–time, equilibrium value. The slip and the ideal result are self–similar, while the conforming curve illustrates a slight negative deviation near $\mathscr{T} = 1$, indicating that anisotropic deformation causes a small deviation in diffusion rates from ideal. Experimental results show similar deviations from ideal mixing for the mass uptake of irradiated photoelastomeric disks when submersed in baths of macromer [1].

Fig. 4.8 illustrates the relative magnitudes of deviations of the ideal (δ) and slip (κ) approximation to the full solution for the parameter set $\epsilon = 0.1$, $\chi = 0.5$, and $\phi_0 = 0.2$, with $\xi_1 = 0.75$ and $\xi_2 = 0$. This parameter set was chosen because it lies near the line indicating that deviations from ideal mixing are about 5% (see Fig. 4.6) and represents typical clinical conditions. Notice that deviations from ideal mixing are near 5% at long time but that the deviations can be significantly larger for intermediate times: here they are as large as 7%. The deviation from the slip approxi-

[4]It should be noted that larger values of ξ_1 can yield aphysical results at small $\mathscr{T}$ for these simple models. Specifically, evaluation of a flux with the form $-\phi\nabla\mu$ should tend to zero as $\phi \to 0$ even as $\mu \to \infty$ logarithmically. Evaulating ϕ with $\bar{\phi}$ in the discretization above, however, allows the logarithmic terms in the chemical potential to dominate, resulting in an artificially larger flux than would be realistically observed. It is for this reason that ξ_1 is not chosen to be near 1.

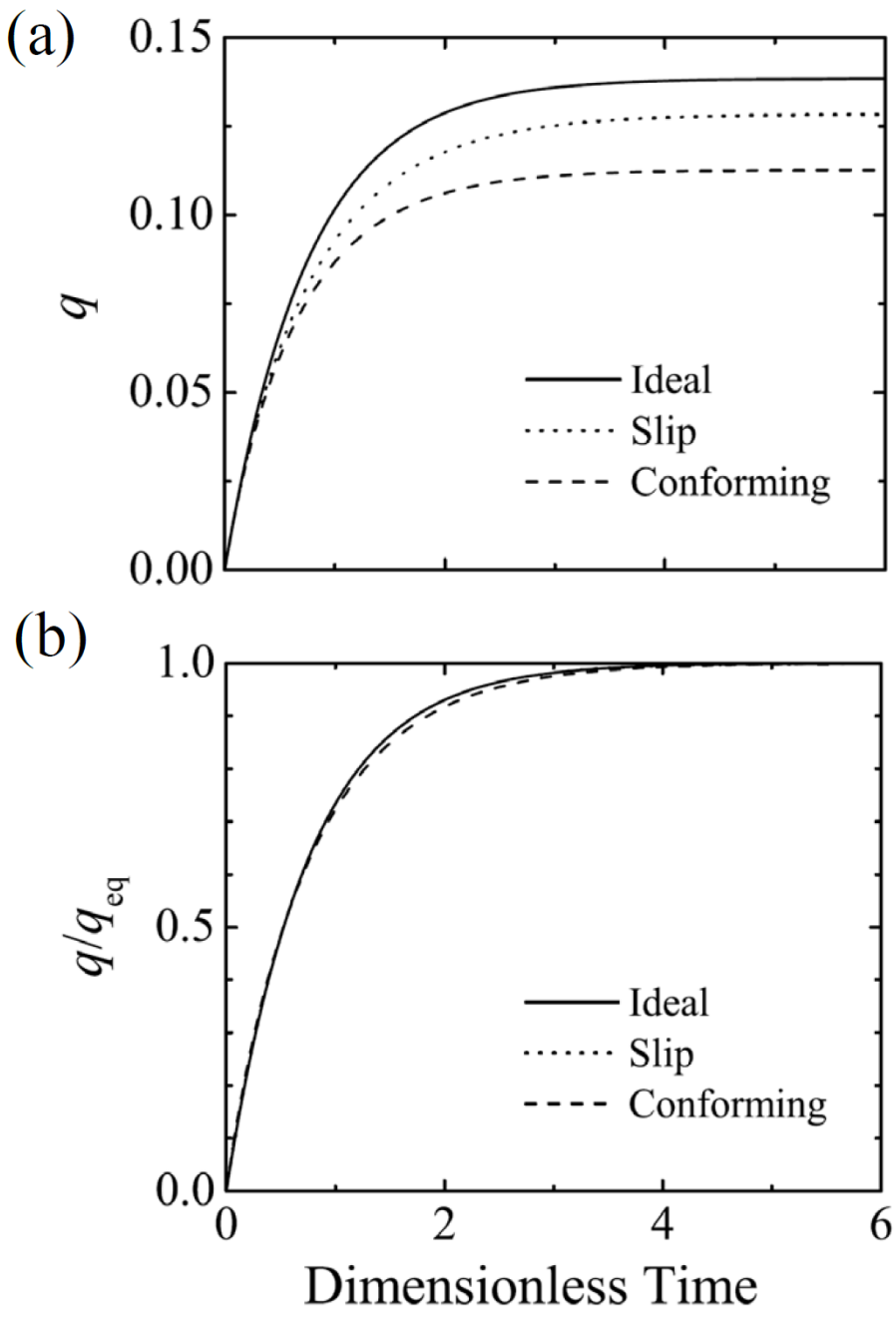

Figure 4.7: Two-cell transient solution results for the parameter set $M_m = 3000$ g/mol, $G_{\text{dry}} = 0.28$ MPa, $\phi_0 = 0.3$, $\xi_1 = 0.75$, and $\xi_2 = 0$. (a) The final equilibrium swelling is greatest for the ideal case, then the slip case, then the conforming case, but (b) the solutions are nearly self–similar.

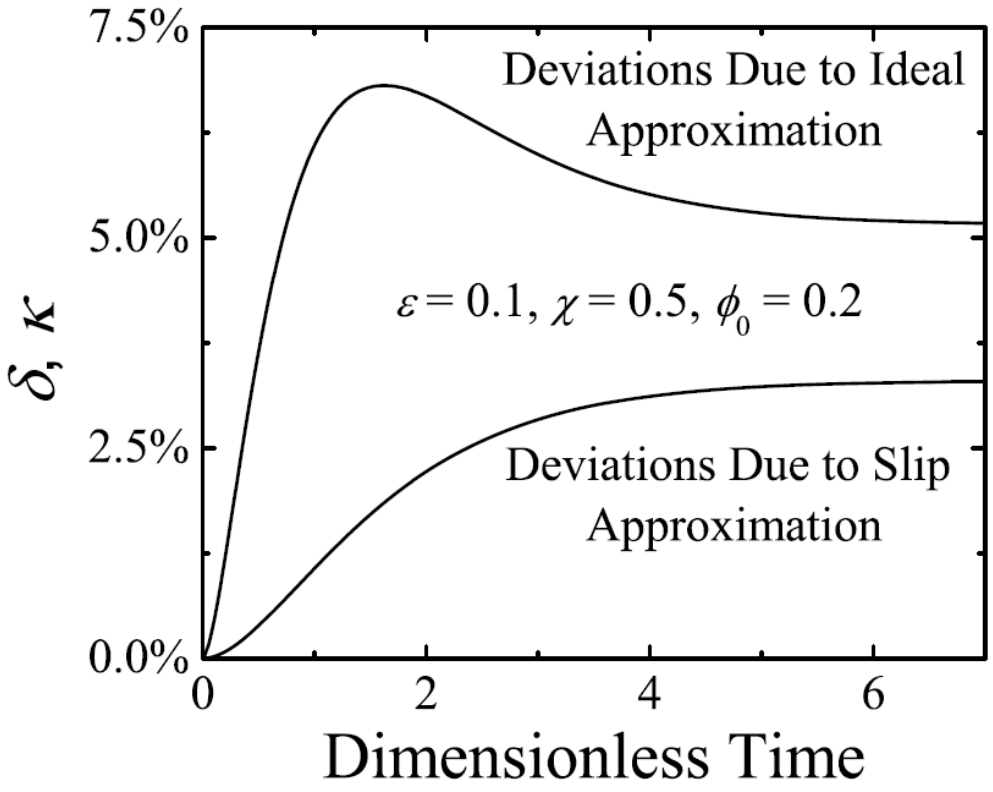

Figure 4.8: A comparison of the deviations from the full solution for both the ideal approximation (top curve) and the slip approximation (bottom curve). The material parameters chosen are $\epsilon = 0.1$, $\chi = 0.5$, and $\phi_0 = 0.2$, with the extents of reaction in each cell chosen as $\xi_1 = 0.75$ and $\xi_2 = 0$. The ideal approximation yields about twice as much deviation as the slip approximation, indicating that specifying the flux as a gradient in chemical potential is a better approximation than a gradient in volume fraction.

mation, however, rise to about half this maximum deviation, with the largest deviation occuring at equilibrium. Running several different choices of parameters yields the same general trends: deviations from ideal mixing rise at intermediate times and then decrease to the equilibrium deviation, while deviations from the slip approximation rise monotonically to the equilibrium deviation. This indicates that using Fig. 4.6 to determine whether the ideal mixing approximation is appropriate at equilibrium does not guarantee that the approximation is good for all time. The slip approximation, on the other hand, will always yield smaller deviations than the ideal approximation for all time. For this reason, we choose to use the slip approximation for the flux (gradient in chemical potential (4.3.24)) when solving transient problems throughout the rest of this thesis. This does not mean that we will ignore the stress coupling between cells: indeed we will still need to solve a stress balance at each point in time. However, we will not include the anisotropic correction to the flux $\sigma^c_{ij,j}$ when updating conservation of mass.

4.4 Conclusion

The twotcell model developed in this chapter provides insight into approximations that can be made throughout the rest of this thesis. We first illustrated that irradiating one cell while leaving a nearby cell unirradiated will result in material transfering from the unirradiated cell to the irradiated one, i.e., the irradiated cell expands while the unirradiated cell contracts. The magnitude of transfer is determined by thermodynamics: the chemical potential of macromer must be the same between the two cells at equilibrium. When the cells are required to deform together, there is also an internal stress balance that must be considered. It was determined that parameter sets at small values of ϵ and χ (differing depending upon the value of ϕ_0) yield very small deviations from an ideal mixing approximation at equilibrium; however, deviations can be more significant as the system develops in time. We therefore proposed a simplification to the model, in which anisotropic stress contributions to the flux are neglected but isotropic stress contributions are not.

In addition to this approximation, we discovered that larger gradients in extent of reaction cause more dramatic shifts in local volume. Also, more macromer initially present in the system, ϕ_0, provides a larger amount of free macromer that can be transferred, and therefore larger possible redistribution. In the next chapter, we will further explore the effects of initial macromer concentration and reaction profile on the magnitude of deformations experienced in a beam of elastomeric photopolymer forced to bend due to irradiation.

Chapter 5

Constant-Curvature Beam

5.1 Introduction

In the previous chapter, we examined a "toy problem" of two cells of elastomeric photopolymer experiencing reaction–diffusion–induced deformation. This illustrated the basic characteristics of the theory developed in Ch. 2 and Ch. 3 and began an examination of the relative importance of the material design parameters introduced in those chapters. In particular, we determined that equilibrium solution results do not deviate significantly from ideal mixing for the clinical parameter sets used in light–adjustable lens applications.

In this chapter, we begin to consider spatially resolved reaction profiles. For clinical use as light–adjustable lenses, elastomeric photopolymers always contain a passive scattering agent swollen into the initial matrix along with the macromer and photoinitatior. This "UV–blocker" ensures that the irradiation intensity decays considerably through the lens so that UV irradiation present in ambient sunlight and during the treatment will not damage the retina. Before we consider the complex reaction profiles and global deformation present in a fully three–dimensional light–adjustable lens, we first examine shape change resulting from this one–dimensional attenuation of light.

For our one–dimensional example, we consider the case of a finitely thick beam (Fig. 5.1a). We assume the beam is sufficiently long enough to ignore variations in the X–direction and that the height, H, and width, W, are roughly the same order of magnitude, with $W > H$. From here on, all coordinates are made dimensionless with H. We wish to determine how this beam deforms when subjected to an irradiation pattern which is uniform in the Y–direction but which varies in the Z–direction. In order to guarantee that all deformation also occurs along the Z–direction, the beam is first constrained to a non–deformable surface at $Z = 0$ and irradiated.

Since the light profile decays with depth into the sample, reaction occurs to a greater extent at the top of the beam where the light profile is more intense and more photoinitiator can be activated than at the bottom of the beam. We characterize the decay in the light profile using an analog of Beer's law and assume there is a one–to–one correspondence between irradiation intensity and

extent of reaction, ξ, specified as the initial condition. The extent of reaction profile exponentially decays according to

$$\xi(Z) = \xi_I \exp\left(\frac{1}{\lambda}(1 - Z)\right), \tag{5.1.1}$$

withξ_I the maximum extent of reaction at the top surface ($Z = 1$), and the subscript I denoting that this parameter is a function of the initial light intensity. The extinction length λ is conceptually connected to the optical information, including the molar absorptivity and concentration of both the UV–blocker and the photoinitiator; we define λ as the dimensionless distance from the top of the beam at which $\xi(Y)$ has decayed from ξ_I to $\xi_I \exp(-1)$. In this manner, λ can be varied from zero (the light profile is extinguished as soon as it enters the sample) to one (the light profile is extinguished at the back of the beam) and beyond (the light profile is extinguished beyond the beam).

Due to the gradients in macromer concentration created by this initial extent of reaction profile, portions of the material which are more highly reacted, say at points $Z > \alpha$, will absorb macromer from portions in which less reaction occurs ($Z < \alpha$). The more intensely reacted zones will swell under the transfer of material whereas the less reacted zones will shrink. Because the sample is cemented to a non–deformable surface, however, local elements cannot deform isotropically. For example, elements at $Z < \alpha$ can only contract along the Z–axis and, as such, are under a state of tension: the elements would like to contract in the X and Y directions as well but are constrained from doing so (Fig. 5.1b). This constraint is experienced at every level of depth: for example, elements at $Z > \alpha$ may expand along the Z–axis but are under a state of compression as they would like to expand along the X and Y directions. Only points at the neutral axis, $Z = \alpha$, are stress free. We will derive expressions for the stresses and strains experienced in this beam after material has transferred to equilibrium (§5.2). The equilibrium stresses and strains will then be relieved by allowing the beam to bend to a constant curvature (Figure 5.1c) in §5.3. The choice to use a bending beam as a sample one–dimensional problem was motivated by the work done by Warner and co–workers on beam bending of liquid–crystal elastomers upon irradiation with a specific frequency of light [8]. These authors observed that there was a maximum degree of curvature at an intermediate extinction length which was around one third of depth into the sample. We will show that elastomeric photopolymers modelled through the two-component theory of Ch. 2 exhibit a similar response. Furthermore, we examine this experienced curvature as a function of the extent of reaction profile (characterized by ξ_I and λ) and the material parameters G_{dry}, M_m, and ϕ_0.

5.2 Beam Constrained to a Solid Surface

Consider a beam of elastomeric photopolymer uniformly swollen to volume ratio Q_0 and constrained at $Z = 0$. This is the reference configuration (Figure 5.2a) and the surface at $Z = 1$ is considered to

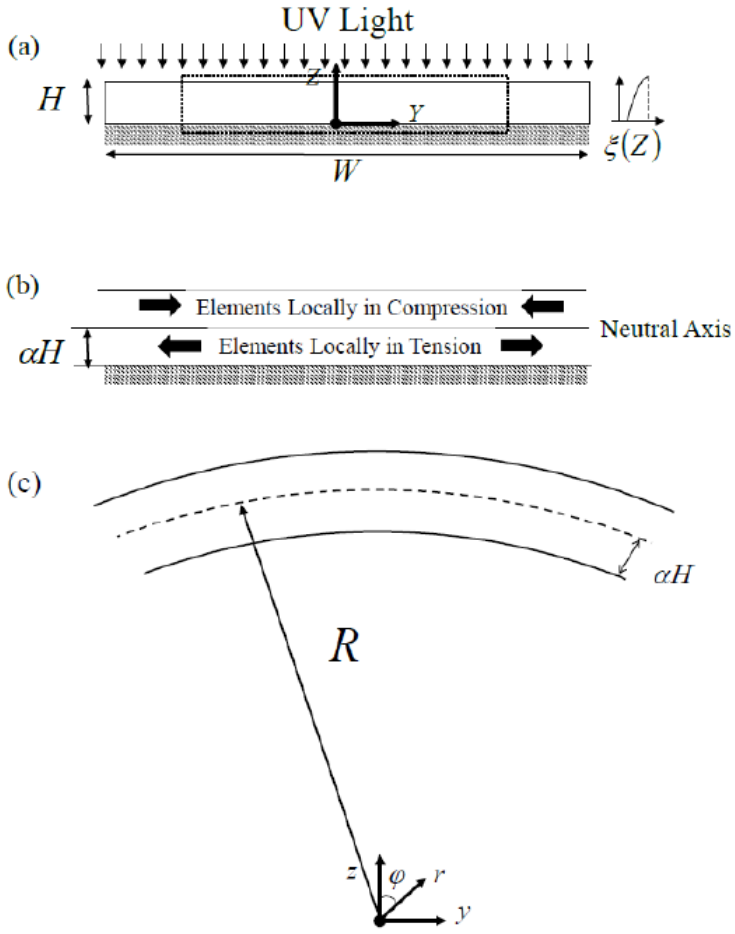

Figure 5.1: (a) A beam of elastomeric photopolymer constrained to a surface is irradiated with light. We consider the beam to be long relative to the cross–section dimensions so we can ignore variations in the X–direction. The irradiation profile is assumed to be uniform in the Y–direction and to decay in the Z–direction due to the scattering nature of the material: more macromer is converted to network near the top surface than at the bottom. This causes diffusion of free macromer from the bottom of the beam to the top. (b) Elements near the bottom would like to shrink but can only do so in the Z direction due to the constraint; these elements experience a local in–plane tensile stress. Likewise, elements near the top can only expand upward and so are in a state of in–plane compression. Elements at the neutral plane, αH, maintain their volume and are stress free. (c) If the constraint is removed, the beam will bend to radius of curvature R to relieve these in–plane stresses.

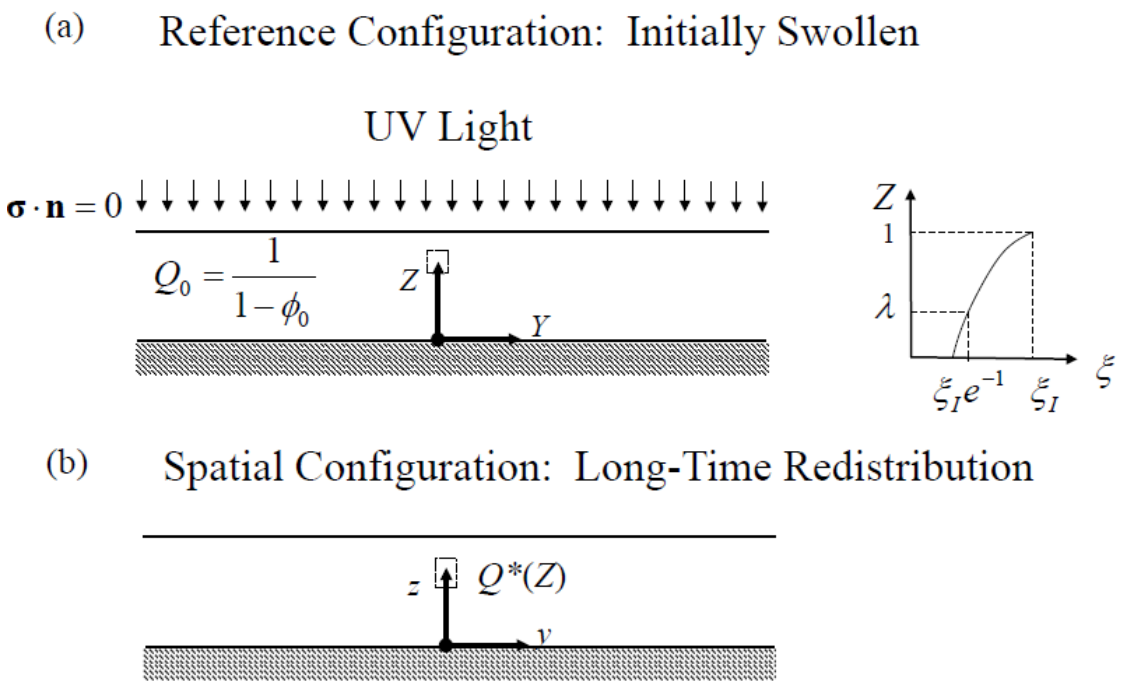

Figure 5.2: The (a) reference and (b) spatial configurations for the constrained beam (§5.2). The reference is taken as a dry network initially swollen to swelling ratio Q_0. When the reference is exposed to the extent of reaction profile (5.1.1), an element at reference coordinate Z will change volume due to redistribution of macromer: $Q^*(Z) < 1$ if the element contracts and $Q^*(Z) > 1$ if it expands. This causes the element to move to spatial coordinate z. The irradiated surface is exposed to an inert fluid and so remains stress–free during this process.

be exposed to an inert fluid so that the surface is stress free ($\sigma_{ij}n_j = 0$). At this stress-free surface, the beam is irradiated with a light source so that the extent of reaction profile decays through the depth by (5.1.1); the profile is uniform in X and Y. A material element at Z in the reference configuration will deform as macromer diffuses from the back to the front. Under the imposed geometrical constraint, material elements can only deform in the Z direction, attaining a volume ratio $Q^*(Z)$ relative to the reference configuration (Figure 5.2b). Material elements near the front of the beam experience a net gain in macromer and expand ($Q^* > 1$), whereas the cells near the back of the beam will experience a net loss of macromer and contract ($Q^* < 1$). We wish to determine the strain field $Q^*(Z)$ at long–time (the spatial configuration will be taken as the long–time solution in this section). The deformation gradient from the initially-swollen system to the spatial configuration is

$$\mathbf{F}^* = \begin{pmatrix} 1 & 0 & 0 \\ 0 & 1 & 0 \\ 0 & 0 & Q^*(Z) \end{pmatrix}. \tag{5.2.1}$$

Using this deformation gradient, we write the system free energy under the two-component assumption (taken from Ch. 2 (2.3.12)):

$$A(Q^*) = \phi \ln \phi + \chi\phi(1-\phi) + \frac{1}{2}\epsilon\,(1-\phi)\left(Q_0^{2/3}(Q^{*2}+2) - 3 - \ln Q_0 - \ln Q^*\right). \tag{5.2.2}$$

Recall that the macromer volume fraction, ϕ, and the volume ratio, Q^*, are connected by the conversion parameter θ^* (2.3.11) according to conservation of mass (2.3.10):

$$Q^* = \frac{\theta^*}{1-\phi}. \tag{5.2.3}$$

We can determine the long–time redistribution of macromer in one of two equivalent ways. One method involves solving the governing equations derived by minimization of the total system energy (given in §2.4) with respect to Q^*, the other by solving the differential equations presented in Ch. 3. Because the two are completely equivalent, we use the differential form here, since it is more illustrative. The general form for the stress at equilibrium (long–time) (3.4.36) is:

$$\sigma_{ij} = -p\delta_{ij} + \mu\delta_{ij} + \sigma_{ij}^c. \tag{5.2.4}$$

Recall that $-p$ emphasizes that only a uniform Lagrange multiplier is needed to capture equilibrium behavior, rather than the spatially dependent $\widetilde{\psi}$ necessary for transient problems. Under the deformation in this section (5.2.1), there are two stresses in the system: the stress along the z–axis, σ_{zz},

and the in–plane stress $\sigma_{xx} = \sigma_{yy}$:

$$\begin{aligned} \sigma_{zz} &= -p + \mu + G\left(Q^{*4/3} - 1\right) \\ \sigma_{xx} = \sigma_{yy} &= -p + \mu + G\left(Q^{*-2/3} - 1\right). \end{aligned} \tag{5.2.5}$$

Because of the absence of shear stresses, the stress balance in the z–direction yields σ_{zz} independent of z ($\sigma_{zz,z} = 0$). This, coupled with the stress-free boundary condition, indicates that $\sigma_{zz} = 0$ for all Z and there is no stress along the axis; this is because the beam can deform along the axis freely. Due to the constraint, however, it may not deform freely in the x and y directions and in–plane stresses develop:

$$\tau \equiv \sigma_{xx} = \sigma_{yy} = GQ^{*-2/3}\left(1 - Q^{*2}\right). \tag{5.2.6}$$

When $Q^* > 1$, $\tau < 0$ and the material elements are under a local state of compression as they wish to expand but cannot. Likewise, elements with $Q^* < 1$ experience a tensile stress $\tau > 0$ keeping them from contracting. The neutral plane, $Y = \alpha$, is determined by the condition of no stress or strain: $Q^* = 1$ and $\tau = 0$.

Solution of $Q^*(Z)$ proceeds point–by–point using $\sigma_{zz} = 0$. This requires determination of the spatially independent Lagrange multiplier p. The closing constraint used to determine p is global conservation of volume, written for the constrained beam as:

$$V = \int_0^1 Q^* dZ = \int_0^1 dZ = V_0. \tag{5.2.7}$$

Consideration of the governing equation $\sigma_{zz} = 0$ as a statement of chemical equilibria allows an alternative method to determine p. We define the effective chemical potential for the constrained beam as:[1]

$$\mu_{cons} \equiv \mu + G\left(Q^{*4/3} - 1\right) = p, \tag{5.2.8}$$

the second equality following from $\sigma_{zz} = 0$ and (5.2.5). As in Ch. 4 with the conforming cells, this effective chemical potential includes both isotropic (in μ) and anisotropic deformation. Analgous to Ch. 2, where isotropically swollen systems were in equilibrium with pure macromer ($\mu = 0$), each material element in the beam can be considered to be in equilibrium with a material element with chemical potential p: $\mu_{cons}(Z) = p$. This analogy allows us to make an educated initial guess for a value of p that will satisfy conservation of volume (5.2.7). First, the macromer left in the beam after reaction is conserved so that the average volume fraction at equilibrium can then be determined:

$$\bar{\phi} \equiv \frac{V_m}{V} = 1 - \frac{V_N}{V} = 1 - \int_0^1 \theta^* dZ. \tag{5.2.9}$$

[1]Note the similarity between μ_{cons} for the constrained beam and μ_α^{conf} for the conforming cells in Ch. 4.

The final equality follows from $V = V_0 = 1$ and the definition of $\theta^* = dV_N/dV_0$ (2.3.11). Second, reaction causes a spatial variation in the modulus of the material G (2.3.22) and we define the average modulus:

$$\bar{G} = \epsilon \left(1 - \bar{\phi}\right)^{1/3} \int_0^1 \theta^{2/3} dZ \tag{5.2.10}$$

(recall that θ and θ^* are related by $\theta^* = \theta/Q_0$). Because of the self–contained nature of the beam, we initially guess that the uniform modified chemical potential after reaction p will correspond to the average chemical potential (obtained by evaluating μ_{cons} (5.2.8) at the average volume fraction $\bar{\phi}$ and average material modulus $\bar{G}$). In practice, this turns out to be nearly exact: for many choices of reaction profiles and material parmeters, the volume conservation constraint (5.2.7) is satisfied within 0.1%. Furthermore, these computations have shown that a material element always exists at which $\phi = \bar{\phi}$ and $G = \bar{G}$: the element at the neutral plane ($Z = \alpha$). Therefore, all elements in the beam can be considered to be in chemical equilibrium with the element that does not deform ($Q^*(Z = \alpha) = 1$).

5.2.1 Stress and Strain Depend Strongly upon the Reaction Profile

We now determine the stress and strain profiles in the constrained beam as a function of the reaction profile parameters ξ_I and λ. Recall that ξ_I is directly related to the intensity of the incident light: the stronger the light, the larger the extent of reaction at the top surface. Stronger light intensity—represented by increasing ξ_I—at fixed exinction length results in steeper gradients in the extent of reaction profile: see the $\xi(Z)$ profiles in Figure 5.3. Steeper gradients in extent of reaction create steeper initial chemical potential gradients and therefore larger magnitudes of macromer transfer across the beam. We therefore expect steeper extent of reaction profiles to generate larger strains and stresses across the beam. This behavior is observed in Figure 5.3. The steepness of the initial extent of reaction profile increases monotonically with ξ_I at fixed λ: the larger the magnitudes of consumption (ξ_I increasing, light intensity increasing), the larger the stresses and strains experienced in the beam. The same is not true of the extinction length. For small extinction lengths (λ small), the light does not penetrate deep into the beam. This yields sharp gradients near the light source, while the majority of the system has significantly smaller gradients (Figure 5.3, $\lambda = 0.1$). Thus, macromer is significantly transferred only in a thin layer near the surface of the beam. We expect the stresses and strains in this case to be inherently asymmetric: large stresses and strains at the front of the beam with hardly any experienced at the back. This is captured by the theory: large compressive stresses are experienced by elements at the front of the beam while the back of the beam experiences significantly reduced tensile stresses. Increasing λ evens out the sharp gradient at the front across the entire sample (compare $\lambda = 0.5$ to $\lambda = 0.1$), yielding a larger net macromer transfer across the entire beam. In this case, the magnitude of the stresses are approximately the same in

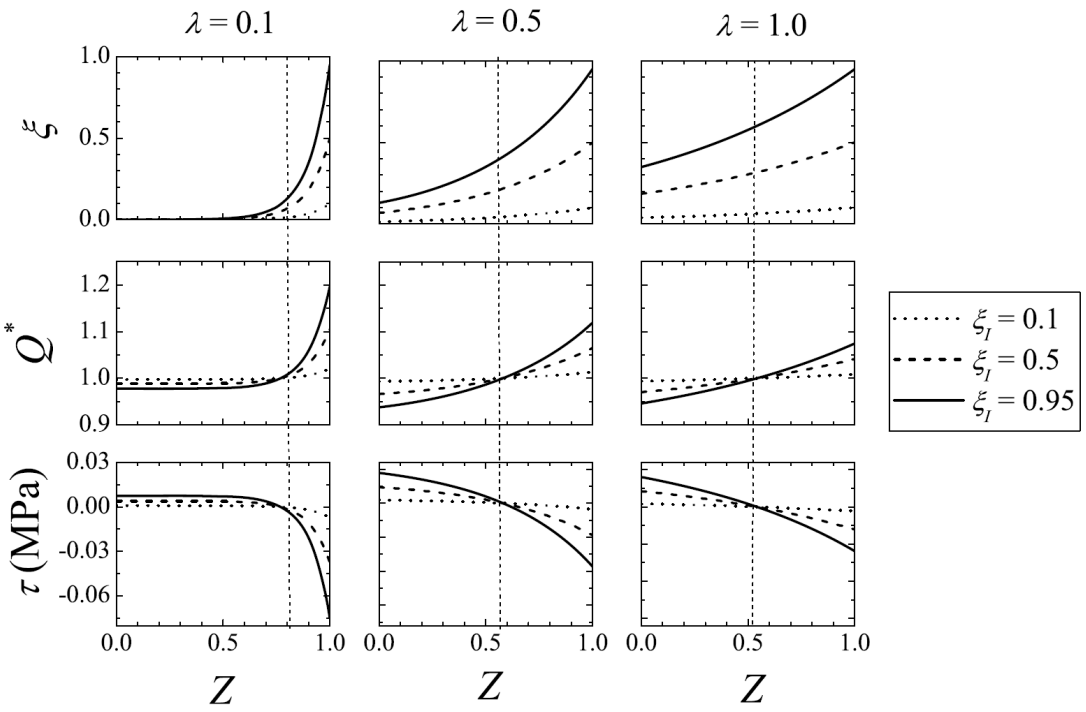

Figure 5.3: The strain (Q^*) and in–plane stress (τ) fields that develop in the constrained beam depend upon the extent of reaction profile ξ (5.1.1). Increasing the extent of reaction magnitude (ξ_I) causes both the stress and strain to increase systematically across the entire beam. Increasing the extinction length λ displays non–monotonic behavior. When the light decays in a thin region near the surface ($\lambda = 0.1$), there are large stresses and strains in the thin region but the majority of the beam is unaffected. When the light penetrates more deeply ($\lambda = 0.5$), the entire beam experiences stress and strain. As λ continues to increase ($\lambda = 1.0$), the initial extent of reaction profile becomes flatter and the magnitude of the stress and strain diminish. Material parameters: $\phi_0 = 0.2$, $M_m = 1000$ g/mol, $G_{\text{dry}} = 0.18$ MPa.

both the back and the front. As λ continues to increase, however, the gradients become more and more shallow (compare $\lambda = 0.5$ to $\lambda = 1.0$) so that less macromer is transferred at larger extinction lengths. This results in the magnitude of the stress diminishing. In the limit of $\lambda \to \infty$, the extent of reaction profile becomes uniform throughout the depth for any choice of ξ_I. In this case, there are no gradients in chemical potential and no diffusion–deformation occurs.

Because ξ_I only serves to determine the magnitude of deformation, the location of the neutral plane (defined by $Q^* = 1$) is only a function of the extinction length λ. For small λ, diffusion–deformation only occurs significantly within a small region near the surface of the lens and the neutral plane is located there ($\alpha > 0.5$). As λ continues to increase, the neutral plane moves more towards the back of the beam (Figure 5.4). At the limit $\lambda \to \infty$, the extent of reaction profiles approach straight lines and the theoretical value of α approaches the midplane ($\alpha = 0.5$).

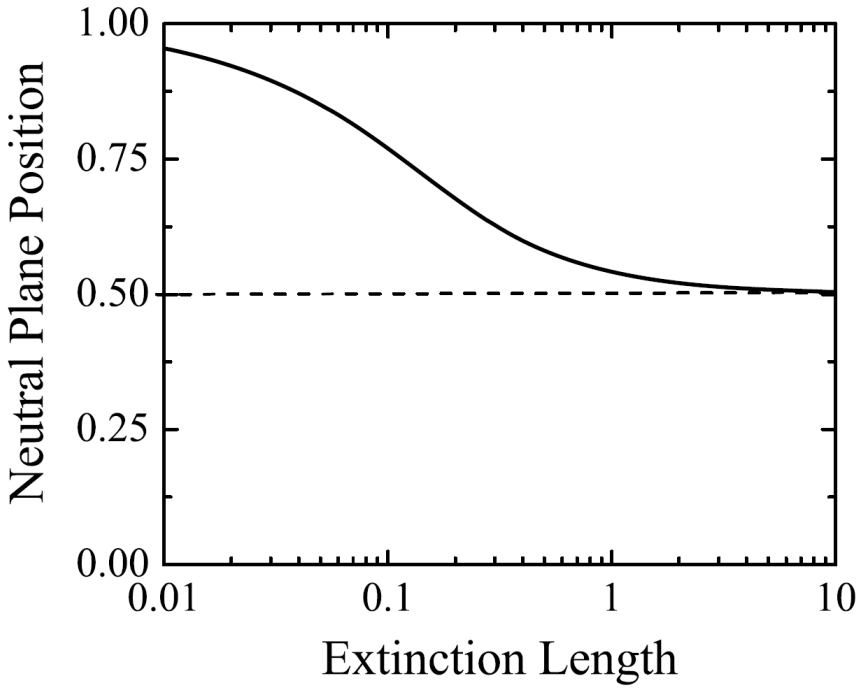

Figure 5.4: The location of the neutral plane (α) as a function of extinction length (λ). In the limit of short extinction length ($\lambda \to 0$), the light does not penetrate far into the beam and the neutral plane is located near the top surface ($\alpha \to 1$). In the limit of deep penetration ($\lambda \to \infty$), the neutral plane is located at the midplane ($\alpha = 0.5$). Reaction profile: $\xi_I = 0.95$. Material parameters: $\phi_0 = 0.2$, $M_m = 1000$ g/mol, $G_{\text{dry}} = 0.18$ MPa.

5.2.2 Effect of Material Parameters

We now examine the effect of the material parameters M_m, G_{dry}, and ϕ_0 on the developed stresses and strains in the constrained beam. In Ch. 4, we determined that for clinically relevant parameter choices of M_m and G_{dry}, the solution to the governing equations could be taken as ideal because the deviations from ideal were found to be small, regardless of the parameter choice. A different way to state the same conclusion is to say that varying M_m and G_{dry} has little effect on the final form of the solution.

With this in mind, we examine changes of parameters under a set reaction profile in Figure 5.5. As expected, stresses and strains are the same regardless of the value of macromer molar mass M_m. The only role that the molar mass plays in the solution is in determining the appropriate time scale for the diffusion–deformation process: the diffusivity of macromer in network is determined solely by the macromer molar mass (§B.4). We will demonstrate this using real-time scales in Ch. 6 when we consider a system with real physical dimensions: the light–adjustable lens. Likewise, there are negligible variations in the strain, Q^*, with network modulus G_{dry}. However, G_{dry} does become important in determining the stress generated inside the beam: the dimensional stresses scale as G_{shear} which is directly proportional to G_{dry} (2.3.21). This makes sense: a stiffer network under the same strain as a softer network must be under a larger stress. Choices of G_{dry} can then be made based upon application: a larger shear modulus could be chosen, for example, for applications where the deformation induced by diffusion is used to do work.

Despite the great utility available in specifying M_m and G_{dry} independently, however, the two cannot be varied arbitrarily. Recall from §2.2.2 that the allowable initial volume fraction ϕ_0 is limited by thermodynamics, as determined from the Flory–Rehner equation. Thus, M_m and G_{dry} must still be judiciously chosen to allow a desired choice of ϕ_0. Unlike the macromer molar mass and network modulus, the choice of ϕ_0 has a significant effect on the solution (Figure 5.5). Just like the surface extent of reaction ξ_I, ϕ_0 determines the initial magnitude of the generated chemical potential gradients. Thus, ϕ_0 can be thought of as parameter which tunes the osmotic pressure: the larger ϕ_0, the more magnitude of material available for redistribution and therefore the larger the experienced strains and stresses.

5.3 Beam Released to a Constant Curvature

The in–plane stresses developed in the constrained beam are compressive above the neutral plane ($Z > \alpha$) and tensile below the neutral plane ($Z < \alpha$). We may think of these stresses as forcing the beam to maintain deformation in keeping with the boundary condition. If the constraint at $Z = 0$ is removed, then we expect the beam to deform so that the in–plane stresses (5.2.6) are relieved. Because of the existence of a neutral plane, a first-order approximation for the deformation of the

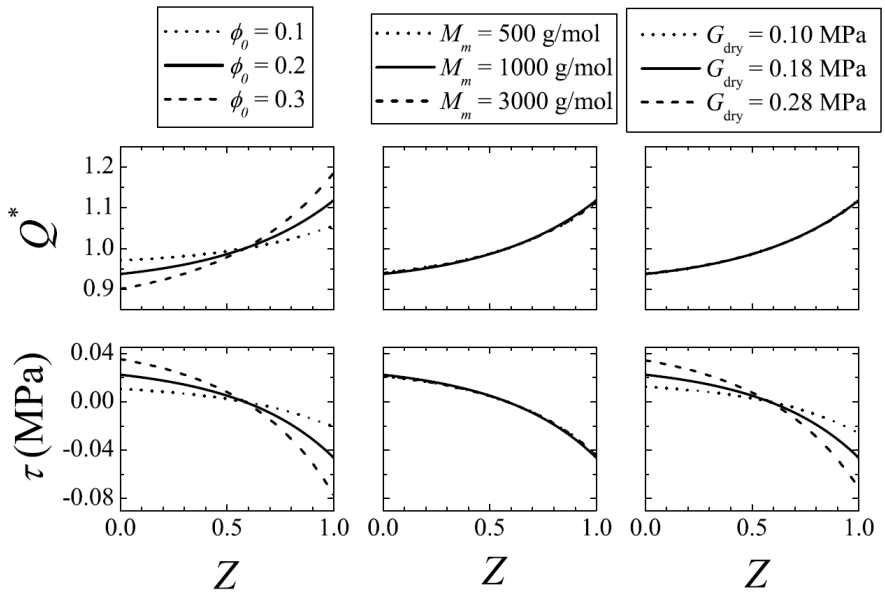

Figure 5.5: The stresses and strains experienced in the constrained beam as a function of material parameters. The solid curve is the same between all three boxes and represents the default parameter set $\phi_0 = 0.2$, $M_m = 1000$ g/mol, and $G_{\text{dry}} = 0.18$ MPa. The first column shows variations in the stress and strain with ϕ_0; M_m and G_{dry} are held at the fixed defaults. The middle column shows variations with M_m (ϕ_0 and G_{dry} at default), while the last column shows variations with G_{dry} (ϕ_0 and M_m at default). Reaction profile: $\xi_I = 0.95$, $\lambda = 0.5$.

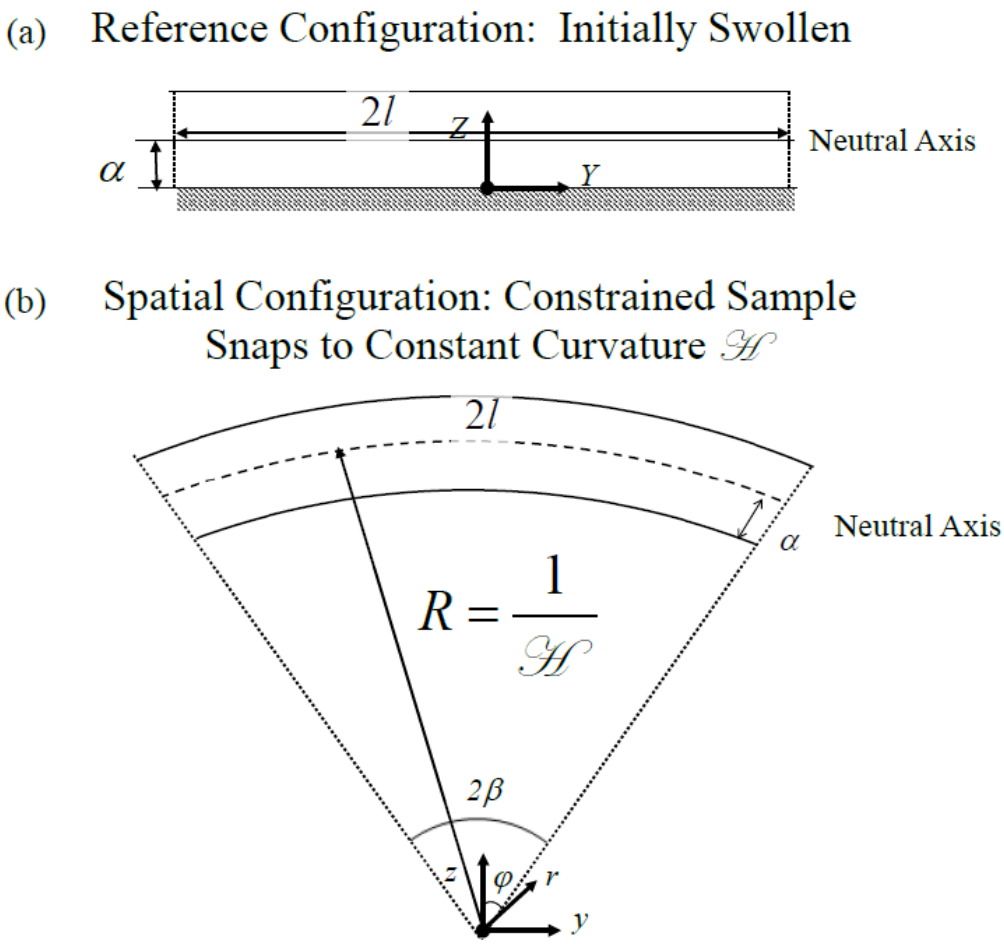

Figure 5.6: §5.3 The (a) reference and (b) spatial configuration for a beam initially constrained while it is irradiated (Fig. 5.2) but now released from the constraint to attain a curvature $\mathscr{K}$ (§5.3). The neutral plane ($Z = \alpha$) is defined as the plane that does not experience any strain upon reaction (§5.2) and is assumed to also remain undeformed by the bending process.

beam is for it to bend. Because one dimension is significantly longer than the other two, we assume the beam will attain a constant cylindrical curvature, $\mathscr{H}$, to be determined (Fig. 5.6b). In this case, planes at a fixed Z deform to a constant value of r in the spatial configuration, independent of Y. Likewise, planes at a fixed value of Y are allowed to rotate an angle φ to account for deformation but must remain as straight lines.[2] Due to the nature of the assumed deformation, each plane at a given value of X does not deform, and the in–plane stress in the x direction will remain the same as that experienced while constrained. Under this assumed deformation, we write:

$$\begin{aligned} r &= r(Z) \text{ only,} \\ \varphi &= \varphi(Y) \text{ only, and} \\ x &= X. \end{aligned} \tag{5.3.11}$$

Noting that $z = r\cos\varphi$ and $y = r\sin\varphi$, we may write the deformation gradient relative to the initially-swollen system in Cartesian coordinates as:

$$\mathbf{F}^* = \begin{bmatrix} 1 & 0 & 0 \\ 0 & r(Z)\cos\varphi(Y)\varphi'(Y) & r'(Z)\sin\varphi(Y) \\ 0 & -r(Z)\sin\varphi(Y)\varphi'(Y) & r'(Z)\cos\varphi(Y) \end{bmatrix}. \tag{5.3.12}$$

Here, we use $'$ to denote differentiation with respect to the appropriate independent variable. With (5.3.12), local volume changes are given by:

$$Q^* \equiv \det \mathbf{F}^* = r(Z)r'(Z)\varphi'(Y). \tag{5.3.13}$$

Experiments performed by Pape indicate that the beam will bend to a constant curvature significantly faster than the time it takes macromer to diffuse. We therefore use the constrained solution, $Q^*(Z)$, as an approximation in determining the initial curvature experienced by the beam. The assumed dependence of Q^* on only Z forces $\varphi'(Y)$ to be a constant (5.3.13). This constant is the curvature of the beam, $\mathscr{H}$, determined as follows. Consider a line segment along the neutral plane ($Z = \alpha$) which initially had length $2l$ before deformation (Fig. 5.6a). Because this line is on the neutral plane, $Q^* = 1$ and the line will maintain its length at $2l$ upon bending (Fig. 5.6b). Defining the angle subtended by this length to be 2β,

$$\begin{aligned} \varphi(l) &= \beta \text{ and} \\ \varphi(-l) &= -\beta. \end{aligned} \tag{5.3.14}$$

[2]This assumed deformation ignores edge effects, which are small for large W relative to H.

With $\varphi'(Y)$ constant, $\varphi(Y) = \beta Y/l$. We call R the radius of curvature measured as the distance from the center of curvature to the neutral plane; it is also the inverse of the curvature $\mathscr{H}$. From geometry:

$$R \equiv \frac{1}{\mathscr{H}} = \frac{l}{\beta} \tag{5.3.15}$$

and $\varphi'(Y) = \mathscr{H}$. Using this expression, we may rewrite (5.3.13) in terms of a single scalar field $q(Z)$:

$$Q^*(Z) = \mathscr{H} r(Z) r'(Z) \equiv \frac{q'(Z)}{2\mathscr{H}}, \tag{5.3.16}$$

defining

$$q(Z) \equiv \mathscr{H}^2 r^2(Z) \tag{5.3.17}$$

as the anisotropic beam deformation field. A physical interpretation of q can be made by placing the deformation gradient (5.3.12) into the free energy expression (2.3.12) to obtain the expression for the free-energy of the bent beam:[3]

$$A(Q^*, r, \mathscr{H}) = \phi \ln \phi + \chi\phi(1-\phi) + \frac{1}{2}\epsilon\,(1-\phi)\left[Q_0^{2/3}\left(1 + r^2\mathscr{H}^2 + (r')^2\right) - 3 - \ln Q_0 - \ln Q^*\right]. \tag{5.3.18}$$

It is illustrative to replace r with the variable q (5.3.17):

$$A(Q^*, q) = \phi \ln \phi + \chi\phi(1-\phi) + \frac{1}{2}\epsilon\,(1-\phi)\left[Q_0^{2/3}\left(1 + q + \frac{Q^{*2}}{q}\right) - 3 - \ln Q_0 - \ln Q^*\right]. \tag{5.3.19}$$

Compared to the free energy in the constrained case (5.2.2), only the first stretching term has changed from

$$Q^{*2} + 2$$

to

$$\frac{Q^{*2}}{q} + q + 1.$$

Note that the change is due solely to the field q. To understand the significance of this change in energy, we write the Cartesian deformation gradient (5.3.12) in cylindrical coordinates:

$$\mathbf{F}^* = \begin{bmatrix} 1 & 0 & 0 \\ 0 & r^2\mathscr{H}^2 & 0 \\ 0 & 0 & (r')^2 \end{bmatrix} = \begin{bmatrix} 1 & 0 & 0 \\ 0 & q & 0 \\ 0 & 0 & \frac{Q^{*2}}{q} \end{bmatrix} \tag{5.3.20}$$

For each material element labelled Z, an element that was constrained to deform only in one direction (z) can now deform in two directions (r and φ). This allows for the alleviation of the in–plane stresses

[3]The functional dependence of the free energy on ϕ is not stated explicit b ly since ϕ is related to Q^* by conservation of mass (2.3.10).

(5.2.6) that developed when the beam was constrained. Using the deformation gradient in cylindrical coordinates (5.3.20), the principle stresses in cylindrical coordinates are (3.4.36):

$$\begin{aligned}\sigma_{xx} &= -p + \mu + G\left(Q^{*-2/3} - 1\right)\\ \sigma_{\varphi\varphi} &= -p + \mu + G\left(qQ^{*-2/3} - 1\right)\\ \sigma_{rr} &= -p + \mu + G\left(\frac{1}{q}Q^{*4/3} - 1\right)\end{aligned} \tag{5.3.21}$$

(note that there are no shear stresses in cylindrical coordinates). We can eliminate p and μ from the expressions with $\sigma_{zz} = 0$ (condition of the constrained case used to determine $Q^*(Z)$):

$$\begin{aligned}\sigma_{xx} = \tau &= GQ^{*-2/3}\left(1 - Q^{*2}\right)\\ \sigma_{\varphi\varphi} &= GQ^{*-2/3}\left(q - Q^{*2}\right)\\ \sigma_{rr} &= GQ^{*4/3}\left(\frac{1}{q} - 1\right).\end{aligned} \tag{5.3.22}$$

Comparing with the constrained stresses (5.2.5), we note that the axial stress in the x–direction (σ_{xx}) remains the same regardless of q because no deformation is allowed in that direction: even after the curvature, it maintains the same deformation as the constrained state. The angular stress and radial stresses have changed, however, due to the deformation field q. Consider an element at the front of the beam that has expanded $Q^* > 1$. Recall that the in–plane stress for this element $\sigma_{yy} < 0$ in the constrained state: the element is locally under compression and would like to expand in the y–direction. According to (5.3.22), then, we expect $q > 1$ at the front so that the in–plane compressive stresses are alleviated; in the extreme case where $q = Q^{*2}$, the angular stresses vanish. However, alleviation of the in–plane stresses near the top ($q > 1$) generates stress along the radial direction σ_{rr} (recall that there is initially no stress in this direction, $\sigma_{zz}(Z) = 0$). For $q > 1$, these stresses are compressive and become larger as q increases. Because there is a competition between the radial and angular stresses, there is a particular value of q for which the net stress will be small. Naively, we assume this will be when $\sigma_{rr} = \sigma_{\varphi\varphi}$ or $\tau_\varphi = 0$, with

$$\tau_\varphi \equiv \sigma_{\varphi\varphi} - \sigma_{rr} = GQ^{*-2/3}q^{-1}\left(q^2 - Q^{*2}\right). \tag{5.3.23}$$

Using similar logic, we can deduce that at the back of the beam ($Q^* < 1$), the elements originally under in–plane tension ($\sigma_{yy} > 0$) will be relieved of this tension when $q < 1$. This is done at the expense of a generated tensile stress in the radial direction. Again, (5.3.23) provides an appropriate measure of the relative magnitudes of these stresses. At each point in the beam, the relative stress (5.3.23) will be zero if $q = Q^*$. This is not possible for a general $Q^*(Z)$ field, however, because of conservation of volume (5.3.16). Rather, given a $Q^*(Z)$ profile obtained for the constrained case, we

must solve the ODE (5.3.16) for the deformation field q under a curvature $\mathscr{H}$. The actual value of the curvature that the beam attains will be one in which the system free energy is minimized. For a general Q^* profile, we will see that the relative stress (5.3.23) is not pointwise zero, but attains a balance across the beam so that the stresses are as small as possible.

We now consider solution of $q(Z)$ from $Q^*(Z)$ using the differential equation (5.3.16). Solution requires a boundary condition: we assume that the final thickness of the bent beam is the same as the original thickness,

$$r(1) - r(0) = 1 \tag{5.3.24}$$

in dimensionless terms. Although conservation of volume has already been satisfied for the $Q^*(Z)$ profile, we make use of it to rewrite this boundary condition in a more useful form:

$$V = \int_0^1 Q^* dZ = \left[\frac{q(Z)}{2\mathscr{H}}\right]_0^1 = \frac{q(1) - q(0)}{2\mathscr{H}} = 1. \tag{5.3.25}$$

The second equality follows from (5.3.16) and the fundamental theorem of calculus, where the final one follows from conservation of volume. Recalling that $q(Z) = r^2(Z)$, we may rewrite the boundary condition (5.3.24) by eliminating $r(1)$ using conservation of volume (5.3.25):

$$q(0) = \left(1 - \frac{\mathscr{H}}{2}\right)^2 = 1 - \mathscr{H} + \frac{1}{4}\mathscr{H}^2. \tag{5.3.26}$$

The second equation that results,

$$q(1) = \left(1 + \frac{\mathscr{H}}{2}\right)^2 = 1 + \mathscr{H} + \frac{1}{4}\mathscr{H}^2, \tag{5.3.27}$$

can not be made to hold exactly: it will only hold to the accuracy with which volume was conserved in the original $Q^*(Z)$ profile (5.3.25). We preferentially choose the first equation (5.3.26) as the boundary condition over the second because it provides a condition at $Z = 0$. This simplifies solution of the ODE (5.3.16) by allowing use of a forward-stepping method.

Upon specifying a Q^* profile, the q profile depends only on the curvature $\mathscr{H}$: once in the boundary condition (5.3.26) and a second time in the differential equation (5.3.16). For the constrained beam before curvature is allowed, $\mathscr{H} = 0$. For this case, the differential equation (5.3.16) and boundary condition (5.3.26) solve to $q(Z) = 1$ for all Z: when the beam is constrained, the angular stress $\sigma_{\varphi\varphi}$ (5.3.22) reduces to the in–plane constrained stress σ_{yy} (5.2.5), as expected. We can thus consider $q(Z) = 1$ to be the initial solution before the beam is allowed to bend. As $\mathscr{H}$ increases from zero, the boundary condition (5.3.26) indicates that $q(0) < 1$ ($\mathscr{H} < 4$). As previously discussed, this represents a decrease in the tensile in–plane stress for the element at the back of the beam at the expense of generating a tensile radial stress. Also, (5.3.27) tells us that the opposite case

occurs at the front of the beam: $q(1) > 1$ and the compressive angular stresses decrease, creating a compressive radial stress.

The actual curvature $\mathscr{H}$ the beam will attain is determined by minimizing the system free energy:

$$F(\mathscr{H}) \equiv \int_0^1 A(\mathscr{H}) Q^*(Z) dZ, \tag{5.3.28}$$

the conservation of volume constraint omitted because the $Q^*(Z)$ profile is specified and already obeys conservation of volume. The free energy per volume $A(\mathscr{H})$ is given by (5.3.19); based upon the above discussion, we treat q as solely a function of $\mathscr{H}$. For a given value of $\mathscr{H}$, we determine q from (5.3.16) and use this to determine the system free energy (5.3.28). The derivative of F with respect to $\mathscr{H}$ is then approximated:

$$\frac{\partial F}{\partial \mathscr{H}} \approx \frac{F(\mathscr{H} + \delta\mathscr{H}) - F(\mathscr{H} - \delta\mathscr{H})}{\delta\mathscr{H}}; \tag{5.3.29}$$

the value $\delta\mathscr{H} = 10^{-6}$ is used to estimate the derivative. The value of $\mathscr{H}$ is then varied using the secant method until this derivative is zero.

To illustrate the effect of curvature on the stresses in the system, we consider a beam of elastomeric photopolymer with $M_m = 1000$ g/mol, $G_{\text{dry}} = 0.18$ MPa, and $\phi_0 = 0.2$. This beam is submitted to an exponentially decaying extent of reaction profile (5.1.1); we take $\xi_I = 0.95$ and $\lambda = 0.5$. The constrained solution for $Q^*(Z)$ under these conditions was shown in §5.2.1 (Fig. 5.3); we illustrate the corresponding q profile obtained by solving the ODE (5.3.16) for several different values of $\mathscr{H}$ in Fig. 5.7a. As can be seen, each of the $q(Z)$ profiles is essentially linear, despite the non–linearity in the $Q^*(Z)$ profile; this is due to the small magnitude of $\mathscr{H}$. As expected, $q < 1$ near the back of the beam, so as to relieve the initial in–plane tensile stress experienced there, and $q > 1$ near the front so as to relieve the compressive in–plane stress; the in–plane stresses after bending ($\sigma_{\varphi\varphi}$) are shown in Fig. 5.7b. Although the bending relieves the in–plane stresses, it generates a corresponding radial stress, compressive at the front and tensile at the back (Fig. 5.7c). The relative stress $\sigma_{\varphi\varphi} - \sigma_{rr}$ (5.3.23) is shown in Fig. 5.7d. The relative stress difference is large for $\mathscr{H} = 0$ and corresponds to the initial in–plane stress τ experienced when the beam is a constrained case (Fig. 5.3). As the curvature increases, the relative stresses decrease in magnitude at both the front and the back of the beam, illustrating the balance between radial and angular stress. Note that no choice of $\mathscr{H}$ yields a state in which the radial and angular stresses are equal at all points ($\tau_\varphi(Z) = 0$). In fact, the closest possible state is at the energy minimizing curvature, $\mathscr{H} = 0.0862$. At this point, the magnitude of the relative stresses are the smallest and the two stresses are as nearly balanced as possible; increasing the curvature beyond this causes larger stress differences (Fig. 5.7e). Thus, the energy-minimizing curvature is the one in which the two stresses are approximately equal.

The reason the two stresses cannot be uniformly equal is due to the location of the neutral plane

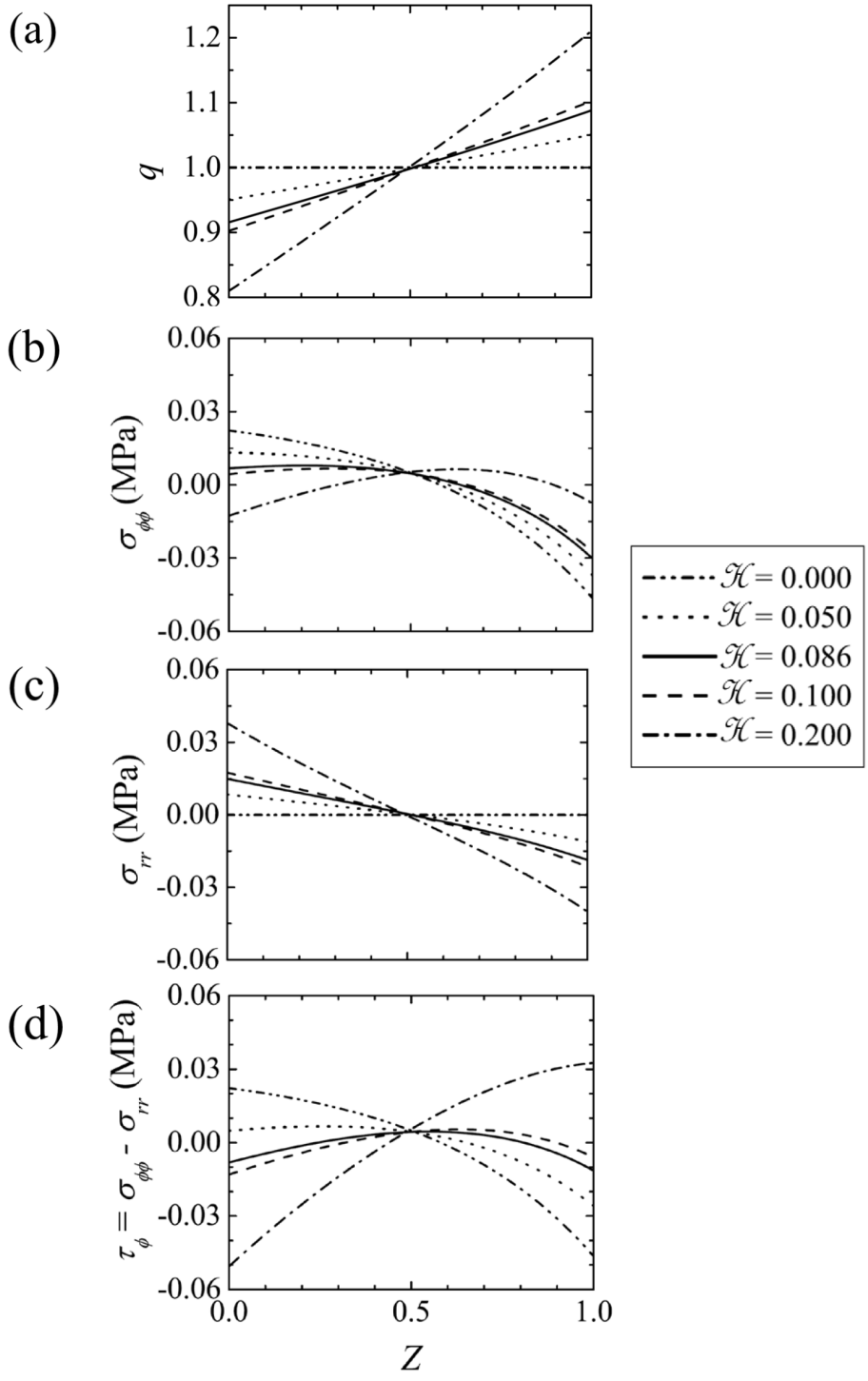

Figure 5.7: The strain and stress fields experienced inside the reacted constrained beam upon release and bending as a function of the curvature $\mathscr{K}$. (a) The deformation field, q; (b) the angular stress, $\sigma_{\varphi\varphi}$; (c) the radial stress, σ_{rr}, and (d) the relative stress, $\tau_\varphi = \sigma_{\varphi\varphi} - \sigma_{rr}$. The curvature $\mathscr{K} = 0.0862$ represents the energy-minimizing curvature. Reaction parameters: $\xi_I = 0.95$, $\lambda = 0.5$. Material parameters: $\phi_0 = 0.2$, $M_m = 1000$ g/mol, and $G_{\text{dry}} = 0.18$ MPa.

in the constrained state. For the small curvatures attained by these beams, the radial stress profiles are approximately linear (Fig. 5.7c) and the radial stress vanishes at a single point, $Z \approx 0.5$. Above this point, the radial stresses are compressive and below they are tensile; they are also equal and opposite in magnitude to either side of the midplane. The angular stresses, on the other hand, vanish further towards the front of the beam, $Z > 0.5$. Furthermore, they are not symmetric about the zero stress point: elements at the front experience significantly larger compressive angular stress than the tensile angular stress experienced by elements at the back. This asymmetry in the angular stresses results directly from the asymmetry in the initial constrained stress profile, τ ($\mathscr{H} = 0$). Because general light decay profiles experience the neutral plane at $Z > 0.5$, the radial and angular stresses cannot be generally equal at all points; the best the system can attain is a compromise between the stresses which are experienced at the energy minimizing curvature.

Before examining the effect of profile and material parameters on the magnitude of the curvature attained, we are now in a position to re-evaluate our assumption that macromer does not diffuse across the beam as it curves. Using the energy-minimizing $\mathscr{H}$, we evaluate the chemical potential in the bent state (2.2.19)

$$\mu_{bent} = \mu_{cons} + GQ^{*4/3}\left(\frac{1}{q} - 1\right) + GQ^{*1/3}\mathscr{H}\frac{(1-\phi)}{\phi'(Z)}\left[1 - \left(\frac{Q^*}{q}\right)^2\right]. \tag{5.3.30}$$

Here, μ_{cons} is the chemical potential in the constrained state (5.2.8) and $\phi'(Z) = d\phi/dZ$.[4] For the case just discussed, the chemical potential is nearly uniform across the beam after bending (dotted curve) compared to the initial gradients created by reaction (dashed curve) (Fig. 5.8). Only in a thin region near the back ($Z = 0$) is there a significant chemical potential gradient after bending. Thus, a small amount of material will transfer from the elements at the back towards the middle at long times after bending (recall the diffusive time scale is slower than the deformation scale). This causes elements in the back to further deswell, slightly increasing the tensile stresses experienced at the back. These slightly stronger tensile stresses at the back will cause a slight increase in the curvature to relieve the stresses. We can therefore view the results presented here as the minimum initial curvature attained by the beam after it is released from the constraint.

5.3.1 Curvature Depends Strongly upon Initial Chemical Potential Gradients

We are now in a position to determine the curvature attained by the beam under the stresses discussed in §5.2.1. We first discuss the effect of the reaction profile on the developed curvature. Based

[4]The derivative of ϕ appears from:

$$\frac{\partial q}{\partial \phi} = \frac{dq}{dZ}\frac{dZ}{d\phi} = q'/\phi' = 2\mathscr{H}Q^*/\phi'.$$

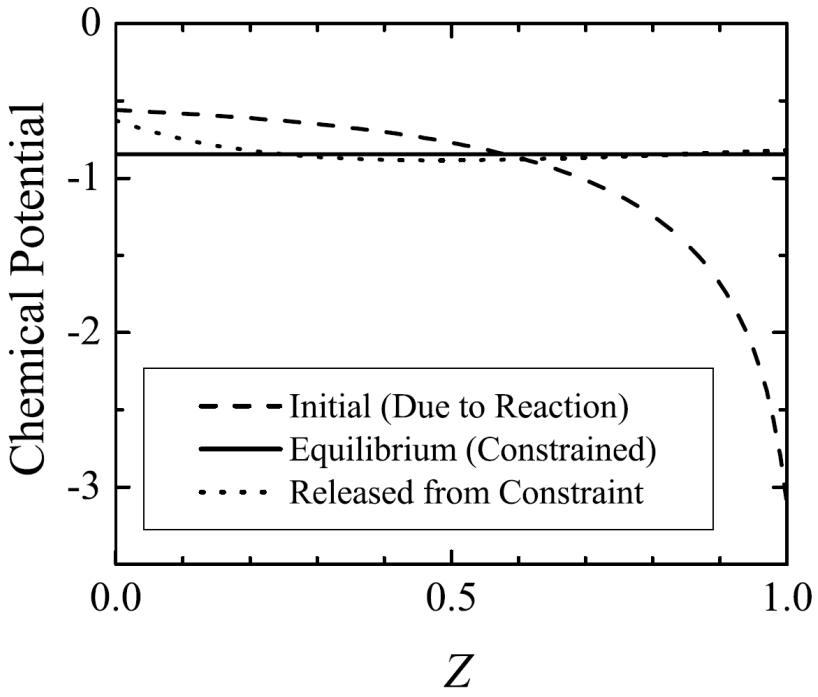

Figure 5.8: The chemical potential field inside the beam: 1) after the initially constrained beam is reacted but before macromer is allowed to diffuse (dashed); 2) after macromer diffusion is completed while the beam is still constrained (solid); and 3) after the beam is bent to the energy minimizing curvature $\mathscr{H} = 0.0862$ (dotted). Reaction parameters: $\xi_I = 0.95$, $\lambda = 0.5$. Material parameters: $\phi_0 = 0.2$, $M_m = 1000$ g/mol, $G_{\text{dry}} = 0.18$ MPa.

upon the stresses that develop when the beam is constrained (Fig. 5.3), we expect the curvature will increase with the surface extent of reaction ξ_I at a fixed value of λ. As we vary λ, however, we know that the stress varies non–uniformly and so we expect the curvature to vary non–uniformly as well. These two results are illustrated in Fig. 5.9. At any given extinction length, the curvature experienced by the beam increases with increasing surface extent of reaction ξ_I. For the largest extent of reaction, $\xi_I = 0.95$, and the material parameters chosen, the maximum curvature attained is small: $\mathscr{H} \approx 0.09$. However, we will see in Ch. 6 that even such tiny changes in surface curvature of a lens can result in significant lens-power corrections. For the beam, the curvature does not vary uniformly with extinction length: at small extinction lengths, the extent of reaction profile is essentially extinguished throughout most of the beam depth and macromer is only converted in a thin boundary layer near the top surface. As macromer redistributes, then, the constrained beam only experiences significant in–plane stresses at the top while the majority of the beam remains essentially stress free (see $\lambda = 0.1$, Fig. 5.3). The beam will only bend slightly to relieve these compressive stresses in the top since more bending induces stresses in the remainder of the stress–free beam. As the extinction length increases, however, the gradient in macromer extends deeper into the beam and more elements towards the back experience tensile stresses due to the redistribution. Bending therefore benefits elements at both the back and the front and the beam attains a maximum curvature at a particular value of the extinction length, $\lambda \approx 0.34$; this is near the value attained by Warner for liquid–crystal elastomers [8]. As the extinction length continues to increase, the extent of reaction profile becomes nearly uniform and gradients in macromer concentration become smaller and smaller. Thus, the generated stresses are smaller across the beam and a smaller curvature suffices to relieve them. In the limit of $\lambda \to \infty$, the beam is uniformly irradiated, there is no redistribution of macromer, and $\mathscr{H} \to 0$.

The behavior demonstrated in Fig. 5.9 illustrates a key concept: larger gradients in macromer volume fraction result in more redistribution, larger stresses, and therefore larger deformation. So far, we have discussed increasing gradients uniformly by increasing the magnitude of the extent of reaction (through the parameter ξ_I) or increasing gradients by allowing light to penetrate in such a way that the gradients are distributed (adjusting the parameter λ). From §5.2.2, we know that there is another way to increase the initial gradients: increasing the initial amount of macromer, ϕ_0. Increasing ϕ_0 has a significant effect on the curvature magnitude (Fig. 5.10). Therefore, we may create a desired curvature either by changing the reaction profile (magnitude ξ_I and extinction length λ) or by changing the initial amount of material, ϕ_0. The other two adjustable material parameters, M_m and G_{dry}, do not have a significant effect on the magnitude of the deformation experienced by the beam (Fig. 5.10). As previously discussed, the macromer molar mass then only serves to determine the time scale for diffusion–induced–deformation, whereas the material modulus serves to determine the magnitude of the internal forces experienced during the deformation.

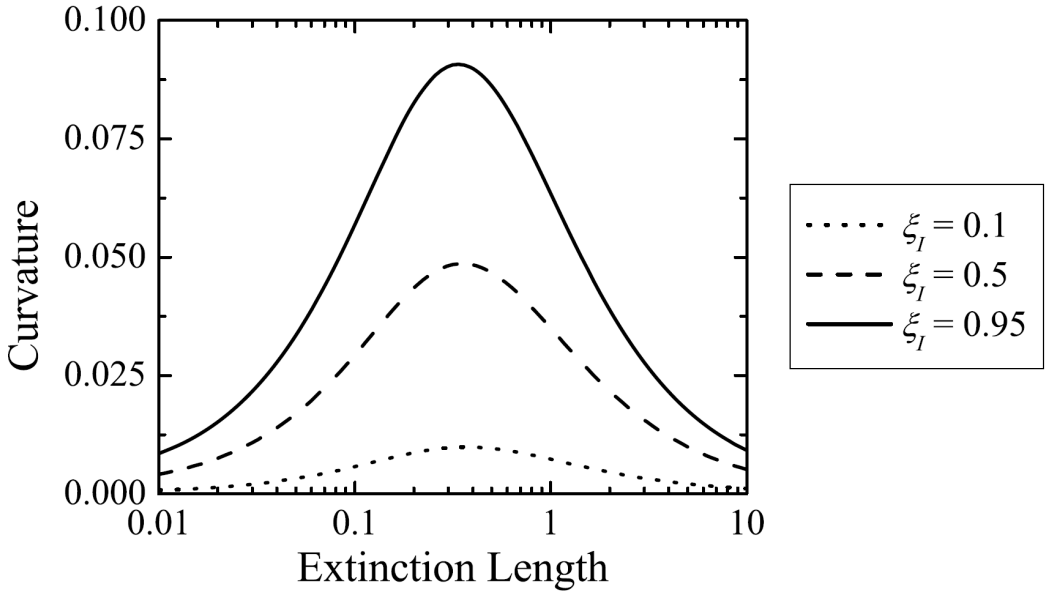

Figure 5.9: A beam of elastomeric photopolymer is exposed to a light source, causing an exponentially decaying extent of reaction profile through the beam. After material has redistributed, the developed stresses in the constrained beam are relieved by releasing the beam. The curvature attained by the beam as it relaxes is determined from the initial extent of reaction profile, characterized by the extent of reaction at the top surface nearest the light source (ξ_I) and extinction length. Because stronger amount of consumption (larger ξ_I) causes larger stresses in the system (Fig. 5.3), the attained curvature is larger ξ_I. Material parameters: $\phi_0 = 0.2$, $M_m = 1000$ g/mol, $G_{dry} = 0.18$ MPa.

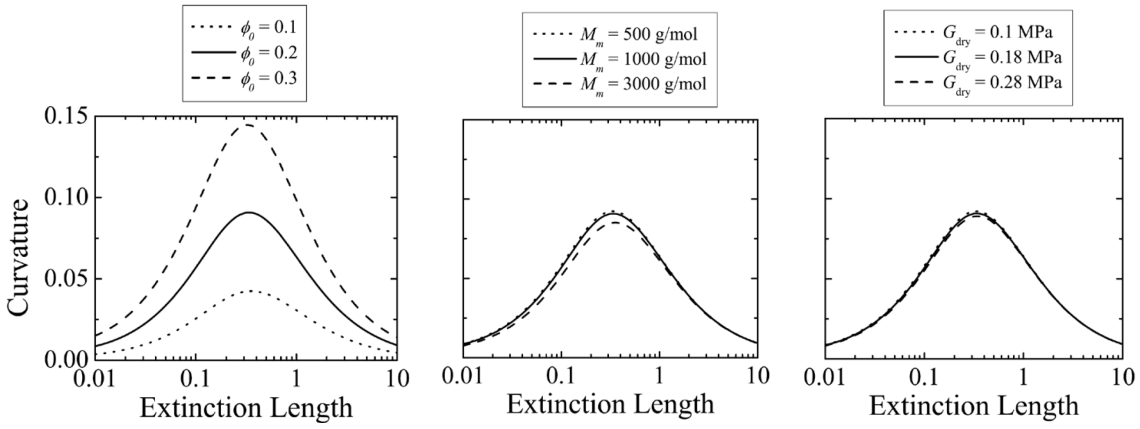

Figure 5.10: Curvature attained by the beam as a function of material parameters. The solid curve is the same between the three boxes and represents the default parameter set $\phi_0 = 0.2$, $M_m = 1000$ g/mol, and $G_{\text{dry}} = 0.18$ MPa. The first box illustrates variations due to ϕ_0 with M_m and G_{dry} held at the default values. The second box illustrates variations due to M_m (ϕ_0 and G_{dry} at default), while the third represents variations due to G_{dry} (ϕ_0 and M_m at default). Reaction profile: $\xi_I = 0.95$, $\lambda = 0.5$.

5.4 Conclusion

In this chapter, we considered the stresses and strains experienced in a beam of elastomeric photopolymer exposed to a spatially decaying extent of reaction profile. To make the problem one–dimensional, we initially constrained the beam to a substrate; this allowed us to theoretically determine the stresses and strains experienced locally due to redistribution of macromer. For an exponentially decaying extent of reaction profile—corresponding to the decay of a light profile through a scattering medium—we determined that the side of the beam exposed to the light source (the front) gained macromer volume from the back and therefore experienced compressive stresses due to the constraint. Likewise, the back lost macromer volume to the front and therefore experienced tensile stresses.

These stresses were then relieved by allowing the beam to bend to a curvature $\mathscr{H}$. We determined that the beam curvature depended strongly upon the magnitude of the initial chemical potential gradients through the beam. Three key parameters were found to contribute to the chemical potential gradients: the extent of reaction near the light source, the extinction length, and the initial volume fraction of macromer. Increasing the extent of reaction near the light source uniformly increases all gradients in the beam, resulting in increased curvature. A similar effect was found by changing the initial volume fraction of macromer, and the amount of macromer available can be considered to be the lever arm for the diffusion–deformation process. Both of these results were found to be in keeping with those seen in Ch. 4: the more material reacted, the larger the deformation.

In this chapter, the introduction of the extinction length allowed determination of the effects of reaction profile shape on deformation. For small extinction lengths, reaction only occurs in a thin region near the light source, developing significant stresses only in the top region. Because the majority of the beam does not experience any stress, the beam does not significantly curve. Allowing the light to penetrate deeper, however, provides a stronger driving force for the beam to curve. We determined that the maximum curvature experienced by the beam was for $\lambda \approx 0.34$, indicating that the extent of reaction profile decayed to $\approx 37\%$ about a third of the way into the beam. As the extinction length increases beyond this point, the macromer profiles after reaction become more and more uniform, less macromer is transferred, and the curvature decreases. Qualitatively similar behavior was observed in a theoretical model on the photo–induced beam bending of nematic elastomers developed by Warner and co–workers [8]: the curvature of the nematic elastomer beam was predicted to be small when the light was not allowed to penetrate deep, went through a maximum curvature at an extinction length of $\lambda \approx 0.37$, and then decayed to zero as the extinction length continued to increase.

Finally, we determined the importance of the other adjustable material parameters: the macromer chain length and the initial network modulus. Together, these two parameters set a limit on the

amount of macromer that can initially be swollen into the network through the Flory–Rehner equation (2.2.23). Other than this limit, however, neither was found to have a significant effect on the final curvature attained by the beam. However, we determined that the dry network modulus sets a magnitude for the dimensional stresses experienced by the beam during redistribution: a stiffer network exposed to the same internal diffusive strain will experience a stronger internal force. The network modulus can therefore be tuned appropriately for applications in which the deformation is used to perform work. The macromer molar mass, on the other hand, is the only material parameter which determines the rate at which the deformation occurs; specifically, the macromer chain length determines the diffusivity (Ch. 3) which sets the time scale for diffusion–deformation. This will be demonstrated in the next chapter on a system that has a physical length scale: the light–adjustable lens. In that chapter, we will also use what we have learned from a one–dimensional extent of reaction profile to analyze profiles in two or more dimensions.

Chapter 6

Light–Adjustable Lens

6.1 Introduction

In the last two chapters, we have seen application of the theory developed in Ch. 2 and Ch. 3 to "toy problems." These results showed that the magnitude of the initial chemical potential gradients—specified by the initial amount of macromer and the reaction profile—determines the magnitude of the final deformation. Other parameters—specifically the network modulus and macromer chain length—set limits on thermodynamically admissible values of the initial macromer volume fraction, but do not contribute significantly to the final deformation. Because these two variables do not affect the final deformation, we observed in Ch. 5 that each can be independently tuned for a secondary purpose: for example, the dry network modulus, G_{dry}, determines the magnitude of the stresses generated following photopolymerization of macromer. This design parameter (G_{dry}) could then be tuned to yield a desired force in applications in which an elastomeric photopolymer is required to do work. The molar mass of macromer determines the diffusivity of macromer (§B.4), which governs the time scale for the diffusion–deformation process. We are now in a position to apply the model to the case of a sample that has specific physical dimensions and for which we can compare experimental results.

The system we choose to study is the light–adjustable lens mentioned in Ch. 1 as a novel biomedical implant developed for cataract surgery patients. The lens is made of silicone and swollen with macromer of molar mass M_m to initial volume fraction of macromer ϕ_0. To protect the retina from the UV radiation from sunlight and used during treatment, a certain amount of UV–blocker is included in the lens along with the macromer and photoinitiator [26]. We parameterize the concentration of scattering agents through the extinction length λ (as in Ch. 5). There are two main regions for the lens (Fig. 6.1) [4,27]: the optical portion of the lens capped on the top and bottom by spherical surfaces, and a cylindrical "square–edge" region outside of the optical region. The square–edge design minimizes posterior capsule opacification observed after cataract surgery [85, 86];[1] it

[1] Posterior capsule opacification is a complication after cataract surgery in which native epithelial cells diffuse

Parameter	Symbol	mm
Total diameter	d	6.00
Interior square–edge lens diameter	d_{se}	5.42
Anterior radius of curvature	R_a	9.37
Posterior radius of curvature	R_p	9.37
Lens thickness	h_{max}	1.20
Square–edge thickness	h_{min}	0.40

Parameters taken from [27]

Table 6.1: Geometric parameters for the light–adjustable lens

is characterized by thickness h_{min} and total diamter d (we will discuss the diameter for the onset of the square–edge, d_{se}, momentarily). The interior of the lens is characterized by three variables. Two of these variables are the radii of curvature associated with the spherical caps: the radius of curvature of the anterior surface is denoted R_a and the posterior radius of curvature is denoted R_p . Although clinical lenses can be created with different values of R_a and R_p [27], we choose $R_a = R_p$ for the initial shape. The final parameter is the internal thickness of the lens, denoted h_{max} . From geometry, we can determine the value of the interior square–edge lens diameter d_{se}:

$$\left(\frac{d_{se}}{2}\right)^2 + \left[R_a - \frac{1}{2}\left(h_{max} - h_{min}\right)\right]^2 = R_a^2. \tag{6.1.1}$$

Physical values chosen for these variables are taken from [27] and shown in Table 6.1. We discuss meshing of this lens object in an Appendix (§C.1). We have meshed the program using MATLAB such that the mesh is more refined through the depth than in the radial direction. The reason for this will be discussed in §6.2.5.

Because we treat reaction as instantaneous (§2.3), the effect of the light intensity profile $I(\boldsymbol{X}, t)$ during irradiation of the lens is incorporated through the extent of reaction profile $\xi(\boldsymbol{X})$ in the model. Sample clinical irradiation profiles taken from [21] are converted directly into extent of reaction profiles via a one–to–one relationship. Specification of the extent of reaction generates a volume fraction profile within the lens that serves as the initial condition. Using the equations of conservation of mass and momentum developed from mixture theory (Ch. 3), we solve for the transient volume fraction profile and deformation.

For computational purposes, we discretize the governing system of equations in §6.2 in the spirit of hybrid particle–finite element approaches [87–90] introduced to us by Robin Selinger and Charles Gartland at Kent State University. Unlike traditional finite element methods, which require construction of global matrices and subsequent solution of matrix equations, this method solves the governing equations node–by–node and element–by–element. Although either method would suffice

behind and grow on the back of the lens, creating a cloudy layer behind the now clear lens. This is sometimes referred to as a "second cataract."

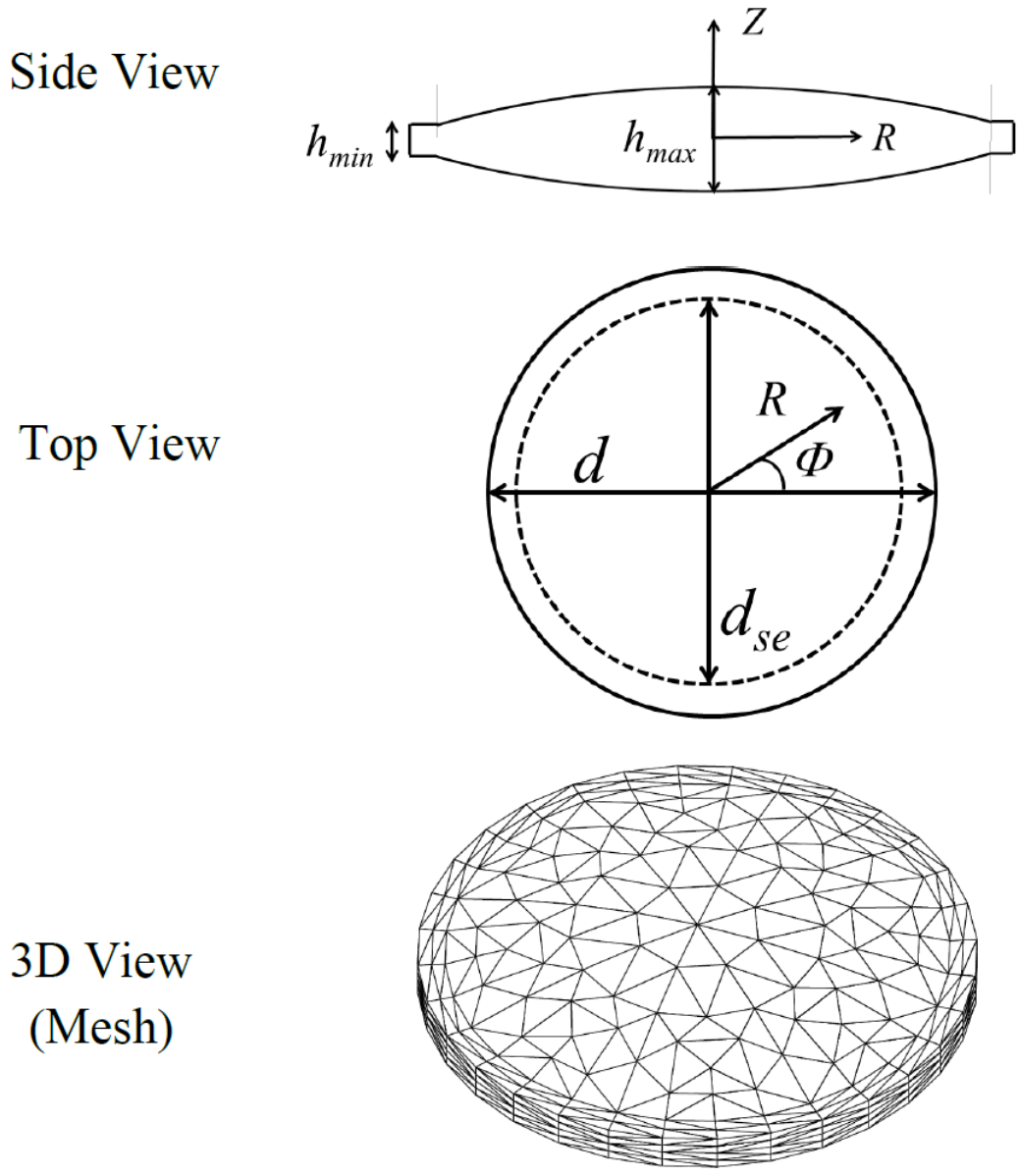

Figure 6.1: The geometry of the light–adjustable lens. Because of the symmetry of the lens in the XY–plane, we may use cylindrical coordinates in the reference $\boldsymbol{X} = (R, \Phi, Z)$. The 3D mesh has 1305 nodes and 6016 four-node tetrahedral elements.

for our problem, the force–free, constraint–free, light–adjustable lens[2] lends itself better to the second approach for the following reason: a traditional finite element approach uses the boundary conditions to maintain the solution translationally and rotationally invariant [91]. This is done by assuring that external deformation is imposed upon a portion of the boundary, reducing the degrees of freedom in the matrix equations and allowing solution. The node–by–node approach, on the other hand, treats each node in a discretized mesh as a particle upon which forces act [87]. The deformation of the object is then found by moving these nodes through integration of Newton's law (the velocity Verlet algorithm) analogous to a molecular dynamics simulation [92]. In this method, the system obeys Newton's third law and all forces are equally and oppositely balanced between the nodes.[3] Therefore, the total force on the system is simply the sum of the forces on the boundary; a system that experiences no forces on the boundary, such as the light–adjustable lens, then automatically experiences no net forces or torques. For this reason, the light–adjustable lens can be made to be rotationally and translationally invariant through a node–by–node approach without the need to imply aphysical boundary conditions constraining the movement of nodes, as would be required by a traditional approach.

Like the present case, Selinger's work on the deformation of liquid crystal elastomers also involves the use of a quasi–static assumption [87]. Relaxation of the local director field is assumed to proceed faster than the time scale for global deformation: the director is in quasi-static equilibrium with the elastic strain at each point in time. Computationally, this is modeled through two different time scale processes. In real time, the elastic strain is developed forward using the velocity Verlet algorithm based upon the evaluated forces at nodes. After each deformation time step, the director is allowed to instantly relax to the nearest stable energetic state before the next strain step. We may make good use of a similar approximation when modeling elastomeric photopolymers [72]. Because relaxation of polymer chains occurs on a much faster time scale than that of diffusion, the diffusion step is rate limiting. We can then treat the deformation as in quasi–static equilibrium with the diffusion process. In this way, the strain field is the slave to the diffusion field and chains relax as fast as molecular diffusion occurs. This same approximation was made by Hong et al. in modeling the diffusion–deformation of rubbery polymer gels [72].

The solution method then proceeds as follows. Starting from the initial condition (set by the extent of reaction profile above), the nodal volume fractions and chemical potentials are used to compute the macromer flux and update the nodal volume fractions (a "diffusion step" in real time). The resulting forces (voilations of the incompressibility condition) are then allowed to relax by adjustment of the nodal positions (an instantaneous "deformation step") without changing the

[2]In vivo, the lens rests in the lens cavity surrounded by inert, viscous aqueous humor. Although there is a force experienced by the haptics to maintain the lens in place, this force is small and acts on a small area. In vitro, experiments can be designed to mimic this by allowing the lens to rest on the surface of a viscous fluid. In this way, deformation can proceed without the influence of external forces or other boundary effects.

[3]This only holds true when the system free energy itself is rotationally and translationally invariant.

volume fraction of macromer. This process is then repeated until equilibrium is achieved. We begin with a brief description of this methodology in §6.2 (details in Appendix C) and then move on to solve a couple of illustrative problems.

6.2 Computational Methodology

6.2.1 Meshing

We begin by discretizing our lens into a finite element mesh and specifying the interpolation in each element. We chose the lowest level of approximation: a mesh of four–noded tetrahedral elements having piecewise constant deformation fields and fluxes. In this chapter, we will consider only axisymmetric lens adjustments, leaving correction of higher-order abberations for future work. Keeping in mind the results of the previous chapters, it is the gradient through the depth due to attenuation of light that causes the steepest gradients in chemical potential for most cases. For these reasons, the mesh size only needs to be moderately fine in the radial direction of the lens relative to the depth. Therefore, our mesh is more refined in the depth–direction (see Appendix C, Fig. C.1) than that of Pandolfi and Ortiz [27].

6.2.2 Initialization

The solution method proceeds as follows. At $t = 0$, we specify the extent of reaction profile $\xi(\boldsymbol{X})$. This profile allows calculation of the initial values of the volume fraction of macromer $\phi(\boldsymbol{X}, t = 0) = \phi_0(1-\xi(\boldsymbol{X}))$, and the conversion parameter, $\theta^*(\boldsymbol{X}) = 1-(1-\xi(\boldsymbol{X}))\phi_0$ at each nodal point from the reference position of that node. Specification of these scalar fields allows calculation of $\mu(\boldsymbol{X})$ from (2.3.18). The imposed profile therefore acts as an initial condition, creating gradients in chemical potential. These gradients drive the diffusion-based shape change.

6.2.3 Diffusion Step

From Ch. 3, the equation for conservation of mass of macromer is (3.3.3):

$$\frac{D\rho_m}{Dt} + \nabla \cdot \mathbf{J}_m = 0 \tag{6.2.1}$$

where ρ_m is the density of macromer, t is time, and $\mathbf{J}_m = \rho_m(\mathbf{v}_m - \mathbf{v})$ is the flux of macromer.[4] In keeping with the scaling analysis performed in Appendix B, the velocity is negligible for a generic

[4] As discussed in Ch. 3, we have set the reaction term to zero because reaction occurs significantly faster than diffusion and we model the reaction as instantaneous at $t = 0$.

time step. Placing this simplification into the above equation yields

$$\frac{\partial \rho_m}{\partial t} = -\nabla \cdot \mathbf{J}_m. \tag{6.2.2}$$

The flux is modeled as a gradient in chemical potential (4.3.24):

$$\mathbf{J}_m = -\rho \mathcal{D} \phi \nabla \mu \tag{6.2.3}$$

with $\mathcal{D}$ being the diffusivity of macromer. For a given macromer, prior research shows $\mathcal{D}$ is insensitive to ϕ over the range from $\phi = 0.1$ to 0.3 (Appendix B.4). Therefore, $\mathcal{D}$ is treated as a uniform material parameter, determined from the molar mass of macromer (Table B.3). Recall from Ch. 4 that this definition for the flux ignores anisotropic deformation contributions because these contributions are small for the deformations experienced in practice. The flux $\mathbf{J}$ is piece-wise constant and is calculated in each tetrahedron through interpolation and the chemical potential at each node. Once all the fluxes are determined, the code can proceed tetrahedron by tetrahedron, evaluating the change in volume fraction for each node as well as the volume of that element. The sums are calculated for node a by adding the contributions from each tetrahedron to which a belongs, information kept in the connectivity of the mesh. To guarantee computation proceeds correctly, we check the total change in volume fraction summed over all nodes for a single tetrahedron: this number should be zero for a single time step, as macromer must be transferred between nodes and cannot be created or destroyed.

Once the diffusion step has updated the values of the volume fraction, the average volume fraction is found in each tetrahedron. These volume-averaged values are used in calculating the system energy and forces which must be relaxed in the second computational step: the deformation step.

6.2.4 Deformation Step

After a small amount of material has been transferred between nearby elements in a diffusion step, some elements will have more material than they began with and some elements will have less. This leads to an aphysical situation: since the nodal positions have not yet moved, the incompressible constraint (2.3.10) is not satisfied. These deviations in density are relaxed by displacing the nodes to reduce a penalty assessed for density deviations. The penalty plays the role of free energy, leading to a psuedo–force on the nodes. To determine the new shape of the lens, these "forces" can be relaxed, moving the nodal points in keeping with the forces so that elements that have gained material increase in volume, whereas elements that have lost shrink. The numerical equivalent of this involves determination of the forces acting on each node in an element and then summing those contributions from all elements to which a given node is attached. We then treat the nodes as

	Length Scale (mm)	**Time (dim'less)**	**Real Time, M_m =**		
			500 g/mol	1000 g/mol	3000 g/mol
h_{mesh}	0.1	1.1×10^{-3}	1.8 min	3.3 min	13 min
h_{max}	1.2	0.16	4.3 hr	7.9 hr	31 hr
$d/2$	3.0	1.0	1.1 days	2.1 days	8.0 days

Table 6.2: The time scales associated with each of the important spatial dimensions for the light–adjustable lens. The real-time values were obtained from diffusivities in [1] modified according to §B.4.

particles in an overdamped molecular dynamic simulation and calculate the displacement of the nodes under the given forces via a velocity Verlet algorithm. As previously mentioned, for the small, elastic deformations considered here, the system is assumed to relax instantaneously at each time step without a corresponding change in the volume fraction.

6.2.5 Separation of Time Scales

The computational procedure at any given time step proceeds by performing a diffusion step followed by relaxation to ensure the shape is in quasi–static equilibrium with the diffusion at that time. At small times, the chemical potential gradients are steep in the z–direction due to attenuation of light. As time progresses, these gradients essentially flatten out on a time scale t_h corresponding to h_{max}, the maximum thickness of the lens:

$$t_h = h_{max}^2/\mathcal{D}. \tag{6.2.4}$$

After this time, the remaining chemical potential gradients are mild variations in the r–direction. These relax on a secondary time scale t_d corresponding to $d/2$, the lens radius:

$$t_d = \frac{d^2}{4\mathcal{D}}. \tag{6.2.5}$$

Table 6.2 illustrates the dimensionless computational time scales (non–dimensionalized by τ based on $d/2$, see §C.3.2) corresponding to each of the important system length scales along with an approximate real-time scale for each macromer molar mass. We will use $\mathscr{T}$ to differentiate dimensionless time from real time t in this chapter. Shorter macromer chains diffuse faster; because deformation is in quasi–static equilibrium with diffusion, deformation also proceeds faster with shorter macromer chains.

The two time scales, t_h and t_d, split the system behavior into two time regimes. At short time, the mesh size and the steepness of the initial chemical potential gradients require the diffusion time step to be sufficiently small to ensure convergence [93]. We have optimized the dimensionless time step to be $\Delta\mathscr{T} = 4.0 \times 10^{-5}$ through trial and error; this is roughly 25 times smaller than the time scale associated with the smallest distance between points in the mesh (h_{mesh}). Such a

	Gradients In:	**Time Range (dim'less)**	$\Delta\mathscr{T}$ **(dim'less)**	**Mesh Used**	
				Diffusion	**Deformation**
Short time	z	0 – 0.16	4.0×10^{-5}	Refined	Refined
Long time	r	0.16 – 1.0	1.0×10^{-3}	Coarse	Refined

Table 6.3: A summary of the computational parameters corresponding to the splitting of time regimes between short and long time

small time step is appropriate to capture the steep-gradient, short-time behavior of the deforming lens. During the long–time final relaxation of the remaining r gradients, however, this time step is unnecessary and computationally wasteful. For this reason, we make use of a coarser mesh (Fig. C.2) at long time, amalgamating tetrahedra and averaging the volume fractions inside. This allows for a longer diffusion step at long times: the optimal value was determined through trial and error to be $\Delta\mathscr{T} = 1.0 \times 10^{-3}$. In order to maintain accuracy of the geometry, however, all refined nodal points are still used during the corresponding relaxation step. Table 6.3 summarizes the differences between the short and long time computational parameters.

6.3 Characterizing Deformation

At any point in time, the nodal positions will have moved due to diffusion–deformation. These shifts, however, are exceedingly small and it is difficult to perceive the changes by visualizing the mesh in time. To illustrate this, consider a lens which is irradiated with light in a central zone of diameter d_i (Fig. 6.2a). Subsequently, the irradiated zone expands as free macromer diffuses into that region, causing the irradiated surface to bulge outwards and decreasing the radius of curvature within that zone (exaggerated in Fig. 6.2b). Simultaneously, the region outside the irradiated zone loses volume and the surface flattens slightly. As an illustration of how small the displacements are, we illustrate the surface mesh points before reaction and at diffusive equilibrium for a large positive adjustment (2 diopters, Fig. 6.2c). The shifts in nodal positions are nearly indistinguishable from the original mesh points: the displacements are on the order of several microns. In fact, a Fitzeau interferometer is needed to measure these micron deviations [21]. For this reason, we use an alternate method to characterize the lens shape in time: the change in lens power.

The lens power is determined by one material property (the difference in refractive index between the lens and the aqueous humor that surrounds it, $n_L - n_A$), the radius of curvature of the anterior surface, the radius of curvature of the posterior surface, and the thickness of the lens (R_a, R_p, and h_{max}, respectively). For simplicity, we consider the case in which the repeat units of the macromer are the same as those of the matrix chains (a good approximation for the material currently in clinical use); thus $n_L - n_A$ can be treated as a uniform constant. During the diffusion–induced deformation process, $R_a(t)$, $R_p(t)$, and $h_{max}(t)$ are computed from the position of the surface nodes

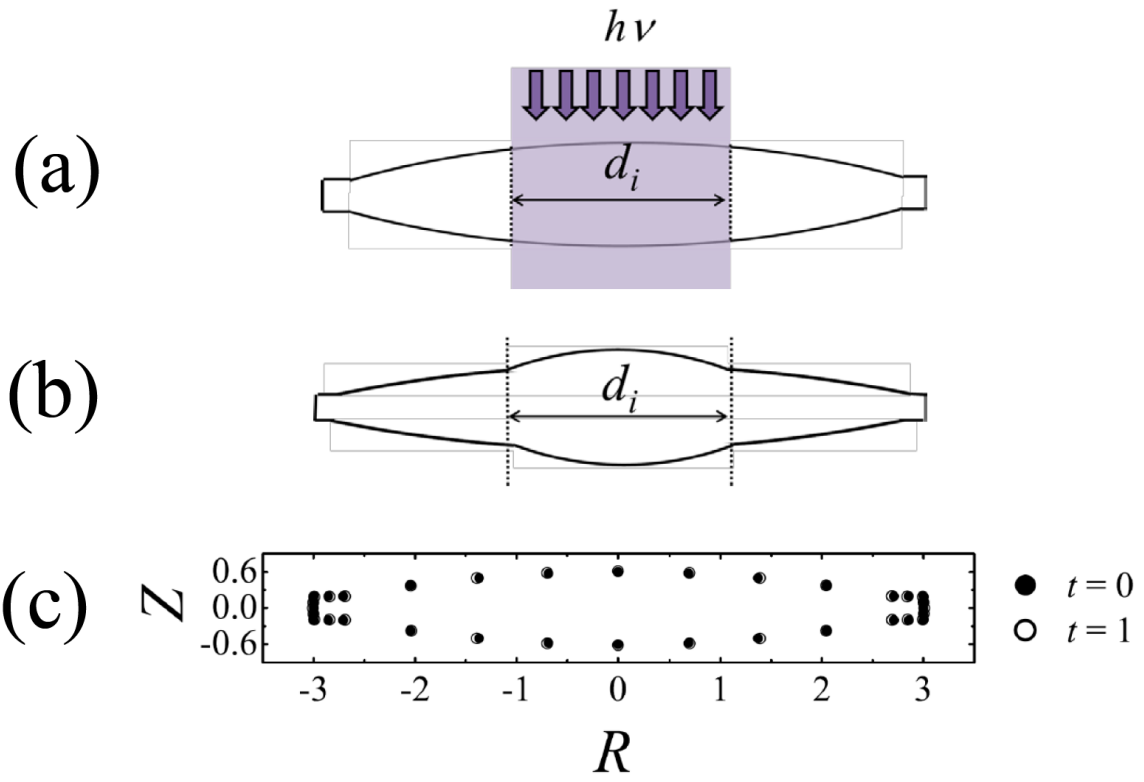

Figure 6.2: (a) A light–adjustable lens is exposed to uniform irradiation in a cylindrical zone of diameter d_i in the interior. Depletion of free macromer creates chemical potential gradients that drive a flux of macromer into the irradiated zone. (b) This causes the surface of the irradiated region to experience an increase in curvature; the unreacted zone simultaneously experiences a decrease in curvature. (c) Actual point movement from the initial shape (time, $\mathscr{T} = 0$) to the final shape ($\mathscr{T} = 1$) when the lens is uniformly reacted to an extent of reaction $\xi = 0.25$ within the interior zone $d_i \leq 3.0$. The displacement of points is on the order of microns yet the lens power change experienced is $\approx +2$ diopters.

at time t.

Because we are only considering spherical (axisymmetric) corrections here, the radius of curvature of a desired zone of the lens can be evaluated using least–squares fit of a spherical cap to the surface nodes in that lens zone. For example, Pandolfi and Ortiz evaluate the least–squares spherical curvature of the anterior and posterior surfaces using nearly all the surface points ($r \leq 2.0$ mm). However, it is insufficient to report a single curvature for a general lens surface. Even a simple axisymmetric extent of reaction profile will result in non–uniform spherical curvature: a lens surface that initially has uniform spherical curvature will experience stronger curvature in the region that has expanded and weaker curvature in the region that has contracted (Fig. 6.2b for example). Like Pandolfi and Ortiz, we measure the curvature over a given radial zone by least–squares fitting a spherical surface through multiple surface nodes [27]; however, we will evaluate the curvatures over multiple zones.

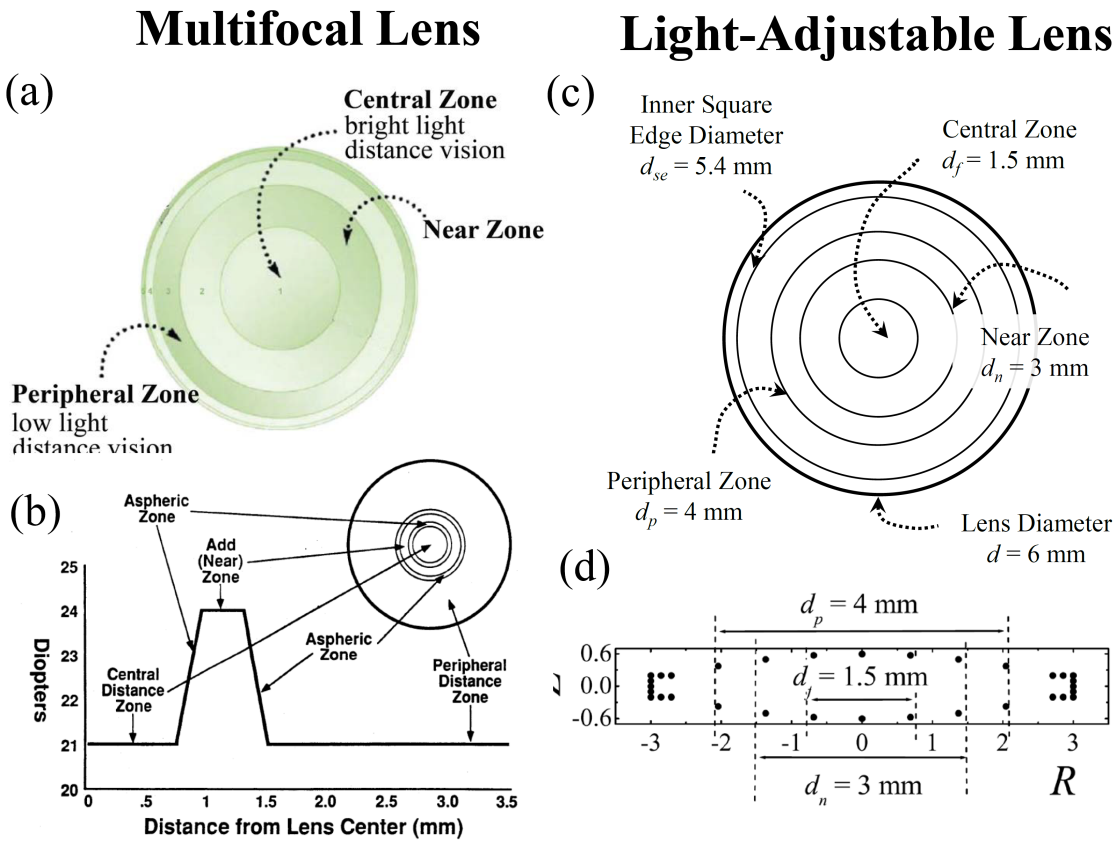

Figure 6.3: (a) The zones for the multifocal lens [5]. (b) The lens power is adjusted differently across the zones of the lens [94]. (c) Equivalent zones defined for the light–adjustable lens. (d) Illustration of the defined light–adjustable lens zones at cross–section $\Phi = 0$

For this reason, we turn to an analogy: multifocal intraocular lenses that are designed to improve both near and distance vision by varying lens power across the lens in concentric zones (Fig. 6.3). For example, the most central portion of the lens ($r \leq 0.75$ mm, Fig. 6.3b), is considered the "distance–dominant central zone for bright light situations, including day–time driving, when the pupils are constricted" (Fig. 6.3a). The design for the patented multifocal lens, illustrated in Fig. 6.3b, has lens power in the "central distance zone" of 21 diopters [94]. Just outside the central zone (0.75 mm $< r <$ 1.5 mm) is the "add (near) zone" adding an additional 3 diopters of lens power for near vision (Fig. 6.3b); the review article by Lane et al. characterize this region as "providing additional near vision in a broad range of moderate to low–light conditions" (Fig. 6.3a). Outside the "add zone" for the patented lens lies the peripheral distance zone, where the lens power is returned to the initial 21 diopters (Fig. 6.3b).

By analogy, we consider the central portion of our lens to most appropriately represent distance vision during bright lighting situations when the pupil is constricted. We denote the central "far" zone with interior diameter $d_f = 1.5$ mm (Fig. 6.3c). We consider the region just outside the central

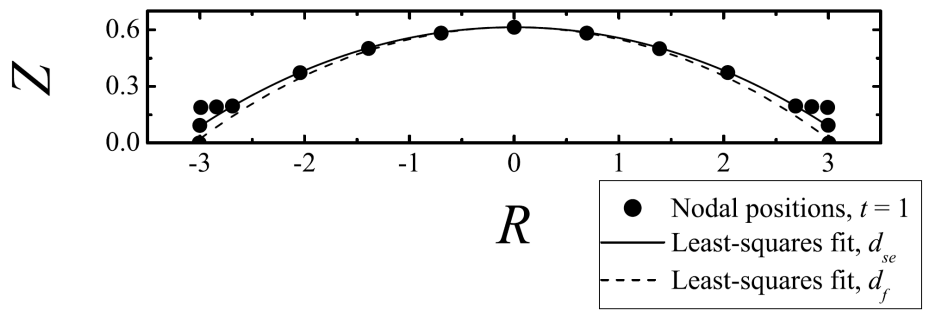

Figure 6.4: Anterior surface node positions ($\Phi = 0$) for the case of uniform irradiation ($\xi = 0.25$) inside the zone $d_i = 3$ mm at equilibrium ($\mathscr{T} = 1$). A radius of curvature $R_A = 8.83$ mm is obtained from a least–squares fit using all the spherical surface points within d_{se} (the solid curve). Fitting only the surface points within d_f yields a smaller radius of curvature ($R_A = 7.89$ mm).

zone (along with the interior central zone) to be the region of the lens primarily used for near vision and denote the corresponding diameter $d_n = 3$ mm [94]. Finally, we define the peripheral zone with $d_p = 4$, the maximum optical radius of the light–adjustable lens [27] (Fig. 6.3d).

An example of this method is illustrated by fitting the anterior radius of curvature to the equilibrium nodal positions in Fig. 6.2c (Figure 6.4). Although the points themselves have not moved significantly, the least–squares fitting radius of curvature depends on whether we use all the points on the surface (within d_{se}, $R_A = 8.83$ mm) or only the points within the central zone (d_f, $R_A = 7.89$ mm). As such, we choose to calcuate the surface curvature separately using the points within each of the three zones defined in (Fig. 6.3d).

For clinical purposes, the lens power is a more useful parameter to report than surface curvature. This can be estimated from the thick-lens equation [95] by calculating the thickness of the lens at any point in time, as well as the anterior and posterior radii of curvature:

$$P(t) = \frac{n_L - n_A}{R_a(t)} + \frac{n_L - n_A}{R_p(t)} - \frac{h_{max}(t)}{n_L}\frac{n_L - n_A}{R_a(t)}\frac{n_L - n_A}{R_p(t)}. \tag{6.3.6}$$

For a lens made of PDMS submersed in a lens cavity filled with aqueous humor, $n_L = 1.4289$ and $n_A = 1.336$ [27]. Using these values and the geometric values in Table 6.1, the initial lens has a power of $P_0 \equiv P(0) = 19.75$ diopters; we report change in lens power $\Delta P(t) = P(t) - P_0$ in diopters. Using the three curvatures calculated for each surface (anterior and posterior), we report three corresponding lens-power changes: ΔP_f, ΔP_n, and ΔP_p. Figure 6.5 summarizes these lens power changes and the zones they represent.

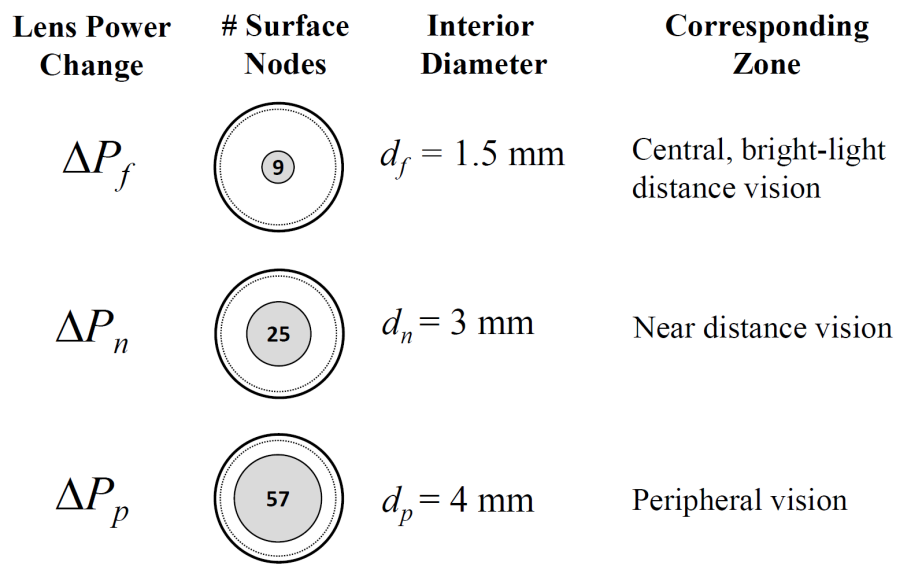

Figure 6.5: Illustration of the zones over which lens power is measured along with the corresponding relevance of that zone

6.4 Lens-Power Adjustments Using Radial Diffusion

To illustrate the mechanism for both positive and negative adjustments of lens power, it is useful to begin with a relatively simple irradiation profile: one that is uniform through the thickness and varies as a step–function in the radial direction (Fig. 6.6). Physically, this corresponds to a transparent lens that is made without any UV blocker. In addition, the concentration of photoinitiator in the lens is sufficiently low that very little attenuation occurs as light passes through the lens. Furthermore, we neglect defraction at the anterior surface because the curvature of the lens is relatively large and model the extent of reaction profile as one–to–one with an extent of reaction profile. As in the one–dimensional beam (Ch. 5), uniform irradiation of such a lens would not produce a gradient in macromer concentration (hence, no deformation). When the irradiation varies as a step–function in the r–direction (axisymmetric profile acting on an axisymmetric body), however, an axisymmetric shape change is induced.

An increase of lens power can be achieved under brief exposure to a "top hat profile" that produces a uniform conversion of macromer ξ_I in the central portion of the lens ($R < d_i/2$) and no reaction in the extremeties ($R > d_i/2$) (Internal, Fig. 6.6). For a given lens composition, the value of ξ_I is determined by the incident irradiance and the irradiation time [1]. In a lens that is initially symmetric about $Z = 0$, the shape retains that symmetry in the absence of UV blocker. As macromer diffuses inward from $r > d_i/2$, the central zone ultimately bulges outward and both the anterior and posterior surfaces become more strongly curved (increasing the lens power, see Fig. 6.2b for an illustration). Clinically, this represents a positive adjustment that corrects hyperopia. We examine

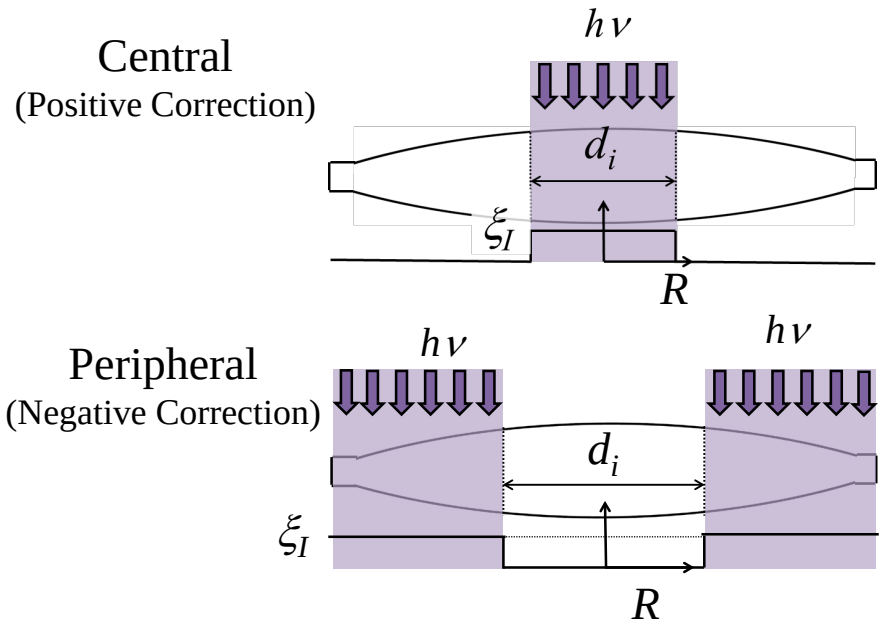

Figure 6.6: Uniform irradiation within a central zone (internal, characterized by ξ_I and d_i) causes a net transfer of material into the center and therefore a positive lens-power adjustment. Irradiation outside of a central zone (external, characterized by ξ_I and d_i) causes material to leave the center and will yield an opposite, negative lens-power adjustment.

in §6.4.1 the transient development of this lens-power correction and show three important features: 1) the transient can be nonmonotonic, 2) the transient response spans from rapid changes when the concentration gradient is steep to terminal relaxation of gradients that span the entire radius of the lens, and 3) extremely precise control of deformation is required to achieve lens adjustments. In §6.4.2, we show that the magnitude of the change in lens power is determined by the amount of macromer consumed during irradiation (and is not sensitive to macromer molar mass or lens shear modulus). Finally, we consider he differences in refractive correction as a function of the state of pupil dilation and how it is affected by the choice of irradiation diameter, d_i. All of the features noted for positive changes are shown in §6.4.4) to also hold for negative adjustments (myopic corrections) produced by irradiating the periphery of the lens to achieve a uniform conversion of macromer xi_I in the extremeties ($R > d_i/2$) and no reaction in the interior ($R < d_i/2$) (External, Fig. 6.6).

6.4.1 Transient Response after Conversion of Macromer

To illustrate the response to photopolymerization of some of the macromer in the central zone of the lens, we consider the case of a lens initially containing 20% macromer ($\phi_0 = 0.2$) distributed uniformly. We then irradiate the central 3- mm-diameter zone with a dose of light that converts one fourth of the macromer to network ($\xi_I = 0.25$) and examine the lens power relevant to intermediate

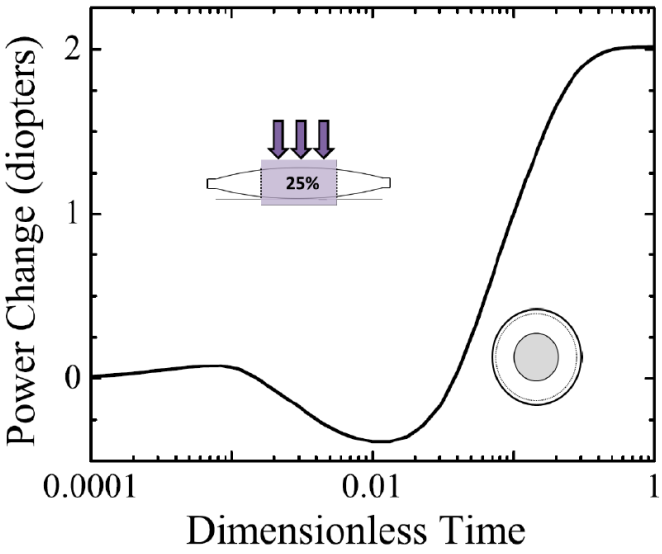

Figure 6.7: The lens power change (ΔP_n, $d_n = 3$ mm) as a function of dimensionless time (log scale) for the extent of reaction profile with $d_i = 3.0$ mm and $\xi_I = 0.25$. The icon illustrating an irradiated cross–section through the lens thickness indicates the extent of reaction profile. The bird's-eye-view icon indicates the region of the surface in which the lens power is calculated using a least–squares fit to the posterior and anterior curvature in that region. Material parameters: $\phi_0 = 0.2$, $M_m = 1000$ g/mol, and $G_{\text{dry}} = 0.18$ MPa.

pupil diameters ($d_n = 3$ mm). Ultimately, the lens power increases by 2 diopters (Figure 6.7). This is significant: after cataract surgery, 98% of patients have refractive errors of 2 diopters or less [4]. Thus, this example provides a relatively large correction relative to patient needs. This relatively large correction is achieved through redistribution of a small fraction of the lens material: just 5% of the material in the central zone and less than 2% of the entire lens material. Because time is made dimensionless using the longest diffusion time in the problem ($\tau = t_d$, (6.2.5)), the lens power approaches its new equilibrium value at dimensionless time of one. For the macromer used in this example ($M_m = 1000$ g/mol with $\mathcal{D} = 50.4 \times 10^{-12}$ m^2/s, §B.4), $\mathscr{T} = 1$ corresponds to approximately 48 hours, in agreement with clinical observations [4]. The transient response can be viewed in terms of three regimes (Table 6.4): 1) a short-time response during which the lens power reaches a minimum, 2) a strong increase in lens power, and 3) a slow approach to the final equilibrium value. Clinically, the irradiation time is approximately 100 s ($\mathscr{T} \approx 5 \times 10^{-4}$ in the present example); note that very little diffusion occurs in that time, validating the "instantaneous reaction" approximation. During the major response ($0.02 < \mathscr{T} < 0.2$), the lens power increases as expected for a reaction profile that depletes macromer in the central zone.

The initial time response is more complicated. Due to the step change in concentration created by the "top hat" irradiation profile, there are steep gradients in chemical potential between elements just inside $r < d_i/2$ and those just outside. At short time, there is a diffusive boundary layer near

Time Regime	Dimensionless Time	Real Time*
Initial Response	< 0.02	< 1 hr
Major Response	$0.02 - 0.2$	1 hr – 10 hrs
Final Equilibrium	1	≈ 2 days

* Obtained for $M_m = 1000$ g/mol, with diffusivity $\mathcal{D} = 50.4 \times 10^{-12}\text{m}^2/\text{s}$

Table 6.4: The real times associated with the characteristic dimensionless time regimes observed in Fig. 6.7

$r = 1.5$ mm whose thickness grows as $\sqrt{\mathscr{T}}$, causing stresses to build up locally. The increase in volume of elements immediately inside the boundary layer is mainly accommodated by radial elongation (Figure 6.8, right, A and B, red shift inside the second concentric ring), relieving some of the stress created by the decrease in elemental volume immediately outside the boundary layer (Figure 6.8, right, A and B, blue shift in the third concentric ring). During this time, the lens has not deformed significantly in the axial direction (Figure 6.8, left, A and B); hence, the initial flattening of the central zone (decrease in lens power up to $\mathscr{T} = 0.01$). At longer time ($\mathscr{T} \geq 0.16$, C and D), the radial displacements stabilize and the axial displacements dominate: the surface inside the irradiated zone (the first and second concentric rings) bulge upward (red shift) while the unirradiated zones (third and fourth concentric rings) contract inward (blue shift). This yields a net positive power change at long time.

The fact that large power changes (2 diopters) correspond to small deformation (20 microns) obtained by consumption of a small amount of macromer (2%) is one of the defining features of the light–adjustable lens (Ch. 1). In general, required clinical corrections can be as small as 0.25 diopters [4], corresponding to deformations on the order of a few microns. This is an extremely precise correction for a system that is ≈ 1 mm thick and several millimeters in diameter. The precise control required for clinical adjustments can be attained by the construction of an intraocular lens with elastomeric photopolymers coupled with the theory developed here. The rest of this section demonstrates the precise degree of control attainable through theory by adjusting the material and irradiation parameters.

6.4.2 Macromer Consumption Controls Adjustment Magnitude

In accord with the behavior of the one–dimensional beam (Ch. 5), the deformation of the lens is determined solely by the amount of macromer consumed: the macromer molar mass and initial network shear modulus had little effect over the range of clinically relevant parameters (Figure 6.10), illustrating that lens power changes negligibly as a function of both (a) the macromer molar mass and (b) the network shear modulus for the range of clnically relevant parameters. Although these two parameters do not affect lens deformation, the macromer molar mass and dry network modulus do serve to determine thermodynamically admissable limits on the initial amount of macromer that

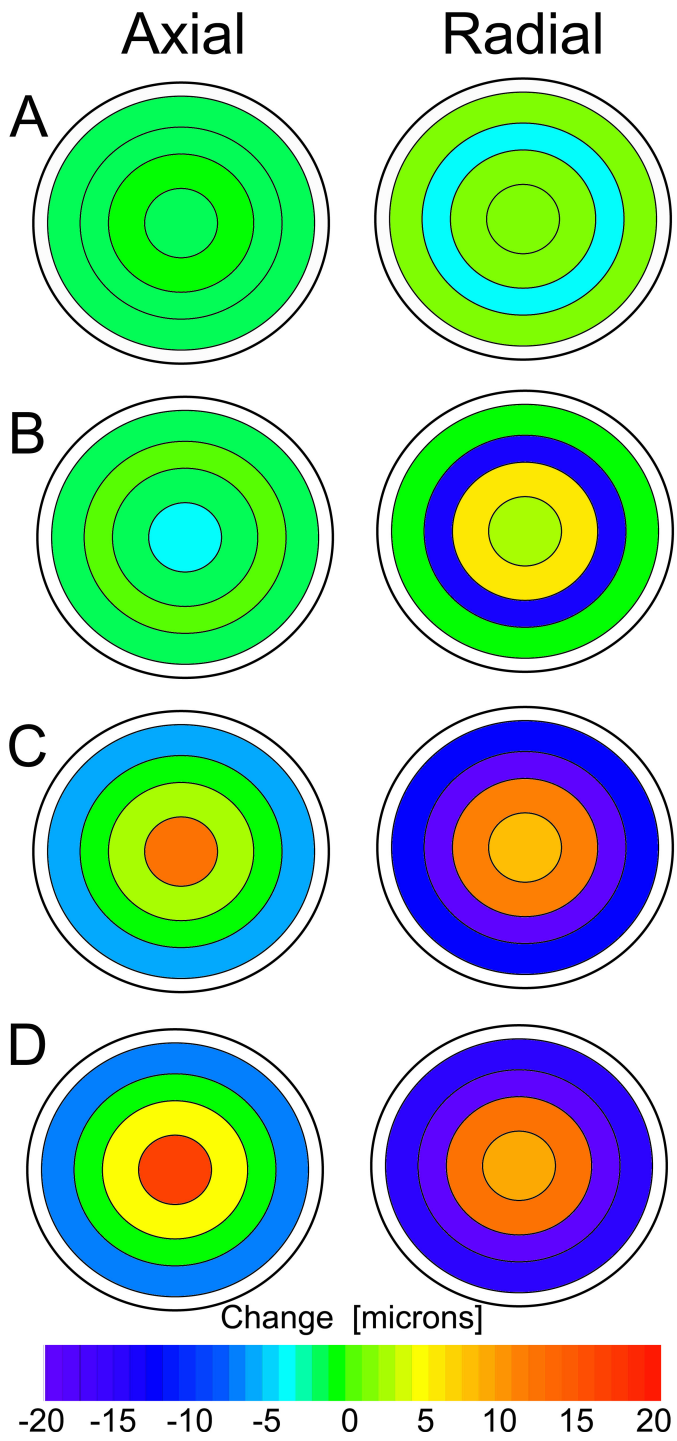

Figure 6.8: The axial (left) and radial (right) displacement (in microns) of surface nodes under the conditions shown in Fig. 6.7 at four different times: (A) $\mathscr{T} = 0.001$, (B) $\mathscr{T} = 0.01$, (C) $\mathscr{T} = 0.16$, and (D) $\mathscr{T} = 1.0$. Because of front/back symmetry, the axial displacment presented is the change in lens thickness and the radial displacement is the same for both the anterior and posterior surface. The four concentric rings are related to the four lens zones (Fig. 6.5): irradiation occurs within the first two concentric rings ($d_i = 3.0$ mm). A red shift indicates elements expanding and a blue shift indicates elements shrinking.

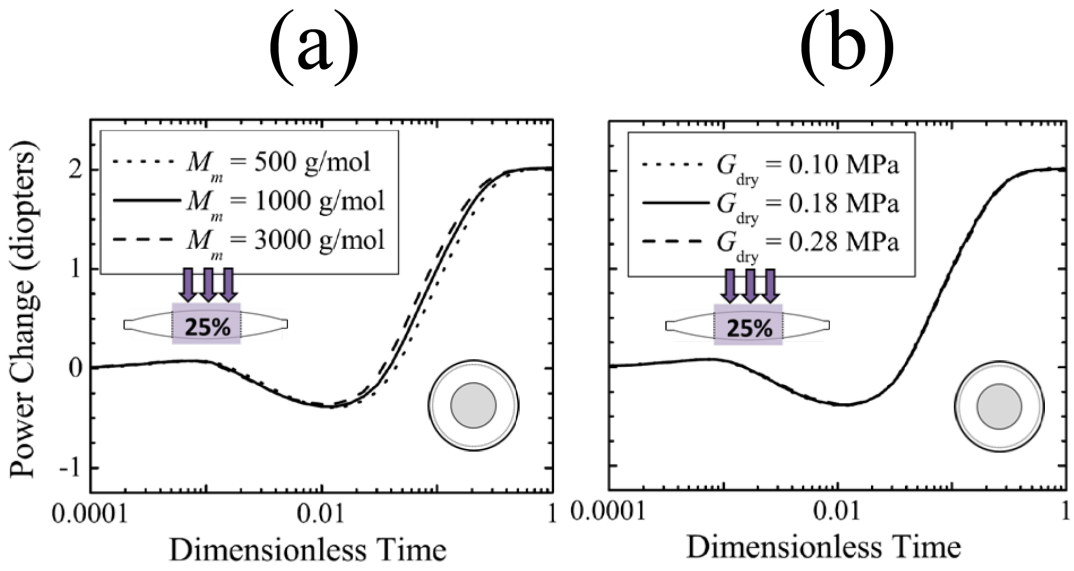

Figure 6.9: The effect of material parameters of the lens-power change for a sample positive correction. (a) Lens-power changes as a function of M_m, $\phi_0 = 0.2$, and $G_{\rm dry} = 0.18$ MPa. (b) Lens-power changes as a function of $G_{\rm dry}$, $\phi_0 = 0.2$, and $M_m = 1000$ g/mol. The solid curve is the same between the two boxes. All results are for a uniform 25% consumption inside the interior diameter $d_i = 3.0$ mm (annotated in the icon of the cross–section through the lens depth). We show the near zone lens-power change (ΔP_n) corresponding to least–squares fitting the surface nodes within the same region ($d_n = 3$ mm, illustrated in the bird's-eye-view icon).

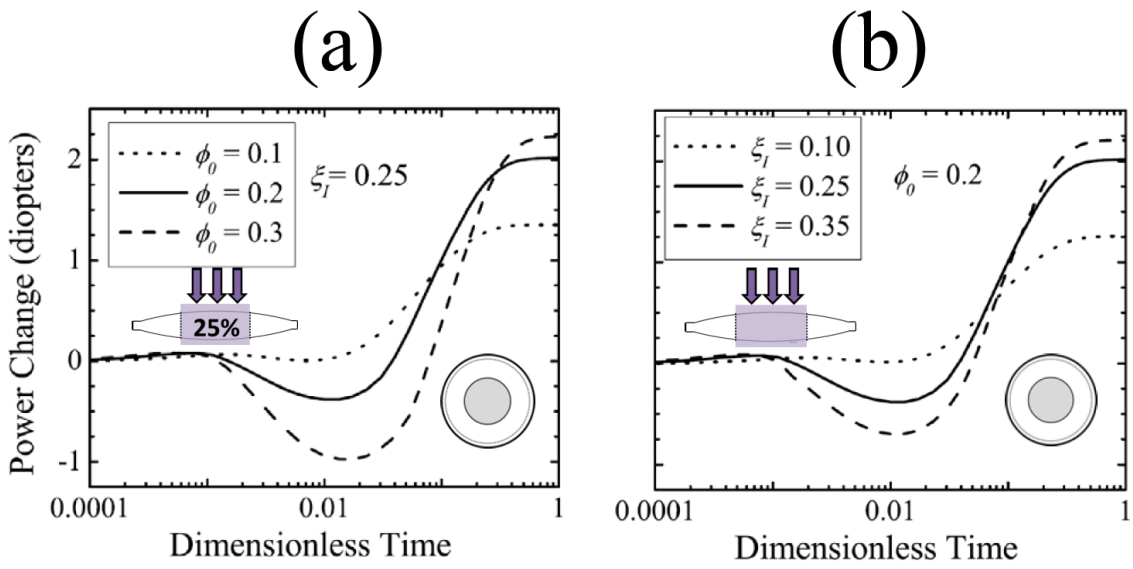

Figure 6.10: The effect of increasing (a) the initial volume fraction of macromer, ϕ_0, and (b) the uniform extent of reaction, ξ_I, on the magnitude of the lens-power change for a sample positive power change. All results are for uniform reaction (ξ_I consumed) inside the interior diameter $d_i = 3.0$ mm (annotated in the icon of the cross section through the lens depth). We report the near zone lens-power change (ΔP_n) corresponding to least–squares fitting the surface nodes within the same region ($d_n = 3$ mm, illustrated in the bird's-eye-view icon). Material parameters: $M_m = 1000$ g/mol and $G_{\text{dry}} = 0.18$ MPa.

can be swollen into the system (recall §2.2.3) and the initial volume fraction does play a significant role (below). For the remainder of this thesis, we set the macromer molar mass and network modulus to $M_m = 1000$ g/mol and $G_{\text{dry}} = 0.18$ MPa, respectively, which gives $\phi_{\text{max}} = 0.59$ (Fig. 2.2) and easily encompasses clinical volume fractions ($\phi_0 < 0.3$). The macromer molar mass also serves to determine the rate at which the diffusion–deformation process proceeds (Table 6.2), with smaller macromer molecules giving faster diffusion.

The magnitude of lens-power changes is determined by the amount of macromer consumed in the interior, determined by both (a) the initial volume fraction, ϕ_0, and (b) the extent of reaction in the irradiated zone, ξ_I (Figure 6.10). The solid curve is the same on both graphs. For both the long–time positive response as well as the negative short–time response, increasing either the initial amount of material present or the amount of material reacted increases the experienced lens power change. Furthermore, pairs of conditions that have nearly matched total volume of macromer converted to network, e.g., ($\phi_0 = 0.1$, $\xi_I = 0.25$) and ($\xi_I = 0.1$, $\phi_0 = 0.2$) (dotted curves, Fig. 6.10) and ($\phi_0 = 0.3$, $\xi_I = 0.25$) and ($\xi_I = 0.35$, $\phi_0 = 0.2$) (dashed curves, Fig. 6.10), produce nearly the same change in lens power. This phenomenon is more precisely examined using three different total consumptions of macromer ($\phi_0 \xi_I$) achieved at two different volume fractions by choice of the extent of reaction (Figure 6.11).

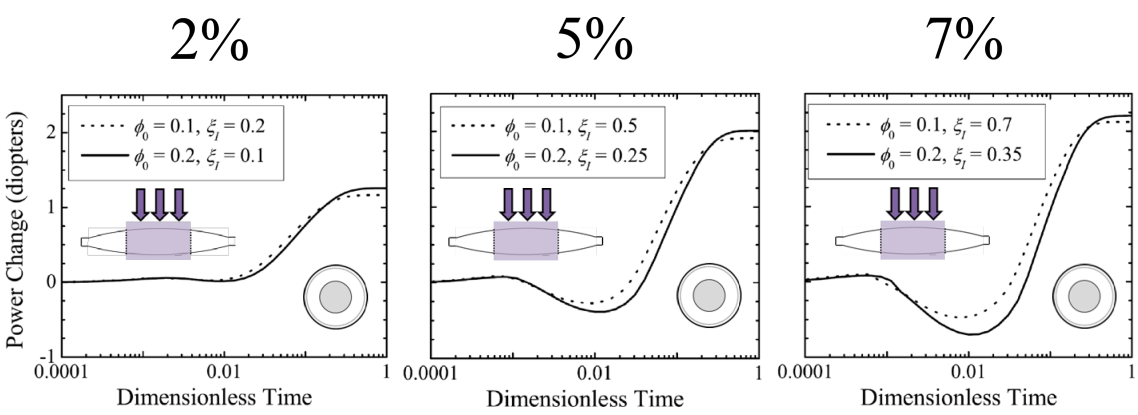

Figure 6.11: Positive power adjustment change for three different total consumptions at two different volume fractions of macromer. In each case, the extent of reaction profile consumes macromer uniformly (ξ_I) inside the interior region $d_i = 3.0$ mm (annotated in the icon of the cross–section through the lens depth). We report the near-zone lens-power change (ΔP_n) corresponding to least–squares fitting the surface nodes within the same region ($d_n = 3$ mm, illustrated in the bird's-eye-view icon). Material parameters: $M_m = 1000$ g/mol, $G_{\text{dry}} = 0.18$ MPa.

For each total consumption, the difference in the final lens power between the two cases is smaller than can be detected by the eye (the difference is < 0.25 diopters). This is true throughout most of the time development except during the initial "ripple effect" described in §6.4.1: during the "ripple", the system with the larger initial amount of macromer ($\phi_0 = 0.2$) experiences a discernably smaller (0.25 – 0.5 diopters greater) minimum in lens power. It is also interesting to note that the relationship between lens-power change and macromer conversion is non-linear: a 2.5–fold increase in the amount of macromer converted to network (from 2% to 5%) only increases the final lens-power change by a factor of 1.6. The relative gain by increasing another 50% (from 5% to 7% macromer consumption) is barely discernable to a human eye (2.0 diopters to 2.25 diopters). Thus we see that there are limits on the extent of lens-power changes that can be achieved by changing the macromer consumption. This is also seen clinically: there are limits to the magnitude of lens-power changes that can be experienced by increasing irradiation dose [4].

6.4.3 Effective Lens Power Depends on Pupil Dilation

To this point, we have reported the lens power that is relevant to intermediate pupil dilation (corresponding to moderate light intensity, as in indoor environments). As lighting conditions change, the diameter of the pupil responds, changing the diameter of the lens that is used for vision (Fig. 6.5). Irradiating the central $d_i = 3$ mm of the lens produces a change in shape that tapers smoothly from increasing the curvature and thickness at the center of the lens to flattening and thinning the peripheral lens (exaggerated in Fig. 6.2b). Consequently, the effective increase in lens power is greatest near the center, which dominates vision under bright light when the pupil contracts (ΔP_f,

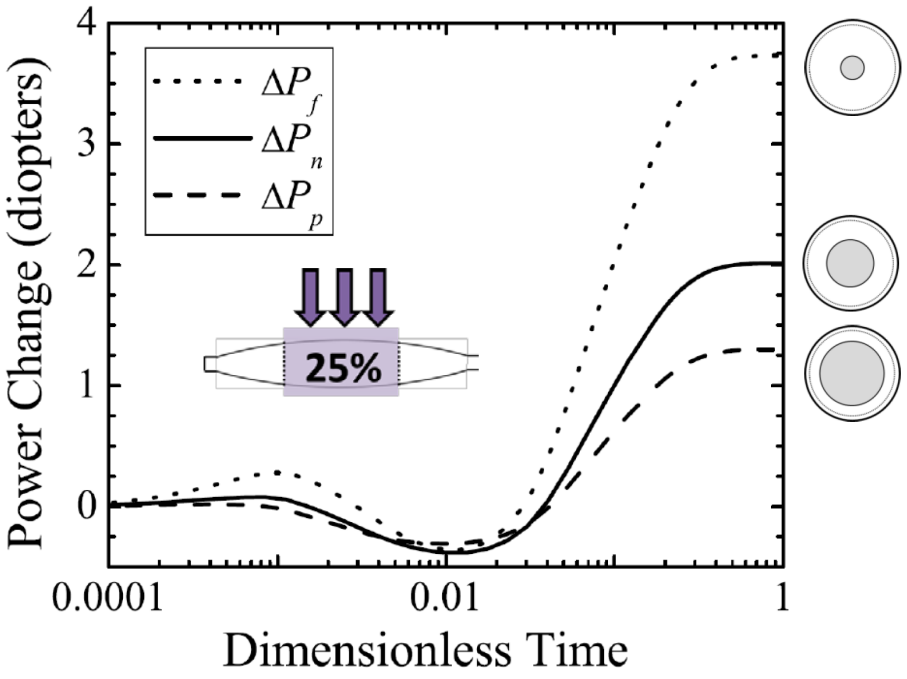

Figure 6.12: Power change as a function of pupil dilation (Fig. 6.5); the bird's-eye-view icons emphasize the three different states. Extent of reaction: central profile with $d_i = 3.0$ mm and $\xi_I = 0.25$. Material parameters: $\phi_0 = 0.2$, $M_m = 1000$ g/mol, and $G_{\text{dry}} = 0.18$ MPa.

Figure 6.12). When the pupil is dilated under dimly lit conditions, most of the lens is used, including some of the area that is flattened due to the net transfer of macromer from the periphery to the center; consequently the change in lens power is relatively small (ΔP_p, Figure 6.12).

The monotonic trend in effective lens power as a function of pupil diameter holds throughout the time window in which most of the adjustment occurs ($0.02 < \mathscr{T} < 0.2$). Indeed, the trend $\Delta P_p < \Delta P_f < \Delta P_f$ holds for any irradiation profile that has only one maxima or only one minima. To create a non-monotonic variation in effective lens power, like the multifocal lens design for patients who have lost accommodation (Figure 6.3, left), an irradiation profile that has multiple extrema must be used.

6.4.4 Parallels between Positive and Negative Adjustments of Lens Power

All of the features noted for a "top hat" irradiation profile (uniform intensity exposure of the central zone) hold for the step–change radial intensity profile that irradiates only the peripheral zone of the lens. In this case, material diffuses from the inside of the lens to the periphery, causing a decrease of volume in the interior and flattening of both the anterior and posterior surfaces in the central zone: a negative correction (*decrease* in lens power, Figure 6.13). As was seen for the "top hat" profile, the adjustment occurs in three stages: a non-monotonic variation at short time ($\mathscr{T} < 0.02$);

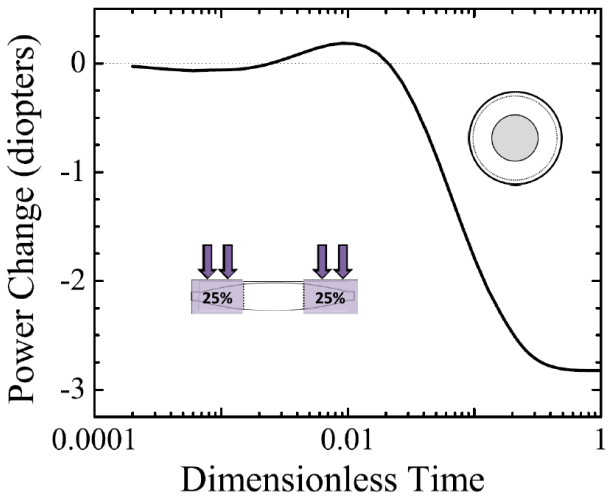

Figure 6.13: Power change associated with peripheral consumption of macromer. The extent of reaction profile is illustrated in the cross section through the lens thickness icon: 25% of macromer is consumed outside the region $d_i = 3.0$ mm. The bird's-eye-view icon indicates the region of the surface in which the lens power is calculated (ΔP_n, $d_n = 3$ mm) using a least–squares fit to the posterior and anterior curvature in that region. Material parameters: $\phi_0 = 0.2$, $M_m = 1000$ g/mol, and $G_{\text{dry}} = 0.18$ MPa.

a strong, monotonic change at intermediate time ($0.02 < \mathscr{T} < 0.2$); and a gradual approach to equilibrium ($0.2 < \mathscr{T} < 1$). Because the central and peripheral profiles are complimentary, we compare the magnitude of the negative power change observed here through peripheral reaction with our initial central reaction (Fig. 6.7). Both profiles have $d_i = 3.0$ mm and $\xi_I = 0.25$; however, the peripheral volume is larger and more total macromer is consumed in the peripheral reaction (3%) than in the central reaction (2%). Based upon our arguments in §6.4.2, we then expect the final magnitude of the negative correction to be larger than the corresponding positive correction. This is observed: the negative correction experienced is stronger for the peripheral reaction ($\Delta P_n = -2.75$) than the corresponding positive correction for the central reaction ($\Delta P_n = 2.0$). All other behavior observed for positive lens corrections—specifically the dependence of the magnitude of the correction on macromer consumption—are also found to hold true for negative corrections.

6.5 Inclusion of UV Blocker Breaks Anterior–Posterior Symmetry

In the previous section, we examined power adjustments achieved using transfer of macromer in the radial direcction. This was done under the assumption that the extent of reaction was uniform inside the irradiated zone, $\xi = \xi(R)$ only. Clinically, intraocular lenses contain a "UV blocker"—a dye that absorbs near UV light in a manner similar to the natural lens. In the light-adjustable

lenses, one of the criteria for selecting the photosensitizer is that it appear colorless, consequently, the photosensitizer also absorbs in the near UV. Therefore, we now consider the case in which the light of the wavelength used to adjust lens power is attenuated as it propagates through the lens. Because the resulting extent of reaction profile decays through the depth, macromer is redistributed in both the axial and radial directions. For axisymmetric irradiation profiles, the general extent of reaction profile is:

$$\xi(R, Z) = f(R)g(R, Z) \tag{6.5.1}$$

with $f(R)$ capturing the extent of reaction profile in the R direction and $g(R, Z)$ capturing the R–dependence of the anterior surface and the decay in intensity once the light enters the lens. As in Ch. 5,

$$g(R, Z) = \xi_I \exp\left(\frac{Z - h(R)}{\lambda}\right) \tag{6.5.2}$$

with λ the extinction length (depth at which the extent of reaction decays to $\exp^{-1} = 0.37\%$), ξ_I the extent of reaction on the anterior surface, and $h(R)$ describing the shape of the anterior surface. Specifically, the shape shown in Fig.6.1 has a square edge from $R = d_{se}/2$ to $d/2$, where $h(R) = h_{min}/2$, and a spherical cap from $R = 0$ to $R = d_{se}/2$, where the radius of curvature is R_a:

$$h(R) = \sqrt{R_a^2 - R^2} + \frac{1}{2}h_{max} - R_a. \tag{6.5.3}$$

For comparison with the preceding section, we first consider $f(R)$ for the top hat profile for positive and corrections (6.6) and then examine profiles that are used in clinical practice §6.5.1.

In the presence of UV blocker, the top hat profile creates a gradient in concentration that depletes macromer preferentially in the anterior part of the central zone. Transfer of macromer from the back to the front of the lens tends to cause posterior elements to shrink and anterior elements to expand. When the central zone is irradiated, this axial transfer reinforces the expansion of anterior segments due to the inward radial flux of macromer (yielding an increase in curvature of the anterior surface). On the other hand, the axial flux competes against the expansion of posterior segments. Since the curvature of both surfaces determine the effective lens power (6.3.6, it is no longer obvious that irradiating the central zone will yield an increase in lens power.

The introduction of UV blocker also adds to the richness of the transient response of the adjustment. Axial gradient involve two length scales: the thickness of the lens, h_{max}, and the extinction length, λ. When $\lambda \ll h_{max}$, this introduces two additional time scales (Table 6.3): the axial redistribution within a characteristic time of $\mathscr{T} = 0.16$ and the radial redistrubtion within the characterstic time $\mathscr{T} = 1.0$. At short times ($\mathscr{T} < 0.16$), then, we expect macromer diffusing away from the posterior surface to dominate influx of macromer from the periphery, resulting in a net outflux of macromer and an initially decreasing posterior curvature. At long times, however, the infux of ma-

terial from the peripheries should gradually reverse this effect, with an end result dependent upon the relative magnitudes of the two.

To illustrate these key concepts, we first report the change in anterior and posterior curvature for a central reaction profile that is uniformly irradiated to 10% within $d_i = 3.0$ mm (dash–dot line, Fig. 6.14). The symmetry of the extent of reaction profile (uniform) ensures that the anterior and posterior curvatures develop at the same rate. We next introduce a decaying extent of reaction profile with the same radial component (central, $d_i = 3.0$ mm). From §6.4.2, however, we know that having a different total macromer consumption amount will yield a different deformation simply from the difference in consumption. Therefore, we choose an extent of reaction at the anterior surface, ξ_I, for the decay profile such that the total amount of macromer left after reaction is equal to the total amount left after the uniform irradiation, measured through the average volume fraction $\bar{\phi}$. Note that a much greater incident irradiation or much longer irradiation time is require to produce $\xi_I = 0.22$ than $\xi_I = 0.1$. In the presence of UV blocker, the anterior and posterior curvature do not develop at the same rate (Fig. 6.14). As expected, the short-time transfer of material from back to front causes the posterior surface to initially decrease in curvature. At long time, this is reversed by the transfer of macromer from the outside to the inside. In this particular case, the transfer of macromer from the outside to the inside is stronger than the loss of macromer from back to front and the final posterior curvature change is positive. The anterior curvature change is approximately the same as for the uniform profile. Because the anterior curvature has not changed, the smaller increase in posterior curvature yields a net smaller lens-power change (Fig. 6.15).

This is true for a fixed total amount of macromer consumed: adding UV blocker (i.e., any finite λ) reduces the change in lens power (6.15). This is because the posterior curvature will always be smaller than for the uniform case as macromer transfers from back to front (we ensure that the same amount of macromer is consumed at all extinction lengths by changing the surface extent of reaction corresponding to strongly inrcreasing the irradiation dose as λ decreases). The magnitude of the positive correction decreases monotonically with decreasing extinction length. It is interesting to contrast this with the beam in Ch. 5: the maximum lens power change observed here does not occur at an intermediate value of extinction length.

Based on these results, we can think of the exponential decay profile through the depth resulting in an opposing negative adjustment. Although this is undesirable for a positive adjustment, the decay of the light profile is used to protect the patient's retina during clinical treatment and, afterward, the recapitulate the UV protection characteristics of the natural lens [26]. This opposing negative adjustment must then be taken into account and profiles must be developed which, in a sense, overadjust to compensate for the transfer of material from front to back. This is particularly true of the lock–in profile (discussed momentarily §6.5.2).

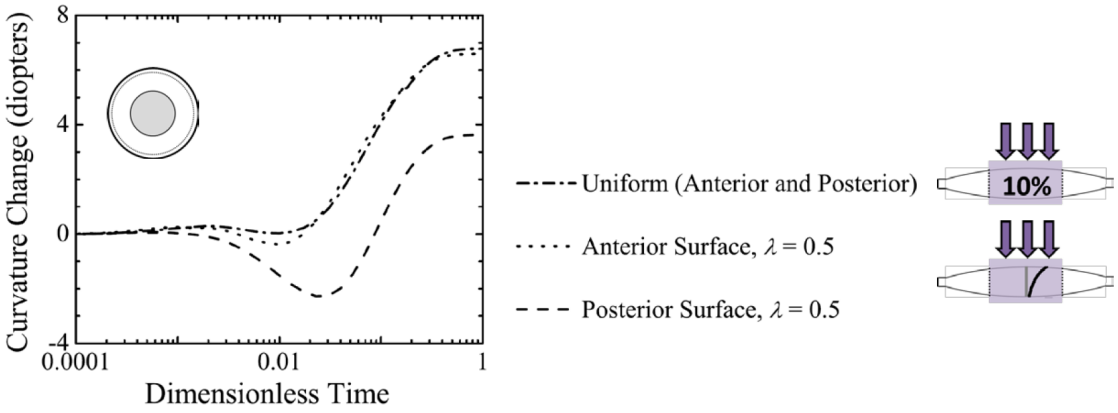

Figure 6.14: Illustration of the effect of introducing an axial extent of reaction decay on the anterior and posterior surface curvature (near zone, denoted by the bird's-eye-view icon). The uniform radial extent of reaction profile with $\xi_I = 0.10$ and $d_i = 3.0$ mm is front/back symmetric and so yields the same anterior and posterior curvature at any point in time. Introducing exponential decay through the depth ($\lambda = 0.5$) causes the anterior and posterior curvatures to develop differently in time. The extent of reaction at the anterior surface for the decaying profiles is taken as $\xi_I = 0.22$ so that the amount of macromer consumed between the two is the same (measured through the average volume fraction after reaction,$\bar{\phi} = 0.1923$). Material parameters: $\phi_0 = 0.2$, $M_m = 1000$ g/mol, and $G_{\text{dry}} = 0.18$ MPa.

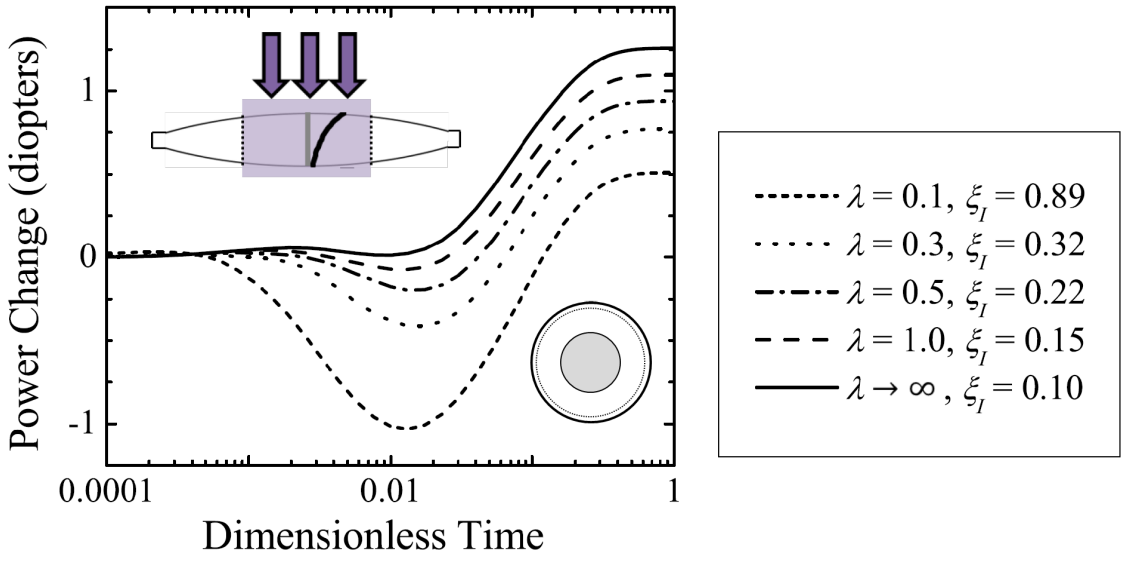

Figure 6.15: The lens-power change (ΔP_n, denoted by the bird's-eye-view icon) experienced for central reaction profiles (positive corrections) as a function of extinction length due to UV blocker (λ). The extent of reaction profiles (all with $d_i = 3.0$ mm) are chosen so the amount of macromer consumed is the same regardless of λ. This is done by changing the extent of reaction on the anterior surface (ξ_I) so that the average volume fraction after reaction in each case is the same ($\bar{\phi} = 0.1923$). Material parameters: $\phi_0 = 0.2$, $M_m = 1000$ g/mol, and $G_{\text{dry}} = 0.18$ MPa.

	A	B (mm^{-2})	C (mm^{-4})	D (mm^{-6})
Positive Adjustment (PA)	1.0000	0.4957	-0.1042	0.0075
Negative Adjustment (NA)	0.5000	-0.0682	0.	0.
Lock–In (LI)	1.0000	0.0865	0.	0.

Table 6.5: The coefficients to the even function (6.5.4) for three clinical sample profiles [21, 27]

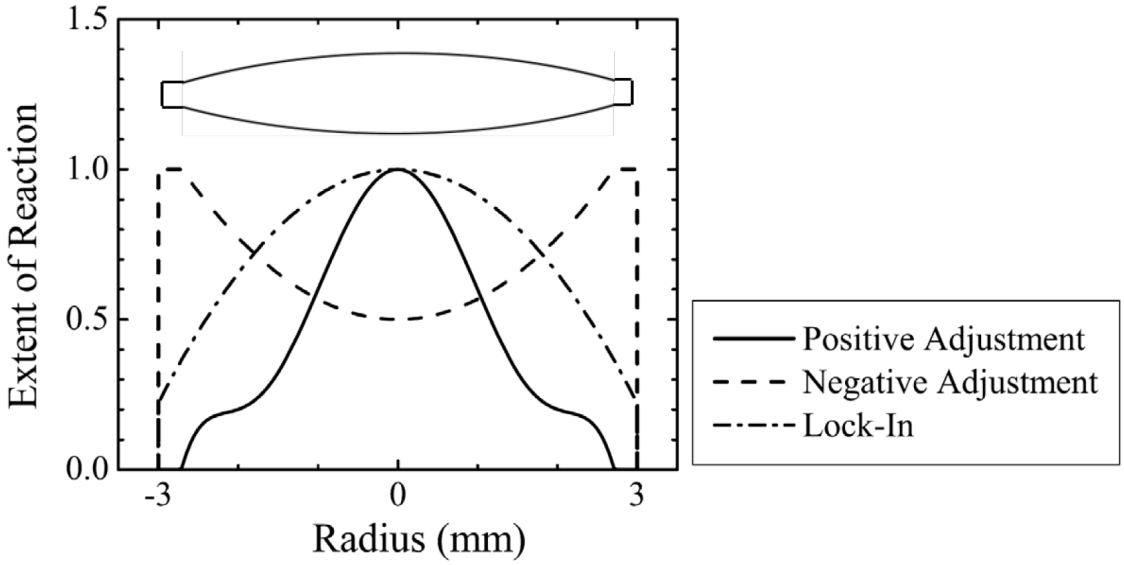

Figure 6.16: The sample radial extent of reaction profiles, $f(R)$, corresponding to coefficients in Table 6.5 [21]. Each profile is an even function (6.5.4) in the main optical region ($r < d_{se}/2$). In the square–edge region, the positive and negative adjustment attain a constant value of zero and one, respectively, whereas the lock–in profile maintains the same functional form.

6.5.1 Clinically Relevant Profiles: Positive and Negative Adjustment

To conclude our study, we expand our radial irradiation profiles from top hat profiles to spatially varying profiles taken directly from current clinical application. We focus on spherical corrections of the form [27]:

$$f(R) = A - Br^2 - Cr^4 - Dr^6. \tag{6.5.4}$$

Coefficients for three sample profiles—"positive adjustment", "negative adjustment", and "lock–in"—are given in Table 6.5; Fig. 6.16 illustrates the shape of these profiles [21]. Note that, as before, the profile that will give positive adjustment preferentially consumes macromer near the center, whereas the negative correction profile consumes macromer preferentially in the periphery of the lens. A key feature of these clinical profiles compared to the top hat profiles discussed above is that the initial gradients are not as steep. For this reason, diffusion at early times occurs throughout the entire radial direction rather than within a small boundary layer. Smoothing out the early gradients in this manner eliminates the early-time "ripple effect" observed for the central top hat

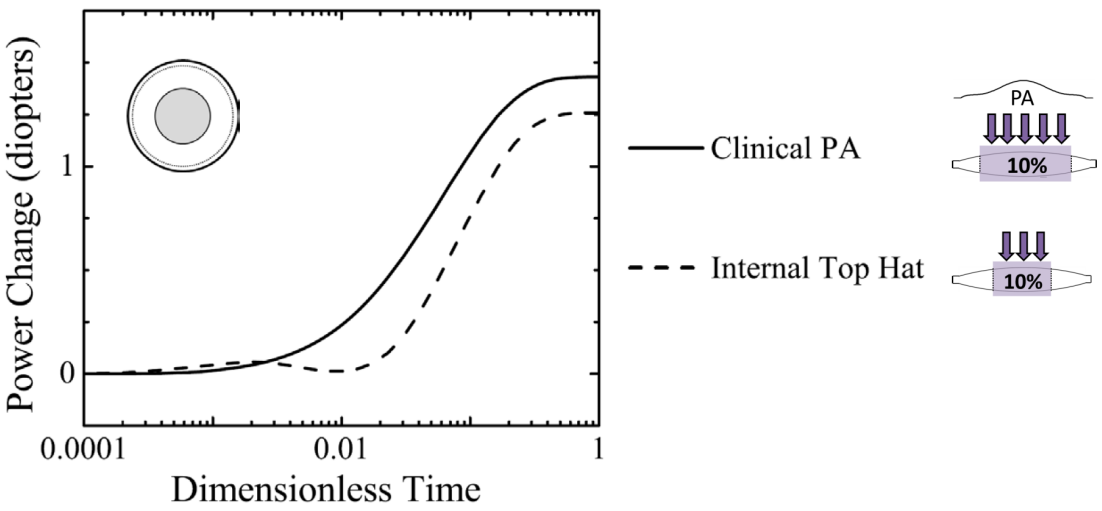

Figure 6.17: Lens-power change (near zone, denoted by the bird's-eye-view icon) for both a central top-hat extent of reaction profile ($d_i = 3.0$ mm) and the positive adjustment profile (PA) of Fig. 6.16. In both cases, there is no UV–blocker and irradiation is assumed to be uniform throughout the depth with $\xi_I = 0.10$. The amount of macromer consumed is nearly identical between the two: $\bar{\phi} = 0.1923$ for the top-hat profile and $\bar{\phi} = 0.1935$ for the positive adjustment profile. Material parameters: $\phi_0 = 0.2$, $M_m = 1000$ g/mol, and $G_{\text{dry}} = 0.18$ MPa.

profile (§6.4.1, Fig. 6.17). In fact, the absence of the initial ripple causes the power correction to be detectable by the human eye earlier on: the positive adjustment profile attains a correction of 0.25 diopters by $\mathscr{T} = 0.008$ whereas the same correction for the top hat profile is not observed until $\mathscr{T} = 0.04$. The corresponding real time for the earliest perceptible change is the same as the order of magnitude of the ripple effect: for this macromer molar mass ($M_m = 1000$ g/mol), $\mathscr{T} = 0.008$ corresponds to $t \approx 20$ min. Although initial responses for the two profiles are different, the final lens power change is the same (1.25 diopters). The clinical radial profile, therefore, gives the same overall lens power change as the top hat profile, but at a faster rate. It is worth noting that developing such a profile was non–trivial and had to be done through experimental trial and error; studies can now be performed on why the profile is optimal and new profiles can be designed with the preliminary work done in this thesis.

We now examine the positive and negative adjustment profiles in the presence of UV blocker. We expect the same behavior seen for the top hat profiles: the transfer of material from the back to the front causes the posterior surface to decrease in curvature, yielding a negative adjustment to the main correction caused by the radial profile. These results are observed: for positive adjustment (Fig. 6.18a) the experienced positive lens-power change decreases with the addition of blocker. This is because the radial profile tends to cause a positive power change while the axial profile tends to cause a negative power change. For the negative adjustment profile (Fig. 6.18b) the negative lens-

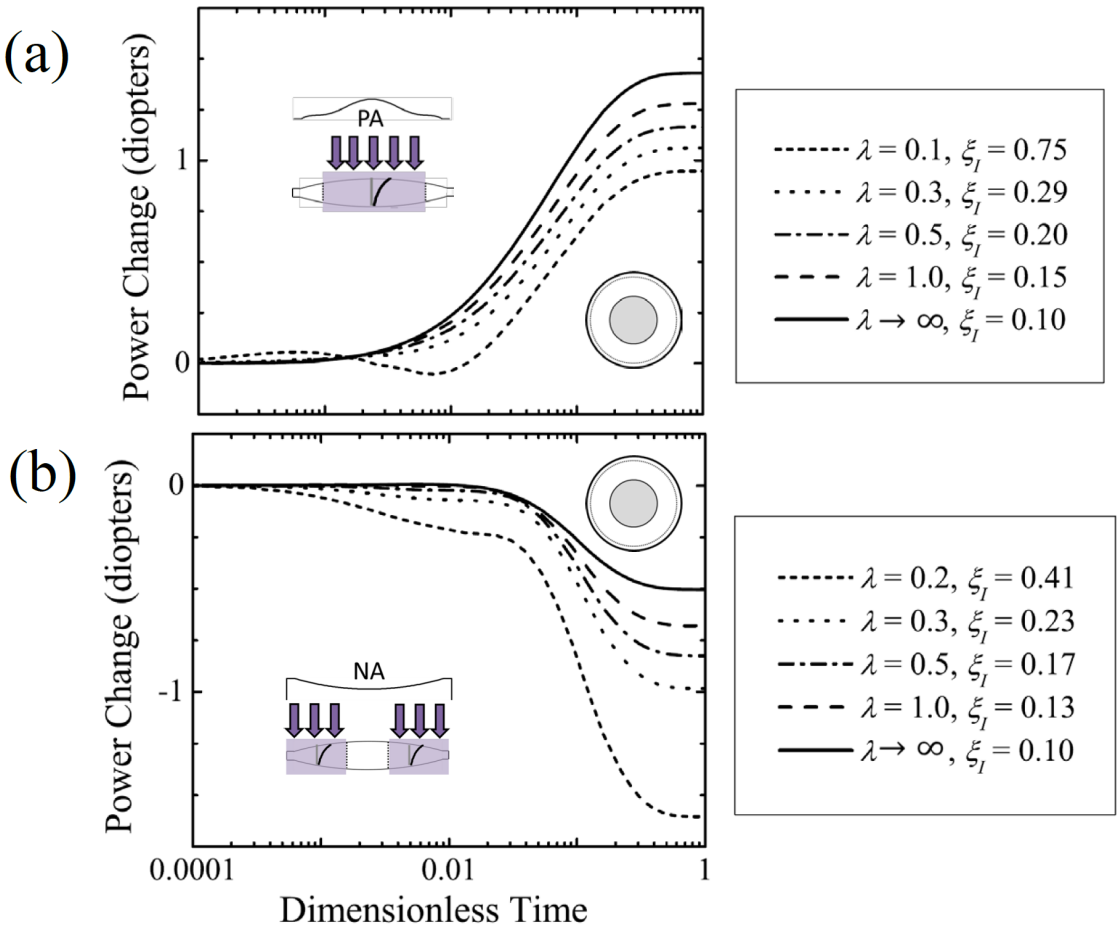

Figure 6.18: Lens-power change (near zone, denoted by the bird's-eye-view icon) for the (a) positive (PA) and (b) negative adjustment (NA) profiles of Fig. 6.16 as a function of the extinction length λ. The amount of macromer consumed is the same within each box: (a) $\bar{\phi} = 0.1935$ for the positive adjustment profile and (b) $\bar{\phi} = 0.1852$ for the negative adjustment profile. Material parameters: $\phi_0 = 0.2$, $M_m = 1000$ g/mol, and $G_{\text{dry}} = 0.18$ MPa.

power change becomes stronger with the addition of blocker: the radial and axial reaction profiles complement each other and magnify the negative correction. In both cases, the steeper the gradient (smaller λ), the stronger the negative correction.

6.5.2 Lock–In: Challenges with UV Blocker

In the above profiles, we have shown that consumption of small amounts of macromer yield clinically significant lens-power changes. In a sense, this makes photoelastomers quite powerful: multiple corrections can be made by iteratively consuming small amounts of material until a desirable final shape is attained. On the other hand, a significant amount of macromer remains in the lens after diffusion–deformation is complete. If this macromer were to remain free in the lens after the appro-

priate correction is attained, ambient light over time would cause further reaction and shift the lens power away from that correction. For this reason, it is necessary to expose the lens to a process called "lock–in" once lens correction is complete. During lock–in, a stronger magnitude of light is used to fully convert the remaining free macromer in the lens so that none remains and the desired shape of the lens is permanent (Ch. 1).

This process is non–trivial, however, due to the presence of UV blocker. To illustrate this, take a simple example in which the lens does not require post–operative adjustment: the base lens itself yields emmetropic vision for the patient. The clinician is now tasked with completely reacting all the macromer inside the lens. If there were no UV–blocker in the lens, the corresponding profile is simple: a uniform profile extending to the extremeties of the lens (Fig. 6.6, $d_i = d = 6$ mm). For this case, macromer is reacted uniformly and therefore no gradients in chemical potential are created, hence no lens-power change (Figure 6.19). The presence of UV blocker will cause the light profile to decay through the depth, decreasing the intensity to a safe value at the back of the lens. However, we have just learned that causing a decay in the axial profile causes material to transfer from back to front, resulting in a flattening of the posterior curvature and a net negative power change. In the case of uniform irradiation through $d_i = 6$ mm, this is especially strong (Fig. 6.19): if $\lambda = 0.33$, the lens power changes by -3.0 diopters! The goal of lock–in is to convert all free macromer into network without changing the lens power, so a uniform profile can clearly not be used when the system has UV blocker.

A non–trivial lock–in profile was developed clinically to overcome this difficulty (Fig. 6.16). Because the net–effect of light decay is to cause a negative correction, the lock–in profile compensates by reacting material more strongly in the central zone to create an equal and opposite positive correction. When a lens with UV blocker is locked–in with this profile, the final lens power change is not discernably changed (Fig. 6.19). The initial transient that appears is due to the differing time scales for diffusion. The steeper initial gradients in the axial direction cause material to initially be transferred back to front, yielding an observed negative power change at short times. On longer time scales, sufficient amounts of material diffuse in from the periphery to increase lens power and mediate the effect of the initial negative power change.

We conclude this work by considering lock–in of the positive and negative adjustments in §6.5.1. Although we have not yet discussed multiple reactions, the derivation for multiple corrections is rather straight–forward and proceeds in a manner similar to that of Ch. 2. Assume that a system has reached equilibrium to a volume fraction profile $\phi_i(\boldsymbol{x})$;[5] here, we use the subscript i to denote the equilibrium volume fraction achieved after the ith reaction. For example, we have already considered the case in which a system begins unreacted: $i = 0$ and $\phi_i \to \phi_0$. We define the conversion parameter

[5]Note that for $i \neq 0$, the equilibrium volume fraction can be a function of space (recall Ch. 4 for the simplest example of this).

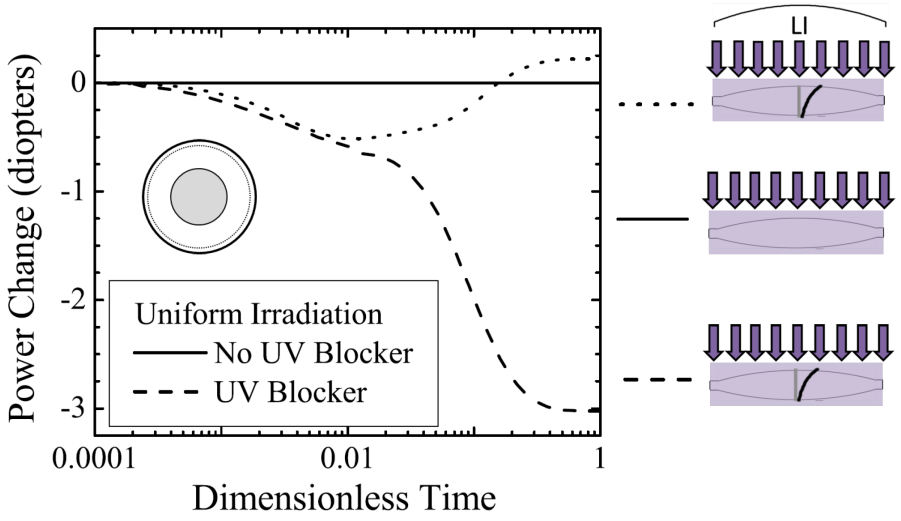

Figure 6.19: Two initially unreacted lenses—one without UV blocker (solid line) and the other with UV blocker (dashed line, $\lambda = 0.33$)—are subjected to a lock–in irradiation profile that is uniform to the lens extremities ($d_i = 6$ mm, $\xi_I = 0.95$). The lens power (measured here with the near-zone power ΔP_n, shown by the bird's-eye-view icon) does not change for the lens with no UV blocker but experiences a significant negative correction for the lens with UV blocker. Also shown is the case of a clinical lock–in profile (Fig. 6.16, $\xi_I = 0.95$, $\lambda = 0.3$). Material parameters: $\phi_0 = 0.2$, $M_m = 1000$ g/mol, and $G_{\text{dry}} = 0.18$ MPa.

for the $i+1$th reaction to be:

$$\theta_{i+1} = \theta_i \left[1 + \left(\frac{\phi_i}{1+\phi_i}\right)\xi_{i+1}\right], \tag{6.5.5}$$

with ξ_{i+1} the extent of reaction for the $i+1$th reaction. For $i = 0$, $\theta_0 = 1$ (the network is the originally cured network) and the expression for θ_1 is the case we have already considered (2.3.9). Note that further reactions change the conversion parameter multiplicatively rather than additively; this is due to the general coupling equation between reaction, diffusion, and deformation:

$$Q_i = \frac{\theta_i}{1-\phi_i} \tag{6.5.6}$$

with Q_i the equilibrium volume ratio after the ith reaction. With these changes, the volume fraction profile ϕ_i and nodal positions obtained at the equilibrium time for one correction can be used as the initial condition for the next correction. Because nodal points do not move significantly during a given correction(Fig. 6.2c), we use the reference coordinates when evaluating the extent of reaction profile for subsequent correction as a first approximation.

To illustrate this method, we have taken the results for a sample positive and negative correction from Fig. 6.18 and subjected them to the clinical lock–in profile. Regardless of whether the correction

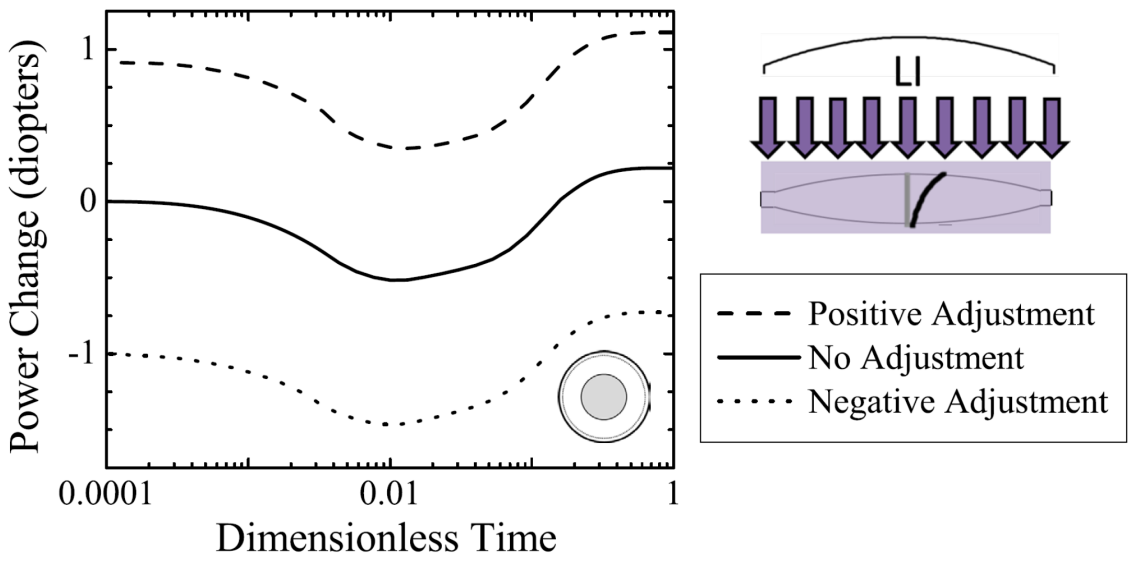

Figure 6.20: Lock–in profile run on three clinical adjustments: 1) positive adjustment (PA, $\lambda = 0.3$, $\xi_I = 0.29$), 2) negative adjustment (NA, $\lambda = 0.3$, $\xi_I = 0.23$), and 3) no adjustment. In each case, the lock–in profile used has $\xi_I = 0.95$, $\lambda = 0.3$. The lens-power change reported is the near-zone power (ΔP_n) shown in the bird's eye view. Material parameters: $\phi_0 = 0.2$, $M_m = 1000$ g/mol, and $G_{\text{dry}} = 0.18$ MPa.

is positive or negative, the lock–in maintains the correction (Fig. 6.20). Furthermore, the lock–in lens power changes are approximately self–similar to the case attained when there is no initial adjustment. This indicates that we can expect nearly the same lens power response to a given correction regardless of the correction history of the sample. This general principle follows from the results we have observed throughout this thesis. First, the deviations from ideal mixing are small for clinical parameter choices (Ch. 4, Fig. 4.6); this ensures that the volume fraction after reaction will be nearly uniform across the lens. In addition, the displacement of points is negligibly small (Fig. 6.2c). Both of these things together indicate that application of a new reaction profile for any system should proceed nearly the same as applying that reaction profile to an initially unreacted system of slightly lower initial volume fraction profile. Such a powerful general principle could be used clinically to develop any desired correction by cataloging a set of base corrections and performing them in sequence. In fact, the larger the initial amount of macromer, the more corrections can be performed. For many applcations, this could be an asset. The only problem with this approach in the light–adjustable lens is that the patient would be required to return to the clinical multiple times; since each correction requires about a week to stabilize, there are obviously limits to this approach.

6.6 Conclusion and Future Work

In this chapter, we have applied the theory developed in Ch. 2 and 3 to the case of the light–adjustable lens. Using a finite element method which solves the system of equations element–by–element, we have illustrated that power changes observed in light–adjustable lenses are due to diffusion. We have determined that the rate at which the power change develops is determined by the size of the free molecules (macromer molar mass) and that the magnitude of the power change is determined by the total amount of macromer consumed inside the system (initial volume fraction times extent of reaction). It was determined that the initial modulus of the material plays no role on the deformation except to specify limits on thermodynamically admissable initial volume fractions. We have also illustrated the ability to create both simple positive and negative adjustments by consuming material preferrentially internally and externally, respectively. The inclusion of UV blocker was determined to cause a net negative power change as material diffuses from the back to the front. We expanded these principles to clinical positive and negative adjustments and discussed the difficulty of achieving lock–in due to the presence of UV blocker. Because of the small amounts of macromer consumed during a given correction, our theory illustrates that corrections can be performed additively: previous correction history does not strongly affect the outcome of the current correction. However, in the clinic, there are practical limitations on the number of check–up treatments a patient must experience. It is therefore desirable to perform multiple corrections at the same time rather than sequentially. As discussed in Ch. 1, this is a non–trivial task: experimentally determined results indicate non–linearity when applying two corrections—such as a positive correction and an astigmatic correction—at the same time. This body of work provides the foundation for exploring the reason for this non–linearity.

There are several other directions in which this work can be taken. The tool kit begun here allows understanding of the forward problem—how things deform under a given reaction profile—but can be used to back postulate profiles that will give desired deformations. To connect this to experiment, would require expansion of the theory to include a more direct connection between extent of reaction field and irradiation field, including the advanced optics of ray tracing neglected here.

Additionally, experiments can be performed to test the quantitative accuracy of this theory. One simple example is the case of a beam bent with light (Ch. 5). Using strips of elastomeric photopolymer resting on an air–water interace, the curvature of the beams in time can be found by measuring the focal point of a beam of light passing through. A similar experimental design could be performed on light–adjustable lenses. It would be particularly powerful to combine theory and experiment: postulate a profile to give a desired deformation, run a simulation to determine if it will give that deformation and perform the experiment to determine the actual deformation. There are also many additional applications that have yet to be examined. For example, a developing

field of technology uses PDMS—the same material as in light–adjustable lenses—in the formation of microfluidic devices [96–99]. We can imagine modifying these devices to be light–adjustable. We can imagine the bending of light–adjustable beams to perform work or fine–adjusting optical elements sent into space remotely with a laser. The possibilities for elastomeric photopolymers have only just begun to be examined.

Appendix A

Governing Equations of Mixture Theory

A.1 Introduction

This appendix lays out the equations of mixture theory following the works of Atkin and Craine [46], Green and Naghdi [45], and Haupt [48]. All of these works expand the basic continuum field theory approach of Truesdell [49] to multiple components. The notation and derivations used by each, however, are slightly different. Also, the physical meaning behind each of the terms is not always clear in the original work since each author takes a very structured, mathematical stance. Here, we provide first principle insight into the derivation of the governing equations, as well as provide a more consistent notation in keeping with the rest of this body of work.

A.2 Kinematics

Consider a mixture of ν components, each labelled by a subscript α. Mixture theory allows a different reference configuration (Ω_α with point labels $\boldsymbol{X}_\alpha$) for all species but assumes the spatial configuration (Ω with points $\boldsymbol{x}$) is shared by all species. The system kinematics are then defined by the ν equations

$$x_i = \chi_i^\alpha(\boldsymbol{X}_\alpha, t). \tag{A.2.1}$$

Each of these is a mapping from the reference configuration of species α to the spatial configuration (see Figure A.1). The species deformation gradient F_{iJ}^α is the derivative of this mapping[1]

$$F_{iJ}^\alpha(\boldsymbol{X}_\alpha, t) = \frac{\partial \chi_i^\alpha}{\partial X_J^\alpha}(\boldsymbol{X}_\alpha, t) \tag{A.2.2}$$

[1]Note that we are following Berkley notation; that is lowercase letters for indices to spatial variables and uppercase letters for indices of reference variables. Of course, the reference is always taken as that of the specific component.

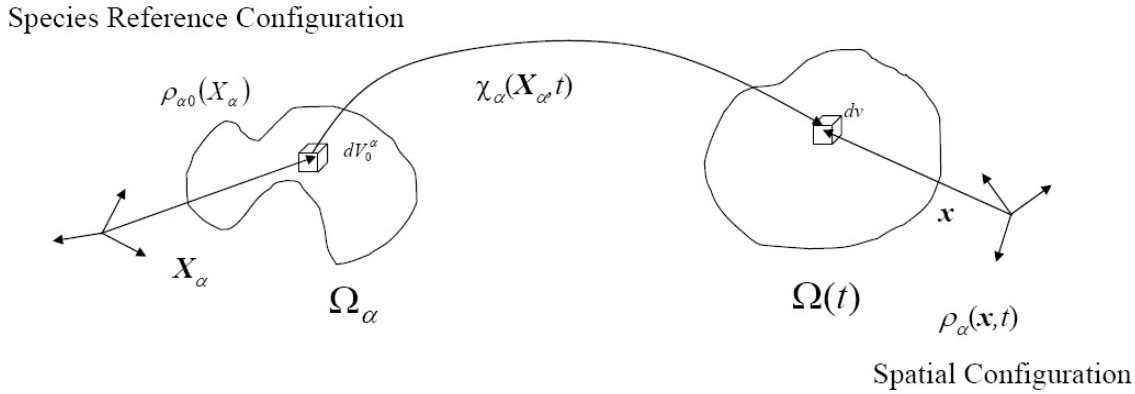

Figure A.1: The kinematics of mixture theory. Each species α has a reference configuration Ω_α (only one shown here). A small volume dV_0^α located at a point $\boldsymbol{X}_\alpha$ in Ω_α is mapped to a volume dv at point $\boldsymbol{x}$ in the spatial configuration Ω via mapping $\boldsymbol{\chi}_\alpha$. The density field of each pure component species is $\rho_{\alpha 0}(\boldsymbol{X}_\alpha)$ while the density field of that species in the spatial configuration is denoted as $\rho_\alpha(\boldsymbol{x}, t)$.

and contains all important information regarding deformation. For example, the determinant of each deformation gradient allows us to relate spatial volumes dv with the reference volume of species α dV_0^α:

$$dv = J_\alpha(\boldsymbol{X}_\alpha, t) dV_0^\alpha \qquad \text{where} \quad J_\alpha = \det F_{iJ}^\alpha. \tag{A.2.3}$$

For each component, define a reference density field $\rho_{\alpha 0}(\boldsymbol{X}_\alpha)$ and a spatial density field $\rho_\alpha(\boldsymbol{x}, t)$. We define the total spatial density $\rho(\boldsymbol{x}, t)$ by:

$$\rho(\boldsymbol{x}, t) = \sum_\alpha \rho_\alpha(\boldsymbol{x}, t). \tag{A.2.4}$$

Note that we cannot define a total reference density since each component has a different coordinate system and possibly different body.

The spatial volume fraction of species α, $\phi_\alpha(\boldsymbol{x}, t)$, is defined as:

$$\phi_\alpha(\boldsymbol{x}, t) \equiv \frac{dv_\alpha}{dv} = \frac{\rho_\alpha(\boldsymbol{x}, t)}{\rho_{\alpha 0}(\boldsymbol{\chi}_\alpha^{-1}(\boldsymbol{x}, t))} \tag{A.2.5}$$

where dv_α is the volume of species α in the small volume element dv.

The time derivative of each mapping is called the species velocity field. The reference velocity field $V_I^\alpha(\boldsymbol{X}_\alpha, t)$ is defined over each component's reference configuration (independent variable $\boldsymbol{X}_\alpha$), and the spatial velocity field $v_i^\alpha(\boldsymbol{x}, t)$ is defined over the spatial configuration (independent variable $\boldsymbol{x}$):

$$V_i^\alpha(\boldsymbol{X}_\alpha, t) = \frac{\partial \chi_i^\alpha}{\partial t}(\boldsymbol{X}_\alpha, t) \tag{A.2.6}$$

and

$$v_i^\alpha(\boldsymbol{x},t) = \frac{\partial \chi_i^\alpha}{\partial t}(\boldsymbol{\chi}_\alpha^{-1}(\boldsymbol{x},t),t) \tag{A.2.7}$$

respectively. The numerical value output by these two fields is identical if the input points to each equation are related by the mapping (A.2.1).

The barycentric velocity $\mathbf{v}(\boldsymbol{x},t)$ defined over the spatial configuration is the density weighted average of the species component velocities:

$$\rho(\boldsymbol{x},t)\mathbf{v}(\boldsymbol{x},t) = \sum_\alpha \rho_\alpha(\boldsymbol{x},t)\mathbf{v}_\alpha(\boldsymbol{x},t). \tag{A.2.8}$$

See §A.5 for notation and identities for taking derivatives of spatial and barycentric variables with respect to time.

A.3 Conservation Principles

A.3.1 Conservation of Mass

Consider mass conservation for species α relative to its reference configuration Ω_α. Because material can react in a mixture theory model, we need to take into account the spatial reaction rate $r_\alpha(\boldsymbol{x},t)$.[2] The general principle yields

$$m_{\alpha 0} + m_{\alpha r}(t) = m_\alpha(t) \tag{A.3.1}$$

where $m_{\alpha 0}$ is the original mass of material α at $t = 0$ (taken as the reference), $m_\alpha(t)$ is the final mass of material at time t, and $m_{\alpha r}(t)$ is the total amount of material that has been created or destroyed at time t through reaction. Writing these in terms of integral expressions of mass densities yields

$$\int_{\Omega_\alpha} \rho_{\alpha 0}(\boldsymbol{X}_\alpha) dV_0^\alpha + \int_0^t \left[\int_{\Omega(\tau)} r_\alpha(\boldsymbol{x},\tau) dv \right] d\tau = \int_{\Omega(t)} \rho_\alpha(\boldsymbol{x},t) dv. \tag{A.3.2}$$

We can rewrite (A.3.2) over the reference configuration by using identity (A.2.3):

$$\int_{\Omega_\alpha} \left\{ \rho_{\alpha 0}(\boldsymbol{X}_\alpha) + \int_0^t r_\alpha(\chi_\alpha(\boldsymbol{X}_\alpha,\tau),\tau) J_\alpha(\boldsymbol{X}_\alpha,\tau) d\tau - \rho_\alpha(\chi_\alpha(\boldsymbol{X}_\alpha,t),t) J_\alpha(\boldsymbol{X}_\alpha,t) \right\} dV_0^\alpha = 0. \tag{A.3.3}$$

With continuous functions over Ω_α, conservation of mass of species α in terms of its reference configuration Ω_α is

$$\rho_{\alpha 0}(\boldsymbol{X}_\alpha) + \int_0^t r_\alpha(\chi_\alpha(\boldsymbol{X}_\alpha,\tau),\tau) J_\alpha(\boldsymbol{X}_\alpha,\tau) d\tau = \rho_\alpha(\chi_\alpha(\boldsymbol{X}_\alpha,t),t) J_\alpha(\boldsymbol{X}_\alpha,t). \tag{A.3.4}$$

[2] We use the spatial reaction rate defined over Ω as opposed to a reference reaction rate since it is more easily connected to experiment.

Define

$$R_\alpha(\boldsymbol{X}_\alpha, t) = \frac{r_\alpha(\chi_\alpha(\boldsymbol{X}_\alpha, t), t)}{\rho_{\alpha 0}(\boldsymbol{X}_\alpha)} \tag{A.3.5}$$

as the rate of creation of species α in terms of volume of species α created per unit time per unit spatial volume ($R_\alpha J_\alpha$ is the volume of species α created per unit time per unit reference volume). With this definition, we introduce conversion parameters $\theta_\alpha(\boldsymbol{X}_\alpha, t)$

$$\theta_\alpha(\boldsymbol{X}_\alpha, t) \equiv \frac{dv_\alpha}{dV_0^\alpha} = 1 + \int_0^t R_\alpha(\boldsymbol{X}_\alpha, \tau) J_\alpha(\boldsymbol{X}_\alpha, \tau) d\tau \tag{A.3.6}$$

as the ratio of the volume of species α in a small element in the spatial configuration to the volume of the species in the reference configuration. This value is greater than one if species α is being created and less than one if it is being consumed. This expression combined with (A.3.4) and (A.2.5) gives a relation between deformations F_{iJ}^α and the volume fraction of each species ϕ_α modified by the reaction parameter θ_α for that species:

$$J_\alpha(\boldsymbol{X}_\alpha, t) = \frac{\theta_\alpha(\boldsymbol{X}_\alpha, t)}{\phi_\alpha(\chi_\alpha(\boldsymbol{X}_\alpha, t), t)}. \tag{A.3.7}$$

Differentiation of (A.3.7) with respect to time yields a mass balance in terms of the spatial configuration

$$\frac{\partial \rho_\alpha}{\partial t}(\boldsymbol{x}, t) + \frac{\partial}{\partial x_i}(\rho_\alpha(\boldsymbol{x}, t) v_i^\alpha(\boldsymbol{x}, t)) = r_\alpha(\boldsymbol{x}, t). \tag{A.3.8}$$

Summation of (A.3.8) yields the relation for conservation of overall mass in terms of the barycentric velocity:

$$\frac{\partial \rho}{\partial t} + \frac{\partial}{\partial x_i}(\rho v_i) = 0. \tag{A.3.9}$$

Note that $\sum r_\alpha = 0$.

A.3.2 Conservation of Linear Momentum

Conservation of linear momentum of species α is found by applying Newton's second law to each species:

$$\frac{d}{dt} p_i^\alpha(t) = G_i^\alpha(t). \tag{A.3.10}$$

Here $p_i^\alpha(t)$ is the momentum of species α at time t, and $G_i^\alpha(t)$ is the resultant force acting on that species. For a body undergoing deformation due to external tractions and internal body forces, we can write this resultant force as

$$G_i^\alpha(t) = \int_{\partial\Omega_\alpha} T_i^\alpha(\boldsymbol{X}_\alpha, t) dS_0^\alpha + \int_{\Omega_\alpha} \rho_{\alpha 0}(\boldsymbol{X}_\alpha) \theta_\alpha(\boldsymbol{X}_\alpha, t) F_i^\alpha(\boldsymbol{X}_\alpha, t) dV_0^\alpha + \int_{\Omega_\alpha} B_i^\alpha(\boldsymbol{X}_\alpha, t) dV_0^\alpha \tag{A.3.11}$$

in the reference configuration. The first term represents the external tractions, the second term the external body forces (such as gravity or electromagnetic forces)[3], and the final term is the internal force per unit reference volume exerted on species α due to the other constituents (a frictional or repulsive force between components). In terms of the spatial configuration, this expression is

$$G_i^\alpha(t) = \int_{\partial\Omega(t)} t_i^\alpha(\boldsymbol{x},t)ds + \int_{\Omega(t)} \rho_\alpha(\boldsymbol{x},t) f_i^\alpha(\boldsymbol{x},t)dv + \int_{\Omega(t)} b_i^\alpha(\boldsymbol{x},t)dv. \tag{A.3.12}$$

Note that $f_i^\alpha = F_i^\alpha$ are the same external body forces, just with a different independent variable (since they are defined per unit mass and not per unit volume), and that $B_i^\alpha = b_i^\alpha J_\alpha$. In addition, we note that the infinitesimal partial surface forces $t_i^\alpha ds = T_i^\alpha dS_0^\alpha$ produce the same values whether measured with respect to the spatial configuration or the reference configuration. By the Cauchy tetrahedron argument, we argue in the usual manner that we can define a partial stress tensor for species α, $\sigma_{ij}^\alpha(\boldsymbol{x},t)$ such that

$$\sigma_{ij}^\alpha(\boldsymbol{x},t) n_j(\boldsymbol{x},t) = t_i^\alpha(\boldsymbol{x},t) \tag{A.3.13}$$

where $n_j(\boldsymbol{x},t)$ is the outward pointing unit normal to the surface $\partial\Omega(t)$. Because $\sum t_i^\alpha(\boldsymbol{x},t) = t_i(\boldsymbol{x},t)$, the total surface traction on the system, we define the total Cauchy stress tensor $\sigma_{ij}(\boldsymbol{x},t)$ via

$$\sigma_{ij}(\boldsymbol{x},t) = \sum_\alpha \sigma_{ij}^\alpha(\boldsymbol{x},t) \tag{A.3.14}$$

so that

$$\sigma_{ij} n_j = t_i. \tag{A.3.15}$$

Note that the definition of the total Cauchy stress in (A.3.14) is a straight sum (not barycentric); in the author's opinion, this leads to the most straightfoward definition of stress. Other authors—namely [45] and [48]—choose to include diffusive stresses in the definition of the total stress in order to make the total conservation of momentum governing equation look like that for a single continua. As long as the appropriate terms are accounted for, in either the stress itself or the governing equation, it is simply a matter of preference.

The Piola transform

$$n_i ds = J_\alpha N_J^\alpha dS_0^\alpha {F_{Ji}^\alpha}^{-1} \tag{A.3.16}$$

and the equivalence of spatial and reference infinitesimal surface forces allows us to define the partial first Piola–Kirchhoff stress tensor $P_{iJ}^\alpha(\boldsymbol{X}_\alpha,t)$ with respect to the reference configuration Ω_α

$$P_{iJ}^\alpha N_J^\alpha = T_i^\alpha \tag{A.3.17}$$

[3]The factor $\theta_\alpha = dv_\alpha/dV_0^\alpha$ appears to map the pure component density $\rho_{\alpha 0}$ to a spatial setting since it is that configuration in which external forces are applied.

where $N_J^\alpha(\boldsymbol{X}_\alpha)$ is the outward pointing unit normal to the surface $\partial\Omega_\alpha$. The relation between $P_{iJ}^\alpha(\boldsymbol{X}_\alpha, t)$ and $\sigma_{ij}^\alpha(\boldsymbol{x}, t)$ is given by:

$$P_{iJ}^\alpha F_{jJ}^\alpha = J_\alpha \sigma_{ij}^\alpha. \tag{A.3.18}$$

Having considered the forces acting upon each species, we now look at the rate of change of momentum. The momentum of species α is defined as:

$$\begin{aligned} p_i^\alpha(t) &= \int_{\Omega(t)} \rho_\alpha(\boldsymbol{x}, t) v_i^\alpha(\boldsymbol{x}, t) dv \\ &= \int_{\Omega_\alpha} \rho_{\alpha 0}(\boldsymbol{X}_\alpha) \theta_\alpha(\boldsymbol{X}_\alpha, t) V_i^\alpha(\boldsymbol{X}_\alpha, t) dV_0^\alpha. \end{aligned} \tag{A.3.19}$$

If we take the time derivative of both sides, we get

$$\begin{aligned} \frac{d}{dt} p_i^\alpha(t) &= \int_{\Omega(t)} \left\{ \frac{D^{(\alpha)}}{Dt} \left(\rho_\alpha v_i^\alpha\right) + \rho_\alpha v_i^\alpha v_{j,j}^\alpha \right\} dv \\ &= \int_{\Omega_\alpha} \rho_{\alpha 0} \left\{ \theta_\alpha A_i^\alpha + R_\alpha J_\alpha V_i^\alpha \right\} dV_0^\alpha. \end{aligned} \tag{A.3.20}$$

Here $A_I^\alpha = A_I^\alpha(\boldsymbol{X}_\alpha, t) = \ddot{\boldsymbol{\chi}}_\alpha(\boldsymbol{X}_\alpha, t)$ is the partial reference acceleration field of species α. To obtain the first result we make use of the Reynold's transport theorem for mixtures (A.5.7), and for the second result the identity

$$\frac{D^{(\alpha)}}{Dt}\Big(\theta_\alpha(\boldsymbol{X}_\alpha, t)\Big) = R_\alpha(\boldsymbol{X}_\alpha, t) J_\alpha(\boldsymbol{X}_\alpha, t) \tag{A.3.21}$$

(all that the $D^{(\alpha)}/Dt$ term represents is a time derivative taking the reference configuration—and, therefore, points $\boldsymbol{X}_\alpha$—as constant; see §A.5). With the aid of the divergence theorem and assuming the fields are continuous, we can combine the time derivative of the momentum (A.3.20) with the forces (A.3.12) to write conservation of species α pointwise as either of the two equivalent

$$\frac{\partial}{\partial t}(\rho_\alpha v_i^\alpha) + (\rho_\alpha v_i^\alpha v_j^\alpha)_{,j} = \sigma_{ij,j}^\alpha + \rho_\alpha f_i^\alpha + b_i^\alpha \tag{A.3.22}$$

$$\rho_\alpha \frac{D^{(\alpha)} v_i^\alpha}{Dt} + r_\alpha v_i^\alpha = \sigma_{ij,j}^\alpha + \rho_\alpha f_i^\alpha + b_i^\alpha. \tag{A.3.23}$$

In the reference configuration, this expression is

$$\rho_{\alpha 0} \left[\theta_\alpha A_i^\alpha + R_\alpha J_\alpha V_i^\alpha\right] = P_{iJ,J}^\alpha + \rho_{\alpha 0} \theta_\alpha F_i^\alpha + B_i^\alpha. \tag{A.3.24}$$

To find the overall (barycentric) conservation of linear momentum, write (A.3.10) for the system

with

$$\begin{aligned} p_i(t) &= \sum_\alpha p_i^\alpha(t) = \sum_\alpha \left\{ \int_{\Omega(t)} \rho_\alpha v_i^\alpha dv \right\} \\ &= \int_{\Omega(t)} \rho v_i dv \end{aligned} \tag{A.3.25}$$

so that (A.5.14)

$$\frac{d}{dt} p_i(t) = \int_{\Omega(t)} \left\{ \rho \frac{Dv_i}{Dt} + \sum_\alpha \left[\rho_\alpha v_i^\alpha \left(v_j^\alpha - v_j \right) \right]_{,j} \right\} dv \tag{A.3.26}$$

and

$$\begin{aligned} G_i(t) &= \sum_\alpha G_i^\alpha(t) = \sum_\alpha \left\{ \int_{\partial\Omega(t)} t_i^\alpha ds + \int_{\Omega(t)} \rho_\alpha f_i^\alpha dv + \int_{\Omega(t)} b_i^\alpha dv \right\} \\ &= \int_{\partial\Omega(t)} t_i ds + \int_{\Omega(t)} \rho f_i dv \\ &= \int_{\Omega(t)} \left\{ \sigma_{ij,j} + \rho f_i \right\} dv. \end{aligned} \tag{A.3.27}$$

Here, we have defined the barycentric external body force f_i by

$$\rho f_i = \sum_\alpha \rho_\alpha f_i^\alpha \tag{A.3.28}$$

and noted that

$$\sum_\alpha b_i^\alpha = 0 \tag{A.3.29}$$

by Newton's third law for the system as a whole. Combining (A.3.26) and (A.3.27) yields the relation for system momentum conservation

$$\rho \frac{Dv_i}{Dt} + \sum_\alpha \left[\rho_\alpha v_i^\alpha \left(v_j^\alpha - v_j \right) \right]_{,j} = \sigma_{ij,j} + \rho f_i. \tag{A.3.30}$$

The additional terms which appear in this expression beyond those normally in the expression for a single continua are those terms we chose not to include in our definition of stress.

A.3.3 Conservation of Energy

In mixture theory, all material bodies are closed with respect to material flow: the reference configurations because they are closed by definition, and the spatial configuration since it must keep track of all points from each of the reference configurations. For a closed system, the first law of thermodynamics states

$$\frac{d}{dt} E(t) = \dot{Q}(t) + \dot{W}(t) \tag{A.3.31}$$

where $E(t)$ is the total system energy, $\dot{Q}(t)$ is the heat flux into the system, and $\dot{W}(t)$ is the power input into the system. Each individual species also must obey the first law of thermodynamics for a closed system

$$\frac{d}{dt}E_\alpha(t) = \dot{Q}_\alpha(t) + \dot{W}_\alpha(t) \tag{A.3.32}$$

with the subscripts now defining partial energy, heat flux, and work for each species. For general mechanical deformation, the energy E_α for a species is the sum of contributions due to component kinetic energy and internal energy:

$$E_\alpha(t) = K_\alpha(t) + U_\alpha(t). \tag{A.3.33}$$

In terms of integrals, these are written as:

$$\begin{aligned} K_\alpha(t) &= \int_{\Omega(t)} \frac{1}{2}\rho_\alpha(\boldsymbol{x},t)v_i^\alpha(\boldsymbol{x},t)v_i^\alpha(\boldsymbol{x},t)dv \\ &= \int_{\Omega_\alpha} \frac{1}{2}\rho_{\alpha 0}(\boldsymbol{X}_\alpha)\theta_\alpha(\boldsymbol{X}_\alpha,t)V_i^\alpha(\boldsymbol{X}_\alpha,t)V_i^\alpha(\boldsymbol{X}_\alpha,t)dV_0^\alpha \end{aligned} \tag{A.3.34}$$

and

$$\begin{aligned} U_\alpha(t) &= \int_{\Omega(t)} \rho_\alpha(\boldsymbol{x},t)u_\alpha(\boldsymbol{x},t)dv \\ &= \int_{\Omega_\alpha} \rho_{\alpha 0}(\boldsymbol{X}_\alpha)\theta_\alpha(\boldsymbol{X}_\alpha,t)U_\alpha(\boldsymbol{X}_\alpha,t)dV_0^\alpha \end{aligned} \tag{A.3.35}$$

where $u_\alpha(\boldsymbol{x},t)$ is the internal energy per unit mass of species α in the spatial configuration and $U_\alpha(\boldsymbol{X}_\alpha,t)$ is the internal energy per unit mass of species α in the reference configuration. Note that the definition (A.3.35) makes the two numerically equivalent when the point $\boldsymbol{x}_i$ corresponds to the point $\boldsymbol{X}_\alpha$; the distinction between the two is solely due to which configuration they are defined over. From here on, we use this nomenclature difference to drop functional dependencies of variables since it should be clear which configuration the variable is defined over. The heat flux for each species α can be defined as follows:

$$\begin{aligned} \dot{Q}_\alpha(t) &= -\int_{\partial\Omega(t)} q_i^\alpha(\boldsymbol{x},t)n_i ds + \int_{\Omega(t)} \rho_\alpha h_\alpha(\boldsymbol{x},t)dv + \int_{\Omega(t)} \psi_\alpha(\boldsymbol{x},t)dv \\ &= -\int_{\partial\Omega_\alpha} Q_I^\alpha(\boldsymbol{x},t)N_I^\alpha dS_0^\alpha + \int_{\Omega_\alpha} \rho_{\alpha 0}\theta_\alpha H_\alpha(\boldsymbol{X}_\alpha,t)dV_0^\alpha + \int_{\Omega_\alpha} \Psi_\alpha(\boldsymbol{X}_\alpha,t)dV_0^\alpha. \end{aligned} \tag{A.3.36}$$

Here, we introduce $q_i^\alpha(\boldsymbol{x},t)$, the partial Cauchy heat flux vector (leaving species α), and $Q_I^\alpha(\boldsymbol{X}_\alpha,t)$, the Piola–Kirchhoff heat flux vector related to the Cauchy heat flux vector by the Piola transform:

$$Q_J^\alpha F_{iJ}^\alpha = J_\alpha q_i^\alpha. \tag{A.3.37}$$

In addition $h_\alpha(\boldsymbol{x},t)$ is the generic internal heating rate for species α in the spatial configuration, and $H_\alpha(\boldsymbol{X}_\alpha,t)$ is the internal heating rate in the reference configuration; $\psi_\alpha(\boldsymbol{x},t)$ is a heating rate due to component interaction (analogous in idea to $b_i^\alpha(\boldsymbol{x},t)$ for the momentum balance) in the spatial configuration, and $\Psi_\alpha(\boldsymbol{X}_\alpha,t)$ is the same rate in the reference configuration. By definition, $\Psi_\alpha = J_\alpha\psi_\alpha$. The partial Cauchy heat flux vectors are simply a breakdown of the total Cauchy heat flux vector

$$q_i(\boldsymbol{x},t) = \sum_\alpha q_i^\alpha. \tag{A.3.38}$$

To define the total system heat flux $\dot{Q}(t)$, we simply sum (A.3.36)

$$\dot{Q}(t) = \sum_\alpha \dot{Q}_\alpha(t) = -\int_{\partial\Omega(t)} q_i n_i ds + \int_{\Omega(t)} \rho h(\boldsymbol{x},t) dv + \int_{\Omega(t)} \sum_\alpha \psi_\alpha dv \tag{A.3.39}$$

with $h(\boldsymbol{x},t)$ the barycentric internal heat source

$$\rho h = \sum_\alpha \rho_\alpha h_\alpha. \tag{A.3.40}$$

Rewriting the heat flux expressions (A.3.38) and (A.3.39) using the divergence theorem yields

$$\begin{aligned}\dot{Q}_\alpha(t) &= \int_{\Omega(t)} \left\{-q_{i,i}^\alpha + \rho_\alpha h_\alpha + \psi_\alpha\right\} dv \\ &= \int_{\Omega_\alpha} \left\{-Q_{I,I}^\alpha + \rho_{\alpha 0}\theta_\alpha H_\alpha + \Psi_\alpha\right\} dV_0^\alpha\end{aligned} \tag{A.3.41}$$

and

$$\dot{Q}(t) = \int_{\Omega(t)} \left\{-q_{i,i} + \rho h + \sum_\alpha \psi_\alpha\right\} dv. \tag{A.3.42}$$

The power input done on the system of species α is due to a combination of external and internal forces:

$$\begin{aligned}\dot{W}_\alpha(t) &= \int_{\partial\Omega(t)} t_i^\alpha v_i^\alpha ds + \int_{\Omega(t)} \rho_\alpha f_i^\alpha v_i^\alpha dv + \int_{\Omega(t)} b_i^\alpha v_i^\alpha dv \\ &= \int_{\partial\Omega_\alpha} T_i^\alpha V_i^\alpha dS_0^\alpha + \int_{\Omega_\alpha} \rho_{\alpha 0}\theta_\alpha F_i^\alpha V_i^\alpha dV_0^\alpha + \int_{\Omega_\alpha} B_i^\alpha V_i^\alpha dV_0^\alpha.\end{aligned} \tag{A.3.43}$$

The first term represents the rate of work done by the external tractions; the second and third terms represent the rate of work done by the external and internal body forces defined above. Using the divergence theorem, and the definition of the partial stress tensors (A.3.13) and (A.3.17), (A.3.43) becomes:

$$\dot{W}_\alpha(t) = \int_{\Omega(t)} \left\{\left[\sigma_{ij,j}^\alpha + \rho_\alpha f_i^\alpha + b_i^\alpha\right] v_i^\alpha + \sigma_{ij}^\alpha L_{ij}^\alpha\right\} dv$$

$$= \int_{\Omega_\alpha} \left\{ \left[P^\alpha_{iJ,J} + \rho_{\alpha 0}\theta_\alpha F^\alpha_i + B^\alpha_i \right] V^\alpha_i + P^\alpha_{iJ}\dot{F}^\alpha_{iJ} \right\} dV^\alpha_0 \tag{A.3.44}$$

where $L^\alpha_{ij}(\boldsymbol{x},t) = v^\alpha_{i,j}(\boldsymbol{x},t)$ is the species spatial velocity gradient and $\dot{F}_{iJ}$ is the material velocity gradient (superscript dot denotes differentiation with respect to time). This can be simplified by using conservation of linear momentum—(A.3.22) and (A.3.24)—to separate out the portion of work which changes the species kinetic energy (A.3.34) from that which is stored in the system:

$$\begin{aligned} \dot{W}_\alpha(t) &= \frac{d}{dt}K_\alpha(t) + \int_{\Omega(t)} \left\{ \sigma^\alpha_{ij}L^\alpha_{ij} + \frac{1}{2}r_\alpha v^\alpha_i v^\alpha_i \right\} dv \\ &= \frac{d}{dt}K_\alpha(t) + \int_{\Omega_\alpha} \left\{ P^\alpha_{iJ}\dot{F}^\alpha_{iJ} + \frac{1}{2}R_\alpha V^\alpha_i V^\alpha_i \right\} dV^\alpha_0. \end{aligned} \tag{A.3.45}$$

Summing the first of these equations for all species yields the overall power input for the system

$$\dot{W}(t) = \sum_\alpha \dot{W}_\alpha(t) = \frac{d}{dt}K(t) + \int_{\Omega(t)} \left\{ \sum_\alpha \left[\frac{1}{2}r_\alpha v^\alpha_i v^\alpha_i + \sigma^\alpha_{ij}L^\alpha_{ij} \right] \right\} dv; \tag{A.3.46}$$

the total system kinetic energy is simply the sum of the species kinetic energies

$$K(t) = \sum_\alpha K_\alpha(t). \tag{A.3.47}$$

Filling in the pieces of (A.3.32), we see that the component energy balance is

$$\begin{aligned} \frac{d}{dt}U_\alpha(t) &= \int_{\Omega(t)} \left\{ -q^\alpha_{i,i} + \rho_\alpha h_\alpha + \psi_\alpha \right\} dv + \int_{\Omega(t)} \left\{ \frac{1}{2}r_\alpha v^\alpha_i v^\alpha_i + \sigma^\alpha_{ij}L^\alpha_{ij} \right\} dv \\ &= \int_{\Omega_\alpha} \left\{ -Q^\alpha_{I,I} + \rho_{\alpha 0}\theta_\alpha H_\alpha + \Psi_\alpha \right\} dV^\alpha_0 + \int_{\Omega_\alpha} \left\{ \frac{1}{2}R_\alpha V^\alpha_i V^\alpha_i + P^\alpha_{iJ}\dot{F}^\alpha_{iJ} \right\} dV^\alpha_0. \end{aligned} \tag{A.3.48}$$

Expanding out the time derivative, we can write this expression in terms of the partial internal energy densities (A.3.35). Using the Reynold's transport theorem and the divergence theorem, we get the equation of conservation of energy for the spatial configuration

$$\rho_\alpha \frac{D^{(\alpha)}u_\alpha}{Dt} + r_\alpha u_\alpha = -q^\alpha_{i,i} + \sigma^\alpha_{ij}L^\alpha_{ij} + \rho_\alpha h_\alpha + \psi_\alpha + \frac{1}{2}r_\alpha v^\alpha_i v^\alpha_i \tag{A.3.49}$$

and for the reference configuration

$$\rho_{\alpha 0}\theta_\alpha \dot{U}_\alpha + R_\alpha U_\alpha = -Q^\alpha_{I,I} + P^\alpha_{iJ}\dot{F}^\alpha_{iJ} + \rho_{\alpha 0}\theta_\alpha H_\alpha + \Psi_\alpha + \frac{1}{2}R_\alpha V^\alpha_i V^\alpha_i. \tag{A.3.50}$$

Noting that $E(t) = \sum_\alpha E_\alpha(t)$, we can rewrite the total system energy balance (A.3.31) using the expressions for the heat input (A.3.39) and power input (A.3.46):

$$\rho \frac{Du}{Dt} = -q_{i,i} + \rho h + \sum_\alpha \left\{ \sigma_{ij}^\alpha L_{ij}^\alpha + \frac{1}{2} r_\alpha v_i^\alpha v_i^\alpha - \left[\rho_\alpha u_\alpha \left(v_i^\alpha - v_i \right) \right]_{,i} + \psi_\alpha \right\}. \tag{A.3.51}$$

Here we define $u(\boldsymbol{x}, t)$ as the barycentric internal energy per unit mass

$$\rho u = \sum_\alpha \rho_\alpha u_\alpha. \tag{A.3.52}$$

In order to be consistent, species interactions should not have an overall affect on the barycentric energy of the system. In terms of variables, this constraint is expressed via

$$\sum_\alpha \left[\psi_\alpha + b_i^\alpha v_i^\alpha \right] = 0 \tag{A.3.53}$$

with the first term being the energy interaction between species and the second term being the rate of work done by the internal body forces. Use of (A.3.53) allows an alternate expression for (A.3.51):

$$\rho \frac{Du}{Dt} = -q_{i,i} + \rho H + \sum_\alpha \left\{ \sigma_{ij}^\alpha L_{ij}^\alpha + \frac{1}{2} r_\alpha v_i^\alpha v_i^\alpha - b_i^\alpha v_i^\alpha - \left[\rho_\alpha u_\alpha \left(v_i^\alpha - v_i \right) \right]_{,i} \right\}. \tag{A.3.54}$$

For a single component, this relation reduces to the well-known equation of a single continua.

A.4 Clasius–Duhem Inequality

In continuum mechanics—and therefore the subset of mixture theory—the Clausius–Duhem inequality is used to postulate constitutive relations that are in keeping with the second law of thermodynamics. The second law of thermodynamics states that for any body $\Omega(t)$, there exists a state function $S(t)$ such that

$$\frac{dS}{dt} \geq \frac{dS_{ext}}{dt} \tag{A.4.1}$$

where $S_{ext}(t)$ is related to the rate of heat input to the system by

$$\frac{dS_{ext}}{dt} = -\int_{\partial\Omega(t)} \frac{q_i}{T} n_i ds + \int_{\Omega(t)} \rho \frac{h}{T} dv. \tag{A.4.2}$$

Here, we introduce the idea of a thermodynamic absolute temperature T. If the equality of (A.4.1) holds, the process is said to be reversible. Otherwise, the process is irreversible. Irreversible processes

always increase the entropy of the system. $S(t)$ can be written in terms of an entropy density

$$S(t) = \int_{\Omega(t)} \rho(\boldsymbol{x},t)s(\boldsymbol{x},t)dv = \int_{\Omega(t)} \sum_{\alpha} \rho_\alpha(\boldsymbol{x},t)s_\alpha(\boldsymbol{x},t)dv \tag{A.4.3}$$

where $s(\boldsymbol{x},t)$ is the entropy per unit mass and $s_\alpha(\boldsymbol{x},t)$ is the partial entropy. Using these in (A.4.1) yields (with (A.5.14)):

$$\rho\frac{Ds}{Dt} + \left(\frac{q_i}{T}\right)_{,i} - \frac{\rho h}{T} + \sum_{\alpha}\left[\rho_\alpha s_\alpha\left(v_i^\alpha - v_i\right)\right]_{,i} \geq 0. \tag{A.4.4}$$

This relation is the Clausius–Duhem inequality. A more useful form of this inequality can be rewritten using the system energy balance (A.3.52) to remove the internal heating term

$$\begin{aligned}\rho\left(T\frac{Ds}{Dt} - \frac{Du}{Dt}\right) + \sum_{\alpha}\Big\{&\sigma_{ij}^\alpha L_{ij}^\alpha - b_i^\alpha v_i^\alpha + \frac{1}{2}r_\alpha v_i^\alpha v_i^\alpha + \\ &T\left[\rho_\alpha s_\alpha\left(v_i^\alpha - v_i\right)\right]_{,i} - \left[\rho_\alpha u_\alpha\left(v_i^\alpha - v_i\right)\right]_{,i}\Big\} - \frac{q_i}{T}T_{,i} \geq 0\end{aligned} \tag{A.4.5}$$

and rewriting in terms of the Helmholtz free energy per unit mass $f(\boldsymbol{x},t) = u(\boldsymbol{x},t) - T(\boldsymbol{x},t)s(\boldsymbol{x},t)$

$$-\rho\left(\frac{Df}{Dt} + s\frac{DT}{Dt}\right) + \sum_{\alpha}\left\{\sigma_{ij}^\alpha L_{ij}^\alpha - b_i^\alpha v_i^\alpha + \frac{1}{2}r_\alpha v_i^\alpha v_i^\alpha\right\} - \Sigma_i T_{,i} - \Theta \geq 0 \tag{A.4.6}$$

where

$$\Sigma_i = \frac{1}{T}\sum_{\alpha}\left[q_i^\alpha + \rho_\alpha T s_\alpha\left(v_i^\alpha - v_i\right)\right] \tag{A.4.7}$$

and

$$\Theta = \sum_{\alpha}\left[\rho_\alpha f_\alpha\left(v_i^\alpha - v_i\right)\right]_{,i}. \tag{A.4.8}$$

The last two variables introduced are a modified heat flux and a term relating to the change in Helmholtz free energy due to diffusion, respectively. The main reason for their inclusion is to simplify the Clasius–Duhem inequality for a two-component system.

A.5 Supplemental Section

We examine the question of differentiation under integral signs. For example, for integrals over a species reference configuration, we wish to examine:

$$\frac{d}{dt}\int_{\Omega_\alpha} Y_\alpha(\boldsymbol{X}_\alpha,t)dV_0^\alpha \tag{A.5.1}$$

where $Y_\alpha(\boldsymbol{X}_\alpha, t)$ is a generic property defined over the reference configuration of species α. Since the species reference is set with respect to time, we can bring the derivative inside the integral. In addition, the marked coordinates $\boldsymbol{X}_\alpha$ do not depend upon time either. For this reason, we can write:

$$\frac{d}{dt}\int_{\Omega_\alpha} Y_\alpha(\boldsymbol{X}_\alpha, t) dV_0^\alpha = \int_{\Omega_\alpha} \frac{\partial Y_\alpha}{\partial t}(\boldsymbol{X}_\alpha, t) dV_0^\alpha. \tag{A.5.2}$$

We will also need to deal with differentiating integrals containing spatial variables $y_\alpha(\boldsymbol{x}, t)$ over the spatial configuration $\Omega(t)$. This looks like:

$$\frac{d}{dt}\int_{\Omega(t)} y_\alpha(\boldsymbol{x}, t) dv. \tag{A.5.3}$$

Now, however, the integral does depend on time. In order to bring the derivative inside, we can make use of the identity $dv = J_\alpha dV_0^\alpha$ so that:

$$\int_{\Omega(t)} y_\alpha(\boldsymbol{x}, t) dv = \int_{\Omega_\alpha} y_\alpha(\boldsymbol{x}, t) J_\alpha(\boldsymbol{X}_\alpha, t) dV_0^\alpha. \tag{A.5.4}$$

Now, we can bring the time derivative inside:

$$\int_{\Omega_\alpha} \frac{D^{(\alpha)}}{Dt}\left[y_\alpha(\boldsymbol{x}, t) J_\alpha(\boldsymbol{X}_\alpha, t)\right] dV_0^\alpha. \tag{A.5.5}$$

Here, we introduce the notation:

$$\frac{D^{(\alpha)}}{Dt} \tag{A.5.6}$$

as the species material gradient. This is essentially a notational convention to remind ourselves that we have made use of (A.5.4) in order to bring the derivative inside the integral. Expanding out the derivative using kinematic definitions, it can be shown that:

$$\frac{d}{dt}\int_{\Omega(t)} y_\alpha(\boldsymbol{x}, t) dv = \int_{\Omega(t)} \left(\frac{D^{(\alpha)} y_\alpha}{Dt} + y_\alpha v^\alpha_{i,i}\right) dv, \tag{A.5.7}$$

which is the Reynold's transport theorem applied to a multicomponent system. From (A.5.2) we see that the species material gradient operating on a property $Y_\alpha(\boldsymbol{X}_\alpha, t)$ defined in the reference configuration is given as

$$\frac{D^{(\alpha)} Y_\alpha}{Dt}(\boldsymbol{X}_\alpha, t) = \frac{\partial Y_\alpha}{\partial t}(\boldsymbol{X}_\alpha, t) \tag{A.5.8}$$

since $\boldsymbol{X}_\alpha$ does not depend upon time. For spatial variables $y_\alpha(\boldsymbol{x}, t)$, on the other hand, $\boldsymbol{x} = \varphi_\alpha(\boldsymbol{X}_\alpha, t)$ does depend upon time. The product rule then gives:

$$\frac{D^{(\alpha)} y_\alpha}{Dt}(\boldsymbol{x}, t) = \frac{\partial y_\alpha}{\partial t}(\boldsymbol{x}, t) + v_i^\alpha(\boldsymbol{x}, t)\frac{\partial y_\alpha}{\partial x_i}(\boldsymbol{x}, t). \tag{A.5.9}$$

For overall material properties, such as the total density defined in (A.2.4) or the barycentric velocity defined in (A.2.4), it becomes convenient to define the total material time derivative as:

$$\frac{Dy}{Dt}(\boldsymbol{x},t) = \frac{\partial y}{\partial t}(\boldsymbol{x},t) + v_i(\boldsymbol{x},t)\frac{\partial y}{\partial x_i}(\boldsymbol{x},t) \tag{A.5.10}$$

with $y(\boldsymbol{x},t)$ being a spatial variable field and v_i being the barycentric velocity defined in (A.2.8).

If a property $y(\boldsymbol{x},t)$ is defined barycentrically, i.e.,:

$$\rho y = \sum_\alpha \rho_\alpha y_\alpha. \tag{A.5.11}$$

The species material derivative and the barycentric material derivative are related by:

$$\sum_\alpha \frac{D^{(\alpha)}}{Dt}(\rho_\alpha y_\alpha) = \frac{D}{Dt}(\rho y) + \sum_\alpha (v_i^\alpha - v_i)\frac{\partial}{\partial x_i}(\rho_\alpha y_\alpha). \tag{A.5.12}$$

Using conservation of mass (A.3.6) and the definition of the partial and total material derivatives, it can be shown that (6/7/06):

$$\sum_\alpha \left[\rho_\alpha \frac{D^{(\alpha)} y_\alpha}{Dt} + r_\alpha y_\alpha\right] = \rho\frac{Dy}{Dt} + \sum_\alpha \left[\rho_\alpha y_\alpha \left(v_i^\alpha - v_i\right)\right]_{,i}. \tag{A.5.13}$$

Combining (A.5.7) and (A.5.13) yields the useful identity (6/7/06):

$$\frac{d}{dt}\int_{\Omega(t)} \rho y dv = \int_{\Omega(t)} \left\{\rho\frac{Dy}{Dt} + \sum_\alpha \left[\rho_\alpha y_\alpha \left(v_j^\alpha - v_j\right)\right]_{,j}\right\} dv. \tag{A.5.14}$$

Appendix B

Material Parameters and Scaling Analysis

B.1 Materials

In this appendix, we include information about the materials used by Pape [1] when used as an example for our theory. In his work, the elastomeric photopolymer consists of a PDMS network (Fig. B.1) swollen with PDMS macromer with bismethacrylate endcaps (Fig. B.2). The photoinitiator used is DMPO (2,2–dimethoxy-1,2–diphenylethan–1–one), which has a strong absorbance in the UV spectra (365 nm). The PDMS precursor chains used to create the networks had average molar masses ranging through 15.2, 22.3, and 41.2 kg/mol, and polydispersity indexes between 1.11 and 1.24. The macromer molecules had average molar masses, M_m, of 500 g/mol, 1000 g/mol, 3000 g/mol, and 5000 g/mol [1].

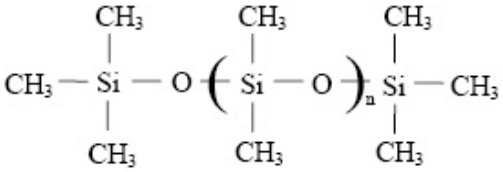

Figure B.1: The chemical structure of a polydimethylsiloxane network

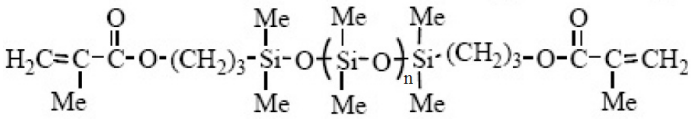

Figure B.2: Chemical structure of a macromer molecule

B.2 Determination of χ for Host Networks

Numerous PDMS host networks were prepared by varying the precursor chain length and initial volume fraction of small molecule diluent [1]. The modulus of the material G_{dry} was determined by rheometry once the diluent was removed. These host networks were then swollen in a bath of macromer of varying molar masses (M_m = 500, 1000, and 3000 g/mol) and the equilibrium swelling ratio was determined. Using the Flory–Rehner equation (2.2.23), the value of the Flory χ interaction parameter was determined for each host network/macromer pairing.

Figure B.3 presents the results obtained for χ by using data obtained in [1]. The χ parameter is found to decrease as macromer molar mass increases. This is because the repulsive effects of the methacrylate endgroups are mitigated by increasing the number of repeat backbone segments chemically similar to the host network. There is also a slight dependence of χ on the host network. This is in keeping with work by other groups that has determined that the interaction parameter can vary with degree of crosslinking in the system [100]. To make use of this data, we fit a linear equation to each molar mass data set and record the slope and intercept. The results are shown in Table B.1. Also shown are the r^2 value for the linear fit and a characteristic value of χ at G_{dry} = 0.18 MPa. The molar masses M_m = 500, 1000, and 3000 g/mol span a broad range of solvents from poor, to near theta, to good, respectively.

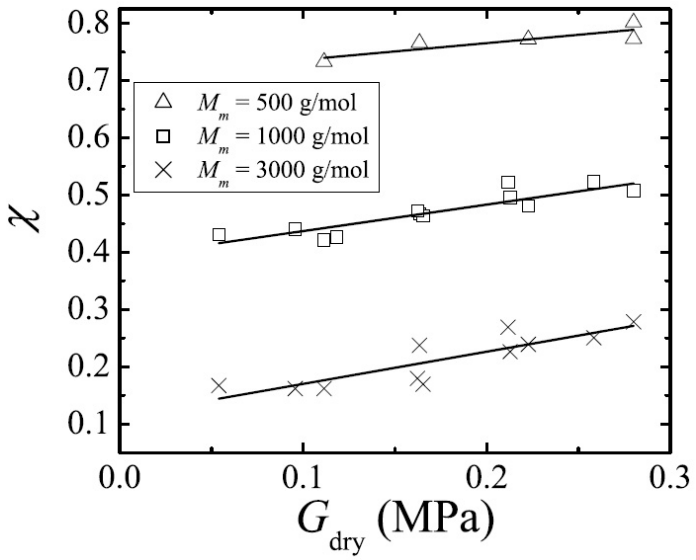

Figure B.3: The Flory interaction parameter χ for bismethacrylate end-capped PDMS macromers swollen into model PDMS host networks as a function of G_{dry} and M_m. Symbols show experimental results. Dry modulus and equilibrium swelling behavior contained in [1] were used to calculate χ from the Flory–Rehner equation (2.2.23). The interaction parameter depends strongly upon M_m, solvent quality varying from poor (M_m = 500 g/mol), to near theta (M_m = 1000 g/mol), to good (M_m = 3000 g/mol). χ also varies with G_{dry}. Linear regression parameters fit to this variation are contained in Table B.1.

M_m, **g/mol**	a **(MPa^{-1})***	b*	r^2	**Sample χ****	**Solvent Quality**
500	0.290	0.708	0.761	0.760	Poor
1000	0.462	0.391	0.793	0.474	Near Theta
3000	0.564	0.113	0.743	0.215	Good

* $\chi = aG_{\text{dry}} + b$

** For $G_{\text{dry}} = 0.18$ MPa, taken as a representative value

Table B.1: Linear regression parameters obtained for χ as a function of G_{dry} and M_m.

B.3 Experimental Parameters to Theoretical Parameters

Taking experimentally obtained network shear modulus and equilibrium swelling data for these materials, we translate sets of material parameters G_{dry} and M_m into theory parameters χ and ϵ (Table B.2). The ϵ parameters are found as a function of the dry network shear modulus G_{dry} through (2.2.17), with G_{os} given by (2.2.15). The corresponding χ parameter is found using the linear interpolation parameters given in Table B.1. It can be seen that ϵ is small, particularly for $M_m = 500$ and 1000 g/mol. The χ parameter ranges between 0 and 1 and capture good ($\chi < 0.5$), theta ($\chi = 0.5$), and poor ($\chi > 0.5$) solvent conditions.

M_m	500 g/mol		1000 g/mol		3000 g/mol	
G_{dry}, MPa	ϵ	χ	ϵ	χ	ϵ	χ
0.10	0.020	0.737	0.039	0.437	0.117	0.169
0.18	0.035	0.760	0.070	0.474	0.211	0.215
0.28	0.055	0.789	0.109	0.520	0.328	0.271

Table B.2: The ϵ and χ parameters for different molar mass macromer, M_m, in different starting networks, characterized by dry modulus, G_{dry}. The χ parameters are obtained from a linear fit to experimental data (Table B.1) and the ϵ parameters are calculated from (2.2.17).

B.4 Determination of Diffusivity from Experimental Data

To determine physically appropriate values of $\mathcal{D}$, we turn to experimental data obtained by Pape [1]. The transient swelling data in Pape's thesis consisted of swelling a dry network isotropically and measuring the mass uptake of macromer as a function of time. The diffusivity was then determined by fitting the initial slope of mass uptake against time data to the solution of

$$\frac{\partial \phi}{\partial t} = \mathcal{D}_{\text{Pape}} \nabla^2 \phi, \tag{B.4.1}$$

the diffusion equation for counter–diffusing small molecules. In this equation, the system flux is specified as

$$J_i^m = -\mathcal{D}_{\text{Pape}} \nabla \phi. \tag{B.4.2}$$

Figure B.4a shows the diffusivities obtained by Pape using (B.4.2) (taken directly from Table 5.1 of [1]). As expected, the diffusivity decreases with increasing M_m: longer macromer molecules diffuse more slowly through the same network. Additionally, the diffusivity of macromer in the network depends strongly upon the network modulus: for example, for $M_m = 1000$ g/mol macromer, increasing the network modulus fivefold (from 0.054 MPa to 0.28 MPa) causes the diffusivity to increase by a factor of three (from 4.1×10^{-12} m^2/s to 12.8×10^{-12} m^2/s). These counter–intuitive changes are attributed by Pape to tighter networks selectively sorbing the smaller molecules from a polydisperse macromer sample.

We renormalize the diffusivity values obtained by Pape according to the constitutive law we have developed for the flux (3.4.37). Doing so removes the dependence of the diffusivity on network modulus, and yields well-defined diffusivity values solely as a function of the macromer molar mass. For the isotropic swelling ($\sigma^c_{ij} = 0$) of an uncured ($\xi = 0$, $\theta = 1$) elastomeric photopolymer, (3.4.37) can be written in terms of a gradient in volume fraction by expanding $\nabla\mu$:

$$\mathbf{J}_m = -\rho\mathcal{D}\left[(1-\phi)(1-2\chi\phi) - \frac{1}{3}\epsilon\phi(1-\phi)^{-2/3} + \frac{1}{2}\epsilon\phi\right]\nabla\phi. \tag{B.4.3}$$

To compare to (B.4.2), we define an apparent diffusivity as

$$\mathcal{D}_{ap}(\phi;\chi,\epsilon) \equiv \mathcal{D}\left[(1-\phi)(1-2\chi\phi) - \frac{1}{3}\epsilon\phi(1-\phi)^{-2/3} + \frac{1}{2}\epsilon\phi\right], \tag{B.4.4}$$

which is a function of the volume fraction of macromer and the material parameters in the system. Consider the contributions to the apparent diffusivity, beginning with the stretching terms which scale with ϵ. The second term represents a penalty to diffusion due to isotropic stretching of network chains and dominates the apparent diffusivity as ϕ becomes larger. In general, it is this term which establishes equilibrium by decreasing the apparent diffusivity to zero near the equilibrium volume fraction. Conversely, the third term represents a positive entropic benefit to adding macromer. In general, this term stems from the configurations available to the network crosslinks; more configurations are available to the network crosslinkswith more volume fraction and larger volume. The first term in the apparent diffusivity represents solely mixing effects. As would be expected, larger values of χ decrease the diffusivity. Under conditions of ideal mixing ($\chi = 0$, $\epsilon \to 0$), we do not recover the equation for counter–diffusion of small molecules (B.4.2), but rather note that $\mathcal{D}_{ap} \to \mathcal{D}(1-\phi)$. This can be explained by recalling the energy contribution of mixing from Ch. 2. Since the network is a large molecule, it does not diffuse and therefore cannot add to the entropy of the system. As such, adding a single macromer molecule results in a significant increase in the number of configurations available to the system. Mixing in more than a single macromer molecule, however, results in net less configurations because the network itself does not diffuse. In this way, the diffusivity continually decreases as more and more macromer is added. Since (B.4.2) was developed for counter–diffusing

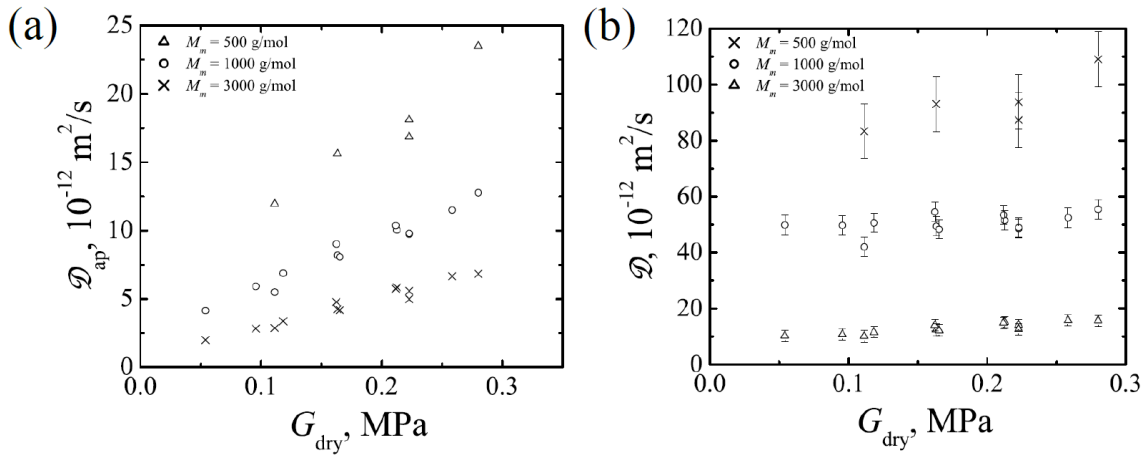

Figure B.4: The diffusivity of methacrylate end–capped macromer molecules with molar mass M_m in PDMS networks. The PDMS networks are characterized by their shear modulus G_{dry}. (a) Apparent diffusivity measured through mass uptake experiments by Pape [1]. Against our intuition, these are seen to increase strongly with network modulus. (b) The diffusivities obtained by Pape are rescaled according (B.4.5). The rescaled diffusivity values depend only upon the macromer chain length and are essentially independent of network modulus. These near-constant values are given in Table B.3.

M_m g/mol	$\mathcal{D}$ 10^{-12} m^2/s
500	93.3 ± 9.8
1000	50.4 ± 3.4
3000	13.1 ± 2.0

Table B.3: The average diffusivity of methacrylate end–capped macromer molecules in PDMS networks depends only on the macromer molar mass M_m. These values are obtained by renormalizing the diffusivity values reported in [1] through (3.3.3).

species, we cannot achieve this limit even at near-ideal conditions.

For this reason, we treat all the reported diffusivities, $\mathcal{D}_{\text{Pape}}$, as apparent diffusivities, $\mathcal{D}_{ap}$. The renormalized value of the diffusivity, $\mathcal{D}$, is obtained from $\mathcal{D}_{\text{Pape}}$ using the appropriate χ and ϵ values:

$$\mathcal{D} = \frac{\mathcal{D}_{\text{Pape}}}{(1-\phi_{eq})(1-2\chi\phi_{eq}) - \frac{1}{3}\epsilon\phi_{eq}(1-\phi_{eq})^{-2/3} + \frac{1}{2}\epsilon\phi_{eq}}. \tag{B.4.5}$$

Here, we use $\phi = \phi_{eq}$, the equilibrium swelling volume fraction obtained from the Flory–Rehner equation (2.2.23) for the appropriate choice of χ and ϵ. This corresponds to the volume fraction at the contact surface between the bath of macromer and the dry network and drives the initial diffusion (where $\mathcal{D}_{\text{Pape}}$ is measured). Figure B.4b shows the data from [1] renormalized through (B.4.5). Renormalized diffusivities still increase as the molecules get smaller (M_m decreases) but dependence upon G_{dry} has been eliminated. In this work, the value of $\mathcal{D}$ for a given macromer molar mass will be taken as the average of the values in Figure B.4b (shown in Table B.3).

B.5 Scaling Analyses

B.5.1 Conservation of Linear Momentum

The pure component densities of macromer and network are about the same:

$$\rho_m \sim \rho,\ \rho_N \sim \rho,$$

$\rho = 0.965$ g/mL for PDMS. Choose the characteristic length ξ so that the characteristic velocity is

$$U \sim \frac{\mathcal{D}}{\xi},$$

and $\mathcal{D}$ the characteristic diffusivity in the system. We may then scale the conservation equations in §3.3.2 using these scales:

$$\nabla \sim \xi^{-1} \qquad \mathbf{v}_m \sim U \qquad \mathbf{v}_N \sim U \qquad t \sim \frac{\xi}{U} \qquad \boldsymbol{\sigma}_m \sim G_{\text{OS}} \qquad \boldsymbol{\sigma}_N \sim G_{\text{OS}} \qquad \boldsymbol{b} \sim \frac{G_{\text{OS}}}{\xi}.$$

In the above, we have taken the characteristic value of the partial stresses and the diffusive body force to be the osmotic modulus G_{OS} and G_{OS}/ξ, respectively, based upon the constitutive relations developed for both (§3.4). We also assume that the velocities of macromer and network scale similarily. Lastly, we have assumed that all important processes have a time scale set by diffusion. Non–dimensionalizing conservation of linear momentum ((3.3.7)–(3.3.8)) with these quantities yields (note that an overbar represents a dimensionless quantity):

$$\frac{1}{\text{El}}\left(\bar{\rho}_m \frac{\partial \bar{\mathbf{v}}_m}{\partial \bar{t}} + \bar{\rho_m}\bar{\mathbf{v}}_m \bar{\nabla}\bar{\mathbf{v}}\right) = \bar{\nabla}\cdot\bar{\boldsymbol{\sigma}}_m + \frac{1}{\text{FrEl}}\bar{\rho}_m\bar{\boldsymbol{g}} + \bar{\boldsymbol{b}} \tag{B.5.1}$$

$$\frac{1}{\text{El}}\left(\bar{\rho}_m \frac{\partial \bar{\mathbf{v}}_m}{\partial \bar{t}} + \bar{\rho_m}\bar{\mathbf{v}}_m \bar{\nabla}\bar{\mathbf{v}}\right) = \bar{\nabla}\cdot\bar{\boldsymbol{\sigma}}_N + \frac{1}{\text{FrEl}}\bar{\rho}_N\bar{\boldsymbol{g}} + \bar{\boldsymbol{b}} \tag{B.5.2}$$

where we have introduced the dimensionless groups:

$$\text{El} \equiv \frac{G_{\text{OS}}}{\rho U^2} \qquad \text{Fr} \equiv \frac{U^2}{g\xi}.$$

The characteristic length scale of a light–adjustable lens is $\xi \sim \mathcal{O}(1\,\text{mm})$. With $\mathcal{D} \sim \mathcal{O}(10^{-11}\ \text{m}^2/\text{s})$ (Table B.3), this yields $U \sim \mathcal{D}/\xi \sim \mathcal{O}\left(1 \times 10^{-8}\text{m/s}\right)$ for the diffusion process. With a characteristic values for the modulus, $G_{\text{dry}} \sim \mathcal{O}(10^5\ \text{Pa})$ and $G_{\text{OS}} \sim G_{\text{dry}}/\epsilon \sim \mathcal{O}(10^6\ \text{Pa})$ (Table B.2), the dimensionless groups attain the following scales:

$$\text{El} \sim \mathcal{O}\left(10^{19}\right) \qquad \text{Fr} \sim \mathcal{O}\left(10^{-14}\right).$$

M_m	Viscosities Measured	Scaling Behavior
500 g/mol	7.465×10^{-3} Pa·s 7.498×10^{-3} Pa·s	$\mu_m \sim \mathcal{O}(10^{-3}$ Pa·s)
5000 g/mol	0.07240 Pa·s 0.07206Pa·s	$\mu_m \sim \mathcal{O}(10^{-2}$ Pa·s)

Table B.4: The viscosity of macromer obtained using cone and plate geometry with a 60 mm, 1° cone on TA instruments Advanced Rheometer 1000. All data obtained at 25°C. These results present only the Newtonian behavior observed over the majority of shear stress.

With these groups, (B.5.1) and (B.5.2) indicate that the inertial contributions to momentum are negligible when compared to the partial stresses and diffusive body force. This is not surprising since the diffusive process proceeds very slowly. In addition, the stresses induced by swelling are large enough to make the only external body forces (due to gravity) negligible.

B.5.2 Dynamic Macromer Stress

We wish to determine the relative importance of the dynamic contribution (3.4.18) to the macromer partial stress relative to the static stress $\hat{\sigma}_{ij}^m \sim G_{\text{OS}}$. To do this, we must scale γ and μ. Several experiments were performed in order to obtain a scaling estimate for macromer viscosity. These rheology tests were performed on a TA Instruments Advanced Rheometer 1000 at 25°C using cone and plate geometry with a 60 mm, 1° cone. Using a shear stress ramp from 1.768×10^{-3} Pa to 17.68 Pa, the data in Table B.4 were obtained. In these experiments, the macromer exhibited non–Newtonian behavior only at low torque; a region in which measurements are the most uncertain. Since the macromer exhibits Netwonian behavior over the majority of shear stresses except in this small portion where uncertainty is high, we have chosen only to report Newtonian viscosities here.

As can be seen, the macromer viscosity μ_m scales as $\mathcal{O}(10^{-2}$ Pa·s) at the highest value of molecular weight. Scaling of D_{ij}^m yields:

$$D_{ij}^m \sim L_{ij}^m \sim \frac{U}{\xi} \sim \mathcal{O}(10^{-5}\ 1/\text{s}) \tag{B.5.3}$$

where values are taken from §B.5.1. With these, $\mu D_{ij}^m \sim \mathcal{O}(10^{-7}$ Pa) and this portion of the dynamic stress (3.4.18) is negligible compared to the static contribution (scales as $G_{\text{OS}} \sim \mathcal{O}(10^6$ Pa)). Because the shear rate of macromer is so small and the osmotic modulus so large, we speculate that the term involving γ is likewise negligible, although we do not have any data to corroborate this.

Appendix C

Finite Element Solution Method

C.1 Meshing

The entire lens can be created by using symmetry operations on a base subset of points and tetrahedra. As such, we specify the points in one sixteenth of the lens, defined in the region $R \leq d/2$, $0 \leq \Phi \leq \pi/4$, $Z \geq 0$. We have also developed a refinement algorithm which divides all the lengths in a coarse-grain mesh in half and thus divides each tetrahedra into four smaller tetrahedra. This allows us to specify the points in the coarse mesh only, and a cross section of the points at $\Phi = 0$ is shown in Fig. C.1a; the refined cross–section can be seen in Fig. C.1b. Points were chosen to guarantee nine nodes through the middle thickness upon refinement (five nodes before refinement), with a slightly larger number of nodes along the radial direction.[1] The extra concentration of points in the square–edge is necessary to correctly capture this region. The final coarse and refined lens mesh are shown in Fig. C.2: the coarse mesh consists of 197 nodes among 752 tetrahedral elements, the fine mesh has 1305 nodes and 6016 tetrahedra; more details on mesh creation are contained in Appendix C. Each mesh is stored as a structure in a MATLAB file to be read as input for a given problem.

Along with the positions of each node, the mesh structure also stores the connections between nodes in a connectivity table. This is used along with surface equations to store the node numbers belonging to each of the five lens surfaces: the anterior and posterior caps, the cylindrical side of the square–edge, and the anterior and posterior annular square–edge areas. The positions of these surface nodes in time are used to determine global deformation measurables at any time step, the most relevant such parameter being the lens-power change (§6.3). In addition, the surface area of each of the five lens surfaces is also determined by summing area contributions from each triangle that defines the surface.

One method to determine the efficacy of our mesh is to compare the discretized volume—

[1] Although this results in several elements with aspect ratios larger in the radial direction than the thickness direction, the elemental aspect ratios are still smaller than the overall aspect ratio.

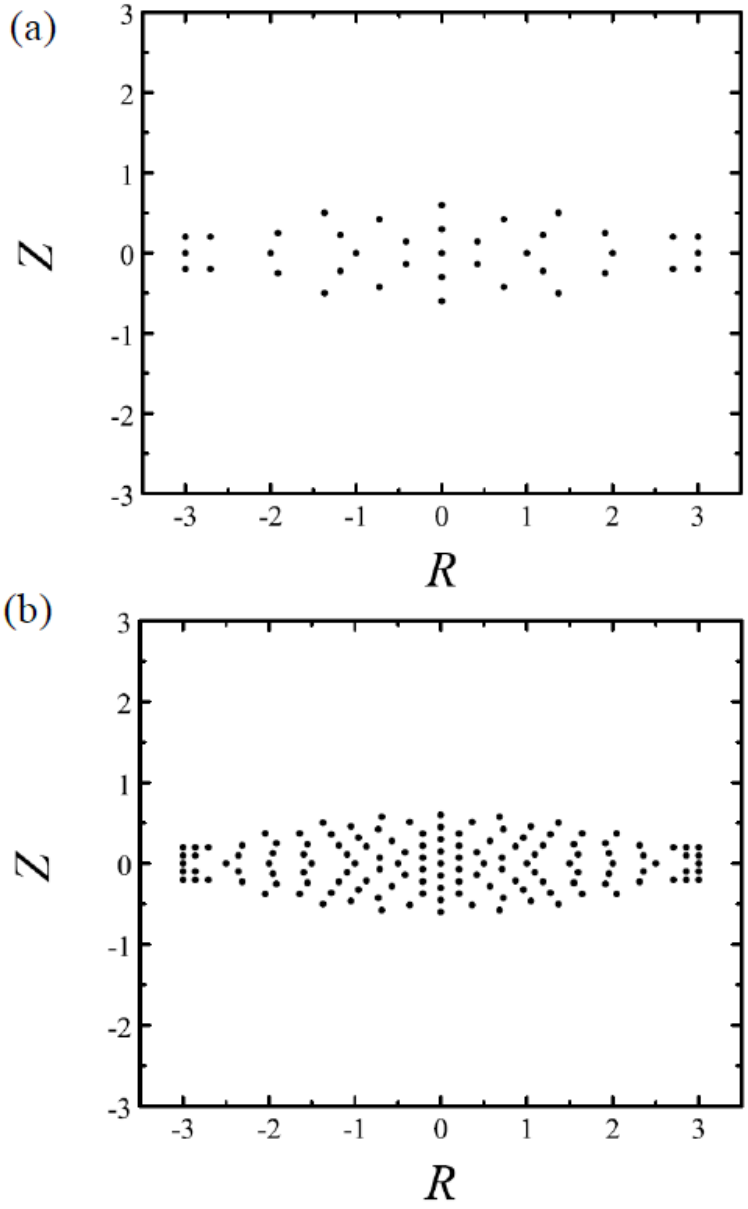

Figure C.1: The cross–section of the light-adjustable lens mesh at $\Phi = 0$ illustrating the internal placement of nodal points. (a) The coarse mesh contains approximately five points throughout the depth which, upon refinement (b), become nine points. The number of points in the radial direction is approximately equal to the number of points through the thickness in both cases.

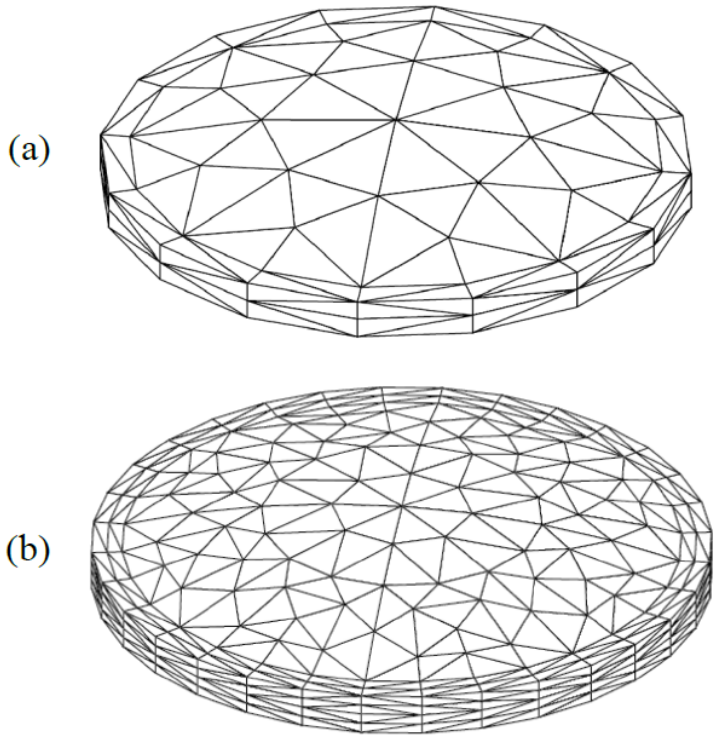

Figure C.2: (a) The coarse lens mesh contains 197 nodes and 752 elements. (b) The refined lens mesh contains 1305 nodes and 6016 elements. Geometric parameters used are taken from Table 6.1 and illustrated in Fig. 6.1. A cross section of the nodes at $\Phi = 0$ is shown in Fig. C.1.

	Coarse Mesh	Refined Mesh	Exact
Initial Volume (mm^3)	19.52	20.31	20.60
Anterior Area (mm^2)	22.92	23.39	23.55
Posterior Area (mm^2)	22.92	23.39	23.55
Square–Edge Annular Area (mm^2)	10.19	10.39	10.46
Square–Edge Side Area (mm^2)	7.49	7.53	7.54

Table C.1: Comparison of the initial volume and surface area to the exact value obtained through geometry. The refined mesh has less than 2% error in the volume and less than 1% error in the surface area.

calculated by adding up elemental volumes—with the exact volume calculated from geometry. Table C.1 shows the results for the lens meshes used here: there is less than 2% error in the refined mesh volume from the geometric value. We also compare the computational surface area to the exact surface area to check the surface connectivities, and the errors for the refined mesh are all found to be significantly less than one percent.

C.2 Procedure for Mesh Creation in MATLAB

1. Determine the smallest subunit of the mesh that cannot be broken down further by symmetry. This smallest subunit will be called the base subset; the full mesh will be created by using symmetry operations on this base subset.

2. Determine all the node positions for the base subset of the mesh structure. Although the number of nodes created needs to be appropriate to the mesh density required, the base subset can be slightly coarser (about 1/2 times) due to mesh refinement (done in Step 12 below). For this thesis, all the node positions were determined by developing a discretization by hand (with computational support to determine the actual values of the nodal points); see §C.2.1 for details on creation of the lens mesh. More advanced programs can be used to create more complicated meshes.

3. In MATLAB program "delaunay3.m" will use a simple Delaunay triangulation to determine the optimal connectivity (formation of tetrahedra) between points. The input to delaunay3.m are "x", "y", and "z", vectors of the X, Y, and Z coordinates of the points, respectively. The output will be a list of sets of four node numbers that correspond to each tetrahedron.

4. Create two .txt files. The "nodes.txt" file needs to have each node number listed along with the X, Y, and Z coordinate of that point (Cartesian coordinates), with each column separated by a tab. The easiest way to do this is to paste the nodal positions into an Excel spreadsheet and create an extra column with the node number out front. This can then be pasted into a .txt file. The "tetras.txt" file can be created by pasting the output of the delaunay3.m into

Excel, putting the element number in front and then pasting the composite into the .txt file.

5. Create a folder for the nodes.txt and tetras.txt file with the name for the mesh.

6. Run InputMesh.m for this base subset, choosing first the "nodes.txt" file and then the "tetras.txt" file just created when queried for input. A MATLAB-friendly structure for the mesh will be created in the new folder called "mesh.mat." One of the resultant fields for this mesh structure is the structure "Volume" which has fields containing the volumes of all elements. Check to make sure that the minimum volume ("Min" field) is not computationally zero. If the minimum volume is too small, some of the tetrahedra created by delaunay3.m are slivers and need to be removed manually from the tetras.txt file before proceeding; the ones that are slivers can be found by expanding the "Elements" field of Volume structure.

7. If symmetry operations need to be run to mirror portions of the mesh, the data for the base subset needs to be fed into the appropriate mirror function. There are currently four mirror function programs, each which mirrors about a plane: MirrorXYPlane.m, MirrorXZPlane.m, MirrorYZPlane.m, and MirrorYEqualsX.m. The output will be a set of the original points as well as all the newly created points. In addition, the code will mirror the tetrahedral connectivity and output a new list of all the elements, new and old. When mirroring points, make sure that all points lie on one side of the mirror plane or else the result will include tetrahedra within tetrahedra. The output to a single mirror step can be used as the input to the subsequent mirror step.

8. Once all mirroring operations have been performed, create the two .txt files with all of the nodes and tetrahedra included. These can replace the old ones or can be saved with different names or in a different folder.

9. Once again, run InputMesh.m, choosing all of the new nodes.txt and tetras.txt files as input. The mesh.mat structure created will store all the important mesh properties into a MATLAB-friendly file in the same folder as the original nodes.txt and tetras.txt. The name of the mesh will be the name of the containing folder. The parameters stored in this structure include the reference configuration position for each node, the connectivity table, the mesh size and mesh size statistics, the initial volume of each element, lists of connected pairs (and the distance between them), a table of the node numbers of the neighbors for each node, the system length scales, and the inverted M matrices used for the finite element code.

10. Discretize the mesh surface into a series of surface patches which can be represented by a single equation. For each surface path you create, you will create a surface structure "S" that has five fields:

(a) S.f: the function handle to the "On" function which returns 0 if the node is not on the surface and 1 if the node is on the surface. The current choices for the On function are: @OnPlanarSurface.m, @OnSphericalCapSurface.m, @OnSphericalSurface.m, @OnxyAnnularSurface.m, and @OnxyCylindricalSurface.m. In general, any surface can be created.

(b) S.Parameters: a vector of parameters used for evaluating the "On" function.

(c) S.Output: the name of the surface area for purposes of output.

(d) S.Eq: the equation to use when determining the midpoint between two points on the surface. Current options are @SphericalAverage.m and @PolarAverage.m.

(e) S.EqParameters: the parameter list to use with the equation that determines the midpoints along the surface. Once all the surface structures are created (which can be done by creating a quick .m file), store all of those structures in "surfaces.mat," a cell of surface structures, and save it in the original folder of the mesh.

11. Run "SetSurfaces.m" and choose the mesh.mat file you just created as the input. This takes the surfaces.mat file you created and appends the information to the mesh.mat file, including determining the node numbers that are on a particular surface, as well as all the triangles that fall along a surface (for purposes of calculating surface area).

12. Run "RefineMesh.m" on the mesh.mat that you just created. This creates a "refined mesh.mat" file that has divided each tetrahedra into eight tetrahedra by adding midpoints along all the sides. If the "SetSurfaces.m" step has been done correctly, the midpoints created from surface points will also be stored as being on the surface. This refinement step is necessary for all current applications: the refined mesh is used at short times to capture steep gradients in chemical potential whereas a coarser mesh is necessary to guarantee convergence at longer times.

C.2.1 Building the Full Lens

For images of lens geometry as well as a table of the appropriate parameters, refer to Fig. 6.1 and Table 6.1 in §6.1.

Because the anterior and posterior radii are the same, our symmetry operations begin by splitting the lens across the middle (symmetry about the XY–plane). We then divide the top section into eight pie slices, taking one of the pie slices as the base subset. This corresponds to 1/16 of the actual mesh. Note that the thickness direction of the lens is taken as the Z–direction and that the R and Θ polar coordinates are associated with the XY–plane.

Table C.2 shows the base subset of points. All points were chosen keeping in mind that the mesh would be refined. A cross–section illustrating the location of points at $\Theta = 0$ ($Y = 0$, Nodes 1–13)

	X	Y	Z
1	0	0	0.6
2	1.368941	0	0.499461
3	2.708505	0	0.2
4	0.728193	0	0.421661
5	1.91327	0	0.252584
6	0	0	0.3
7	1.185538	0	0.224697
8	0.419572	0	0.140601
9	0	0	0
10	3	0	0.2
11	3	0	0
12	1	0	0
13	2	0	0
14	1.888608	0.782287	0.374293
15	0.967988	0.967988	0.499461
16	1.915202	1.915202	0.2
17	0.51491	0.51491	0.421661
18	1.352886	1.352886	0.252584
19	0.838302	0.838302	0.224697
20	0.296682	0.296682	0.140601
21	2.12132	2.12132	0.2
22	2.12132	2.12132	0
23	0.707107	0.707107	0
24	1.414214	1.414214	0
25	2.771639	1.14805	0.2
26	2.771639	1.14805	0
27	2.502332	1.0365	0.2

Table C.2: The base subset of points used to generate the full-lens mesh. These points were obtained using the discretization scheme shown in Figure C.3

is shown in Fig. C.3a. These points are replicated at $\Theta = \pi/4$ (Nodes 15–24), as demonstrated in the top view (Fig. C.3b). Three additional points were included at $\Theta = \pi/8$ to ensure that the lens is well defined: Nodes 25–27, defining the square edge, and Node 14, which is just inside the surface of the lens.

1. The first points (1, 2, and 3) define the anterior (and through mirroring, the posterior) surface of the lens, located at radius of curvature R_a from the center of curvature (not shown due to scale). Node 1 is at the top of the lens, located at (0,0,$t_{max}/2$); Node 3 is located at ($d_i/2$,0,t_{min}). Node 2 is located on the surface half-way in between these two points, defined by the spherical angle β. This azimuthal angle is defined relative to the spherical coordinate system located at the center of curvature of the lens.

2. The haptics are modelled with three nodes: Node 3 (just discussed) and Nodes 10 and 11.

3. The midplane is divided into four equally spaced points (Nodes 9, 11, 12, and 13).

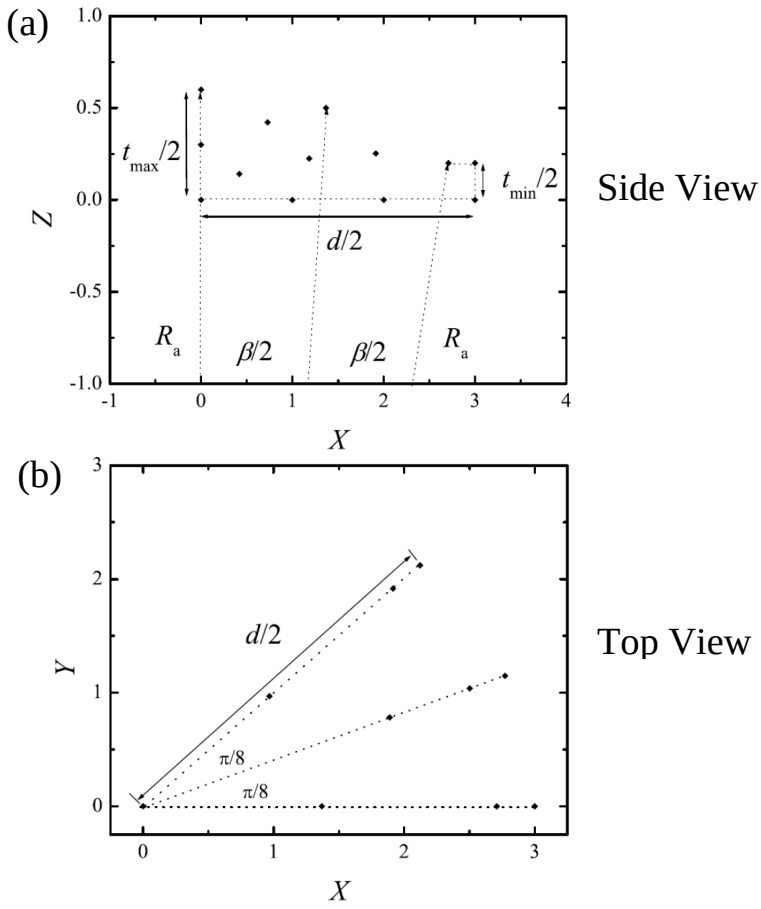

Figure C.3: Cross sections of the base subset illustrating the discretization method. (a) A side view of the XZ plane illustrates that the lens has two main sections: the inner optical volume and the outer square edge. The thickness of the lens in the middle is denoted $h_{\max}$ and the thickness of the square edge is denoted as $h_{\min}$. The radius of curvature of the anterior surface is denoted R_a. Three points are created through the thickness and four points along the radius. Points in between the surfaces are modelled on surface of constant radius from the center of curvature.

4. In order to capture steep gradients through the cross–section, we discretize three points through the depth; with refinement, this will yield nine nodes through the depth (five total with the mirror image, plus four more for refinement). Each of these points through the depth creates a "shell": a concentric spherical cap inside of the exterior spherical cap defining the top of the lens. Label the shells from the top to the midplane with k, $k = 1$ being the top shell. The top shell ($k = 1$) is already defined, so we turn to the $k = 2$ shell. Nodes 4 and 5 are located at spherical angles $\beta/4$ and $3\beta/4$; we do not include a point along the Z–axis since this point will appear with refinement. For $k = 3$, the axis point is included (Node 6 at $t_{max}/4$) and "mid–point" at $\beta/2$ (Node 7). The final shell ($k = 4$) includes one point (Node 8) at $\beta/4$.

Running these nodes through delaunay3.m yields the base subset connectivity table given in Table C.2.1 (47 tetrahedra); visualization of this base subset is seen in Fig. C.4. This base subset is mirrored across the $Y = X$ plane using MirrorYEqualsX.m to complete 1/8 of the mesh. This 1/8 of mesh is then mirrored three times using MirrorYZPlane.m, MirrorXZPlane.m, and MirrorXY-Plane.m, respectively, to complete the lens. Alternatively, these steps can all be completed in one step by running "RunFullLens.m" using the base subset points. This program also initializes the surfaces for the mesh based upon a lens mesh. Figure C.5 illustrates the lens output through these operations. This is the coarse grain mesh used at long times. Running RefineMesh.mat on this coarse mesh will generate the refined mesh.

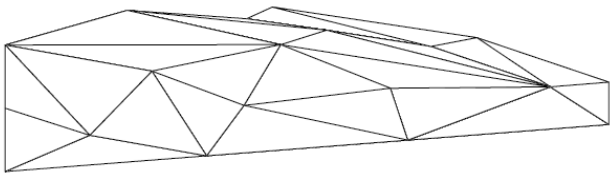

Figure C.4: Visualization of the base subset for the full-lens mesh viewing from the origin

C.2.2 Creating Mesh Visualization in MATLAB

1. alpha( ) sets the transparency of the figure. The argument is between zero and one so that:
   - 0: transparent
   - 1: completely solid.
2. Edit → Colormap → Tools → White will make the mesh black and white for printing.
3. Showaxes('hide') will hide the axes

1	16	26	24	22
2	15	4	2	1
3	27	13	26	11
4	27	13	26	24
5	27	13	24	14
6	27	16	24	14
7	27	16	26	24
8	27	16	21	22
9	17	15	4	1
10	17	15	4	19
11	12	13	24	14
12	18	19	24	14
13	18	15	19	14
14	18	16	24	14
15	18	15	16	14
16	3	27	25	26
17	3	27	13	11
18	3	5	13	14
19	3	27	13	14
20	3	5	2	14
21	20	17	4	1
22	7	12	4	19
23	7	15	4	2
24	7	15	4	19
25	7	12	19	14
26	7	15	2	14
27	7	15	19	14
28	7	5	2	14
29	7	5	13	14
30	7	12	13	14
31	8	20	4	1
32	6	8	20	9
33	6	8	20	1
34	23	8	12	9
35	23	8	20	9
36	23	8	20	17
37	23	8	12	4
38	23	8	17	4
39	23	19	24	14
40	23	12	24	14
41	23	12	19	14
42	23	17	4	19
43	23	12	4	19
44	27	25	26	21
45	27	26	21	22
46	3	25	26	11
47	3	10	25	11

Table C.3: The connectivity table generated by placing the base subset point locations (Table C.2) into the MATLAB delaunay3.m. Figure C.4 illustrates the mesh through MATLAB visualization software.

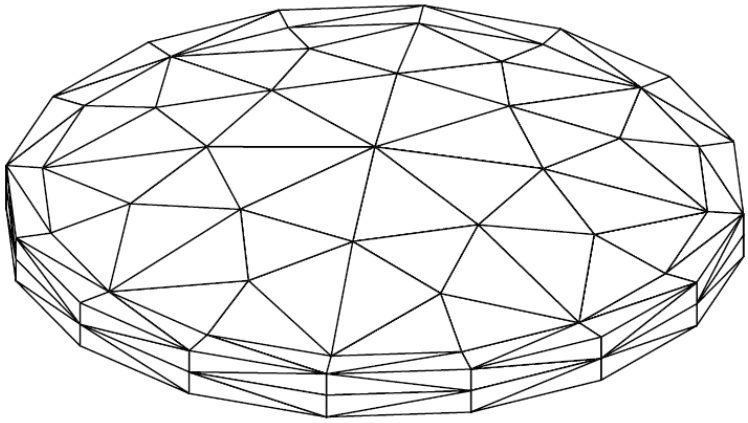

Figure C.5: Illustration of the mesh obtained by mirroring the base subset (Fig. C.4) about the $Y = X$ plane, then about the YZ, XZ, and XY planes. This coarse–grain mesh is used to solve for the long-time solution.

.

C.3 Interpolation

Consider the interpolation over a single, four–noded tetrahedral element within a mesh. We define four spatial shape functions $\eta_a(\boldsymbol{x})$ over the tetrahedron ($a = 1, 2, 3, 4$), each corresponding to one of the four corner nodes of that tetrahedron, $\boldsymbol{x}$ marking the spatial location of any point within the tetrahedron. These shape functions linearly interpolate the value of any variable within the tetrahedron: they have a value of unity at the corresponding node and a value of zero at the other three nodes: i.e., $\eta_a(\boldsymbol{x}_b, t) = \delta_{ab}$, $\boldsymbol{x}_b$ being the position of node b in that tetrahedron.

Finding the value of the shape function η_a at any internal point $\boldsymbol{x} = (x, y, z)$ in the tetrahedron is straightforward. Note that we choose to use Cartesian coordinates for the code computations even though the lens admits itself to cylindrical coordinates. This serves only to simplify the resulting governing equations, and the results are tranformed back into cylindrical coordinates for ease of interpretation. Define m_{1a}, m_{2a}, m_{3a}, and m_{4a} for each shape function a such that

$$\eta_a(\boldsymbol{x}) = m_{1a} + m_{2a}x + m_{3a}y + m_{4a}z, \tag{C.3.1}$$

the linear interpolating scheme of η_a being obvious. The interpolating values m_{ab} can be determined by making use of the orthogonality relationship for the shape functions $\eta_a(\boldsymbol{x}_b) = \delta_{ab}$. For the shape

function corresponding to node $a = 1$, for example:

$$\begin{aligned}
\eta_1(\bar{\boldsymbol{x}}_1) &= 1 = m_{11} + m_{21}x_1 + m_{31}y_1 + m_{41}z_1 \\
\eta_1(\bar{\boldsymbol{x}}_2) &= 0 = m_{11} + m_{21}x_2 + m_{31}y_2 + m_{41}z_2 \\
\eta_1(\bar{\boldsymbol{x}}_3) &= 0 = m_{11} + m_{21}x_3 + m_{31}y_3 + m_{41}z_3 \\
\eta_1(\bar{\boldsymbol{x}}_4) &= 0 = m_{11} + m_{21}x_4 + m_{31}y_4 + m_{41}z_4
\end{aligned}, \tag{C.3.2}$$

$\boldsymbol{x}_1 = (x_1, y_1, z_1)$, $\boldsymbol{x}_2 = (x_2, y_2, z_2)$, etc., being the (known) locations of the corner nodes. This is a system of four equations in four unknowns which can be solved by writing the matrix equation:

$$\begin{bmatrix} 1 & x_1 & y_1 & z_1 \\ 1 & x_2 & y_2 & z_2 \\ 1 & x_3 & y_3 & z_3 \\ 1 & x_4 & y_4 & z_4 \end{bmatrix} \begin{pmatrix} m_{11} \\ m_{21} \\ m_{31} \\ m_{41} \end{pmatrix} = \begin{pmatrix} 1 \\ 0 \\ 0 \\ 0 \end{pmatrix}. \tag{C.3.3}$$

There are three similar equations for the other three shape functions $a = 2$, $a = 3$, and $a = 4$: all four equations can be written compactly as

$$\begin{bmatrix} 1 & x_1 & y_1 & z_1 \\ 1 & x_2 & y_2 & z_2 \\ 1 & x_3 & y_3 & z_3 \\ 1 & x_4 & y_4 & z_4 \end{bmatrix} \begin{bmatrix} m_{11} & m_{12} & m_{13} & m_{14} \\ m_{21} & m_{22} & m_{23} & m_{24} \\ m_{31} & m_{32} & m_{33} & m_{34} \\ m_{41} & m_{42} & m_{43} & m_{44} \end{bmatrix} = \begin{bmatrix} 1 & 0 & 0 & 0 \\ 0 & 1 & 0 & 0 \\ 0 & 0 & 1 & 0 \\ 0 & 0 & 0 & 1 \end{bmatrix} = \mathbf{I}, \tag{C.3.4}$$

$\mathbf{I}$ being the identity matrix. It is clear from this equation that the matrix of m values, m_{ab}, is simply the inverse of the first matrix in the above equation. The first matrix—which only contains information about the nodal positions—then solely determines the interpolated shape functions m_{ab}. It also provides a simple way to calculate the volume of the tetrahedron:

$$V_{tet} = \frac{1}{6} \begin{vmatrix} 1 & x_1 & y_1 & z_1 \\ 1 & x_2 & y_2 & z_2 \\ 1 & x_3 & y_3 & z_3 \\ 1 & x_4 & y_4 & z_4 \end{vmatrix}. \tag{C.3.5}$$

We call the matrix m_{ab} the *spatial interpolation matrix* .

Gradients in the shape function represent vectors that point directly at the node they are asso-

ciated with. From (C.3.1), the spatial gradient of a shape function is given by

$$\nabla\eta_a = \begin{bmatrix} \frac{\partial\eta_a}{\partial x} \\ \frac{\partial\eta_a}{\partial y} \\ \frac{\partial\eta_a}{\partial z} \end{bmatrix} = \begin{bmatrix} m_{2a} \\ m_{3a} \\ m_{4a} \end{bmatrix}. \tag{C.3.6}$$

Note that m_{1a} does not appear in the gradient: interpolation of the gradient of general variables does not require knowing the first row. We define the *spatial gradient interpolation matrix*, m^*_{ia}, as the matrix m_{ab} with the first row removed. As would be expected from the nomenclature, this matrix interpolates gradients in a general variable, whereas the spatial interpolation matrix interpolates actual values.

An example of a variable we wish to interpolate over the tetrahedron is the volume fraction of macromer ϕ. Let the value of the volume fraction at node a at a particular point in time be $\phi_a(t)$. The value of ϕ interpolated at a point $\boldsymbol{x}$ inside that tetrahedron at that time can be found through

$$\phi(\boldsymbol{x}, t) = \sum_{a=1}^{4} \phi_a(t)\eta_a(\boldsymbol{x}). \tag{C.3.7}$$

At any one of the nodes (say b, for example), $\boldsymbol{x} = \boldsymbol{x}_b$, $\eta_a(\boldsymbol{x}_b) = \delta_{ab}$, and $\phi = \phi_b$. Locations within the interior of the tetrahedron have a volume fraction corresponding to a weighted average of the corner node values depending on the respective shape function. This weighting is found by placing (C.3.1) in the above equation, yielding an equation of the form

$$\phi(\boldsymbol{x}, t) = (m_{1a}\phi_a(t)) + (m_{2a}\phi_a(t))\, x + (m_{3a}\phi_a(t))\, y + (m_{4a}\phi_a(t))\, z, \tag{C.3.8}$$

where we have supressed summations in favor of using Einstein notation. A similar discretization can be performed for any scalar variable, say the chemical potential μ (2.3.18):

$$\mu(\boldsymbol{x}, t) = (m_{1a}\mu_a(t)) + (m_{2a}\mu_a(t))\, x + (m_{3a}\mu_a(t))\, y + (m_{4a}\mu_a(t))\, z. \tag{C.3.9}$$

The nodal values of the chemical potential μ_a can be found from the nodal values of the volume fraction and the conversion parameter, specified during the initial time step. From (C.3.9), it is easy to see that gradients in chemical potential can be written as

$$\nabla\mu = \begin{bmatrix} m_{2a}\mu_a \\ m_{3a}\mu_a \\ m_{4a}\mu_a \end{bmatrix}, \tag{C.3.10}$$

which can be written more compactly using the spatial gradient interpolation matrix:

$$\mu_{,i} = m^*_{ia}\mu_a. \tag{C.3.11}$$

These gradients in chemical potential drive the diffusion-based shape change.

C.3.1 Initialization

Using the interpolation specified above on a four–node tetrahedral mesh, the two-tiered solution method proceeds as follows: At $t = 0$, we specify the extent of reaction profile $\xi(\boldsymbol{X})$. This profile allows calculation of the initial values of the volume fraction of macromer $\phi(\boldsymbol{X}, t = 0) = \phi_0(1-\xi(\boldsymbol{X}))$ and the conversion parameter $\theta^*(\boldsymbol{X}) = 1 - (1 - \xi(\boldsymbol{X}))\phi_0$ at each nodal point from the reference position of that node. Specification of these scalar fields allows calculation of $\mu(\boldsymbol{X})$ from (2.3.18). The imposed profile therefore acts as an initial condition, creating gradients in chemical potential throughout the mesh which will be relieved through diffusion. Specific extent of reaction profiles will be illustrated in the studies below.

C.3.2 Diffusion Step

From Ch. 3, the equation for conservation of mass of macromer is (3.3.3):

$$\frac{D\rho_m}{Dt} + \nabla \cdot \mathbf{J}_m = 0 \tag{C.3.12}$$

where ρ_m is the density of macromer, t is time, and $\mathbf{J}_m = \rho_m(\mathbf{v}_m - \mathbf{v})$ is the flux of macromer.[2] In keeping with the scaling analysis performed in Appendix B, the velocity is negligible for a generic time step. Placing this simplification into the above equation yields

$$\frac{\partial\rho_m}{\partial t} = -\nabla \cdot \mathbf{J}_m. \tag{C.3.13}$$

The flux is modeled as a gradient in chemical potential (4.3.24):

$$\mathbf{J}_m = -\rho\mathcal{D}\phi\nabla\mu \tag{C.3.14}$$

with $\mathcal{D}$ being the diffusivity of macromer, assumed to be a uniform material parameter. Recall from Ch. 4 that this definition for the flux ignores anisotropic deformation contributions because these contributions are small for the deformations experienced in practice. Placing (C.3.14) in (C.3.13), the equation is made dimensionless by defining the time scale for diffusion, τ, and the system

[2] As discussed in Ch. 3, we have set the reaction term to zero because reaction occurs significantly faster than diffusion and we model the reaction as instantaneous at $t = 0$.

length scale, H; we take H as 1 mm for the lenses considered in Ch. 6 (Table 6.1). Time is made dimensionless such that it varies from zero to one by using the time it takes macromer to diffuse through the largest spatial dimension L: $\tau = L^2/\mathcal{D}$; for the lens, $L = d/2 = 3$ mm (Table 6.1). Denoting dimensionless variables with an overbar,

$$\frac{\partial \phi}{\partial \bar{t}} = -\bar{L}^2 \bar{\nabla} \cdot \bar{\mathbf{J}}. \tag{C.3.15}$$

Here we define the dimensionless largest spatial dimension $\bar{L} = L/H$, and dimensionless flux $\bar{\mathbf{J}} = -\phi \bar{\nabla} \mu$. This equation holds pointwise over the entire (dimensionless) domain of the object. From here on, we drop all overbars and assume that all variables are dimensionless.

The variational form of our differential equation (6.2.2) is found through interpolation over a tetrahedron. This is equivalent to forcing the differential equations to hold from a volume–averaged perspective rather than pointwise. In particular, consider a single node a with shape function η_a defined in §C.3. Multiplying (C.3.15) by the shape function and integrating over a tetrahedron T containing node a, we arrive at

$$\int_T \phi_{,t} \eta_a dV = -L^2 \int_T \nabla \cdot \mathbf{J} \eta_a dV. \tag{C.3.16}$$

We use the subscript $,t$ to denote partial differentiation with respect to time and T to denote the dimensionless domain of the tetrahedron. Integration by parts allows us to rewrite (C.3.16)

$$\int_T \phi_{,t} \eta_a dV = L^2 \left[\int_T \mathbf{J} \cdot \nabla \eta_a dV - \int_{\partial T} \eta_a \mathbf{J} \cdot \boldsymbol{n} dS \right] \tag{C.3.17}$$

with ∂T representing the surface of the tetrahedron. The surface integrals in (C.3.17) will vanish when we sum (C.3.17) over all internal tetrahedra that contain node a: a tetrahedra that has a contribution $(\eta_a \mathbf{J}) \cdot \boldsymbol{n}$ on one face will have an equal and opposite contribution $(\eta_a \mathbf{J}) \cdot -\boldsymbol{n}$ from the adjacent tetrahedra which shares that same face.[3] For elements on the system boundary, however, this term will depend upon the specific boundary conditions of the problem. The unique property of our system—that material neither enters nor leaves—allows us to use the simple boundary condition $\mathbf{J} \cdot \boldsymbol{n} = 0$ for all external surfaces. The summation of (C.3.17) over all tetrahedra that contain node a thus proceeds to

$$\sum_{T'} \int_T \phi_{,t} \eta_a dV = L^2 \sum_{T'} \int_T \mathbf{J} \cdot \nabla \eta_a dV, \tag{C.3.18}$$

with $\sum_{T'}$ representing the sum over all tetrahedra that contain node a.

We now use an interpolation scheme to evaluate the above integrals. Using linear interpolation

[3] We have not yet approximated our solution with a discretization and, as such, the variables $\mathbf{J}$ and η_a are continuous across tetrahedra.

(§C.3), the integrals are approximated over a tetrahedra via first–order numerical quadrature:

$$\int_T f(\boldsymbol{x})dV \approx \frac{f(\boldsymbol{x}_1)+f(\boldsymbol{x}_2)+f(\boldsymbol{x}_3)+f(\boldsymbol{x}_4)}{4}|T|. \tag{C.3.19}$$

Here, $f(\boldsymbol{x}_b)$ is the function evaluated at nodal point b and $|T|$ is the volume of the tetrahedron evaluated from the nodal positions via (C.3.5). This approximation applied to the left–hand-side integral of (C.3.18) yields

$$\int_T \phi_{,t}\eta_a dV \approx \frac{(\phi_{,t}\eta_a)|\boldsymbol{x}_1+(\phi_{,t}\eta_a)|\boldsymbol{x}_2+(\phi_{,t}\eta_a)|\boldsymbol{x}_3+(\phi_{,t}\eta_a)|\boldsymbol{x}_4}{4}|T| = \phi_{,t}(\boldsymbol{x}_a,t)\cdot\frac{1}{4}|T|. \tag{C.3.20}$$

To arrive at the second equality, we have again used the orthogonality of the shape functions: $\eta_a(\boldsymbol{x}_b)=\delta_{ab}$. The orthogonality is again used along with the linear interpolation for ϕ (C.3.7) to write $\phi_{,t}(\boldsymbol{x}_a,t)=\dot{\phi}_a(t)$ (we use a superscript dot to denote time differentation when it is the only variable). Since this variable is independent of position, it can be brought outside the summation in (C.3.18). We finish the discretization by approximating the time derivative with an explicit forward Euler time step:

$$\sum_{T'}\int_T \phi_{,t}\eta_a dV \approx \sum_{T'}\frac{1}{4}\dot{\phi}_a(t)|T'| \approx \frac{\phi_a(t_{m+1})-\phi_a(t_m)}{t_{m+1}-t_m}\cdot\frac{1}{4}\sum_{T'}|T'| \tag{C.3.21}$$

with t_{m+1} being the current time step and t_m being the past time step. We define $\Delta t_m = t_{m+1}-t_m$ as the change in the time step at time t_m. The summation in (C.3.21) represents an effective "volume" of node a. This can be seen by conceptually dividing the mass of each tetrahedron evenly among its four nodes. The mass of any given node, then, is a quarter of the masses of all the surrounding tetrahedra:

$$m_a = \frac{1}{4}\sum_{T'}\rho|T'|, \tag{C.3.22}$$

with $\rho|T'|$ being the mass of any tetrahedra $|T'|$ to which a belongs. Assuming the density of all tetrahedra are the same (incompressible), it is easy to see that the sum in (C.3.21) represents the volume of the node. Nodes that are attached to more tetrahedra or larger tetrahedra will have a greater "volume" than nodes that are attached to fewer or smaller tetrahedra.

We now consider the right–hand side of (C.3.18). In the linear approximation, gradients in the shape function and chemical potential are constant over any given tetrahedron (see (C.3.11) and (C.3.6) above). The dimensionless flux $\mathbf{J}=-\phi\nabla\mu$ can be made constant in any tetrahedra using the constant chemical potential gradient and the average value of the volume fraction in the tetrahedron. This simplification allows the right–hand side of (C.3.18) to be expressed as

$$L^2\sum_{T'}\int_T \mathbf{J}\cdot\nabla\eta_a dV = L^2\sum_{T'}\mathbf{J}(T')\cdot\nabla\eta_a(T')|T'| = L^2\sum_{T'}J_i m^*_{ia}|T'|, \tag{C.3.23}$$

the last step following from the expression for the gradient of the shape function (C.3.6). The flux at any point can be calculated easily from the gradient of the chemical potential. The summand in (C.3.23) represents the movement of macromer to or from a point in the tetrahedron T'. As previously noted, the gradient of shape function a (represented by m^*_{ia}) is a vector which points directly at node a. Taking the dot product of the flux with this vector represents the movement of material to or from the node, determined by the relative orientation of the vectors:

$$\Delta\phi_a = J_i m^*_{ia}. \tag{C.3.24}$$

The sum represents the net transfer of macromer volume to or from the node due to all nearby neighboring elements: some depositing macromer and some removing macromer.

Placing both (C.3.21) and (C.3.23) into (C.3.18) yield the implementation for the diffusion time step, now explicitely written for node a:

$$\phi_a(t_{m+1}) = \phi_a(t_m) + L^2 \Delta t_m \frac{\sum_{T'} \Delta\phi_a |T'|}{\frac{1}{4}\sum_{T'} |T'|}. \tag{C.3.25}$$

The computational procedure of (C.3.25) is as follows. First, the flux $\mathbf{J}$ is calculated in each tetrahedra from the spatial gradient interpolation matrix m^*_{ia} and the current chemical potential (C.3.11). Once all the fluxes are determined, the code can proceed tetrahedron by tetrahedron, evaluating the change in volume fraction for each node as well as the volume of that element. The sums are calculated for node a by adding the contributions from each tetrahedron to which a belongs, information kept in the connectivity of the mesh. To guarantee computation proceeds correctly, we check the total change in volume fraction summed over all nodes for a single tetrahedron: this number should be zero for a single time step, as macromer must be transferred between nodes and cannot be created or destroyed.

Once the diffusion step has updated the values of the volume fraction, the average volume fraction is found in each tetrahedron using linear interpolation (§C.3). These volume-averaged values are used in calculating the system energy and forces which must be relaxed in the second computational step: the deformation step.

C.3.3 Deformation Step

After a small amount of material has been transferred between nearby elements in a diffusion steps, some elements will have more material than they began with and some elements will have less. This leads to an aphysical situation: since the nodal positions have not yet moved, the incompressible constraint 2.3.10 is not satisfied. These deviations in density are relaxed by displacing the nodes to reduce a penalty assessed for density deviations. The penalty plays the role of free energy, leading

to a psuedo–force on the nodes. To determine the new shape of the lens, these "forces" can be relaxed, moving the nodal points in keeping with the forces so that elements that have gained material increase in volume, whereas elements that have lost shrink. The numerical equivalent of this involves determination of the forces acting on each node in an element and then summing those contributions from all elements to which a given node is attached (§C.3.3.1). We then treat the nodes as particles in a molecular dynamic simulation and calculate the displacement of the nodes under the given forces via a velocity Verlet algorithm (§C.3.3.2). As previously mentioned, for the small, elastic deformations considered here, the system is assumed to relax instantaneously at each time step without a corresponding change in the volume fraction.

We seek to determine the spatial positions of each node in time $\boldsymbol{x}(\boldsymbol{X}, t)$ (recall that each reference position $\boldsymbol{X}$ is used to label a particular node). Using the linear interpolation scheme described above, the spatial position of any reference point $\boldsymbol{X} = (X, Y, Z)$ at time t is given by $\boldsymbol{x}(t) = (x(t), y(t), z(t))$:

$$\begin{aligned} x(t) &= \kappa_1(t) + \kappa_2(t)X + \kappa_3(t)Y + \kappa_4(t)Z \\ y(t) &= \lambda_1(t) + \lambda_2(t)X + \lambda_3(t)Y + \lambda_4(t)Z \\ z(t) &= \nu_1(t) + \nu_2(t)X + \nu_3(t)Y + \nu_4(t)Z. \end{aligned} \tag{C.3.26}$$

The mapping parameters $\kappa_a(t)$, $\lambda_a(t)$, and $\nu_a(t)$ are functions of time only: these parameters are spatially constant over any given tetrahedron in keeping with the linear interpolation scheme. Since a tetrahedron is defined by four nodes, we can write the above equations four times—one for each corner node 1, 2, 3, and 4—to yield the matrix equations

$$\begin{aligned} \begin{pmatrix} x_1 \\ x_2 \\ x_3 \\ x_4 \end{pmatrix} &= \begin{bmatrix} 1 & X_1 & Y_1 & Z_1 \\ 1 & X_2 & Y_2 & Z_2 \\ 1 & X_3 & Y_3 & Z_3 \\ 1 & X_4 & Y_4 & Z_4 \end{bmatrix} \begin{pmatrix} \kappa_1 \\ \kappa_2 \\ \kappa_3 \\ \kappa_4 \end{pmatrix} \\ \begin{pmatrix} y_1 \\ y_2 \\ y_3 \\ y_4 \end{pmatrix} &= \begin{bmatrix} 1 & X_1 & Y_1 & Z_1 \\ 1 & X_2 & Y_2 & Z_2 \\ 1 & X_3 & Y_3 & Z_3 \\ 1 & X_4 & Y_4 & Z_4 \end{bmatrix} \begin{pmatrix} \lambda_1 \\ \lambda_2 \\ \lambda_3 \\ \lambda_4 \end{pmatrix} \\ \begin{pmatrix} z_1 \\ z_2 \\ z_3 \\ z_4 \end{pmatrix} &= \begin{bmatrix} 1 & X_1 & Y_1 & Z_1 \\ 1 & X_2 & Y_2 & Z_2 \\ 1 & X_3 & Y_3 & Z_3 \\ 1 & X_4 & Y_4 & Z_4 \end{bmatrix} \begin{pmatrix} \nu_1 \\ \nu_2 \\ \nu_3 \\ \nu_4 \end{pmatrix}, \end{aligned} \tag{C.3.27}$$

with $\boldsymbol{x}_1 = (x_1, y_1, z_1)$ being the spatial position of the corner node defining the tetrahedron labeled

"1", $\boldsymbol{X}_2 = (X_2, Y_2, Z_2)$ being the reference position of corner node labeled "2", etc. Note that the middle matrices in the above equations are the same and are defined completely by the nodal locations of the tetrahedron in the reference configuration. In fact, the determinant of this matrix is related to the reference volume of any given tetrahedron by definition:

$$V_{0,tet} = \frac{1}{6}\begin{vmatrix} 1 & X_1 & Y_1 & Z_1 \\ 1 & X_2 & Y_2 & Z_2 \\ 1 & X_3 & Y_3 & Z_3 \\ 1 & X_4 & Y_4 & Z_4 \end{vmatrix}. \tag{C.3.28}$$

The inverse of this matrix, M_{ab}, is reminiscent of the spatial interpolation matrix defined above. We call M_{ab} the *reference interpolation matrix* which can be used to determine the κs, λs, and νs for any position of the nodes $x_{ai} = (x_a, y_a, z_a)$ through (C.3.27)

$$\kappa_a = M_{ab}x_b, \qquad \lambda_a = M_{ab}y_b \qquad \text{and} \qquad \mu_a = M_{ab}z_b. \tag{C.3.29}$$

These parameters represent gradients in spatial points with respect to the reference positions and therefore determine the deformation gradient (C.3.26):

$$\mathbf{F}^* = \begin{bmatrix} \kappa_2 & \kappa_3 & \kappa_4 \\ \lambda_2 & \lambda_3 & \lambda_4 \\ \nu_2 & \nu_3 & \nu_4 \end{bmatrix}. \tag{C.3.30}$$

Using (C.3.29), this can be written as:

$$F^*_{iJ} = M^*_{Jb}x_{bi} \tag{C.3.31}$$

where M^*_{Jb} is M_{ab} with the first row removed (similar to m^*_{ia} in the diffusion interpolation) and we use index notation (repeated indices indicates a sum). This is the *reference gradient interpolation matrix*, used to interpolate the deformation gradient. Note that F^*_{iJ} does not depend upon the translation of the system (contained in κ_1, λ_1, or ν_1, (C.3.26)). This is in keeping with the deformation gradient being translationally invariant.

At $t = 0$, the spatial nodes are located in the same position as in the reference, and $\mathbf{F}^* = \mathbf{I}$. Future spatial positions will be determined by calculating the forces on each node and allowing those forces to relax. The deformation gradient for the tetrahedra is then calculated from (C.3.31) using the current nodal positions x_{ai} and the matrices M_{ab}. The matrices M_{ab}—unique for each tetrahedron and determined by the reference—will be the same at all time steps and can be stored upon creation of the mesh.

C.3.3.1 Pseudo–Force Calculation

We treat the volume fraction of macromer as fixed during the deformation step. Recall, however, that these two variables are mutually dependent by conservation of mass (2.3.10):

$$\det F^*_{iJ} = Q^* = \frac{\theta}{1-\phi}. \tag{C.3.32}$$

As the nodal points move to relax built up stresses in the deformation step, the volume of any given element—evaluated from $\det F^*_{iJ}$—will not generally satisfy the determined volume fraction field (C.3.32). We must therefore penalize such deformations in order to guarantee local incompressibility (C.3.32). Denote changes in tetrahedral volume beyond those due to imcompressibility as Q_M:

$$\det \mathbf{F}^* = Q^* Q_M. \tag{C.3.33}$$

Clearly, we wish to force the material to deform in such a way as to enforce $Q_M = 1$ in keeping with (C.3.32). To capture this physics, we must then introduce a constraint on the energy that will be minimized in the deformation step: deformations which produce deviations of Q_M from one being severly penalized. We take this penalty to be of the same form as the compressible extension to the neo–Hookean model, used by other authors to enforce local incompressibility [27, 101]:

$$E(\mathbf{F}^*, \phi) = A(\mathbf{F}^*, \phi) + \frac{1}{2} K \ln^2 Q_M. \tag{C.3.34}$$

Here, E denotes the computational free energy per unit spatial volume, distinguished from the thermodynamic energy $A(\mathbf{F}^*, \phi)$ (2.3.12) by the constraint that has arisen purely from our computational methodology. The computational constraint parameter K can be thought of as the (dimensionless) bulk modulus of the material. The real bulk modulus for an incompressible material is infinite; for computational purposes, we choose a large, yet finite, value of K. An appropriate value of K is one which does not cause locking of material elements but also does not produce large changes in the total system volume in time. For the meshes and materials considered here, an optimal value of $K = 2 \times 10^4$ has been determined which yields less than a tenth of a percent decrease in volume in the final state. Larger values of K tend to lead to locking while smaller values of K yield larger volume decreases. In order to insure rotation invariance, the computational energy (C.3.34) must also be rotationally invariant. Since our free energy A (2.3.12) depends only upon the invariants of the deformation gradient, this is guaranteed but was verified during programming.

The computational energy per unit volume (C.3.34) can be used to calculate the computational forces acting upon each node in a tetrahedron. These forces are aphysical because they are calculated from a computational energy (C.3.34) but can be thought of as acting upon each node to move it to a position which will ensure that the energy is minimized at each time step. Each tetrahedron has a

value of the deformation gradient F^*_{iJ} determined by the locations of its nodal points (C.3.31); this deformation gradient is piece–wise constant across tetrahedra. The components of the computational force on node a associated with the movement of nodal points in a tetrahedron to which a belongs are:

$$\begin{aligned} F_{ax} &= -\frac{\partial(EV_{0,tet}\det\mathbf{F}^*)}{\partial x_a} \\ F_{ay} &= -\frac{\partial(EV_{0,tet}\det\mathbf{F}^*)}{\partial y_a} \\ F_{az} &= -\frac{\partial(EV_{0,tet}\det\mathbf{F}^*)}{\partial z_a} \end{aligned} \tag{C.3.35}$$

with F_{ax} being the x component of the force acting on node a, F_{ay} the y component and F_{az} the z component. The factor $V_{0,tet}\det\mathbf{F}^* = V_{tet}$ appears since E is defined per spatial volume. We can write the equation more concisely by using index notation, subscript i again representing the spatial dimensions x, y and z and subscript a still representing node numbers

$$F_{ai} = -V_{0,tet}\frac{\partial(E\det\mathbf{F}^*)}{\partial x_{ai}} \tag{C.3.36}$$

x_{ai} being the ith spatial component of node a. As previously discussed, the volume fraction is held fixed during the deformation step so the computational energy in (C.3.34) is treated as solely a function of the deformation gradient F^*_{iJ}. To evaluate the derivative in terms of F^*_{iJ}, we use the interpolation of F^*_{iJ} (C.3.31):

$$\frac{\partial}{\partial x_{ai}} = \frac{\partial}{\partial F^*_{jJ}}\frac{\partial F^*_{jJ}}{\partial x_{ai}} = \frac{\partial}{\partial F^*_{iJ}}M^*_{Ja} \tag{C.3.37}$$

so that

$$F_{ai} = -V_{0,tet}\frac{\partial(E\det\mathbf{F}^*)}{\partial F^*_{iJ}}M^*_{Ja}. \tag{C.3.38}$$

Treating ϕ as constant when evaluating the derivative in (C.3.38), the computational forces are:

$$F_{ai} = -V_{0,tet}\det F^*_{iJ}\left[(E + K\ln Q_M)F^{*-1}_{iJ} + \frac{\partial A}{\partial F^*_{iJ}}\right]M^*_{Ja} \tag{C.3.39}$$

The calculations of the net computational force on each node in the system proceeds as follows. First, the nodal positions for each tetrahedron are used to interpolate the deformation gradient in that element via (C.3.31). The energy (C.3.34) and computational forces (C.3.39) are then evaluated for each tetrahedra using this calculated deformation gradient, the material parameters and the average volume fraction in the element calculated after the diffusion step. Using connectivity tables, the net computational forces on all nodes are found by summing the contributions to each node from all elements to which it is attached. Since there are no external forces acting on the system, these are

the net forces which can be considered to be exerted on each node and are used to determine the movement of the nodes by the velocity Verlet algorithm.

C.3.3.2 Movement of Nodal Points Under a Force

The velocity Verlet algorithm determines the movement of a set of discrete particles under an imposed set of computational forces by integrating Newton's laws of motion in time. We analogously assume each node in our mesh is a "particle" with an appropriate mass upon which forces are acting. To determine the nodal positions in time, we can then integrate Newton's laws of motion. A key feature of our computation scheme simplifies the velocity Verlet algorithm from the full form used in molecular dynamics: the instant relaxation of network strands. Computationally, this allows the system to take as many relaxation steps as necessary before proceeding with another step of diffusion. In addition, we do not need to specify the physics of relaxation because the resultant time steps are all purely computational: as long as the computational forces are relaxed to the nearest energy minima, the path taken to get there can be specified for ease of computation. Thus, there are only two limitations on the size of this computational time scale. Too large a time scale can cause a deformation in which tetrahedra have inverted or have otherwise degenerated from simplectic form: the time scale must be chosen to yield movements which are a sizable factor smaller than the smallest mesh size. Too small a time scale, on the other hand, will result in unnecessarily slow computation time.

Because the deformation steps have no corresponding real time scale, we simplify the velocity Verlet algorithm by specifying our system to be overdamped. This eliminates the possibility of overshoot in determining the relaxed state at the current time step. The overdamped simplification yields a linear relationship between the computational velocity of any node and the computational force exerted on that node:

$$v_{ai} = \frac{1}{\eta} F_{ai} \tag{C.3.40}$$

η the overdamped friction factor. We use the term "computational velocity" to denote that v_{ai} does not represent a real velocity but rather the direction of movement of the node in computational time. Since an equivalent computational acceleration is negligible for overdamped systems, the updated nodal positions can be found directly from the nodal computational velocities through:

$$x_{ai}(s + \Delta s_M) = x_{ai}(s) + v_{ai}\Delta s_M. \tag{C.3.41}$$

Here, s represents the (again aphysical) computational time scale used in the relaxation and Δs_M is the computational time step. The combination of (C.3.40) and (C.3.41) yields a single computational

parameter used for the relaxation $e = \Delta s_M/\eta$:

$$\Delta x_{ai} = x_{ai}(s + \Delta s_M) - x_{ai}(s) = eF_{ai}. \tag{C.3.42}$$

For the meshes created here (with mesh size $h_{mesh} = 0.1$), $e = 8 \times 10^{-6}$ gives reasonably fast, guaranteed convergence. To ensure choice of method does not affect the solution, a full velocity Verlet algorithm was also programmed (treating acceleration proportional to force by the nodal mass) and the relaxed nodal positions were determined to be the same. As expected, however, the full form took more computational steps to relax because of overshoot. The overdamped algorithm is deemed superior for computational use.

Finally, computational limits require a convergence criteria for the relaxation step. We choose to relax the computational forces until the largest force (magnitude) in the system is below a certain threshold, F_{tol}. The computational energy E for several sample runs was tracked with deformation step to determine an optimal value for F_{tol}. It was determined for a few trial runs that the computational energy for $K = 2 \times 10^4$ and $e = 8 \times 10^{-6}$ continually decreased per deformation step until a plateau with residual around $F_{tol} = 0.1$. Subsequent deformation steps result in negligible changes in nodal positions, indicating that the system has converged. In addition, a sample reaction profile was chosen and diffusion–deformation was run as a function of F_{tol}. The global deformation output (measured in terms of changes in lens power, discussed below) was compared to F_{tol}: at $F_{tol} = 0.1$, the global deformation did not vary significantly with F_{tol}. We therefore take $F_{tol} = 0.1$ as a convergence criteria for all of the runs illustrated in this thesis.

C.4 Outputs

The inputs to our computer code are a mesh (§C.1), a list of material parameters and an extent of reaction profile. Initialization involves relaxing the mesh (which can have small initial computational forces due to mesh construction) and evaluating the volume fraction profile from the extent of reaction profile (§C.3.1). As the computational diffusion and relaxation occurs, data is output at logarithmically placed time steps. The data includes detailed information regarding the position of each node at each output time as well as the nodal volume fraction and chemical potential. In addition, global deformation parameters are also calculated. The total mesh volume is calculated by summing the volumes of each tetrahedra (evaluated from the nodal positions using (C.3.5)) and compared to the original volume determined during mesh construction (Table C.1): the percent change in volume is reported to determine how well conservation of volume holds. The surface areas are also reported at each output time step as well as the total system energy, average volume fraction and run time.

C.5 Measurment of Local Curvature

For an arbitrary profile and an arbitrary number of surface points, a method has been developed to measure Gaussian curvature at a node. This consists of summing the internal angles β_i of all triangles that contain the node and comparing the value to 2π [102, 103]:

$$\kappa_{Gauss} = \frac{3\left(2\pi - \sum_i \beta_i\right)}{\sum_i S_i}. \tag{C.5.43}$$

Here S_i is the area of triangle i and both sums are over all triangles that contain the node. Positive Gaussian curvature is associated with a puckered configuration whereas negative Gaussian curvature occurs at saddle points (note that $\kappa_{Gauss} = 0$ for a planar surface). This is a particularly powerful method and can be used to capture fine curvature along a surface [103]. This would be particularly useful, for example, to measure astimagic and aspheric corrections in lenses under non–axisymmetric extents of reaction. Current code implements this method although we do not report it for the axisymmetric cases considered in Ch. 6.

Bibliography

[1] E. Pape. *Light Adjustable Macromer–Doped Elastomers: The Thermodynamics, Transport, and Photochemistry of Silicones.* PhD thesis, California Institute of Technology, 2006.

[2] B. J. Randleman. "Cataract Surgery." http://www.medicinenet.com/cataract_surgery/article.htm. (Edited 7/21/2011).

[3] L. Bellan. The evolution of cataract surgery: The most common eye procedure in older adults. *Geriatrics and Aging*, 11(6):328–332, 2008.

[4] D. M. Schwartz. Light-adjustable lens. *Trans. Am. Ophthalmol. Soc.*, 101:416–436, 2003.

[5] S. Lane, M. Morris, L. Nordan, M. Packer, N. Tarantino, and R. B. Wallace III. Multifocal intraocular lenses. *Ophthalmol. Clin. N. Am.*, 19:89–105, 2006.

[6] G. N. Kraser. Small incision intraocular lens with adjustable refractive power. U. S. Patent # 4,950,289. 1990.

[7] K. N. Long, T. F. Scott, H. J. Qi, C. N. Bowman, and M L. Dunn. Photomechanics of light-activated polymers. *J. Mech. Phys. Solids*, 57(7):1103–1121, 2009.

[8] M. Warner and L. Mahadevan. Photo-induced deformation of beams, plates and films. *Phys. Rev. Lett.*, 92(13):134302, 2004.

[9] D. Corbett and M. Warner. Linear and nonlinear photoinduced deformations of cantilevers. *Phys. Rev. Lett.*, 99:174302, 2007.

[10] M. Warner, C. D. Modes, and D. Corbett. Suppression of curvature in nematic elastica. *P. Roy. Soc. A—Math Phy.*, 466(2124):3561–3578, 2010.

[11] M. Warner, C. D. Modes, and D. Corbett. Curvature in nematic elastica responding to light and heat. *P. Roy. Soc. A—Math Phy.*, 466(2122):2975–2989, 2010.

[12] L. Jin, Y. Lin, and Y. Huo. A large deflection light-induced bending model for liquid crystal elastomers under uniform or non-uniform illumination. *Int. J. Solids Struct.*, 48(22-23):3232–3242, 2011.

[13] R. L. B. Selinger, B. L. Mbanga, and J. V. Selinger. Modeling liquid crystal elastomers: actuators, pumps, and robots - art. no. 69110A. In L. C. Chien, editor, *Emerging Liquid Crystal Technologies III*, volume 6911 of *P. Soc. Photo-Opt. Inst.*, page A9110. SPIE, 2008: Conference on Emerging Liquid Crystal Technologies III, San Jose, CA, Jan 20–22, 2008.

[14] M. Chen, X. Xing, Z. Liu, Y. Zhu, H. Liu, Y. Yu, and F. Cheng. Photodeformable polymer material: towards light-driven micropump applications. *Appl. Phys. A—Mater.*, 100(1):39–43, 2010.

[15] Q. Luo and L. Tong. Constitutive modeling of photostrictive materials and design optimization of microcantilevers. *J. Intel. Mat. Syst. Str.*, 20(12):1425–1438, 2009.

[16] A. Bhargava and M. B. Cortie. Prospects for light-activated nano-devices based on shape-memory polymers. *J. Nanophotonics*, 1:012503, 2007.

[17] W. J. Joo, N. J. Kim, H. Chun, I. K. Moon, and N. Kim. Polymeric photorefractive composite for holographic applications. *Polymer*, 42(24):9863–9866, 2001.

[18] W. S. Colburn. Review of materials for holographic optics. *J. Imaging Sci. Techn.*, 41(5):443–456, 1997.

[19] J. A. Jenney. Holographic recording with photopolymers. *J. Opt. Soc. Am.*, 60(9):1155, 1970.

[20] J. Jethmalani, R. Grubbs, J. Kornfield, D. Schwart, C. Sandstedt, and E. Pape. Lenses capable of post-fabrication modulus change. U. S. Patent # 6,813,097. 2002.

[21] D. M. Schwartz, C. Sandstedt, S. Chang, J. Kornfield, and R. Grubbs. Light-adjustable lens: development of in vitro nomograms. *Trans. Am. Ophthalmol. Soc.*, 102:67–74, 2004.

[22] A. Chayet, C. A. Sandstedt, S. H. Chang, P. Rhee, B. Tsuchiyama, and D. Schwartz. Correction of residual hyperopia after cataract surgery using the light adjustable intraocular lens technology. *Am. J. Ophthalmol.*, 147(3):392–397, 2009.

[23] A. Chayet, C. Sandstedt, S. Chang, P. Rhee, B. Tsuchiyama, R. Grubbs, and D. Schwartz. Correction of myopia after cataract surgery with a light–adjustable lens. *Ophthalmology*, 116(8):1432–1435, 2009.

[24] A. Chayet, C. Sandstedt, S. Chang, P. Rhee, B. Tsuchiyama, R. Grubbs, and D. Schwartz. Use of the light-adjustable lens to correct astigmatism after cataract surgery. *Brit. J. Ophthalmol.*, 94(6):690–692, 2010.

[25] A. Lichtinger, C. A. Sandstedt, D. M. Schwartz, and A. S. Chayet. Correction of astigmatism after cataract surgery using the light adjustable lens: a 1–year follow–up pilot study. *J. Refract. Surg.*, 27(9):638–641, 2011.

[26] L. Werner, W. Chang, J. Haymore, B. Haugen, N. Romaniv, C. Sandstedt, S. Chang, and N. Mamalis. Retinal safety of the irradiation delivered to light–adjustable intraocular lenses evaluated in a rabbit model. *J. Cataract Refr. Surg.*, 36(8):1392–1397, 2010.

[27] A. Pandolfi and M. Ortiz. A numerical model of light adjustable lens. *Comput. Mech.*, 44:133–143, 2009.

[28] S. K. Patel, S. Malone, C. Cohen, J. R. Gillmor and R. H. Colby. Elastic–modulus and equilibrium swelling of poly(dimethylsiloxane) networks. *Macromolecules*, 25:5241–5251, 1992.

[29] S. K. Patel and C. Cohen. Dynamic light–scattering from swollen poly(dimethylsiloxane) networks. *Macromolecules*, 25(20):5252–5258, 1992.

[30] K. Sivasailam and C. Cohen. Scaling behavior: Effect of precursor concentration and precursor molecular weight on the modulus and swelling of polymeric networks. *J. Rheol.*, 44(4):897–915, 2000.

[31] S. H. Yoo, C. Cohen and C. Hui. Mechanical and swelling properties of pdms interpenetrating polymer networks. *Polymer*, 47:6226–6235, 2006.

[32] P. J. Flory. Thermodynamics of high polymer solutions. *J. Chem. Phys.*, 10:51–61, 1942.

[33] P. J. Flory and Jr. J. Rehner. Statistical mechanics of cross-linked polymer networks II Swelling. *J. Chem. Phys.*, 11(11):521–526, 1943.

[34] P. Flory and J. Rehner. Effect of deformation on the swelling capacity of rubber. *J. Chem. Phys.*, 12(10):412–414, 1944.

[35] P. Flory. *Principles of Polymer Chemistry*, chapter XI, XIII. Cornell University Press, 1953.

[36] T. Tanaka, L. Hocker, and G. B. Benedek. Rayleigh–scattering in simple gels. *B. Am. Phys. Soc.*, 18(5):782, 1973.

[37] T. Tanaka and D. J. Fillmore. Kinetics of swelling of gels. *J. Chem. Phys.*, 70(3):1214–1218, 1979.

[38] Y. Li and T. Tanaka. Kinetics of swelling and shrinking of gels. *J. Chem. Phys.*, 92(2):1365, 1990.

[39] M. Doi. *Dynamics and Patterns in Complex Fluids*, pages 100–112. Springer, Berlin., 1990.

[40] T. Yamaue and M. Doi. Theory of one-dimensional swelling dynamics of polymer gels under mechanical constraint. *Phys. Rev. E*, 69:041402, 2004.

[41] T. Yamaue and M. Doi. Swelling dynamics of constrained thin-plate gels under an external force. *Phys. Rev. E*, 70:011401, 2004.

[42] T. Yamaue and M. Doi. The stress diffusion coupling in the swelling dynamics of cylindrical gels. *J. Chem. Phys.*, 122:084703, 2005.

[43] M. Doi and T. Yamaue. Variational bounds for the relaxation times of swelling gels. *Phys. Rev. E*, 71:041404, 2005.

[44] T. Yamaue, T. Tanigiuchi, and M. Doi. The simulation of the swelling and deswelling dynamics of gels. *Mol. Phys.*, 102(2):167, 2004.

[45] A. E. Green and P. M. Naghdi. On basic equations for mixtures. *Int. J. Eng. Sci.*, 3:231–241, 1969.

[46] R. J. Atkin and R. E. Craine. Continuum theories of mixtures — basic theory and historical development. *Q. J. Mech. Appl. Math*, 29(2):209–244, 1976.

[47] K. R. Rajagopal and L. Tao. *Mechanics of Mixtures*. World Scientific, 1995.

[48] P. Haupt. *Continuum Mechanics and Theory of Materials*, pages 144–152. Springer, Berlin, 2002.

[49] C. Truesdell. *Rational Thermodynamics*. Springer, New York, 1984.

[50] B. D. Coleman and W. Noll. The thermodynamics of elastic materials with heat conduction and viscosity. *Arch. Ration. Mech. Anal.*, 13:167–178, 1963.

[51] B. Loret and F. M. F. Simões. A framework for deformation, generalized diffusion, mass transfer and growth in multi-species multi-phase biological tissues. *Eur. J. Mech. A—Solids*, 24:757–781, 2005.

[52] K. Garikipati, E. M. Arruda, K. Grosh, H. Narayanan, and S. Calve. A continuum treatment of growth in biological tissue: the coupling of mass transport and mechanics. *J. Mech. Phys. Solids*, 52:1595–1625, 2004.

[53] A. E. Green and T. R. Steel. Constitutive equations for interacting continua. *Int. J. Eng. Sci.*, 4(4):483–500, 1966.

[54] T. R. Steel. Applications of a theory of interacting continua. *Q. J. Mech. Appl. Math.*, 20(1):57–72, 1967.

[55] M. Massoudi and C. L. Rao. Vertical flow of a multiphase mixture in a channel. *Math. Prob. in Eng.*, 6:505–526, 2001.

[56] B. Loret and F. M. F. Simões. Articular cartilage with intra- and extrafibrillar waters: a chemo-mechanical model. *Mech. Mater.*, 36(5–6):515–541, 2004.

[57] B. Loret and F. M. F. Simões. ICIST Report. DTC, Lisboa, Portugal, 2004.

[58] R. N. Vaishnav, J. T. Young, J. S. Janicki, and D. J. Patel. Nonlinear anisotropic elastic properties of the canine aorta. *Biophys. J.*, 12:1008–1027, 1972.

[59] J. J. Shi, K. R. Rajagopal and A. S. Wineman. Applications of the theory of interacting continua to the diffusion of a fluid through a non-linear elastic media. *Int. J. Eng. Sci.*, 19:871, 1981.

[60] L. R. Treloar. *The Physics of Rubber Elasticity.* Oxford University Press, Inc., 1975.

[61] M. V. Gandhi, K. R. Rajagopal, and A. S. Wineman. Some nonlinear diffusion problems within the context of the theory of interacting continua. *Int. J. Eng. Sci.*, 25(11–12):1441, 1987.

[62] A. S. Wineman and K. R. Rajagopal. Shear induced redistribution of fluid within a uniformly swollen nonlinear elastic cylinder. *Int. J. Eng. Sci.*, 30(11):1583, 1992.

[63] K. R. Rajagopal, A. S. Wineman, and J. J. Shi. The diffusion of a fluid through a highly elastic spherical membrane. *Int. J. Eng. Sci.*, 10:1171, 1983.

[64] D. R. Paul and O. M. Ebra-Lima. Pressure-induced diffusion of organic liquids through highly swollen polymer membranes. *J. Appl. Polym. Sci.*, 14:2201, 1970.

[65] K. R. Rajagopal, A. S. Wineman, and M. Gandhi. On boundary conditions for a certain class of problems in mixture theory. *Int. J. Eng. Sci.*, 24(8):1453, 1986.

[66] K. R. Rajagopal. Diffusion through polymeric solids undergoing large deformations. *Mat. Sci. and Tech.*, 19:1175, 2003.

[67] S. C. Prasad and K. R. Rajagopal. On the diffusion of fluids through solids undergoing large deformations. *Math. Mech. Solids*, 11:291, 2006.

[68] S. Baek and A. R. Srinivasa. Diffusion of a fluid through an elastic solid undergoing large deformation. *Int. J. Non. Mech.*, 39:201, 2004.

[69] S. Baek and T. J. Pence. Inhomogeneous deformation of elastomer gels in equilibrium under saturated and unsaturated conditions. *J. Mech. Phys. Sol.*, 59:561–582, 2011.

[70] S. R. De Groot and P. Mazur. *Non–Equiibrium Thermodynamics.* North-Holland Publishing Company, Amsterdam, 1962.

[71] H. Ziegler. *Progress in Solid Mechanics*, volume 4, chapter 2. North Holland Publishing Company, 1963.

[72] W. Hong, X. Zhao, J. Zhou, and Z. Suo. A theory of coupled diffusion and large deformation in polymeric gels. *J. Mech. Phys. Solids*, 56:1779–1793, 2008.

[73] W. Hong, Z. Liu, and Z. Suo. Inhomogeneous swelling of a gel in equilibrium with a solvent and mechanical load. *Int. J. Solids Struct.*, 46:3282–3289, 2009.

[74] J. Zhang, X. Zhao, Z. Suo, and H. Jiang. A finite element method for transient analysis of concurrent large deformation and mass transport in gels. *J. Appl. Phys.*, 105:093522, 2009.

[75] M. Doi. Gel dynamics. *J. Phys. Soc. Jpn.*, 78(5):052001, 2009.

[76] S. A. Chester and L. Anand. A coupled theory of fluid permeation and large deformations for elastomeric materials. *J. Mech. Phys. Solids*, 58(11):1879–1906, 2010.

[77] P. J. Flory. Molecular theory of rubber elasticity. *Polymer*, 20:1317–1320, 1979.

[78] N. Mills. Incompressible mixtures of newtonian fluids. *Int. J. Eng. Sci.*, 4:97, 1966.

[79] M. Rubenstein and H. Colby. *Polymer Physics*, chapter 7. Oxford University Press, Inc., 2004.

[80] K. Okumura. Toughness of double elastic networks. *Europhys. Lett.*, 67(3):470–476, 2004.

[81] S. Ahmed and F. R. Jones. A review of particulate reinforcement theories for polymer composites. *J. Mater. Sci.*, 25(12):4933–4942, 1990.

[82] E. H. Kerner. The elastic and thermo-elastic properties of composite media. *P. Phys. Soc. Lond. B*, 69(8):808–813, 1956.

[83] S. P. Malone, C. Vosburgh, and C. Cohen. Validity of the swelling method for the determination of the interaction parameter. *Polymer*, 34(24):5149–5153, 1993.

[84] M. J. Crochet and P. M. Naghdi. On constitutive equations for flow of fluid through an elastic solid. *Int. J. Eng. Sci.*, 4:383, 1966.

[85] O. Nishi, K. Nishi, and K. Sakanishi. Inhibition of migrating lens epithelial cells at the capsular bend created by the rectangular optic edge of a posterior chamber intraocular lens. *Ophthalmic Surg. Las.*, 29(7):587–594, 1998.

[86] A. J. Kruger, J. Schauersberger, C. Abela, G. Schild, and M. Amon. Two year results: sharp versus rounded optic edges on silicone lenses. *J. Cataract Refr. Surg.*, 26(4):566 – 570, 2000.

[87] B. L. Mbanga, F. Ye, J. V. Selinger, and R. L. B. Selinger. Modeling elastic instabilities in nematic elastomers. *Phys. Rev. E*, 82:051701, 2010.

[88] E. P. Fahrenthold and B. A. Horban. A hybrid particle–element method for hypervelocity impact simulation. *Int. J. Imp. Eng.*, 23:237–248, 1999.

[89] R. E. Rudd and J. Q. Broughton. Coarse-grained molecular dynamics and the atomic limit of finite elements. *Phys. Rev. B*, 58(10):R5893–R5896, 1998.

[90] J. Q. Broughton, F. F. Abraham, N. Bernstein, and E. Kaxiras. Concurrent coupling of length scales: Methodology and application. *Phys. Rev. B*, 60(4):2391–2403, 1999.

[91] T. J. R. Hughes. *The Finite Element Method: Linear Static and Dynamic Finite Element Analysis*. Dover Publications, Inc., Mineola, New York, 2000.

[92] M. Allen and D. Tildesely. *Computer Simulations of Liquids*. Clarendon, Oxford, 1987.

[93] R. Courant, K. Friedric, and H. Lewy. On the partial difference equations of mathematical physics. *IBM J. Res. Dev.*, 11(2):215, 1967.

[94] B. Christie and A. Gupta. Multifocal intraocular lenses. U. S. Patent # 5,112,351. 2002.

[95] F. C. Pedrotti and L. S. Pedrotti. *Introduction to Optics, 2nd ed.*, page 64. Prentice Hall, Englewood Cliffs, New Jersey, 1993.

[96] D. C. Duffy, J. C. McDonald, O. J. A. Schueller, and G. M. Whitesides. Rapid prototyping of microfluidic systems in poly(dimethylsiloxane). *Analytical Chemistry*, (70):4974–4984, 1998.

[97] D. C. Duffy, O. J. A. Schueller, S. T. Brittain, and G. M. Whitesides. Rapid prototyping of microfluidic switches in poly(dimethylsiloxane) and their actuation by electro-osmotic flow. *J. Micromech. Microeng.*, (9):211–217, 1999.

[98] K. Hosokawa, K. Hanada, and R. Maeda. A polydimethylsiloxane (PDMS) deformable diffraction grating for monitoring of local pressure in microfluidic devices. *J. Micromech. Microeng.*, (12):1–6, 2002.

[99] A. D. Stroock, S. K. W. Dertinger, A. Ajdari, J. Mezic, H. A. Stone, and G. M. Whitesides. Chaotic mixer for microchannels.

[100] G. B. McKenna, K. M. Flynn, and Y. H. Chen. Mechanical and swelling behavior of crosslinked natural–rubber – Consequences of the Flory–Rehner hypothesis. *Polym. Commun.*, 29:272–275, 1988.

[101] A. Olah, E. Hillborg, and G. Vancso. Hydrophobic recovery of uv/ozone treated poly(dimethylsiloxane): adhesion studies by contact mechanics and mechanism of surface modification. *Appl. Surf. Sci.*, 239:410–423, 2005.

[102] C. Lin and M. J. Perry. *Proceedings of IEEE Workshop on Computer Vision: Representation and Control*, page 38. IEEE Community Society Press, Silver Spring, MD, 1982.

[103] R. L. B. Selinger, J. V. Selinger, A. P. Malanoski, and J. M. Schnur. Shape selection in chiral self-assembly. *Phys. Rev. Lett*, 93(15):158103, 2004.